Multiphase kinetics of molecular diffusion, phase transitions and chemical reactions in liquid, semi-solid and glassy organic aerosols

Thomas Berkemeier
geb. am 27.10.1988 in Salzkotten

Dissertation
zur Erlangung des Grades
'Doktor rerum naturalium (Dr. rer. nat.)'
im Promotionsfach Chemie
am Fachbereich Chemie, Pharmazie und Geowissenschaften
der Johannes Gutenberg-Universität in Mainz
Max Planck Graduate Center
Mainz, Juni 2016

I hereby declare that I wrote the dissertation submitted without any unauthorized external assistance and used only sources acknowledged in the work. All textual passages which are appropriated verbatim or paraphrased from published and unpublished texts as well as all information obtained from oral sources are duly indicated and listed in accordance with bibliographical rules. In carrying out this research, I complied with the rules of standard scientific practice as formulated in the statutes of Johannes Gutenberg-University Mainz to insure standard scientific practice.

Abstract

Atmospheric aerosols play a key role in climate, air quality and public health. Aerosol particles enable the formation of clouds and precipitation and can cause adverse health effects upon inhalation, which is of high interest to the general public. Secondary organic aerosols (SOA) constitute a large and abundant subclass of atmospheric particles, but their formation rates and properties are difficult to describe with current models due to the immense variety in their molecular composition. The physical and chemical properties and interactions of organic aerosols are not only strongly dependent on their formation pathway, but are variable upon changing environmental conditions or can be altered by chemical transformation with atmospheric oxidants. Detailed and robust models are needed to describe and unravel the complex gas-particle interactions, which are crucial to comprehend the climate and health effects of organic aerosols.

In this study, kinetic multi-layer models of gas-particle interactions and aerosol surface and bulk chemistry (KM-GAP, KM-SUB) have been developed and applied to elucidate the multiphase chemical kinetics of molecular diffusion, phase transitions and chemical reactions in liquid, semi-solid and glassy organic aerosols. The focal points of this thesis can be summarized as follows:

(1) Development of a comprehensive kinetic framework and classification scheme for gas uptake by aerosol and cloud particles. According to this framework, reaction systems can be associated with one of two major kinetic regimes (reaction-diffusion or mass transfer regime), each of which comprises four distinct limiting cases, characterised by a dominant reaction location (surface or bulk) and a single rate-limiting process (chemical reaction, bulk diffusion, gas-phase diffusion or mass accommodation). This approach enables efficient characterization and comparison of different reaction systems, conditions, and studies in a more consistent and robust manner than previous approaches. For the treatment of secondary organic aerosol formation, the kinetic framework was extended to incorporate gas phase reactions and related to *molecular corridors*, which are ensemble pathways describing the chemical evolution and volatility of organic aerosol components as a function of molar mass and oxygen-to-carbon ratio.

(2) Development of a computational method (Monte-Carlo genetic algorithm, MCGA) for efficient, automated and unbiased global optimization of kinetic model parameters by simultaneous fitting to multiple experimental data sets. The MCGA approach utilizes a sequence of heuristic and deterministic optimization methods to contain the solution of an inverse modelling problem and to explore the space of solutions with similar model output. It tackles an immanent problem of complex models whose extensive kinetic parameter set might not be uniquely determined from a limited set of input data. Ambiguity in the derived kinetic parameter values can be reliably detected using the new set of tools. The method was successfully applied to several reaction systems of practical relevance, including the oligomerisation

of proteins, heterogeneous reactions of HO_x radicals, chemical ageing of organic aerosols and production of reactive oxygen species (ROS) in human lung lining fluid.

(3) Characterization of water uptake and ice nucleation by organic aerosol particles in atmospheric updrafts. Depending on temperature and humidity, the viscosity and phase state of organic particles can change between liquid, semi-solid and glassy. Mass transport by diffusion can be significantly retarded and the phase and morphology of (semi-)solid organic particles can thus significantly deviate from thermodynamic equilibrium. In particular, a semi-solid or glassy phase state may hamper the uptake of water vapour but promote the nucleation of ice. Model simulations along characteristic trajectories of atmospheric updraft show that glassy states and solid/liquid core-shell morphologies can persist long enough to let heterogeneous ice nucleation in the deposition and immersion mode prevail over homogeneous ice nucleation. The predominant cloud formation pathway is strongly dependent on temperature, updraft velocity, particle size and chemical composition. For example, naphthalene or aged pinene SOA particles are more likely to act as heterogeneous ice nuclei than isoprene or fresh pinene SOA particles.

(4) Elucidation of the reaction pathways and rate parameters of ozone uptake and oxidation of liquid, semi-solid and glassy organic matter. The KM-SUB model and MCGA optimization tools were used to analyse a large measurement data set of ozone uptake by the reactive, unsaturated SOA surrogate shikimic acid in a coated-wall flow tube experiment. Characteristic diffusion and reaction rate coefficients were derived from the experimental data and are consistent with earlier assessment of ozone and water diffusivity in SOA. The highly non-linear dependence of the observed ozone uptake coefficients on ozone concentration, relative humidity, and reaction time was successfully reproduced by the model. Moreover, the model revealed a surface oxidation mechanism involving long-lived reactive oxygen intermediates (ROIs), possibly primary ozonides or O atoms. The ROIs appear to enable ozone destruction through an effective self-reaction mechanism, which may be of general relevance for atmospheric aerosols.

(5) Determination of the organic nitrate contribution to secondary organic aerosol formation upon ozonolysis of α-pinene. A radioactive tracer technique was applied to quantify the amount of nitrogen containing compounds incorporated into the particle phase of SOA formed from the monoterpene α-pinene, which is an important atmospheric SOA precursor. The results of kinetic experiments in a flow reactor show that organic nitrates may strongly contribute to new particle formation and nanoparticle growth, during which organic nitrate mass fractions of up to 40% and close correlations with SOA particle number concentrations were observed. The dominant pathway of nitrate formation appears to be the reaction of organic peroxyl radical (RO_2) with nitrogen monoxide (NO) and to be initiated by the oxidation of the alkene precursor with secondary hydroxyl radicals (OH). Measurement and model results suggest that organic nitrates may be among the extremely low volatility organic compounds (ELVOC) that are supposed to play an important role in the nucleation and growth of atmospheric nanoparticles.

Zusammenfassung

Atmosphärische Aerosole spielen eine überaus wichtige Rolle für das Klima, die Luftqualität und die menschliche Gesundheit. Aerosolpartikel ermöglichen die Bildung von Wolken und Niederschlag und können der Gesundheit bei Einatmung erheblich schaden. Sekundäre organische Aerosole (SOA) bilden dabei eine wichtige und überall vorkommende Unterklasse von atmosphärischen Partikeln. Durch die immense Vielfalt in ihrer chemischen Zusammensetzung können ihre Bildung und ihre Eigenschaften jedoch bis heute nicht ausreichend durch Modelle beschrieben werden. Die physikalischen und chemischen Eigenschaften, sowie die Wechselwirkungen organischer Aerosole, sind nicht nur stark von der Art ihrer Bildung abhängig, sondern können auch durch wechselnde Umweltbedingungen und Reaktion mit atmosphärischen Spurengasen verändert werden. Zur Beschreibung der komplexen Gas-Partikel-Wechselwirkungen werden detaillierte und gleichermaßen robuste Modelle benötigt, um die Auswirkungen auf das Klima und die menschliche Gesundheit besser zu verstehen.

Diese Studie beschäftigt sich mit der Entwicklung und Verbesserung kinetischer Mehrschichtenmodelle für die Gas-Partikel-Wechselwirkungen in Aerosolen und Wolken sowie ihrer Oberflächen- und Partikelchemie (KM-GAP, KM-SUB). Diesen werden angewandt auf die Multiphasenkinetiken von molekularen Diffusionsprozessen, Phasenübergängen und chemischen Reaktionen in flüssigen, halbfesten und glasartigen organischen Aerosolen. Die Schwerpunkte dieser Studie können wie folgt zusammengefasst werden:

(1) Entwicklung eines umfassenden Grundkonzeptes und Klassifizierungssystems für die Spurengasaufnahme von Aerosol- und Wolkenpartikeln. Nach diesem Rahmenkonzept können Reaktionssysteme mit einem von zwei übergeordneten Regimes (das Reaktions-Diffusions-Regime und das Massentransfer-Regime) assoziiert werden. Jedes dieser Regimes umfasst vier Grenzfälle kinetischen Verhaltens, welche durch den vorherrschenden Ort der Reaktion (Oberfläche oder Partikelbulk) und einen einzelnen raten-limitierenden Schritt (chemische Reaktion, Bulkdiffusion, Gasphasendiffusion und Massenaufnahme) gekennzeichnet sind. Die Methode ermöglicht die effiziente Charakterisierung und den Vergleich verschiedener Reaktionssysteme, Reaktionsbedingungen und Studien in einer konsistenteren und robusteren Art und Weise als bisherige Herangehensweisen. Für die Untersuchung der Bildung sekundärer organischer Aerosole wurde das kinetische Grundkonzept um chemische Reaktionen in der Gasphase erweitert und in Bezug zu *molekularen Korridoren* gesetzt. Dies sind übergeordnete Reaktionspfade, welche die chemische Evolution und die Flüchtigkeit organischer Aerosolkomponenten als Funktion ihrer Masse und ihres Sauerstoff-zu-Kohlenstoff Verhältnisses beschreiben.

(2) Entwicklung einer Rechenmethode (Monte-Carlo Genetischer Algorithmus, MCGA) für die effiziente, automatisierte und unverzerrte globale Optimierung kinetischer Modellparameter durch simultane Anpassung an viele experimentelle Datensätze. Der MCGA-Ansatz besteht aus einer Sequenz aus heuristischen und deterministischen

Optimierungsmethoden, um die Lösung eines inversen Modellierungsproblems einzugrenzen und den gefundenen Lösungsraum zu erkunden. Diese Herangehensweise bekämpft das immanente Problem komplexer Modelle, deren umfassende kinetische Parametersätze durch endliche Umfänge von Eingabedaten nicht eindeutig bestimmbar sein können. Uneindeutigkeiten in den abgeleiteten kinetischen Parametern können durch die neu entwickelten Werkzeuge nun verlässlich ermittelt werden. Die neue Methode wurde für diverse Reaktionssysteme mit praktischer Relevanz erfolgreich angewandt, darunter die Oligomerisierung von Proteinen, die heterogene Reaktionen von HO_x Radikalen, die chemische Alterung von organischen Aerosolen und die Bildung reaktiver Sauerstoffspezies (englisch *reactive oxygen species*, ROS) in der menschlichen Lungenflüssigkeit.

(3) Charakterisierung der Wasseraufnahme und Eisnukleation organischer Aerosolpartikel in atmosphärischen Aufwinden. In Abhängigkeit von Temperatur und Feuchte kann die Viskosität und der Aggregatzustand von organischen Aerosolpartikeln zwischen flüssig, halbfest und glasartig variieren. Der Transport von Molekülen kann daher signifikant verlangsamt sein und die (halb-)festen Partikel können so in ihrem Aggregatzustand und ihrer Morphologie vom thermodynamischen Gleichgewichtszustand abweichen. Insbesondere halb-feste und glasartige Phasen können die Aufnahme von Wasserdampf erschweren, jedoch die Nukleation von Eis begünstigen. Modellrechnungen entlang charakteristischer Trajektorien atmosphärischer Aufwinde zeigen, dass glasartige Aggregatzustände und fest/flüssige Kern-Schale-Morphologien lange genug existieren können, dass die heterogene Nukleation von Eis im Depositions- und Immersionmodus gegenüber homogener Eisnukleation überwiegt. Der vorherrschende Mechanismus für die Wolkenbildung ist dabei stark von der Temperatur, der Geschwindigkeit des atmosphärischen Aufwindes, der Partikelgröße und ihrer chemischen Zusammensetzung abhängig. So fungieren Naphthalin- und gealterte Pinen-SOA-Partikel mit höherer Wahrscheinlichkeit als heterogene Eiskeime als Isopren- oder frische Pinen-SOA-Partikel.

(4) Aufklärung der Reaktionspfade und -ratenkoeffizienten der Oxidation von flüssiger, halbfester und glasartiger organischer Materie. Das KM-SUB Modell und die MCGA Optimierungsmethode wurden auf einen umfassenden Datensatz der Ozonaufnahme des reaktiven, ungesättigten SOA Stellvertreterstoffes Shikimisäure angewandt. Aus den experimentellen Daten wurden charakteristische Diffusions- und Reaktionsratenkoeffizienten abgeleitet, welche mit früheren Abschätzungen des Diffusionsvermögens von Wasser und Ozon in SOA gut übereinstimmen. Die hochgradig nichtlineare Feuchte-, Konzentrations- und Zeitabhängigkeit der Ozonaufnahme konnte im Modell erfolgreich reproduziert werden. Des Weiteren offenbart das Modell einen Oberflächen-Oxidationsmechanismus unter Bildung reaktiver Sauerstoffzwischenstufen (englisch *reactive oxygen intermediates*, ROI), möglicherweise Primärozonide oder O-Atome. Die Daten legen den Schluss nahe, dass ROIs den Ozonabbau durch einen effektiven Selbstreaktions-Mechanismus ermöglichen, welcher von genereller Bedeutung für atmosphärische Aerosole sein könnte.

(5) Ermittlung des Beitrags von Organonitraten zur Bildung sekundärer organischer Aerosole während der Ozonolyse von α-Pinen, einem wichtigen atmosphärischen Ausgangsstoff. Hierzu wurde eine radioaktive Indikatortechnik angewandt um die Menge an stickstoffhaltigen organischen Verbindungen zu quantifizieren, welche in die Partikelphase von α-Pinen-SOA gelangen. Die kinetischen Experimente in einem Strömungsrohr zeigen, dass Organonitrate stark zur Bildung neuer Partikel und ihrem Wachstum beitragen können. Der Massenanteil der Organonitrate erreichte dabei bis zu 40% und zeigte eine enge Korrelation zur Anzahlkonzentration der SOA-Partikel. Der vorherrschende Bildungspfad ist vermutlich die Reaktion von organischen Peroxylradikalen (RO_2) mit Stickstoffmonoxid (NO) und wird durch die Oxidation des Ausgangsolefins mit dem Hydroxyl-Radikal (OH) initiiert. Die Messungen und Modellrechnungen legen nahe, dass die kondensierenden Organonitrate zur Klasse der extrem schwerflüchtigen organischen Verbindungen (englisch *extremely low volatility organic compounds*, ELVOC) gehören, welche eine wichtige Rolle in der Nukleation und dem Wachstum von atmosphärischen Nanopartikeln spielen könnten.

Contents

1. Introduction

1.1. Atmospheric Aerosols

Atmospheric aerosols have an important impact on Earth's climate by directly scattering and absorbing solar and terrestrial radiation (Intergovernmental Panel on Climate Change (IPCC): Climate, 2013). Aerosol particles serve as nuclei for ice crystals and cloud droplets and hence also indirectly increase Earth's cloud albedo (Twomey, 1977; Albrecht, 1989). Aerosols are thus not only potent climate forcers, but also affect the hydrological cycle (Ramanathan et al., 2001). Aerosol particles are important for atmospheric chemistry as they provide surfaces for heterogeneous chemical reactions, which has implications for the abundance and distribution of reactive gases and other trace compounds in the atmosphere (Andreae and Crutzen, 1997). Unlike many long-lived trace gases, aerosol particles can be removed efficiently from the atmosphere through dry or wet deposition, depending on meteorological conditions (Tsigaridis et al., 2014), but can also reach lifetimes of days to weeks, leading to long-range transport on the hemispheric scale (Williams et al., 2002). Atmospheric aerosols can also cause adverse health effects by damaging respiratory and cardiovascular systems (Pöschl, 2005; Pöschl and Shiraiwa, 2015).

Aerosol particles arise from a variety of sources, which are usually classified due to their primary or secondary nature. Primary aerosols are readily formed particles such as salt particles from sea spray, mineral dust, soot and ash from volcanic eruptions, fossil fuel and biomass burning as well as biological particles such as pollen (Finlayson-Pitts et al., 2000; Seinfeld and Pandis, 2006). Secondary sources of aerosol particles include inorganic gases such as SO_2 or NO_2 and volatile organic compounds (VOC) from natural or anthropogenic origin, which themselves do not form particulates. Upon reaction with atmospheric trace gases such as ozone or the OH radical, these compounds can exhibit sufficiently low vapour pressures to condense as sulphate, nitrate or secondary organic aerosol (SOA) onto pre-existing or newly formed particles (Hallquist et al., 2009; Ziemann and Atkinson, 2012; Kulmala et al., 2013). SOA particles are of high environmental relevance due to their ubiquitous abundance (Zhang et al., 2007; Jimenez et al., 2009) and exhibit a high compositional complexity (Goldstein and Galbally, 2007). Typical precursors for SOA include isoprene and terpenes from biogenic origin as well as aromatics, alkanes, polycyclic aromatic hydrocarbons (PAHs) and fatty acids from anthropogenic origin (Hallquist et al., 2009). After initial oxidation of the precursor gas, further processing of organic compounds can proceed through repeated reaction with atmospheric oxidants, often referred to as chemical ageing, dimerisation (Kalberer, 2004) or autoxidation (Crounse et al., 2013), leading to highly multifunctional compounds,

which have a high likeliness of participating in particle nucleation or initial nanoparticle growth (Ehn et al., 2014).

An important class of oxidised compounds typically encountered in organic aerosols is organic nitrates. These compounds form in the presence of reactive nitrogen oxides ($NO_x \equiv NO$, NO_2) and are incorporated into the particle phase to large degrees as shown in laboratory and field measurements (Day et al., 2010; Rollins et al., 2010; Fry et al., 2014). Formation of organic nitrates affects the total atmospheric budget of oxidised nitrogen and alters the total aerosol mass yield from secondary sources (Kroll et al., 2006; Ng et al., 2007). Organic nitrogen compounds in general can be strong light absorbers, forming so-called brown carbon, which plays an important role in photochemistry and have a net warming effect on earth's climate (Andreae and Gelencsér, 2006; George et al., 2015; Laskin et al., 2015).

The formation, growth and fate of secondary organic aerosols is governed by a multitude of physical and chemical processes, which, given the large diversity of organic molecules that can potentially be formed by the many available precursors, has occupied many researchers in the past decades (Hallquist et al., 2009). However, despite recent advancements in experimental and analytical tools, computational methods and field measurements on oxygenated organics, large parts of the life cycle of atmospheric SOA remain difficult to predict (Zhang et al., 2007; Jimenez et al., 2009; Williams et al., 2010; Donahue et al., 2011; Kroll et al., 2011). Organic aerosols are generally under-represented in global climate models (Kanakidou et al., 2005; Tsigaridis et al., 2014). This is largely due to uncertainties in emission inventories (Granier et al., 2004), but also the result of neglecting processes such as particle-phase chemistry in most chemical transport models (Hallquist et al., 2009; Tsigaridis et al., 2014).

1.2. Multiphase Processes

Heterogeneous reactions are multiphase processes that alter the physical and chemical properties of organic aerosol particles (George and Abbatt, 2010; Shiraiwa et al., 2013), but the effects of these reactions remain poorly understood. Heterogeneous chemical reactions on aerosol particles are traditionally described by calculating gas uptake using so-called "'resistor"' models, which superimpose single physical or chemical processes in analogy to electrical circuits (Hanson et al., 1994; Worsnop et al., 2002). These models provide analytical expressions for simplified limiting cases. Recently, numerical models were developed that allow a more complete consideration of the time- and depth-resolved chemical and physical behaviour of aerosol particles, leading to a better understanding of these reaction systems. These models describe single particles or thin films by division into compartments such as near-surface gas phase, surface and particle bulk, and further subdivision of the particle bulk into thin layers to achieve depth-resolution (Pöschl et al., 2007). Specific models provide a focus on chemistry, such as KM-SUB (Shiraiwa et al., 2010), include gas-particle partitioning, such as KM-GAP (Shiraiwa et al., 2012) or give

a very detailed description of water diffusion, such as the ETH Diffusion Model (Zobrist et al., 2011).

Particular uncertainty in the current understanding of the multiphase chemistry of organic aerosols can be ascribed to the role of molecular transport mechanisms such as surface-bulk exchange and bulk diffusion, which are strongly dependent on particle phase state in their rate (Shiraiwa et al., 2011a). Traditionally, organic aerosols are assumed as liquid, exhibiting instantaneous equilibrium conditions in gas-particle partitioning (Pankow, 1994). Recently, however, studies have shown that organic aerosol particles may exhibit an amorphous (semi-)solid or glassy phase state (Zobrist et al., 2008; Virtanen et al., 2010; Koop et al., 2011), which has far reaching consequences for the way particle transformation and growth have to be described. Typically, substances or mixtures are regarded as (semi-)solid when exhibiting viscosities $> 10^2$ Pa·s (Koop et al., 2011). Bulk viscosity and molecular diffusivity are closely linked through the Stokes-Einstein relation (Einstein, 1905, 1908). Consequences of a non-liquid particle phase state are non-equilibrium growth, leading to incorporation and trapping of molecules with high vapour pressures into the particle phase (Riipinen et al., 2011; Vaden et al., 2011; Perraud et al., 2012); reduced diffusion rates and hence significantly retarded chemical transformation processes (Shiraiwa et al., 2011a) and suppressed hygroscopic growth yielding reduced cloud activation properties (Mikhailov et al., 2009; Pajunoja et al., 2015).

Water uptake and hygroscopic growth of aerosol particles are multiphase processes leading to the activation of aerosols to cloud droplets under water-supersaturated conditions. Such particles are termed active cloud condensation nuclei (CCN), which after growth above a critical diameter quickly take up water (Köhler, 1936). This mechanism is impeded when diffusion of water molecules is kinetically limited by a viscous organic matrix, leading to a discrepancy between equilibrium and actual aerosol composition in atmospheric updraft situations. Another major pathway of cloud formation is the nucleation and growth of ice crystals. At temperatures below 273 K, and at atmospheric pressure, solid ice is the thermodynamically favoured phase of water. Freezing or deposition of solid water onto particles under ice supersaturated conditions ($S_{\mathrm{ice}} > 1$), is however often prohibited by the lack of a nucleus as molecular template, a so-called active heterogeneous ice nucleus (IN) (Hoose and Möhler, 2012). At even higher supersaturations ($S_{\mathrm{ice}} > 1.4$), ice can form homogeneously in the aqueous phase without existence of a solid nucleus (Pruppacher and Klett, 1997; Koop et al., 2000). It was originally assumed that the glassy state of organic aerosols may suppress or retard ice nucleation due to kinetic limitations in water uptake (Zobrist et al., 2008; Murray, 2008), but more recently glassy aerosols were found to be active IN themselves (Murray et al., 2010; Wagner et al., 2012; Wilson et al., 2012).

1.3. Research Objectives

Understanding heterogeneous and multiphase processes in atmospheric aerosols is central for assessing their effects on climate, air quality and public health. Chemical reactions in multiphase systems such as aerosols and clouds are usually strongly coupled to a complex sequence of mass transport processes, which complicates the deduction of individual rates of the entangled processes (Kolb et al., 2010). Current kinetic models are often either too simplified to describe these systems satisfactorily in the case of traditional resistor models or need a large set of input parameters which are difficult to constrain by experiment in the case of recently developed kinetic flux models. Thus, the research goals of this PhD project were to advance the development of kinetic models for gas-particle interactions and aerosol chemistry, to develop supporting tools and to promote the application of these models to systems of relevance for atmospheric chemistry.

The specific objectives and activities of the PhD work can be summarised as follows:

1. Develop a framework of classifying heterogeneous reaction and SOA formation systems by their predominant limiting processes in order to (i) bridge between newly developed kinetic flux models and traditional resistor model formulations and (ii) help directing future laboratory experiments into regimes where kinetic parameters can be isolated and reliably determined.

2. Develop an automated, unbiased optimisation method to reliably fit kinetic models of aerosol chemistry to large sets of laboratory data. Test and demonstrate the suitability of an inverse modelling approach for problems in multiphase chemical kinetic studies, investigate the uniqueness of the obtained kinetic parameter sets, and compare the inferred parameter values, particularly diffusion coefficients, against experimentally determined values.

3. Investigate the competition between cloud droplet formation and ice nucleation on glassy organic aerosol particles for relevant atmospheric trajectories in collaboration with Prof. Dr. Thomas Koop (Bielefeld University).

4. Elucidate the interplay of phase transitions, mass transport and chemical reaction in reference systems of primary and secondary organic aerosol chemistry, such as the oxidation of oleic acid and shikimic acid by ozone. Find mechanisms that describes these systems with a common set of kinetic parameters under a wide range of experimental conditions such as reactant concentration, relative humidity, and aerosol particle size.

5. Investigate the mechanism and yields of organic nitrate formation during nucleation and growth of secondary organic aerosol particles using advanced radioactive-tracer techniques and gas phase kinetic modelling in collaboration with Prof. Dr. Markus Ammann (Paul Scherrer Institute, Villigen, Switzerland).

2. Results and Conclusions

2.1. Overview

The methods developed and the results obtained in the course of this PhD project are described in a total of 15 manuscripts for publication in peer-reviewed scientific journals. The main results of the PhD project are described in six manuscripts (five first-author and one second-author manuscript) which are attached in Appendix B. Five of the papers have already been published in internationally leading journals of atmospheric science and physical chemistry. Further results obtained with the methods developed and applied in the course of this PhD project have been published in nine additional papers, including three second-author papers.

An overview of the studies and of the connections between them is given in Figure 2.1. The main results and conclusions of each study are summarized below.

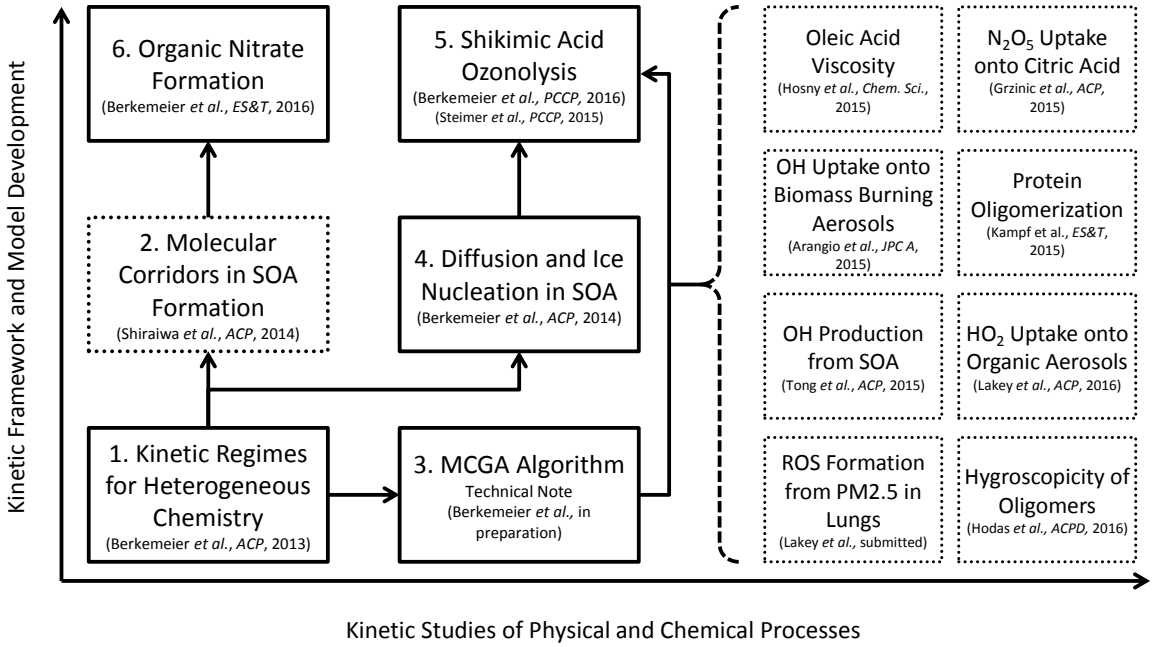

Figure 2.1.: *Structure and results of the PhD project evolving in two dimensions: progress in kinetic framework and model development is indicated on a vertical axis whereas progress with respect to kinetic studies of physical and chemical processes is depicted in the horizontal dimension. Boxes represent projects associated with manuscripts for peer-reviewed publication in an international scientific journal. Dotted boxes indicate co-authored papers. Arrows show connections between studies.*

2.2. Individual Studies

2.2.1. Kinetic Regimes of Aerosol and Cloud Chemistry

A kinetic model framework for gas uptake and heterogeneous reaction in atmospheric aerosols and clouds was developed along with a general classification scheme to use with kinetic models. The framework is capable of describing reaction systems falling in eight specific limiting cases, in accord with previous resistor model approaches, but extends into wider regimes of kinetic behaviour. Major regimes are the reaction-diffusion regime and the mass transfer regime, each including four limiting cases in which reaction is limited by a single process: chemical reaction, bulk diffusion, gas-phase diffusion or mass accommodation. A reaction system can then be described as a superposition of limiting cases, described by three characterisation parameters: the reaction location (particle surface or bulk), the saturation ratio of the reactive trace gas and a parameter assessing the mixing of reactants. For details see Appendix B.1, Berkemeier *et al.*, Atmos. Chem. Phys., 2013.

2.2.2. Molecular Corridors of Secondary Organic Aerosol Formation

The kinetic framework for heterogeneous reaction in atmospheric aerosols was extended to include gas-particle interactions and formation of secondary organic aerosols (SOA), yielding four additional limiting cases of gas-phase reaction and mass transfer. Based on molecular identification of SOA oxidation products, we show that the evolution of SOA from a variety of VOC precursors follows characteristic *molecular corridors* with an inverse correlation between volatility and molar mass. Heterogeneous processing of particles along the corridors follows the earlier determined regimes of heterogeneous reaction, i.e. it is governed by reaction-, diffusion-, or accommodation-limited multiphase chemical kinetics. For details see Appendix B.2, Shiraiwa *et al.*, Atmos. Chem. Phys., 2014.

2.2.3. Monte Carlo Genetic Algorithm for Inverse Modelling

A method was developed that is capable of solving the inverse modelling problem associated with fitting a large set of model input parameters to experimental data. The Monte-Carlo Genetic Algorithm (MCGA) combines direct Monte-Carlo sampling of an optimisation hyper-surface with a genetic algorithm as heuristic global optimisation method. It is shown that the local environment of optimisation results and parameter-parameter correlations can be further explored using a simplex expansion method (SIMEX), which utilizes the principle of simplex optimisation (Nelder-Mead algorithm (Nelder and Mead, 1964)) to perform multi-dimensional variation of optimisation results. These tools can be used to assess the uniqueness of a kinetic parameter set and hence the degree to which physicochemical parameters can be determined. The methods have been successfully applied in several studies and shall soon be published in full detail, see Appendix B.3, Berkemeier *et al.*, in preparation, 2016.

2.2.4. Water Uptake and Ice Nucleation on (Semi-)Solid Organic Particles

A novel semi-empirical method was developed that estimates the diffusion coefficients of water in organic matrices as a function of relative humidity and oxidation degree. Using a numerical diffusion model, time scales of particle deliquescence as well as various ice nucleation pathways were estimated for a wide variety of organic substances, including secondary organic aerosol (SOA) from the oxidation of isoprene, α-pinene, naphthalene, and dodecane. The simulations show that, in typical atmospheric updrafts, glassy states and solid/liquid core-shell morphologies can persist for long enough that heterogeneous ice nucleation can prevail over homogeneous ice nucleation. For details see Appendix B.4, Berkemeier *et al.*, Atmos. Chem. Phys., 2014.

2.2.5. Ozone Uptake and Reactive Oxygen Intermediates on Liquid and (Semi-)Solid Organic Aerosols

A comprehensive data set of ozone uptake by shikimic acid (Steimer et al., 2015), a surrogate compound for secondary organic aerosol (SOA), was described using the kinetic multi-layer model KM-SUB (Shiraiwa et al., 2010). The optimisation of the kinetic parameters was facilitated by the MCGA optimisation method developed earlier (Berkemeier et al., 2016a, in preparation). The data could be described with bulk diffusion coefficients as low as 10^{-12} cm^2 s^{-1} for ozone and 10^{-20} cm^2 s^{-1} for shikimic acid under dry conditions, increasing by several orders of magnitude with increasing relative humidity due to a gradual, moisture-induced phase change. Our results suggest that the chemical reaction mechanism involves long-lived reactive oxygen intermediates, likely primary ozonides or O atoms, which may provide a pathway for self-reaction and catalytic destruction of ozone at the surface. For details see Appendix B.5, Berkemeier *et al.*, Phys. Chem. Chem. Phys., 2016.

2.2.6. New Particle and Organic Nitrate Formation upon Ozonolysis of α-Pinene in the Presence of Nitrogen Oxides

The chemical kinetics and yields of organic nitrate production during new particle formation and growth of secondary organic aerosols (SOA) were investigated using the short-lived radioactive tracer ^{13}N in flow reactor studies of α-pinene oxidation with ozone. Direct and quantitative measurements of the nitrogen content indicate that organic nitrates accounted for ~40% of SOA mass during initial particle formation, decreasing to ~15% upon particle growth to the accumulation mode size range (>100 nm) and depletion of nitrogen monoxide (NO). The experiments show a tight correlation between organic nitrate content and SOA particle number concentrations, implying that at least a fraction of the condensing organic nitrates are extremely low volatility organic compounds (ELVOC) that may play an important role in the nucleation and growth of

atmospheric nanoparticles. A lumped gas-phase mechanism is derived from the Master Chemical Mechanism (Jenkin et al., 1997; Saunders et al., 2003) to describe SOA and organic nitrate formation at a largely reduced complexity. For details see Appendix B.6, Berkemeier *et al*., Environ. Sci. Technol., 2016.

2.3. Conclusions and Outlook

This PhD project continued and extended the development of a family of kinetic flux models of aerosol and cloud chemistry based on the PRA framework (Pöschl et al., 2007): the kinetic multi-layer model of surface and bulk chemistry, KM-SUB (Shiraiwa et al., 2010), and the kinetic multi-layer model of gas-particle interactions in aerosols and clouds, KM-GAP (Shiraiwa et al., 2012). Using computational tools and frameworks for analysis of model behaviour, elusive kinetic parameters such as reaction rate coefficients and diffusion coefficients were obtained for multiphase chemical reaction systems, which were not readily accessible for kinetic modelling in the past. These tools allowed to accurately describe gas uptake onto organic aerosols over the entire range of phase states from liquid to (semi-)solid and provided additional evidence for the formation of long-lived reactive oxygen intermediates (ROIs) on the surface of atmospheric aerosols (Shiraiwa et al., 2011b; Berkemeier et al., 2016b, in preparation).

For the first time, a method for the estimation of water diffusion coefficients in secondary organic aerosol particles was developed and has meanwhile been confirmed to predict diffusion with good accuracy (Price et al., 2015; Lienhard et al., 2015). Utilizing these diffusion coefficients, the possible pathways of cloud condensation and ice nucleation by (semi-)solid organic aerosols were predicted and assigned to certain temperature and updraft scenarios.

The formation of organic nitrates in secondary organic aerosols was investigated using a radioactive-tracer technique. The experiments provided quantitative formation yields for this substance class that, while showing a high contribution of up to 40% of particle mass, is inaccessible with common analytical methods. The results revealed new insights into their formation mechanism and support that organic nitrates are among the extremely low volatility organic compounds (ELVOC) that were found to play an important role in the nucleation and growth of atmospheric nanoparticles (Ehn et al., 2014; Tröstl et al., 2016).

Going forward, model systems of increasing complexity can be described and mechanisms developed to add to the holistic picture of the life cycle of atmospheric aerosols from nucleation over nanoparticle growth to condensation, evaporation and chemical transformation. Future challenges include the treatment of more complex reaction mixtures, coupling detailed gas- and particle-phase chemistry and dealing with inhomogeneous or phase-separated particles. For many of these applications, the molecular mechanisms of interfacial processes play a crucial role and should be further investigated with the developed process models in combination with data from laboratory experiments and field measurements.

3. Bibliography

Albrecht, B. A.: Aerosols, Cloud Microphysics, and Fractional Cloudiness, Science, 245, 1227–1230, 1989.

Andreae, M. O. and Crutzen, P. J.: Atmospheric Aerosols: Biogeochemical Sources and Role in Atmospheric Chemistry, Science, 276, 1052–1058, 1997.

Andreae, M. O. and Gelencsér, A.: Black carbon or brown carbon? The nature of light-absorbing carbonaceous aerosols, Atmos. Chem. Phys., 6, 3131–3148, 2006.

Berkemeier, T., Ammann, M., Krieger, U. K., Peter, T., Spichtinger, P., Pöschl, U., Shiraiwa, M., and Huisman, A. J.: *Technical Note*: Monte-Carlo genetic algorithm (MCGA) for model analysis of multiphase chemical kinetics using multiple experimental data sets, in preparation, 2016a.

Berkemeier, T., Huisman, A. J., Ammann, M., Krieger, U. K., Peter, T., Shiraiwa, M., and Pöschl, U.: Reconciling multiphase reactivity of oleic acid with ozone using a kinetic flux model, in preparation, 2016b.

Crounse, J. D., Nielsen, L. B., Jørgensen, S., Kjaergaard, H. G., and Wennberg, P. O.: Autoxidation of organic compounds in the atmosphere, J. Phys. Chem. Lett., 4, 3513–3520, 2013.

Day, D. A., Liu, S., Russell, L. M., and Ziemann, P. J.: Organonitrate group concentrations in submicron particles with high nitrate and organic fractions in coastal southern California, Atmos. Environ., 44, 1970–1979, 2010.

Donahue, N. M., Epstein, S. a., Pandis, S. N., and Robinson, a. L.: A two-dimensional volatility basis set: 1. organic-aerosol mixing thermodynamics, Atmos. Chem. Phys., 11, 3303–3318, 2011.

Ehn, M., Thornton, J. A., Kleist, E., Sipilä, M., Junninen, H., Pullinen, I., Springer, M., Rubach, F., Tillmann, R., Lee, B., Lopez-Hilfiker, F., Andres, S., Acir, I.-H., Rissanen, M., Jokinen, T., Schobesberger, S., Kangasluoma, J., Kontkanen, J., Nieminen, T., Kurtén, T., Nielsen, L. B., Jørgensen, S., Kjaergaard, H. G., Canagaratna, M., Maso, M. D., Berndt, T., Petäjä, T., Wahner, A., Kerminen, V.-M., Kulmala, M., Worsnop, D. R., Wildt, J., and Mentel, T. F.: A large source of low-volatility secondary organic aerosol, Nature, 506, 476–479, 2014.

Einstein, A.: Über die von der molekularkinetischen Theorie der Wärme geforderte Bewegung von in ruhenden Flüssigkeiten suspendierten Teilchen, Ann. Phys., 322, 549–560, 1905.

Einstein, A.: Elementare Theorie der Brownschen Bewegung, Zeit. f. Elektrochem., 14, 235–239, 1908.

Finlayson-Pitts, B. J., Pitts, J. N., and Jr.: Chemistry of the Upper and Lower Atmosphere, Academic Press, San Diego, 2000.

Fry, J. L., Draper, D. C., Barsanti, K. C., Smith, J. N., Ortega, J., Winkler, P. M., Lawler, M. J., Brown, S. S., Edwards, P. M., Cohen, R. C., and Lee, L.: Secondary Organic Aerosol Formation and Organic Nitrate Yield from NO_3 Oxidation of Biogenic Hydrocarbons, Environ. Sci. Technol., 48, 11 944–11 953, 2014.

George, C., Ammann, M., D'Anna, B., Donaldson, D. J., and Nizkorodov, S. A.: Heterogeneous Photochemistry in the Atmosphere, Chem. Rev., 115, 4218–4258, 2015.

George, I. J. and Abbatt, J. P. D.: Heterogeneous oxidation of atmospheric aerosol particles by gas-phase radicals, Nat. Chem., 2, 713–722, 2010.

Goldstein, A. H. and Galbally, I. E.: Known and Unexplored Organic Constituents in the Earth's Atmosphere, Environ. Sci. Technol., 41, 1514–1521, 2007.

Granier, C., Artaxo, P., and Reeves, C. E., eds.: Emissions of Atmospheric Trace Compounds, Kluwer Academic Publishers, Dordrecht, The Netherlands, 2004.

Hallquist, M., Wenger, J. C., Baltensperger, U., Rudich, Y., Simpson, D., Claeys, M., Dommen, J., Donahue, N. M., George, C., Goldstein, A. H., Hamilton, J. F., Herrmann, H., Hoffmann, T., Iinuma, Y., Jang, M., Jenkin, M. E., Jimenez, J. L., Kiendler-Scharr, A., Maenhaut, W., McFiggans, G., Mentel, T. F., Monod, A., Prévôt, A. S. H., Seinfeld, J. H., Surratt, J. D., Szmigielski, R., and Wildt, J.: The formation, properties and impact of secondary organic aerosol: current and emerging issues, Atmos. Chem. Phys., 9, 5155–5236, 2009.

Hanson, D. R., Ravishankara, A. R., and Solomon, S.: Heterogeneous reactions in sulfuric acid aerosols: A framework for model calculations, J. Geophys. Res., 99, 3615–3629, 1994.

Hoose, C. and Möhler, O.: Heterogeneous ice nucleation on atmospheric aerosols: a review of results from laboratory experiments, Atmos. Chem. Phys., 12, 9817–9854, 2012.

Intergovernmental Panel on Climate Change (IPCC): Climate, ed.: Climate Change 2013: The Physical Science Basis, Cambridge University Press, Cambridge, United Kingdom and New York, NY, USA, 2013.

Jenkin, M. E., Saunders, S. M., and Pilling, M. J.: The tropospheric degradation of volatile organic compounds: a protocol for mechanism development, Atmos. Environ., 31, 81–104, 1997.

Jimenez, J. L., Canagaratna, M. R., Donahue, N. M., Prévôt, A. S. H., Zhang, Q., Kroll, J. H., DeCarlo, P. F., Allan, J. D., Coe, H., Ng, N. L., Aiken, A. C., Docherty, K. S., Ulbrich, I. M., Grieshop, A. P., Robinson, A. L., Duplissy, J., Smith, J. D., Wilson, K. R., Lanz, V. A., Hueglin, C., Sun, Y. L., Tian, J., Laaksonen, A., Raatikainen, T., Rautiainen, J., Vaattovaara, P., Ehn, M., Kulmala, M., Tomlinson, J. M., Collins, D. R., Cubison, M. J., Dunlea, E. J., Huffman, J. A., Onasch, T. B., Alfarra, M. R., Williams, P. I., Bower, K., Kondo, Y., Schneider, J., Drewnick, F., Borrmann, S., Weimer, S., Demerjian, K., Salcedo, D., Cottrell, L., Griffin, R., Takami, A., Miyoshi, T., Hatakeyama, S., Shimono, A., Sun, J. Y., Zhang, Y. M., Dzepina, K., Kimmel, J. R., Sueper, D., Jayne, J. T., Herndon, S. C., Trimborn, A. M., Williams, L. R., Wood, E. C., Middlebrook, A. M., Kolb, C. E., Baltensperger, U., and Worsnop, D. R.: Evolution of organic aerosols in the atmosphere, Science, 326, 1525–1529, 2009.

Kalberer, M.: Identification of Polymers as Major Components of Atmospheric Organic Aerosols, Science, 303, 1659–1662, 2004.

Kanakidou, M., Seinfeld, J. H., Pandis, S. N., Barnes, I., Dentener, F. J., Facchini, M. C., Van Dingenen, R., Ervens, B., Nenes, A., Nielsen, C. J., Swietlicki, E., Putaud, J. P., Balkanski, Y., Fuzzi, S., Horth, J., Moortgat, G. K., Winterhalter, R., Myhre, C. E. L., Tsigaridis, K., Vignati, E., Stephanou, E. G., and Wilson, J.: Organic aerosol and global climate modelling: a review, Atmos. Chem. Phys., 5, 1053–1123, 2005.

Köhler, H.: The nucleus in and the growth of hygroscopic droplets, Trans. Faraday Soc., 32, 1152–1161, 1936.

Kolb, C. E., Cox, R. A., Abbatt, J. P. D., Ammann, M., Davis, E. J., Donaldson, D. J., Garrett, B. C., George, C., Griffiths, P. T., Hanson, D. R., Kulmala, M., McFiggans, G., Pöschl, U., Riipinen, I., Rossi, M. J., Rudich, Y., Wagner, P. E., Winkler, P. M., Worsnop, D. R., and O' Dowd, C. D.: An overview of current issues in the uptake of atmospheric trace gases by aerosols and clouds, Atmos. Chem. Phys., 10, 10 561–10 605, 2010.

Koop, T., Luo, B., Tsias, A., and Peter, T.: Water activity as the determinant for homogeneous ice nucleation in aqueous solutions, Nature, 406, 611–614, 2000.

Koop, T., Bookhold, J., Shiraiwa, M., and Pöschl, U.: Glass transition and phase state of organic compounds: dependency on molecular properties and implications for secondary organic aerosols in the atmosphere, Phys. Chem. Chem. Phys., 13, 19 238–19 255, 2011.

Kroll, J. H., Ng, N. L., Murphy, S. M., Flagan, R. C., and Seinfeld, J. H.: Secondary Organic Aerosol Formation from Isoprene Photooxidation, Environ. Sci. Technol., 40, 1869–1877, 2006.

Kroll, J. H., Donahue, N. M., Jimenez, J. L., Kessler, S. H., Canagaratna, M. R., Wilson, K. R., Altieri, K. E., Mazzoleni, L. R., Wozniak, A. S., Bluhm, H., Mysak, E. R., Smith, J. D., Kolb, C. E., and Worsnop, D. R.: Carbon oxidation state as a metric for describing the chemistry of atmospheric organic aerosol, Nat. Chem., 3, 133–139, 2011.

Kulmala, M., Kontkanen, J., Junninen, H., Lehtipalo, K., Manninen, H. E., Nieminen, T., Petaja, T., Sipila, M., Schobesberger, S., Rantala, P., Franchin, A., Jokinen, T., Jarvinen, E., Aijala, M., Kangasluoma, J., Hakala, J., Aalto, P. P., Paasonen, P., Mikkila, J., Vanhanen, J., Aalto, J., Hakola, H., Makkonen, U., Ruuskanen, T., Mauldin, R. L., Duplissy, J., Vehkamaki, H., Back, J., Kortelainen, A., Riipinen, I., Kurten, T., Johnston, M. V., Smith, J. N., Ehn, M., Mentel, T. F., Lehtinen, K. E. J., Laaksonen, A., Kerminen, V.-M., and Worsnop, D. R.: Direct Observations of Atmospheric Aerosol Nucleation, Science, 339, 943–946, 2013.

Laskin, A., Laskin, J., and Nizkorodov, S. a.: Chemistry of Atmospheric Brown Carbon, Chem. Rev., 115, 4335–4382, 2015.

Lienhard, D. M., Huisman, A. J., Krieger, U. K., Rudich, Y., Marcolli, C., Luo, B. P., Bones, D. L., Reid, J. P., Lambe, A. T., Canagaratna, M. R., Davidovits, P., Onasch, T. B., Worsnop, D. R., Steimer, S. S., Koop, T., and Peter, T.: Viscous organic aerosol particles in the upper troposphere: diffusivity-controlled water uptake and ice nucleation?, Atmos. Chem. Phys., 15, 13 599–13 613, 2015.

Mikhailov, E., Vlasenko, S., Martin, S. T., Koop, T., and Pöschl, U.: Amorphous and crystalline aerosol particles interacting with water vapor: conceptual framework and experimental evidence for restructuring, phase transitions and kinetic limitations, Atmos. Chem. Phys., 9, 9491–9522, 2009.

Murray, B. J.: Inhibition of ice crystallisation in highly viscous aqueous organic acid droplets, Atmos. Chem. Phys., 8, 5423–5433, 2008.

Murray, B. J., Wilson, T. W., Dobbie, S., Cui, Z., Al-Jumur, S. M. R. K., Möhler, O., Schnaiter, M., Wagner, R., Benz, S., Niemand, M., Saathoff, H., Ebert, V., Wagner, S., and Kärcher, B.: Heterogeneous nucleation of ice particles on glassy aerosols under cirrus conditions, Nat. Geosci., 3, 233–237, 2010.

Nelder, J. and Mead, R.: A simplex method for function minimization, Comput. J., 7, 308–313, 1964.

Ng, N. L., Chhabra, P. S., Chan, A. W. H., Surratt, J. D., Kroll, J. H., Kwan, A. J., McCabe, D. C., Wennberg, P. O., Sorooshian, A., Murphy, S. M., Dalleska, N. F., Flagan, R. C., and Seinfeld, J. H.: Effect of NOx level on secondary organic aerosol (SOA) formation from the photooxidation of terpenes, Atmos. Chem. Phys., 7, 5159–5174, 2007.

Pajunoja, A., Lambe, A. T., Hakala, J., Rastak, N., Cummings, M. J., Brogan, J. F., Hao, L., Paramonov, M., Hong, J., Prisle, N. L., Malila, J., Romakkaniemi, S., Lehtinen, K. E. J.,

Laaksonen, A., Kulmala, M., Massoli, P., Onasch, T. B., Donahue, N. M., Riipinen, I., Davidovits, P., Worsnop, D. R., Petäjä, T., and Virtanen, A.: Adsorptive uptake of water by semisolid secondary organic aerosols, Geophys. Res. Lett., 42, 3063–3068, 2015.

Pankow, J. F.: An absorption model of gas/particle partitioning of organic compounds in the atmosphere, Atmos. Environ., 28, 185–188, 1994.

Perraud, V., Bruns, E. A., Ezell, M. J., Johnson, S. N., Yu, Y., Alexander, M. L., Zelenyuk, A., Imre, D., Chang, W. L., Dabdub, D., Pankow, J. F., and Finlayson-Pitts, B. J.: Nonequilibrium atmospheric secondary organic aerosol formation and growth, Proc. Natl. Acad. Sci. USA, 109, 2836–2841, 2012.

Pöschl, U.: Atmospheric aerosols: composition, transformation, climate and health effects, Angew. Chem. Int. Ed. (English), 44, 7520–7540, 2005.

Pöschl, U. and Shiraiwa, M.: Multiphase Chemistry at the Atmosphere-Biosphere Interface Influencing Climate and Public Health in the Anthropocene, Chem. Rev., 115, 4440–4475, 2015.

Pöschl, U., Rudich, Y., and Ammann, M.: Kinetic model framework for aerosol and cloud surface chemistry and gas-particle interactions Part 1: General equations, parameters, and terminology, Atmos. Chem. Phys., 7, 5989–6023, 2007.

Price, H. C., Mattsson, J., Zhang, Y., Bertram, A. K., Davies, J. F., Grayson, J. W., Martin, S. T., O'Sullivan, D., Reid, J. P., Rickards, A. M. J., and Murray, B. J.: Water diffusion in atmospherically relevant α-pinene secondary organic material, Chem. Sci., 6, 4876–4883, 2015.

Pruppacher, H. R. and Klett, J. D.: Microphysics of Clouds and Precipitation, Kluwer Academic Publishers, Dordrecht, 1997.

Ramanathan, V., Crutzen, P. J., Kiehl, J. T., and Rosenfeld, D.: Aerosols, Climate, and the Hydrological Cycle, Science, 294, 2119–2124, 2001.

Riipinen, I., Pierce, J. R., Yli-Juuti, T., Nieminen, T., Häkkinen, S., Ehn, M., Junninen, H., Lehtipalo, K., Petäjä, T., Slowik, J., Chang, R., Shantz, N. C., Abbatt, J., Leaitch, W. R., Kerminen, V.-M., Worsnop, D. R., Pandis, S. N., Donahue, N. M., and Kulmala, M.: Organic condensation: a vital link connecting aerosol formation to cloud condensation nuclei (CCN) concentrations, Atmos. Chem. Phys., 11, 3865–3878, 2011.

Rollins, A. W., Smith, J. D., Wilson, K. R., and Cohen, R. C.: Real Time In Situ Detection of Organic Nitrates in Atmospheric Aerosols, Environ. Sci. Technol., 44, 5540–5545, 2010.

Saunders, S. M., Jenkin, M. E., Derwent, R. G., and Pilling, M. J.: Protocol for the development of the Master Chemical Mechanism, MCM v3 (Part A): tropospheric

degradation of non-aromatic volatile organic compounds, Atmos. Chem. Phys., 3, 161–180, 2003.

Seinfeld, J. H. and Pandis, S. N.: Atmospheric chemistry and physics: from air pollution to climate change, Wiley, New York, 2006.

Shiraiwa, M., Pfrang, C., and Pöschl, U.: Kinetic multi-layer model of aerosol surface and bulk chemistry (KM-SUB): the influence of interfacial transport and bulk diffusion on the oxidation of oleic acid by ozone, Atmos. Chem. Phys., 10, 3673–3691, 2010.

Shiraiwa, M., Ammann, M., Koop, T., and Pöschl, U.: Gas uptake and chemical aging of semisolid organic aerosol particles, Proc. Natl. Acad. Sci. USA, 108, 11 003–11 008, 2011a.

Shiraiwa, M., Sosedova, Y., Rouvière, A., Yang, H., Zhang, Y., Abbatt, J. P. D., Ammann, M., and Pöschl, U.: The role of long-lived reactive oxygen intermediates in the reaction of ozone with aerosol particles, Nat. Chem., 3, 291–295, 2011b.

Shiraiwa, M., Pfrang, C., Koop, T., and Pöschl, U.: Kinetic multi-layer model of gas-particle interactions in aerosols and clouds (KM-GAP): linking condensation, evaporation and chemical reactions of organics, oxidants and water, Atmos. Chem. Phys., 12, 2777–2794, 2012.

Shiraiwa, M., Yee, L. D., Schilling, K. A., Loza, C. L., Craven, J. S., Zuend, A., Ziemann, P. J., and Seinfeld, J. H.: Size distribution dynamics reveal particle-phase chemistry in organic aerosol formation, Proc. Natl. Acad. Sci. USA, 110, 11 746–11 750, 2013.

Steimer, S. S., Berkemeier, T., Gilgen, A., Krieger, U. K., Peter, T., Shiraiwa, M., and Ammann, M.: Shikimic acid ozonolysis kinetics of the transition from liquid aqueous solution to highly viscous glass, Phys. Chem. Chem. Phys., 17, 31 101–31 109, 2015.

Tröstl, J., Chuang, W. K., Gordon, H., Heinritzi, M., Yan, C., Molteni, U., Ahlm, L., Frege, C., Bianchi, F., Wagner, R., Simon, M., Lehtipalo, K., Williamson, C., Craven, J. S., Duplissy, J., Adamov, A., Almeida, J., Bernhammer, A.-K., Breitenlechner, M., Brilke, S., Dias, A., Ehrhart, S., Flagan, R. C., Franchin, A., Fuchs, C., Guida, R., Gysel, M., Hansel, A., Hoyle, C. R., Jokinen, T., Junninen, H., Kangasluoma, J., Keskinen, H., Kim, J., Krapf, M., Kürten, A., Laaksonen, A., Lawler, M., Leiminger, M., Mathot, S., Möhler, O., Nieminen, T., Onnela, A., Petäjä, T., Piel, F. M., Miettinen, P., Rissanen, M. P., Rondo, L., Sarnela, N., Schobesberger, S., Sengupta, K., Sipilä, M., Smith, J. N., Steiner, G., Tomè, A., Virtanen, A., Wagner, A. C., Weingartner, E., Wimmer, D., Winkler, P. M., Ye, P., Carslaw, K. S., Curtius, J., Dommen, J., Kirkby, J., Kulmala, M., Riipinen, I., Worsnop, D. R., Donahue, N. M., and Baltensperger, U.: The role of low-volatility organic compounds in initial particle growth in the atmosphere, Nature, 533, 527–531, 2016.

Tsigaridis, K., Daskalakis, N., Kanakidou, M., Adams, P. J., Artaxo, P., Bahadur, R., Balkanski, Y., Bauer, S. E., Bellouin, N., Benedetti, A., Bergman, T., Berntsen, T. K., Beukes, J. P., Bian, H., Carslaw, K. S., Chin, M., Curci, G., Diehl, T., Easter, R. C., Ghan, S. J., Gong, S. L., Hodzic, A., Hoyle, C. R., Iversen, T., Jathar, S., Jimenez, J. L., Kaiser, J. W., Kirkevåg, A., Koch, D., Kokkola, H., H. Lee, Y., Lin, G., Liu, X., Luo, G., Ma, X., Mann, G. W., Mihalopoulos, N., Morcrette, J. J., Möller, J. F., Myhre, G., Myriokefalitakis, S., Ng, N. L., O'Donnell, D., Penner, J. E., Pozzoli, L., Pringle, K. J., Russell, L. M., Schulz, M., Sciare, J., Seland, Shindell, D. T., Sillman, S., Skeie, R. B., Spracklen, D., Stavrakou, T., Steenrod, S. D., Takemura, T., Tiitta, P., Tilmes, S., Tost, H., Van Noije, T., Van Zyl, P. G., Von Salzen, K., Yu, F., Wang, Z., Wang, Z., Zaveri, R. A., Zhang, H., Zhang, K., Zhang, Q., and Zhang, X.: The AeroCom evaluation and intercomparison of organic aerosol in global models, Atmos. Chem. Phys., 14, 10 845–10 895, 2014.

Twomey, S.: The Influence of Pollution on the Shortwave Albedo of Clouds, J. Atmos. Sci., 34, 1149–1152, 1977.

Vaden, T. D., Imre, D., Beranek, J., Shrivastava, M., and Zelenyuk, A.: Evaporation kinetics and phase of laboratory and ambient secondary organic aerosol, Proc. Natl. Acad. Sci. USA, 108, 2190–2195, 2011.

Virtanen, A., Joutsensaari, J., Koop, T., Kannosto, J., Yli-Pirila, P., Leskinen, J., Makela, J. M., Holopainen, J. K., Pöschl, U., Kulmala, M., Worsnop, D. R., and Laaksonen, A.: An amorphous solid state of biogenic secondary organic aerosol particles, Nature, 467, 824–827, 2010.

Wagner, R., Möhler, O., Saathoff, H., Schnaiter, M., Skrotzki, J., Leisner, T., Wilson, T. W., Malkin, T. L., and Murray, B. J.: Ice cloud processing of ultra-viscous/glassy aerosol particles leads to enhanced ice nucleation ability, Atmos. Chem. Phys., 12, 8589–8610, 2012.

Williams, B. J., Goldstein, A. H., Kreisberg, N. M., and Hering, S. V.: In situ measurements of gas/particle-phase transitions for atmospheric semivolatile organic compounds., Proc. Natl. Acad. Sci. USA, 107, 6676–6681, 2010.

Williams, J., de Reus, M., Krejci, R., Fischer, H., and Ström, J.: Application of the variability-size relationship to atmospheric aerosol studies: estimating aerosol lifetimes and ages, Atmos. Chem. Phys., 2, 133–145, 2002.

Wilson, T. W., Murray, B. J., Wagner, R., Möhler, O., Saathoff, H., Schnaiter, M., Skrotzki, J., Price, H. C., Malkin, T. L., Dobbie, S., and Al-Jumur, S. M. R. K.: Glassy aerosols with a range of compositions nucleate ice heterogeneously at cirrus temperatures, Atmos. Chem. Phys., 12, 8611–8632, 2012.

Worsnop, D. R., Morris, J. W., Shi, Q., Davidovits, P., and Kolb, C. E.: A chemical kinetic model for reactive transformations of aerosol particles, Geophys. Res. Lett., 29, 57, 2002.

Zhang, Q., Jimenez, J. L., Canagaratna, M. R., Allan, J. D., Coe, H., Ulbrich, I., Alfarra, M. R., Takami, A., Middlebrook, A. M., Sun, Y. L., Dzepina, K., Dunlea, E., Docherty, K., DeCarlo, P. F., Salcedo, D., Onasch, T., Jayne, J. T., Miyoshi, T., Shimono, A., Hatakeyama, S., Takegawa, N., Kondo, Y., Schneider, J., Drewnick, F., Borrmann, S., Weimer, S., Demerjian, K., Williams, P., Bower, K., Bahreini, R., Cottrell, L., Griffin, R. J., Rautiainen, J., Sun, J. Y., Zhang, Y. M., and Worsnop, D. R.: Ubiquity and dominance of oxygenated species in organic aerosols in anthropogenically-influenced Northern Hemisphere midlatitudes, Geophys. Res. Lett., 34, L13 801, 2007.

Ziemann, P. J. and Atkinson, R.: Kinetics, products, and mechanisms of secondary organic aerosol formation, Chem. Soc. Rev., 41, 6582, 2012.

Zobrist, B., Marcolli, C., Pedernera, D. A., and Koop, T.: Do atmospheric aerosols form glasses?, Atmos. Chem. Phys., 8, 5221–5244, 2008.

Zobrist, B., Soonsin, V., Luo, B. P., Krieger, U. K., Marcolli, C., Peter, T., and Koop, T.: Ultra-slow water diffusion in aqueous sucrose glasses, Phys. Chem. Chem. Phys., 13, 3514–3526, 2011.

A. Personal List of Publications

Journal Articles

1. Berkemeier, T., Ammann, M., Krieger, U. K., Peter, T., Spichtinger, P., Pöschl, U., Shiraiwa, M., and Huisman, A. J.: *Technical Note*: Monte-Carlo genetic algorithm (MCGA) for model analysis of multiphase chemical kinetics using multiple experimental data sets, *in preparation*.

2. Lakey, P. S. J., Berkemeier, T., Tong, H., Arangio, A. M., Lucas, K., Pöschl, U., and Shiraiwa, M.: Chemical exposure-response relationship between air pollutants and reactive oxygen species in the human respiratory tract, *submitted*, (2016).

3. Berkemeier, T., Ammann, M., Mentel, T. F., Pöschl, U., and Shiraiwa, M.: Organic nitrate contribution to new particle formation and growth in secondary organic aerosols from α-pinene ozonolysis, *Environ. Sci. Technol.*, DOI:10.1021/acs.est.6b-00961, (2016).

4. Hodas, N., Zuend, A., Schilling, K., Berkemeier, T., Shiraiwa, M., Flagan, R. C., and Seinfeld, J. H.: Discontinuities in hygroscopic growth below and above water saturation for laboratory surrogates of oligomers in organic atmospheric aerosols, *Atmos. Chem. Phys. Discuss.*, DOI:10.5194/acp-2016-236, (2016).

5. Lakey, P. S. J., Berkemeier, T., Krapf, M., Dommen, J., Steimer, S. S., Whalley, L. K., Ingham, T., Baeza-Romero, M. T., Pöschl, U., Shiraiwa, M., Ammann, M., and Heard, D. E.: The effect of viscosity on the HO_2 uptake by sucrose and secondary organic aerosol particles, *Atmos. Chem. Phys. Discuss.*, DOI:10.5194/acp-2016-284, (2016).

6. Berkemeier, T., Steimer, S. S., Krieger, U. K., Peter, T., Pöschl, U., Ammann, M., and Shiraiwa, M.: Ozone uptake on glassy, semi-solid and liquid organic matter and the role of reactive oxygen intermediates in atmospheric aerosol chemistry, *Phys. Chem. Chem. Phys.* **18**, 12662-12674, (2016).

7. Tong, H., Arangio, A. M., Lakey, P. S. J., Berkemeier, T., Liu, F., Kampf, C. J., Pöschl, U., and Shiraiwa, M.: Hydroxyl radicals from secondary organic aerosol decomposition in water, *Atmos. Chem. Phys.* **16**, 1761-1771, (2016).

8. Hosny, N. A., Fitzgerald, C., Vysniauskas, A., Athanasiadis, T., Berkemeier, T., Uygur, N., Pöschl, U., Shiraiwa, M., Kalberer M., Pope, F. D., Kuimova, M. K.: Direct

imaging of changes in aerosol particle viscosity upon hydration and chemical aging, *Chem. Sci.* **7**, 1357-1367, (2016).

9. Weber, B., Berkemeier, T., Ruckteschler, N., Caesar, J., Heintz, H., Ritter, H., and Braß, H.: Development and calibration of a novel sensor to analyze the water content of biological soil crusts and surface soils, *Methods Ecol. Evol.* **7**, 14-22, (2016).

10. Steimer, S. S., Berkemeier, T., Gilgen, A., Krieger, U. K., Peter, T., Shiraiwa, M., and Ammann, M.: Shikimic acid ozonolysis kinetics in the transition from liquid aqueous solution to highly viscous glass, *Phys. Chem. Chem. Phys.* **17**, 31101-31109, (2015).

11. Kampf, C. J., Liu, F., Reinmuth-Selzle, K., Berkemeier, T., Meusel, H., Shiraiwa, M., and Pöschl, U.: Proteine Cross-Linking ad Oligomerization through Dityrosine Formation upon Exposure to Ozone, *Environ. Sci. Technol.* **49**, 10859-10866, (2015).

12. Gržinić, G., Bartels-Rausch, T., Berkemeier, T., Türler, A., and Ammann, M.: Viscosity controls humidity dependence of N_2O_5 uptake to citric acid aerosol, *Atmos. Chem. Phys.* **15**, 13615-13625, (2015).

13. Arangio, A., Slade, J. H., Berkemeier, T., Pöschl, U., Knopf, D. A., and Shiraiwa M.: Multiphase chemical kinetics of OH radical uptake by molecular organic markers of biomass burning aerosols: humidity and temperature dependence, surface reaction and bulk diffusion, *J. Phys. Chem. A* **119**, 4533-4544, (2015).

14. Berkemeier, T., Shiraiwa, M., Pöschl, U., and Koop, T.: Competition between water uptake and ice nucleation by glassy organic aerosol particles. *Atmos. Chem. Phys.* **14**, 12513-12531, (2014).

15. Budke, C., Dreyer, A., Jaeger, J., Gimpel, K., Berkemeier, T., Bonin, A. S., Nagel, L., Plattner, C., DeVries, A. L., Sewald, N., Koop, T.: Quantitative Efficacy Classification of Ice Recrystallization Inhibition Agents. *Cryst. Growth Des.* **14**, 4285-4294 (2014).

16. Shiraiwa, M., Berkemeier, T., Schilling-Fahnestock, K. A., Seinfeld, J. H., Pöschl, U.: Molecular corridors and kinetic regimes in the multiphase chemical evolution of secondary organic aerosol. *Atmos. Chem. Phys.* **14**, 8323-8341 (2014).

17. Berkemeier, T., Huisman, A. J., Ammann, M., Shiraiwa, M., Koop, T. and Pöschl, U.: Kinetic regimes and limiting cases of gas uptake and heterogeneous reactions in atmospheric aerosols and clouds: a general classification scheme. *Atmos. Chem. Phys.* **13**, 6663-6686 (2013).

18. Nagel, L., Plattner, C., Budke, C., Majer, Z., Devries, A. L., Berkemeier, T., Koop, T. and Sewald, N. Synthesis and characterization of natural and modified antifreeze glycopeptides: glycosylated foldamers. *Amino Acids* **41**, 719-732 (2011).

Oral presentations

1. Berkemeier, T., Steimer, S. S., Krieger, U. K., Peter, T., Pöschl, U., Ammann, M., and Shiraiwa, M.: Ozone uptake on glassy, semi-solid and liquid organic matter and the role of reactive oxygen intermediates in atmospheric aerosol chemistry, General Assembly of the European Geosciences Union, Vienna, Austria, 18th - 22nd April 2016.

2. Berkemeier, T., Steimer, S. S., Pöschl, U., Ammann M. and Shiraiwa M., Multiphase chemical kinetics of ozone uptake on organic aerosol particles in glassy solid, semisolid and liquid phase state, European Aerosol Conference, Milano, Italy, 6th - 11th September 2015.

3. Berkemeier, T., Shiraiwa, M., Pöschl, U. and Koop, T. Competition of homogeneous and heterogeneous ice nucleation on secondary organic aerosol particles: The role of particle phase state, General Assembly of the European Geosciences Union, Vienna, Austria, 27th April - 2nd May 2014.

4. Berkemeier, T., Shiraiwa, M., Pöschl, U. and Koop, T. Competition between heterogeneous ice nucleation and amorphous deliquescence of glassy organic aerosols, Earth System Science Conference, Jena, Germany, 11th - 14th March 2014.

5. Berkemeier, T., Shiraiwa, M. and Pöschl, U. Kinetic modelling of gas-particle interactions: Heterogeneous reactions and SOA formation, PEGASOS Annual Meeting, Athens, Greece, 3rd - 7th February 2014.

6. Berkemeier, T., Shiraiwa, M., Pöschl U. and Koop, T. Estimating amorphous deliquescence time scale of SOA from biogenic and anthropogenic precursors: Implications for heterogeneous ice nucleation on glassy aerosols, European Aerosol Conference, Prague, Czech Republic, 1st - 6th September 2013.

7. Berkemeier, T. Kinetic flux models: The key element for determination of basic physico-chemical parameters in multiphase aerosol (reaction) systems?, IMPRS PhD Symposium, Frankfurt/Main, Germany, 10th June 2013.

Poster presentations

1. Berkemeier, T., Ammann, M., Mentel, T. F., Pöschl, U., and Shiraiwa, M. Organic nitrate contribution to new particle formation and growth in secondary organic aerosols from α-pinene ozonolysis, General Assembly of the European Geosciences Union, Vienna, Austria, 17th - 22nd April 2016.

2. Berkemeier, T., Steimer, S. S., Pöschl, U., Ammann M. and Shiraiwa M. Multiphase kinetic modelling of ozone uptake on organic aerosol particles in glassy, semi-solid and liquid state, Gordon Research Conference on Atmospheric Chemistry, Waterville Valley, New Hampshire, USA, 2nd - 7th August 2015.

3. Berkemeier, T., Shiraiwa, M., Pöschl, U. and Koop, T. Modelling water diffusion in glassy organic aerosols: Implications for water uptake and ice nucleation, CSF conference "“Towards a Molecular-Level Understanding of Atmospheric Aerosols"”, Ascona, Switzerland, 1st - 5th September 2014.

4. Berkemeier, T., Huisman, A. J., Ammann, M., Shiraiwa, M., Koop, T. and Pöschl, U.: Kinetic regimes and limiting cases of gas uptake and heterogeneous reactions in atmospheric aerosols and clouds: a general classification scheme, General Assembly of the European Geosciences Union, Vienna, Austria, 8th April - 12th April 2013.

B. Selected Publications

1. Berkemeier, T., Huisman A. J., Ammann, M., Shiraiwa, M., Koop, T. and Pöschl, U. Kinetic regimes and limiting cases of gas uptake and heterogeneous reactions in atmospheric aerosols and clouds: a general classification scheme. *Atmos. Chem. Phys.* **13**, 6663-6686 (2013).

2. Shiraiwa, M., Berkemeier, T., Schilling-Fahnestock, K. A., Seinfeld, J. H., Pöschl, U.: Molecular corridors and kinetic regimes in the multiphase chemical evolution of secondary organic aerosol. *Atmos. Chem. Phys.* **14**, 8323-8341 (2014).

3. Berkemeier, T., Ammann, M., Krieger, U. K., Peter, T., Spichtinger, P., Pöschl, U., Shiraiwa, M., and Huisman, A. J.: *Technical Note*: Monte-Carlo genetic algorithm (MCGA) for model analysis of multiphase chemical kinetics using multiple experimental data sets, *in preparation*.

4. Berkemeier, T., Shiraiwa, M., Pöschl, U., and Koop, T.: Competition between water uptake and ice nucleation by glassy organic aerosol particles. *Atmos. Chem. Phys.* **14**, 12513-12531, (2014).

5. Berkemeier, T., Steimer, S. S., Krieger, U. K., Peter, T., Pöschl, U., Ammann, M., and Shiraiwa, M.: Ozone uptake on glassy, semi-solid and liquid organic matter and the role of reactive oxygen intermediates in atmospheric aerosol chemistry, *Phys. Chem. Chem. Phys.* **18**, 12662-12674, (2016).

6. Berkemeier, T., Ammann, M., Mentel, T. F., Pöschl, U., and Shiraiwa, M.: Organic nitrate contribution to new particle formation and growth in secondary organic aerosols from α-pinene ozonolysis, *Environ. Sci. Technol.*, DOI:10.1021/acs.est.6b-00961, (2016).

B.1. Berkemeier *et al.*, Atmos. Chem. Phys., 2013

Kinetic regimes and limiting cases of gas uptake and heterogeneous reactions in atmospheric aerosols and clouds: a general classification scheme

Thomas Berkemeier[1,2,3], Andrew J. Huisman[2,*], Markus Ammann[4], Manabu Shiraiwa[3,5], Thomas Koop[1] and Ulrich Pöschl[3]

[1]Bielefeld University, Faculty of Chemistry, 33615 Bielefeld, Germany
[2]ETH Zürich, Institute for Atmospheric and Climate Science, 8092 Zürich, Switzerland
[3]Max Planck Institute for Chemistry, Multiphase Chemistry Department, 55128 Mainz, Germany
[4]Paul Scherrer Institute, Laboratory of Environmental Chemistry, 5232 Villigen PSI, Switzerland
[5]California Institute of Technology, Division of Chemistry and Chemical Engineering, 91125 Pasadena, CA, USA
∗now at: Union College, Department of Chemistry, 12308 Schenectady, NY, USA

Atmospheric Chemistry and Physics **13**, 6663-6686, (2013).

Author contributions.

TB, AJH, MA, MS, TK and UP designed research. TB, AJH, MA, MS, TK and UP discussed results. TB, MS and UP developed the model. TB performed kinetic modeling. TB, AJH and UP wrote the paper.

Atmos. Chem. Phys., 13, 6663–6686, 2013
www.atmos-chem-phys.net/13/6663/2013/
doi:10.5194/acp-13-6663-2013

Atmospheric Chemistry and Physics Open Access

Kinetic regimes and limiting cases of gas uptake and heterogeneous reactions in atmospheric aerosols and clouds: a general classification scheme

T. Berkemeier[1,2,3], A. J. Huisman[2,*], M. Ammann[4], M. Shiraiwa[3,5], T. Koop[1], and U. Pöschl[3]

[1]Faculty of Chemistry, Bielefeld University, Bielefeld, Germany
[2]Institute for Atmospheric and Climate Science, ETH Zürich, Zürich, Switzerland
[3]Multiphase Chemistry Department, Max Planck Institute for Chemistry, Mainz, Germany
[4]Laboratory of Radiochemistry and Environmental Chemistry, Paul Scherrer Institute, Villigen, Switzerland
[5]Division of Chemistry and Chemical Engineering, California Institute of Technology, Pasadena, California, USA
[*]now at: Department of Chemistry, Union College, Schenectady, NY, USA

Correspondence to: A. J. Huisman (huismana@union.edu)

Received: 30 November 2012 – Published in Atmos. Chem. Phys. Discuss.: 9 January 2013
Revised: 17 May 2013 – Accepted: 30 May 2013 – Published: 15 July 2013

Abstract. Heterogeneous reactions are important to atmospheric chemistry and are therefore an area of intense research. In multiphase systems such as aerosols and clouds, chemical reactions are usually strongly coupled to a complex sequence of mass transport processes and results are often not easy to interpret.

Here we present a systematic classification scheme for gas uptake by aerosol or cloud particles which distinguishes two major regimes: a reaction-diffusion regime and a mass transfer regime. Each of these regimes includes four distinct limiting cases, characterised by a dominant reaction location (surface or bulk) and a single rate-limiting process: chemical reaction, bulk diffusion, gas-phase diffusion or mass accommodation.

The conceptual framework enables efficient comparison of different studies and reaction systems, going beyond the scope of previous classification schemes by explicitly resolving interfacial transport processes and surface reactions limited by mass transfer from the gas phase. The use of kinetic multi-layer models instead of resistor model approaches increases the flexibility and enables a broader treatment of the subject, including cases which do not fit into the strict limiting cases typical of most resistor model formulations. The relative importance of different kinetic parameters such as diffusion, reaction rate and accommodation coefficients in this system is evaluated by a quantitative global sensitivity analysis. We outline the characteristic features of each limiting case and discuss the potential relevance of different regimes and limiting cases for various reaction systems. In particular, the classification scheme is applied to three different datasets for the benchmark system of oleic acid reacting with ozone in order to demonstrate utility and highlight potential issues. In light of these results, future directions of research needed to elucidate the multiphase chemical kinetics in this and other reaction systems are discussed.

1 Introduction

Tropospheric aerosols are composed of organic and inorganic substances originating from direct emission of particles and from condensation of gas-phase species (Kanakidou et al., 2005; Pöschl, 2005; Hallquist et al., 2009; Ziemann and Atkinson, 2012). Aerosols are climate forcers (Streets et al., 2004; Yu et al., 2006; IPCC, 2007; Stevens et al., 2009; Carslaw et al., 2010; Mahowald et. al., 2011) and are implicated in human health effects (Bates, 1993; Jakab et al., 1995; McConnell et al., 2002; Nel, 2005; Heal et al., 2012; Shiraiwa et al., 2012d) as well as other undesirable phenomena

such as reduced visibility in urban and rural areas. At this time, the physical and chemical properties of aerosols are still poorly understood and despite extensive experimental and modelling efforts, many of the processes central to heterogeneous chemical processing of aerosols remain unclear (Kolb et al., 2010).

Most previous studies of the gas uptake into aerosol particles have used "resistor" models which account for physical and chemical processes for a single or at most a few physical domains within the aerosol particle by analogy to electrical circuits (an overview of resistor models in the canonical system of oleic acid–ozone heterogeneous reaction is given in Zahardis and Petrucci, 2007). Such models allow analytical expressions to be derived for uptake of trace gases or loss of condensed phase material in simplified, limiting cases. These analytical expressions can be used to calculate the underlying kinetic parameters such as reaction rate coefficients or the accommodation coefficient (which are applicable to a reaction system under any conditions) or the trace gas uptake coefficient γ (which is specific to the experimental conditions at which it was measured). Using this sort of framework has been fruitful in the past for a wide range of gas/particle processes, and was particularly successful in assessing key heterogeneous interactions of relevance to stratospheric ozone depletion (Hanson et al., 1994). Analysis based on limiting cases has found widespread acceptance and also forms the basis for the recent evaluations by the IUPAC Subcommittee for Gas Kinetic Data Evaluation (Crowley et al., 2010). Because a wide variety of processes are important to multiphase chemistry, it is less well understood than pure gas-phase chemistry (e.g. Abbatt et al., 2012) and new methods are needed to facilitate analysis and discussion.

Recently developed depth-resolved models for single particles or thin films that focus on chemistry, such as KM-SUB (Shiraiwa et al., 2010), and water diffusion, such as the ETH Diffusion Model (Zobrist et al., 2011), allow a more complete consideration of the time- and depth-resolved chemical and physical behaviour of aerosol particles, leading to a better understanding of these reaction systems. Shiraiwa et al. (2011a) have shown that resistor models are not sufficient for systems in which the bulk material is radially inhomogeneous in concentration owing to, e.g. diffusion limitations.

Due to the complexity of numerical models such as these, it is often unclear which process is most important to model outputs. Sensitivity analysis provides a simple means of identifying the model parameters which most strongly influence the results (and thus are related to the rate-limiting process). Although many previous studies have employed a local approach, advanced computational tools exist to systematically calculate sensitivity coefficients and take into account higher order parameter effects (the "global methods" in Saltelli et al., 2008). As reviewed in Cariboni et al. (2007), global sensitivity methods have been applied to fields such as ecological modelling, and in atmospheric science advanced sensitivity methods have been applied to models of single gas-phase chemical reactions (e.g. Dunker, 1984) and regional ozone formation (Martien and Harley, 2006). However, to the authors' knowledge this type of sensitivity analysis has not been applied previously to a depth-resolved or resistor-style model of the physicochemical behaviour of single aerosol particles.

Kinetic regimes and limiting cases allow classification of system behaviour for analysis and comparison of model outputs with experimental results. In this work, we propose an enhanced set of limiting cases which can be used for conceptual discussion and analysis along with a systematic, numerically-based method for assigning a limiting case to a reaction system. This classification is compared with the outcome of a global sensitivity analysis to ensure that the system behaviour is consistent with the assignment. The classification system proposed here is broadly applicable and standardized, so that it is portable across many systems. This taxonomy will be useful as a common ground for discussion of heterogeneous chemical processes and as a tool for analysis.

2 Conceptual framework

2.1 Representation of aerosol reaction systems and definitions

Following the terminology of Pöschl et al. (2007) (the "PRA framework"), we will discuss the reaction of a trace gas species X and a condensed-phase substrate Y. These compounds are assumed to react in a single step, second-order reaction in either (i) a single bulk layer or (ii) between a quasi-static surface layer of Y and a sorption layer of X. The domains of the gas and condensed phase discussed here are illustrated schematically in Fig. 1 along with the principle mass transport and reaction processes.

In this paper we reserve the term *limiting case* for a system which is governed by a single, clearly defined rate-limiting process. Examples of limiting cases are systems which are limited solely by slow chemical reaction, or by slow diffusion of reactants X and Y. We reserve the term *kinetic regime* for a system which is governed by a few (often only one or two) clearly defined rate-limiting processes. For example, systems which exhibit reaction and/or bulk diffusion limitation fall into a single kinetic regime. Referencing the concepts of reacto-diffusive length and flux (Schwartz and Freiberg, 1981; Hanson et al., 1994; Pöschl et al., 2007), we term this important example the reaction-diffusion regime.

2.2 Derivation of limiting cases and kinetic regimes

The cases of limiting behaviour presented here arise from three properties that are fundamental to every aerosol reactive system in which a gas X reacts with condensed phase Y:

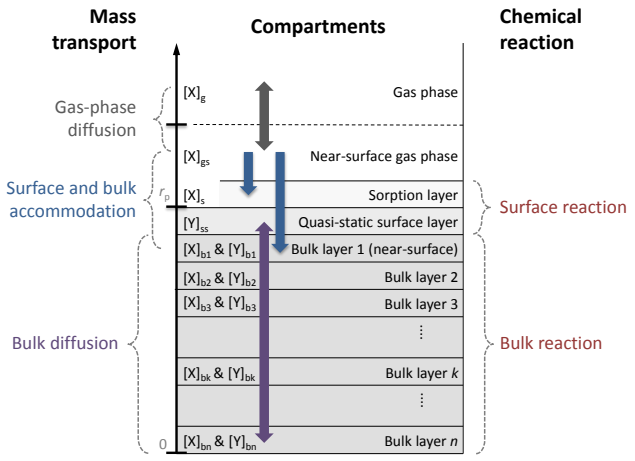

Fig. 1. Processes and compartments discussed in this paper (adapted from Shiraiwa et al., 2010), assuming a system which is either planar or spherically symmetric. Key processes are highlighted. Diffusion of gaseous trace gas X is assumed to influence the near surface gas-phase concentration $[X]_{gs}$ within one mean free path λ_X of the particle surface (r_p). Following Pöschl et al. (2007), surface accommodation denotes the mass flux of X from the near-surface gas phase to the particle surface, whereas bulk accommodation also includes the subsequent transport into the near-surface bulk. Surface reaction occurs within or between the sorption layer and the quasi-static surface layer consisting of bulk material Y. Reaction and diffusion can take place in n individually resolved bulk layers. All symbols are defined in Table A1.

i. the reaction location, as assessed by the Surface to Total Loss rate Ratio (STLR)

ii. the supply of reactive gas, as assessed by the Saturation Ratio (SR)

iii. the heterogeneity of the system with respect to depth above and below the surface, as assessed by the Mixing Parameter (MP).

Each of the three quantities (STLR, SR, MP) is formulated as a dimensionless parameter ranging from 0 to 1 to allow comparison against a common set of criteria which are not linked to any specific chemical reaction.

Every unique combination of extreme behaviour in the three classification properties leads to a limiting case. This can be visualized in three dimensions as a cube in which each dimension corresponds to one of the classification properties, as shown in Fig. 2. Since all possible cases of kinetic behaviour form the interior of the cube and the faces describe extreme behaviour in one of the classification properties, the eight limiting cases can be depicted as a small volume at each of the vertices, touching three faces each. The eight cases obtained in this way are limited by a single process each and are clearly distinct since they differ in at least one fundamental classification property.

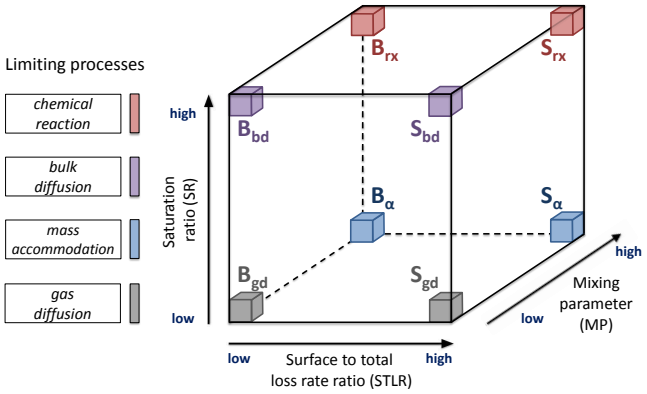

Fig. 2. Kinetic cube: the eight limiting cases can be depicted as the vertices of a cube in which every direction refers to a classification criterion (STLR, SR, MP). They are classified into four types of limiting behaviour: limitation by chemical reaction, bulk diffusion, mass accommodation (including surface and bulk accommodation) and gas diffusion.

To facilitate discussion, we introduce a compact symbolic representation for each limiting case which is used in Fig. 2 and throughout this manuscript. The reaction location is indicated by a central "S" or "B" for surface and bulk, respectively, and a subscript indicates the process which limits reactive uptake. The possible subscripts are: "rx" to indicate chemical reaction; "bd" to indicate bulk diffusion; "α" to indicate accommodation; "gd" to indicate gas-phase diffusion. This framework thus distinguishes four different types of limitation, which are colour-coded in Fig. 2.

A particular strength of numerical modelling (either depth-resolved models or numerically solved resistor models) is the ability to work in the "gray area" between well-defined limiting cases. The framework proposed here is compliant with systems in which one or two classification parameters do not exhibit extreme behaviour: these fall into the kinetic regimes defined above. In order to illustrate the concept of a kinetic regime, a few of the many possible regimes are shown in Fig. 3. A straightforward way to generate a regime is to connect the volume which represents two limiting cases to form a volume, which also contains the additional space between the limiting cases and towards the centre of the cube. The resulting regime includes the behaviour of both limiting cases and all systems with classification parameters located in the additional volume. A kinetic regime is thus much broader in its definition than a limiting case. This is depicted in Fig. 3b, where surface and bulk reaction limiting cases with the same limiting process (boxes of the same colour) are connected. We name the four resulting regimes for the process which limits the reactive loss of Y: the reaction, bulk diffusion, gas diffusion and accommodation regimes.

Another possibility is shown in Fig. 3b, where the reaction and bulk diffusion regimes are linked to form a reaction-diffusion regime. This reaction-diffusion regime

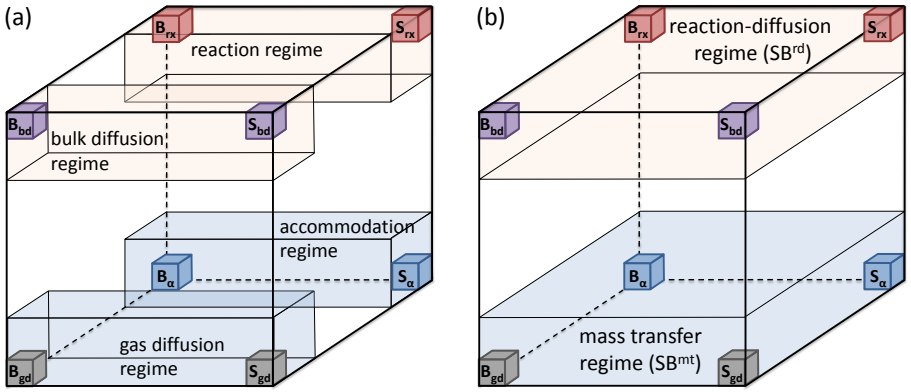

Fig. 3. Visualization of regimes as volumes of the kinetic cube in Fig. 2. **(a)** shows regimes resulting from the connection of each surface and bulk case. Regime names indicate the limiting process (the reaction regime is limited by reaction rate coefficients etc.). **(b)** shows a combination of the regimes in **(a)** in which the reaction and bulk diffusion regimes together form the reaction-diffusion regime and the accommodation and gas diffusion regimes together form the mass transfer regime.

thus includes systems which are limited by reaction, bulk diffusion, or both processes in situations where they are tightly coupled (reacto-diffusive limitation). We note that the term "reacto-diffusive" traditionally referred to bulk reaction systems with a strong gradient in X and no gradient in Y (see e.g. Danckwerts, 1951; Schwartz, 1986; Hanson et al., 1994; Davidovits et al., 1995; Ravishankara, 1997; Kolb et al., 1998; Ravishankara and Longfellow, 1999; Davidovits et al., 2006; Pöschl et al., 2007; Kolb et al., 2010). Throughout this paper we will refer to this case as the "traditional reacto-diffusive case". However, our definition of the reaction-diffusion regime also includes cases with gradients in the bulk material Y in both bulk and surface reaction systems. In these systems, a reacto-diffusive steady state forms when both the diffusion of reactants towards the reaction site and the actual chemical reaction are limiting trace gas uptake. The complementary regime is a combination of the accommodation and gas diffusion regimes, which we will refer to as the "mass transfer"-limited regime as both are related to the transfer of X from the gas to the particle phase.

To facilitate discussion of regimes, we introduce additional symbols which are similar to that of the limiting cases defined above. Again, "S" and "B" are used to indicate reaction location, and superscripts are used to avoid confusion in identifying the rate-limiting processes. Additional possible superscripts are "rd" to indicate reaction-diffusion limitation and "mt" to indicate mass transfer limitation. In case the surface contribution parameter STLR does not show extreme behaviour, a regime can still be specified if the other classification parameters are consistent. For example, if STLR is $\sim$0.5 but saturation ratio SR is high, we can assign the behaviour as SB^{rd}, where the central symbol is "SB" to indicate that both surface and bulk reactions contribute. The traditional reacto-diffusive case as defined above (bulk reaction, gradient only in X) will be denoted as B^{rd}_{trad} to distinguish it from the broad manifold of possible behaviours encompassed in our reaction-diffusion regime, SB^{rd}. In addition to the regimes already presented here, a variety of other regimes are possible; a few of them are documented in Appendix B.

2.3 Classification scheme and criteria

Here we present a sequential method to apply the three parameters defined above to unambiguously determine the limiting case of a reacting aerosol particle. These classification parameters will be described in detail in Sects. 2.3.1–2.3.3. An overview of the process is given in Fig. 4 and the resulting limiting cases and kinetic regimes are summarised in Table 1.

In the following sections, each of the three classification parameters is framed as a question to provide insight into the processes which most strongly influence the gas uptake. It is important to note that multiple functional forms of SR and MP exist; one of each is chosen for use depending on the result of the previous classification parameters. For example, the mixing parameter for a reaction which occurs primarily at the surface should not reflect a depthwise gradient in bulk X.

A conceptual discussion of the physical and chemical behaviour of each limiting case is possible without appealing to any specific numerical model, but the process of calculating parameter values to assign a limiting case for some experimental data requires the output of a depth-resolved model. The criteria are constructed assuming that model outputs are discretized into spherical or planar layers for droplets and films, respectively, as such discretized treatment is common in current-generation models (see Fig. 1).

2.3.1 Criterion 1: surface to total loss rate ratio (STLR)

This term answers the question: *What is the dominant reaction location, surface or bulk?* The surface to total loss rate ratio (STLR) is used to determine which locality, if any, dominates the chemical loss of Y. The loss rates at the surface, L_s

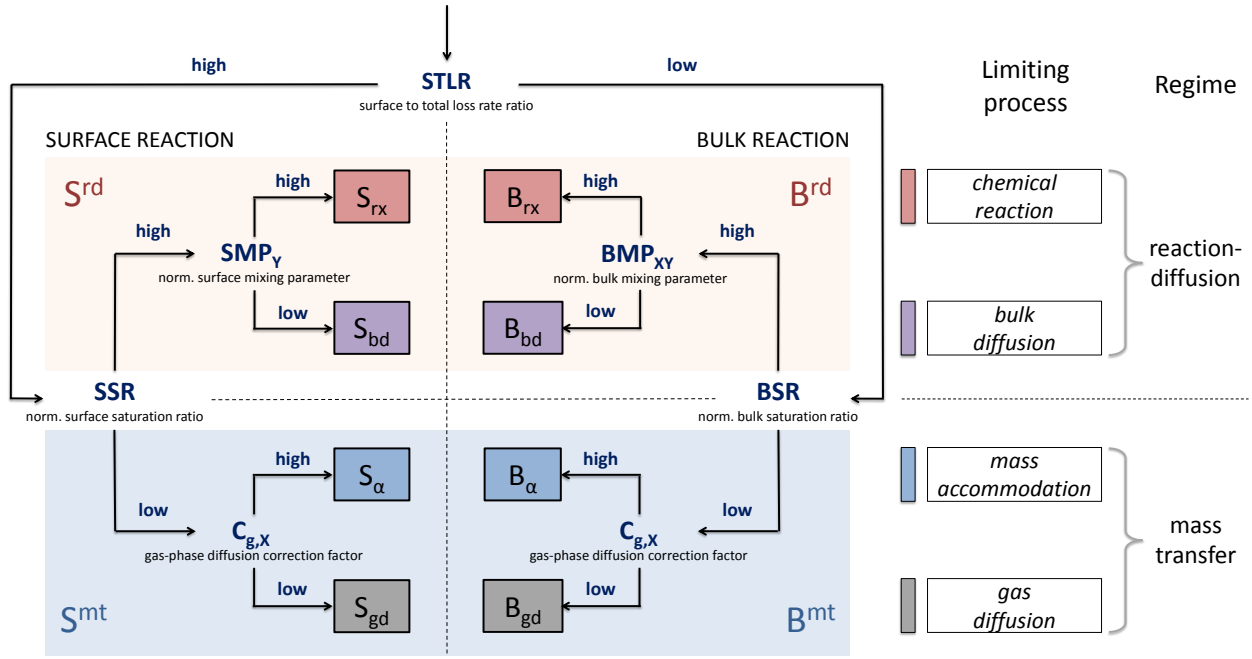

Fig. 4. Classification scheme for distinction of limiting cases. The decision process proceeds in three steps according to Sect. 2. Surface dominated cases (left half) and bulk dominated cases (right half) are distinguished in the first step by comparing the surface to the total loss rate (STLR). Reaction-diffusion systems (top half) and mass transfer-limited systems (bottom half) are distinguished in the second step by evaluating the saturation ratio (SR). In the last step mixing of the components is considered. Note that even though the scheme appears to be symmetric for surface and bulk reaction systems, the classification parameters differ between the left and the right side of the diagram in the second and third decision step. The reaction-diffusion and mass transfer regimes are indicated by large shaded boxes and the respective regime symbols are given in their outward corners.

Table 1. The principle regimes and limiting cases, defined in terms of two and three classification parameters, respectively. The classification properties are the surface to total loss rate ratio (STLR), the saturation ratio(s) (SR) and the mixing parameter(s) (MP). When more than one expression for a classification property is possible (SR/MP), the expression is listed along with a rough criterion.

STLR	SR	Regime	MP	Limiting Case	Description
≈ 1	SSR ≈ 1	S^{rd}	$SMP_Y \approx 1$ $SMP_Y \approx 0$	S_{rx} S_{bd}	Surface reaction limited by chemical reaction Surface reaction limited by bulk diffusion of condensed reactant Y
≈ 1	SSR ≈ 0	S^{mt}	$C_{g,X} \approx 1$ $C_{g,X} \approx 0$	S_α S_{gd}	Surface reaction limited by surface accommodation of X Surface reaction limited by gas-phase diffusion of X
≈ 0	BSR ≈ 1	B^{rd}	$BMP_{XY} \approx 1$ $BMP_{XY} \approx 0$	B_{rx} B_{bd}	Bulk reaction limited by chemical reaction Bulk reaction limited by bulk diffusion of volatile reactant X and condensed reactant Y
≈ 0	BSR ≈ 0	B^{mt}	$C_{g,X} \approx 1$ $C_{g,X} \approx 0$	B_α B_{gd}	Bulk reaction limited by bulk accommodation of X Bulk reaction limited by gas-phase diffusion of X

and in the k-th bulk layer, L_{bk}, can be calculated as follows:

$$L_s = k_{SLR}[X]_s[Y]_{ss} \quad (1)$$

$$L_{bk} = k_{BR}[X]_{bk}[Y]_{bk} \quad (2)$$

Here k_{SLR} and k_{BR} are the second-order reaction rate coefficients in the bulk and in the surface layer, respectively, [X] and [Y] are the concentrations of the reactants and the subscripts s, ss, and bk indicate the sorption layer, the quasi-static surface layer, and the k-th bulk layer, respectively (see also Fig. 1 above). For a total of n bulk layers, the STLR can then be calculated as:

$$\mathrm{STLR} \equiv \frac{L_s}{L_s + \sum_{k=1}^{n} L_k}. \quad (3)$$

In Fig. 4, the STLR decision distinguishes the surface (left half) from the bulk reaction cases (right half). The numerical interpretation of STLR is

1. As STLR approaches zero, the reaction occurs primarily in the bulk.

2. As STLR approaches unity, the reaction occurs primarily at the surface.

2.3.2 Criterion 2: saturation ratio (SR)

This term answers the question: *Is the supply of external gas limiting the reaction rate?* This criterion classifies particles by the abundance of X at the surface or in the first bulk layer, and is thus used as a proxy for the balance between supply of X (from the gas phase) and loss of X (by desorption, surface reaction, bulk reaction, and diffusion into the bulk) in those locations. In Fig. 4, this decision step distinguishes the reaction-diffusion regime with high SR (top, SB^{rd} regime) from the mass transfer regime with low SR (bottom, SB^{mt} regime). In both the surface and the bulk case detailed below, the actual concentration of X in the locale where reaction occurs is compared to the saturation value of X which would be achieved in the absence of reacto-diffusive loss, leading to a direct determination of which regime a system expresses, reaction-diffusion limitation or mass transfer limitation.

SR in surface-reaction dominated cases

In cases where surface reaction dominates (STLR ≈ 1), the SR is calculated as the Surface Saturation Ratio (SSR). With this parameter, the surface concentration of X is compared to the surface saturation concentration $[X]_{s,sat}$. In the absence of reaction or diffusion into the bulk, the saturation concentration of X at the surface is determined by the rates of adsorption and desorption k_a and k_d:

$$[X]_{s,sat} = \frac{k_a}{k_d} \cdot [X]_g = K_{ads,X} \cdot [X]_g \quad (4)$$

Here $[X]_g$ is the near-surface gas-phase concentration of X and $K_{ads,X}$ is a Langmuir-type adsorption equilibrium constant (see Fig. 1). The SSR is defined as the ratio of X to its saturation concentration at adsorption equilibrium:

$$\mathrm{SSR} = \frac{\theta_{s,X}}{\theta_{s,sat,X}} = \frac{[X]_s}{[X]_{s,sat}} \quad (5)$$

where $\theta_{s,X}$ is surface coverage as defined in Pöschl et al. (2007) and $\theta_{s,sat,X}$ (not to be confused with $\theta_{s,max} = 1$) is the saturation coverage achievable at the equilibrium surface concentration defined in Eq. (4).

SR in bulk-reaction dominated cases

In cases where bulk reaction dominates (STLR ≈ 0), the SR is calculated as the Bulk Saturation Ratio (BSR). In this parameter, the concentration of X in the first subsurface bulk layer ($[X]_{b1}$) is compared to the saturation concentration ($[X]_{b,sat}$) achievable under equilibrium conditions in the absence of reacto-diffusive loss:

$$\mathrm{BSR} = \frac{[X]_{b1}}{[X]_{b,sat}} \quad (6)$$

Here we suggest that $[X]_{b,sat}$ should be defined in terms of the Henry's law equilibrium constant and the gas-phase concentration $[X]_g$. The numerical interpretation common to both representations of the saturation ratio SR is:

1. As SR approaches zero, the system is starved of X and is mass transfer-limited (SB^{mt} regime).

2. As SR approaches unity, the system is adequately supplied with X and experiences reaction-diffusion limitation (SB^{rd} regime).

2.3.3 Criterion 3: mixing parameters (MP)

This term answers the question: *What is limiting the reaction rate: mixing or chemistry?* Much of the additional information in depth-resolved models is included in the parameter set which represents the spatial heterogeneity in the system. In the case of a surface reaction, a slow diffusion of Y to the surface may hinder the reaction, while in the bulk, reaction speed may be limited by the diffusion of X and possibly the diffusion of Y. In mass transfer-limited systems, only mixing in the gas phase has to be considered. Thus, three different mixing parameters (MP) are used to assess mixing in reacting particles: (i) The surface mixing parameter of Y, SMP_Y, for reaction-diffusion-limited surface reaction systems (S^{rd}); (ii) the bulk mixing parameter of X and Y, BMP_{XY}, for reaction-diffusion-limited bulk reaction systems (B^{rd}) and (iii) the gas-phase diffusion correction factor, $C_{g,X}$, for mass transfer-limited systems (SB^{mt}). In Fig. 4, this classification step divides the reaction-diffusion and mass transfer-limited regimes each into well-mixed cases (top half) and cases which are limited by bulk or gas-phase gradients (bottom half).

MP in surface reaction-diffusion-limited systems

In surface reaction-diffusion limited systems (S^{rd} regime, STLR ≈ 1, SSR ≈ 1), the reaction rate may be limited by the availability of Y at the surface. Assuming that Y is non-volatile, a deficit in Y at the surface is caused by reaction with X and incomplete mixing with the particle bulk. Thus, we define SMP_Y as the ratio of the actual surface concentration $[Y]_{ss}$ to the maximum possible surface concentration $[Y]_{ss,max}$:

$$SMP_Y = \frac{[Y]_{ss}}{[Y]_{ss,max}}. \quad (7)$$

Here we propose $[Y]_{ss,max} = [Y]_{bn} \cdot \delta_Y$, namely that the maximum possible surface concentration of Y should be linked to the bulk concentration at the centre of the particle (layer n) and a geometric factor δ_Y to relate the molecular volume concentration (cm^{-3}) to a molecular area concentration (cm^{-2}). Referencing the surface concentration against the innermost bulk layer gives maximum sensitivity to depthwise gradients in Y. It is important to note that the maximum surface concentration $[Y]_{ss,max}$ may change as the reaction proceeds due to decreased abundance of Y in layer n. The numerical interpretation of SMP_Y is:

1. As SMP_Y approaches zero, a strong gradient in Y exists from the centre of the bulk to the surface of the particle, and the system falls within the bulk diffusion-limited surface reaction case S_{bd}.

2. As SMP_Y approaches unity, Y is well-mixed throughout the particle and the system falls within the reaction-limited surface reaction case S_{rx}.

MP in bulk reaction-diffusion-limited systems

In bulk reaction-diffusion-limited systems (B^{rd} regime, STLR ≈ 0, BSR ≈ 1), a gradient in X and/or Y may limit the reaction rate, so that expressions for both the mixing of X and Y in the bulk are needed. For both species, the reacto-diffusive length will be compared to the particle size to assess the degree of mixing. In general, the reacto-diffusive length is the depth-wise distance over which the concentration of a material decreases to $1/e$ of its original value. The reacto-diffusive length will increase as the diffusivity of the material increases and will decrease as the reaction rate coefficient becomes higher. For compounds X and Y which react with one another, the reacto-diffusive length can be expressed as:

$$l_{rd,X} = \sqrt{\frac{D_{b,X}}{k_{BR} \cdot [Y]_{eff}}} \quad (8)$$

$$l_{rd,Y} = \sqrt{\frac{D_{b,Y}}{k_{BR} \cdot [X]_{eff}}} \quad (9)$$

where $[X]_{eff}$ and $[Y]_{eff}$ are the effective concentrations of X and Y in the region where the reaction occurs and $D_{b,X}$ and $D_{b,Y}$ are the diffusion constants of each material in the bulk matrix. This formulation is needed in the case of a strong depth-wise gradient in the reaction partner, in which case the simple average concentration might be misleading. Specifically, we propose that the effective concentration should be calculated as the volume- and loss rate-weighted concentration:

$$[X]_{eff} = \frac{\sum_{k=1}^{n} L_k V_k [X]_{bk}}{\sum_{k=1}^{n} L_k V_k} \quad (10)$$

$$[Y]_{eff} = \frac{\sum_{k=1}^{n} L_k V_k [Y]_{bk}}{\sum_{k=1}^{n} L_k V_k} \quad (11)$$

where V_k is the volume of the k-th layer. This definition of the effective concentration of the reaction partner in the zone where the reaction occurs allows the use of the reacto-diffusive length of each species to gauge the degree of mixing of X and Y within the particle.

We define the BMP_X and BMP_Y, the bulk mixing parameters for X and Y, respectively, to be:

$$BMP_X = \frac{l_{rd,X}}{l_{rd,X} + \frac{r_p}{e}} \quad (12)$$

$$BMP_Y = \frac{l_{rd,Y}}{l_{rd,Y} + \frac{r_p}{e}} \quad (13)$$

so that both BMPs approach unity as their reacto-diffusive length becomes much larger than the particle radius r_p and approach zero as their reacto-diffusive length becomes much smaller than the particle radius. In BMP_X and BMP_Y, we have chosen to scale the particle radius by $1/e$ to be consistent with the e-folding characteristic of the reacto-diffusive length.

Finally, as the presence of a gradient in only one compound is insufficient to drive a system into the B_{bd} limiting case, we define BMP_{XY} as the average of BMP_X and BMP_Y:

$$BMP_{XY} = \frac{BMP_X + BMP_Y}{2} \quad (14)$$

The numerical interpretation of BMP_{XY} is:

1. As BMP_{XY} approaches zero, strong gradients in both X and Y limit loss rate and the system falls within the bulk diffusion-limited bulk reaction case B_{bd}.

2. As BMP_{XY} approaches unity, X and Y are well-mixed throughout the particle and the system falls within the reaction-limited bulk reaction case B_{rx}.

A strong gradient solely in bulk X is insufficient to cause bulk diffusion limitation and thus to bring about a B_{bd} limiting case classification. For details and justification see Appendix C.

MP in mass transfer-limited systems

For either bulk or surface reactions (any value of STLR), there are two scenarios which lead to mass transfer limitation

(SSR and/or BSR ≈ 0): either trace gas reactant X is depleted in the near-surface gas phase (see Fig. 1) or the accommodation process is inefficient. This distinction is important as in the second case a physical or chemical change in the system might result in increased accommodation efficiency, leading to significant changes in reaction system behaviour. A simple and physically meaningful metric to distinguish these two cases is the gas-phase diffusion correction factor for uptake by aerosols (Pöschl et al., 2007), $C_{g,X}$, which we take as the gas-phase mixing parameter.

$$C_{g,X} = \frac{[X]_{gs}}{[X]_g} = \frac{1}{1 + \gamma_X \frac{0.75+0.28\ Kn_X}{Kn_X(1+Kn_X)}} \quad (15)$$

As can be seen, $C_{g,X}$ can be calculated in two ways, either directly via model output of $[X]_{gs}$ and $[X]_g$, which are the trace gas concentrations near the surface and far from the particle, respectively; or via model output of γ_X and Kn_X, which are the net uptake coefficient of X and the Knudsen number of the diffusive system. The Knudsen number (see Pöschl et al., 2007) is the ratio of the mean free path of the trace gas molecule λ_X to the particle radius, where λ_X depends on the gas-phase diffusivity $D_{g,X}$ and the mean thermal velocity of the gas ω_X ($\lambda_X \approx 70$ nm at atmospheric pressure for ozone) so that

$$Kn_X = \frac{\lambda_X}{r_p} = \frac{3\ D_{g,X}}{r_p\ \omega_X}. \quad (16)$$

The numerical interpretation of $C_{g,X}$ is:

1. As $C_{g,X}$ approaches zero, the system shows a strong spatial gradient in $[X]_g$ and the system is limited by diffusion of gas phase X to the particle surface, characteristic for S_{gd} or B_{gd} limiting cases in the SB^{gd} regime.
2. As $C_{g,X}$ approaches unity, no spatial concentration gradient exists in $[X]_g$ and the system is therefore limited by accommodation. It is thus assigned to either a S_α or B_α limiting case (both of which fall within the SB^α regime).

3 Examples of atmospheric relevance

The limiting cases described above are meant to provide a conceptual framework for chemical kinetics in atmospheric particles and allow physical and chemical intuition to be applied in a complex system. A few examples of well-known systems which fall into well-defined limiting cases are the following:

3.1 Well-mixed bulk reaction systems [B_{rx}]

Many of the slow aqueous phase reactions fall into this limiting case, which arises when both trace gas X and bulk constituent Y are plentiful and ubiquitous throughout the particle. This is the case for the reaction of O_3 with SO_2 under acidic conditions (where formation of HSO_3^- or SO_3^{2-} is not likely, cf. Seinfeld and Pandis, 2006), the self-reaction of HO_2 in absence of transition metal ions (cf. Abbatt et al., 2012, and references therein, especially George et al., 2011), or reactions involving NO_2 (Ammann et al., 2005). Such reactions are typically not a major sink of the trace gas involved from the gas phase, but are important in terms of aerosol aging if they are the principle transformation of the condensed phase compound.

3.2 Well-mixed surface reaction systems [S_{rx}]

Many relevant reactions on solid surfaces, such as ice, mineral dust, or soot fall into this limiting case (e.g. surface oxidation of polycyclic aromatic hydrocarbons by ozone, Shiraiwa et al., 2009). Moreover, gas uptake by liquid aqueous substrates can also be limited by chemical reaction at the surface. For example, the reaction of Cl_2 with Br^- has a strong surface component, especially at low Cl_2 gas-phase concentrations (Hu et al., 1995). Similarly, Knipping et al. (2000) as well as Knipping and Dabdub (2002) suggested a surface reaction between the OH radical and Cl^- under atmospheric conditions via formation of a surface complex (Laskin et al., 2003; Shaka' et al., 2007).

3.3 Mass transfer-limited systems [S_α, B_α; S_{gd}, B_{gd}]

Surface accommodation limitation necessarily occurs during the equilibration of fresh surface upon exposure to X, e.g. HCl on H_2SO_4 (Morris et al., 2000; Behr et al., 2001, 2009), but also for all other surface precursor mediated processes mentioned above. If transfer into aqueous droplets is fast, bulk accommodation is rate limiting until solubility equilibrium begins to limit uptake. For soluble gases, this may be the dominant case for uptake into the aqueous phase in clouds. Each of the accommodation limited cases mentioned above may become gas-phase diffusion-limited as the particle becomes sufficiently large (and *Kn* becomes small). This may be important in laboratory experiments with supermicron droplets and for cloud droplet or aerosol growth.

3.4 Bulk diffusion-limited systems [S_{bd}, B_{bd}]

In the past, reactions in atmospheric aerosols were assumed to occur in well-mixed droplets with no limitation due to diffusion in the condensed phase. However, recent evidence shows that aqueous particles may transition into highly viscous semi-solid or glassy states (Zobrist et al., 2008; Virtanen et al., 2010; Koop et al., 2011), which lead to strong diffusional limitations on reaction rate. Diffusion of one or both reactants in the bulk may become rate limiting. Examples include the nitration of amorphous protein (Shiraiwa et al., 2011a, 2012c), the reaction of NO_3 with levoglucosan (Shiraiwa et al., 2012b), and (non-reactive) uptake of water to dissolve a glassy aerosol (Mikhailov et al., 2009; Zobrist et al., 2011; Koop et al., 2011; Tong et al., 2011).

3.5 Changes in kinetic behaviour as a function of time and ambient conditions

Each of the examples given above references a single limiting case, and in many cases the limiting case or regime assignment may remain constant throughout the majority of a reaction. However, the limiting case or kinetic regime will almost certainly change in the first moments of reaction or as reaction products accumulate. For example, in a bulk reaction dominated system, the uptake of soluble trace gases into liquid particles could be initially accommodation-limited (B_α) and thereafter pass into the bulk diffusion-limited B_{bd} case for viscous droplets or into the well-mixed B_{rx} case for slow bulk phase reactions. This demonstrates that a system may evolve from one limiting case to another in time. Although time-invariant kinetic parameters are used in the case study of oleic acid–ozone in Sect. 6, the classification system described here is compliant with temporally varying parameters such as changing bulk diffusivities $D_{b,X}$ and $D_{b,Y}$ as a reaction proceeds (e.g. as in Pfrang et al., 2011). This might occur when reaction products alter the viscosity of the bulk matrix. The classification framework is also independent of model choice; a model that explicitly treats product formation along with evaporation of volatile products could be used with the framework as proposed above.

In addition to noting that the kinetic behaviour will change as the reaction proceeds, we caution against the logical error of assuming that the kinetic regime or limiting case observed in one experiment will be the same under ambient conditions or in another experiment under different conditions. For this reason, we recommend that the limiting case for an aerosol system under ambient conditions should be calculated as part of a standard analysis, especially if experimental conditions are significantly different than ambient. For example, the reaction of ozone with bromide (a potentially important reaction for the liberation of halogens out of aqueous sea-salt) is dominated by a surface reaction (S_{rx}) at atmospherically relevant ozone concentrations, while it is dominated by a bulk reaction (B_{rx}) at very high ozone concentration (Oldridge and Abbatt, 2011).

4 Numerical modelling of limiting cases

Up to this point, the limiting cases and regimes have been described in terms of trends in the parameters, but the actual assignment of a reaction system to a limiting case requires a set of numerical criteria and a model to generate the time- and depth-resolved data. In this section we describe our choice of depth-resolved model and propose a set of numerical criteria for differentiation of aerosol behaviour along with a global analysis method to confirm that the numerical criteria result in distinct limiting cases.

Table 2. Kinetic input parameters in the KM-SUB representation of aerosol chemistry.

Parameter	Description	Units
k_{BR}	2nd order bulk reaction rate coefficient	$cm^3\,s^{-1}$
k_{SLR}	2nd order surface reaction rate coefficient	$cm^2\,s^{-1}$
$D_{b,X}$	Bulk diffusion coefficient of X in Y	$cm^2\,s^{-1}$
$D_{b,Y}$	Self-diffusion coefficient of Y	$cm^2\,s^{-1}$
$H_{cp,X}$	Henry's law solubility coefficient of X in Y	$mol\,cm^{-3}\,atm^{-1}$
$\tau_{d,X}$	Desorption lifetime of X	s
$\alpha_{s,0,X}$	Surface accommodation coefficient of X on bare Y	–
$D_{g,X}$	Gas-phase diffusion coefficient of X	$cm^2\,s^{-1}$

4.1 KM-SUB model description and method

In the following analyses, we have chosen to employ the KM-SUB model of Shiraiwa et al. (2010), but this set of limiting cases and classification criteria could be used with any model which produces time- and depth-resolved outputs. KM-SUB is a kinetic model that treats mass transport and chemical reaction at the surface and in the bulk of aerosol particles. It follows the nomenclature of the PRA framework and consists of model compartments as outlined in Sect. 2.1 and shown in Fig. 1. KM-SUB solves a set of ordinary differential equations for the flux-based mass balance to and from each layer, resolving the following processes: gas-phase diffusion, adsorption and desorption onto the particle surface, surface-bulk exchange, bulk diffusion of trace gas and bulk material as well as surface and bulk reactions. The original gas-phase diffusion correction term in KM-SUB was replaced by an explicit near-surface gas-phase layer (following the treatment of gas flux through a virtual surface, found in Eq. 12 of Pöschl et al., 2007). Effectively, the kinetic behaviour of a physical system is described in this modified version of KM-SUB by the eight parameters given in Table 2 (not including experimental observables such as particle radius r_p, gas phase concentration $[X]_g$, etc.). The number of layers calculated by the model was adjusted until model results converged to ensure adequate depthwise resolution.

The KM-SUB model was used to calculate idealised limiting case profiles which are not tied to any specific chemical system (see Sect. 5.1) and also to simulate the reaction of oleic acid–ozone for the experimental conditions of Ziemann (2005), Lee and Chan (2007) and Hearn et al. (2005) in Sect. 6. Because the limiting case is likely to change one or more times upon the onset of reaction (see Sect. 3.5), it is necessary to determine the limiting case at a specific point in time or at a specific point in the reaction. Our results show that limiting behaviour tends to be stable over long parts of the simulations after the initial rapid changes. As

the KM-SUB model does not explicitly treat the products of this reaction, limiting cases were assigned at the point where 50 % of the initial reactant Y was consumed using the numerical criteria of Sect. 4.2. However, in these experiments the limiting case assignments are the same if the assignment is made at either 10 % or 50 % reaction course (see Table 6 below), so comparison with previous studies which used initial rate methods is possible.

4.2 Numerical criteria and partially defined behaviour

Even though a system may exhibit steady state reactivity over a long period of time, the situation cannot be necessarily assigned to one of the limiting cases. An ideal system would have binary behaviours (e.g. only surface or bulk reactions, but not both), but in real systems some mixed character is expected. The ability to assign a limiting case (or lack thereof) is thus a consequence of the physical system under study and the conditions of each experiment. The exact positions of such boundaries for limiting cases and regimes are rather subjective and may change depending on the application. Here, we employ a 9 : 1 criterion for limiting cases, such that at least 90 % of the behaviour is represented by the kinetic regime definition at each classification step. The boundaries for regimes are more relaxed at 3 : 1 criteria, so that more space can be classified. Although knowledge of the system's kinetic regime is less valuable than the confirmation of (single-process) limiting behaviour, such a classification might still be useful. Prominent examples of systems which could be classified by a regime, but not a limiting case are heterogeneous kinetics in the bulk reaction-diffusion kinetic regime (B^{rd}), such as the reaction of HCl with HOCl in sulfuric acid solutions (Hanson and Lovejoy, 1996; Donaldson et al., 1997, and references therein), the hydrolysis of $ClONO_2$ (Deiber et al., 2004), or the reaction of O_3 with iodide (Rouvière et al., 2010). In these examples, kinetic regimes can help by providing a less stringent classification than a limiting case. However, unless the numerical criteria are set at 1 : 1 with no unspecified region, there will be some combinations of classification parameters for which no assignment is possible.

4.3 Global sensitivity analysis

The best indication that an assignment to a limiting case is justified and that the choice of numerical criteria is sufficiently strict is given by a sensitivity analysis which confirms that the system is controlled by a single process and responds appropriately to changes in the associated input parameters (e.g. S_α cases should depend only on the surface accommodation coefficient $\alpha_{s,0}$ and not on the surface reaction rate coefficient k_{SLR} etc.). In general, sensitivity towards an input parameter λ_i can be expressed through its sensitivity coefficient $S(\lambda_i)$, which may be defined as

$$S(\lambda_i) = \left(\frac{\Delta Y_{\text{model}}}{\Delta \lambda_i} \right). \quad (17)$$

However, the values of S_i cannot be compared directly because they depend on the magnitudes of the input parameters (λ_i) which are being varied and the observed model output Y_{model}. Thus we employ a normalised sensitivity coefficient (following Saltelli et al., 2008) which allows the influence of input parameters to be directly compared:

$$S^n(\lambda_i) = \frac{\frac{1}{Y_{\text{model}}} \partial Y_{\text{model}}}{\frac{1}{\lambda_i} \partial \lambda_i} = \frac{\partial \ln(Y_{\text{model}})}{\partial \ln(\lambda_i)} \quad (18)$$

For the computation of sensitivity coefficients we employ a variation on the Elementary Effects (EE) Method as proposed by Morris (1991). The EE method is a simple global screening method that uses a one-at-a-time sampling approach (other approaches are also possible, for a summary see e.g. Saltelli et al., 2008). The method follows a randomly generated trajectory through input parameter space, and records the changes in model output Y_{model} due to changes in each input parameter λ_i. Only one parameter is varied at each step, and all previous changes are kept, which leads to generation of a full set of local sensitivity coefficients. To account for biases due to the random trajectory generation, a large number of trajectories are generated and a representative sample is chosen so that the entire input parameter space is adequately represented. The global sensitivity coefficient is thus finally obtained by taking the arithmetic mean μ_i of all computed local values. The associated standard deviation σ_i is a measure for interactions between and nonlinearity of the input parameters λ_i.

In this study, we use the total loss rate, $L_{\text{tot}} = L_s + \sum_k L_k$, as model output characteristic for the reaction system. The result of this analysis is a set of normalised sensitivity coefficients, which indicate the strength of the model response to changes in each input parameter. Crucially, this sensitivity analysis is only possible in the context of a specific chemical system, physical size (distribution) of aerosol particles, and for a given set of kinetic constants. For this study we perform sensitivity analyses in the context of the oleic acid–ozone system (see Sect. 6.5 below), but recommend the analysis to be performed for each new system to ensure that appropriate numerical limits are chosen. Even within the same chemical system with the same kinetic constants, the calculated sensitivities will change in response to differing experimental conditions such as gas-phase oxidant concentration or particle size.

The interpretation of the normalised sensitivity coefficients can be achieved by connecting the input parameter λ_i to the original model output Y_{model} by the power law relationship:

$$Y_{\text{model}} \propto \lambda_i^{S^n(\lambda_i)}. \quad (19)$$

In words, this indicates that the model output responds to changes in input parameter λ_i in proportion to the $S^n(\lambda_i)$-th power of the change. For example, a $S^n(\lambda_i)$ of -1 would indicate inverse dependence on input parameter λ_i etc.

5 Identification of limiting cases and scaling from laboratory to ambient conditions

The limiting cases and regimes described above are essentially statements of which underlying processes are most influential to a reaction for a given set of conditions. As such, they have the potential to aid experimental planning by suggesting which parameters should be adjusted to maximise experimental effectiveness. If the underlying kinetic parameters such as reaction rate coefficients and diffusivities are extracted from experimental data, these parameters would provide direct insight into the physicochemical processes at work in the system and are portable to different conditions.

However, the kinetic parameters of a system can be obtained only from comprehensive studies, often requiring fits to data from multiple experiments. Without these parameters it is not possible to perform calculations with a depth-resolved model to make an immediate assignment of limiting case or regime behaviour. Fortunately, the limiting cases display some characteristic behaviours which can provide insight into the reaction system from experimental observables (e.g. reactive uptake coefficient as a function of time) and from responses to controlled variables (e.g. change in reactive uptake coefficient γ_X as a function of particle radius r_p or gas-phase oxidant concentration $[X]_g$). In this section we will present the characteristic behaviours of the limiting cases and summarise how each limiting case behaves with respect to time, r_p, and $[X]_g$, which will allow an experimentalist to narrow the list of possible limiting cases by visual inspection of experimental data and possibly plan future experiments based on those conclusions.

In particular, the sensitivity coefficients given in Sect. 5.2 provide an indication of how experimental results will change as a function of time or other experimentally controllable factors like r_p or oxidant concentration. In the discussion that follows we will give special attention to the interchangeability of time and oxidant concentration, which is a necessary condition for usage of the net exposure metric (concentration of oxidant $\times$ time) for application to atmospheric concentrations and time scales. Renbaum and Smith (2011) recently showed that under constant precursor concentrations, the exposure metric was valid for the reaction of OH and Cl radicals with squalane, brassidic acid, and 2-octyldodecanoic acid. However, other studies have found that the exposure metric breaks down when scaling from laboratory to ambient conditions, as summarised by Renbaum and Smith (2011).

5.1 Characteristic decay shapes

An overview of the eight distinct limiting cases and several regimes is given in Table 3 along with their characteristic limiting process(es). Each limiting case has a single rate-limiting process by definition and exhibits a characteristic behaviour as a function of time. A set of idealised KM-SUB parameter sets has been obtained by modifying the typical base case for the reaction oleic acid and ozone, see Appendix D for details.

The computed behaviours for these archetypal limiting cases are shown in Fig. 5 as a function of time for the total number of molecule Y remaining (N_Y) and for the effective uptake coefficient ($\gamma_{eff,X} = \gamma_X \cdot C_{g,X}$). These two quantities are the observables in experimental studies which in general either measure bulk Y (N_Y) or gas-phase X ($\gamma_{eff,X}$). Typical data for N_Y are shown on a linear time axis with linear (Fig. 5a) and logarithmic (Fig. 5b) y-axes. Data for $\gamma_{eff,X}$ are shown on a logarithmic y-axis with a linear (Fig. 5c.) and logarithmic (Fig. 5d) time axis. All N_Y data are normalised against the initial value $N_{Y,0}$ and all time data are scaled to t_{99} (the time at which 99 % of the bulk material has reacted).

A set of limiting cases showing linear decay behaviour of N_Y in time (S_α, B_α, S_{gd}, B_{gd}; see panel a) arises when transport over a certain interface creates a bottle-neck that limits the reaction (effectively, a 0-th order-type reaction). In panels c and d, these behaviours are characterised by time-invariant values of $\gamma_{eff,X}$. As opposed to panels a and b, not all lines with similar shape are overlapping since reaction speeds slightly differ between the chosen input parameter sets and no normalisation for $\gamma_{eff,X}$ has been carried out. However, the qualitative lineshape is consistent, independent of the actual reaction speed.

In panel b, the B_{rx} and S_{rx} cases appear linear and can therefore be classified as mono-exponential decays, pointing towards a first-order type process. A similar shape is found for the S_{bd} case after an initial fast decay that might be due to quick depletion of near-surface bulk layers. Hence, the system is not a true S_{bd} limiting case in the first moments of the reaction as the gradient in Y has yet to develop. The initial decay of $\gamma_{eff,X}$ for the S_{bd} case is well-resolved in panel d, showing a linear decrease in log-log space with slope $\frac{1}{2}$. This is characteristic for cases that are not in reacto-diffusive steady state, an inherent property of bulk diffusion-limited cases.

The same initial decay of $\gamma_{eff,X}$ can thus be found for the B_{bd} limiting case (bulk reaction limited by bulk diffusion). This case furthermore shows a nonlinear, higher-order exponential decay in N_Y as characteristic feature (panels a and b). The reaction slows down significantly once the diffusional gradients in X and Y are developed. As the rate of formation of the gradients and the location where the gradients form is not prescribed, this limiting case is expected to encompass a range of behaviours and will not have a single defining characteristic.

Table 3. List of kinetic regimes and limiting cases and their respective controlling processes. Limiting cases are characterised by being controlled by one process, while systems in the regimes shown here are controlled by at most two processes. The parameters which influence the processes are given in a separate column and are defined in Table 2.

Limiting Processes	Parameters	Regime/Limiting Case		Limiting Process	Parameter(s)
Reaction and diffusion (surface)	k_{SLR}, $D_{b,Y}$, K_{ads}	S^{rd}	S_{rx} S_{bd}	Chemical reaction at surface Bulk diffusion of Y	k_{SLR}, K_{ads}^{a} $D_{b,Y}$
Mass transfer of X to surface	$\alpha_{s,0,X}$, $D_{g,X}$	S^{mt}	S_{α} S_{gd}	Surface accommodation of X Gas-phase diffusion of X	$\alpha_{s,0,X}$ $D_{g,X}$
Reaction and diffusion (bulk)	k_{BR}, $D_{b,X}$, $D_{b,Y}$, H_X	B^{rd}	B_{rx} B_{trad}^{rd} B_{bd}	Chemical reaction in bulk Equal parts reaction and diffusion Bulk diffusion of X and Y	k_{BR}, H_X k_{BR}, $D_{b,X}$, H_X $D_{b,X}$, H_X, $D_{b,Y}$
Mass transfer of X to bulk	$\alpha_{s,0,X}$, $D_{g,X}$, $D_{b,X}$, H_X	B^{mt}	B_{α} B_{gd}	Bulk accommodation of X Gas-phase diffusion of X	$\alpha_{s,0,X}$, $D_{b,X}$, H_X^{b} $D_{g,X}$

[a] K_{ads} is not a direct input parameter of the model, but inherently depends on $\tau_{d,X}$ and $\alpha_{s,0,X}$ as shown in Eq. (4).
[b] These parameters altogether determine the bulk accommodation coefficient $\alpha_{b,X}$.

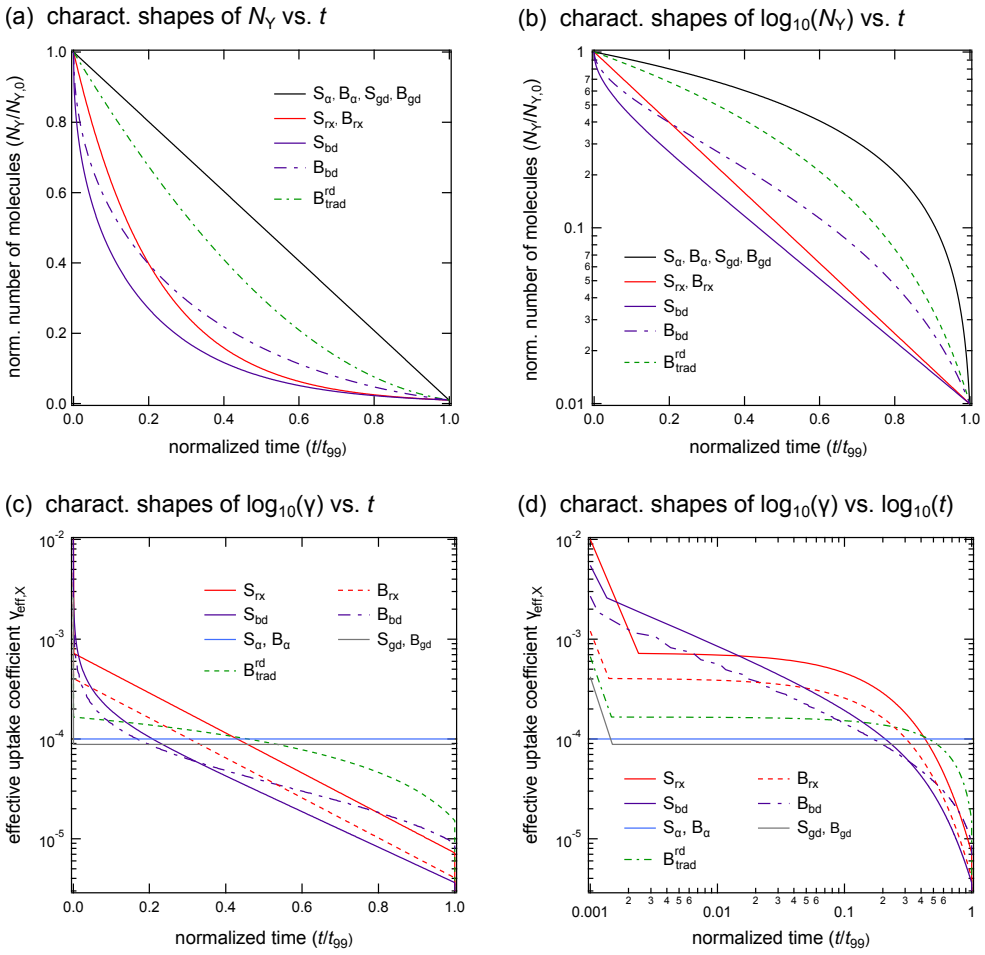

Fig. 5. Normalised representation of the decay shapes of the total amount of Y (N_Y, panels **a** and **b**) and the effective reactive uptake coefficient ($\gamma_{eff,X}$, panels **c** and **d**) for all limiting cases on linear and logarithmic time scales (see Sect. 5.1 for a more complete description). In addition to the eight regular limiting cases, we also display the traditional reacto-diffusive case, B_{trad}^{rd}. Note that B_{trad}^{rd} is not a limiting case, but a distinct scenario in the reaction-diffusion regime.

Table 4. Scalability of limiting cases with respect to r_p and $[X]_g$ expressed by the normalised sensitivity coefficient of each archetypal case (see Eq. 19). Square brackets indicate the range of possible values.

Limiting Case	$S^n(\mathrm{rp})$	$S^n([\mathrm{X}]\mathrm{g})$
S_{rx}	-1	[0, 1]
S_{bd}	-2	0
S_α	-1	1
S_{gd}	-2	1
B_{rx}	0	1
B_{bd}	-2	[$\sim$ 0, 1]
B_α	[-2, -1]	1
B_{gd}	-2	1
B^{rd}_{trad}, *	-1	1

* Note that B^{rd}_{trad} is not a limiting case, but a distinct scenario in the reaction-diffusion regime.

In addition to the eight limiting cases, the traditional reacto-diffusive bulk reaction case B^{rd}_{trad} can be recognised by showing a quadratic decay of N_Y as a function of time in linear space. In panel d, it resembles the S_{rx} and B_{rx} cases, but can be distinguished from those two in the linear representation, panel c.

5.2 Scalability of each limiting case

The typical response of each limiting case to changes in oxidant concentration $[X]_g$ and particle radius r_p was investigated using the global sensitivity method described in Sect. 4.3 and the results are given in Table 4. The standard kinetic method of performing "experiments" (here, simulations) at differing $[X]_g$ and r_p to determine the response (linear, inverse, etc.) yielded identical results. The results of the sensitivity analysis performed on the limiting cases displayed above indicate that the exposure metric is acceptable to use (i.e. linear response to $[X]_g$, $S^n([X]_g) = 1$) as long as a transport process is not saturated.

In the example of S_{rx} behaviour above, all surface sites were occupied (surface coverages $\theta_{s,sat} = \theta_{s,max} = 1$ and $\theta_s \approx \theta_{s,sat}$) and thus changes in $[X]_g$ had no effect on the reaction rate. In this situation, it is typical that the measured uptake coefficient γ_X is inversely proportional to $[X]_g$. However, S_{rx} behaviour can also be observed when $\theta_{s,sat} < \theta_{s,max}$ if the adsorption equilibrium constant K_{ads} dictates that only partial surface coverage can be achieved at equilibrium with gas-phase X (here $\theta_s \approx \theta_{s,sat}$, but $\theta_{s,sat} < \theta_{s,max}$). Here, increasing $[X]_g$ will increase the surface coverage, leading to a faster overall rate of reaction. In this non-saturated S_{rx} case, the gas uptake is thus also sensitive to K_{ads}, which in turn depends on both accommodation coefficient $\alpha_{s,0}$ and desorption lifetime τ_d.

The lack of sensitivity to $[X]_g$ in the bulk diffusion-limited cases (S_{bd} and B_{bd}, see Table 4) arises due to the rate-limitation that the diffusion of Y poses. This process is obviously not accelerated by an increase in trace gas concentration. Thus, S_{bd} behaviour, which is entirely limited by diffusion of Y, shows no dependence on $[X]_g$. B_{bd} cases still respond to an increase in $[X]_g$ since the combined diffusion of X and Y is rate-limiting here. Thus, the sensitivity to $[X]_g$ will always be smaller than unity but higher than zero in a B_{bd} case.

Thus, in addition to the explanations already offered for failures of scalability (e.g. secondary chemistry, absorption of other gases etc., see Renbaum and Smith, 2011), we found that systems in which the transport from bulk material to the reaction site is rate limiting (i.e. S_{bd} and B_{bd} behaviour) or surface saturation effects play a role (certain S_{rx} cases with $\theta_s = \theta_{s,sat} \approx \theta_{s,max}$) will not act in accordance with the exposure metric.

The sensitivity analysis also provided information on the expected response of each limiting case to changes in particle size. The data displayed in Table 4 for $S^n(r_p)$ show the influence of particle size on reactive half-life. Using Eq. 19 to interpret the sensitivity coefficients, these results show that the reactive half-life of systems which are limited by surface-related processes have an inverse dependence on particle size ($S^n(r_p) = -1$), systems which are limited by diffusion have an inverse-square dependence on particle size ($S^n(r_p) = -2$), and that the B_{rx} limiting case does not depend on particle size at all ($S^n(r_p) = 0$). We note that in bulk accommodation-limited bulk reaction cases, B_α, the value of $S^n(r_p)$ is typically -1 if limitation arises due to inefficient accommodation of X on the surface, but may decrease to -2 when transport across the surface-bulk interface is the rate-limiting step. For a more detailed description of these two different B_α scenarios, see Appendix C.

Taken together, these characteristic behaviours and sensitivities can provide some insight into an experiment based only on the raw data. After making a preliminary assignment based on the decay shape of one dataset, the sensitivities in Sect. 5.2 can be used together with additional experiments to confirm this assignment.

6 Case study: the oleic acid–ozone reaction system

The oleic acid–ozone reaction system is an extremely well studied system which has often been used as a benchmark for heterogeneous chemistry systems (see, e.g. the review of Zahardis and Petrucci, 2007), so it is reasonable that we apply the proposed classification scheme to this reaction system. We emphasise that this case study is meant to demonstrate the applicability of the classification system and is not intended to infer new mechanistic information on the oleic acid system.

We will begin with a brief overview of the current state of the art in modelling this system and then apply the classification scheme described above to previously published

datasets. A comparison of these results with one another and with current work is difficult as each study uses a different nomenclature for the limiting cases which they consider. In the following discussion, the common symbol set proposed above will be used to facilitate comparisons between previous studies and this work. We stress that our fits to the experimental data are not equally likely to represent reality and we do not attempt to judge between them.

6.1 Background

In the past, limiting cases similar to those discussed here have been derived by both Smith et al. (2002) and Worsnop et al. (2002) for this reaction system, including resistor model-based analytical expressions for comparison to experimental results. In the era before depth-resolved computation of aerosol reaction was common, Smith et al. (2003) solved the partial differential equations of diffusion and reaction for this system to provide results resolved in time and depth, but assumed the surface was saturated with respect to trace gas, a crucial assumption which disallows mass transfer-limited behaviour and constrains all results to the reaction-diffusion regime.

The relationships between the limiting cases proposed here and those already published by Smith et al. (2002) (including revisions made in Hearn et al., 2005) as well as in Worsnop et al. (2002) are depicted in Table 5. The most striking differences between these cases and previous schemes is the under-representation of the mass transfer regime: although Worsnop et al. offer a mass transfer-limited case, this only applies to a bulk reaction and is not necessarily a case limited by a single process. It thus represents a range of cases, all of which fall within our definition of the B^{mt} regime (bulk reactions limited by mass transfer). Furthermore, we consider Case 2 of Worsnop et al. (2002), Case 1b of Smith et al. (2002) and Case 2 of Hearn et al. (2005) to be representations of the traditional reacto-diffusive case B^{rd}_{trad} within the reaction-diffusion regime, as all have a formulation which shows dependence on both the diffusion of X and the reaction rate coefficient and thus depend on more than one process to determine reactive uptake. To achieve true bulk diffusion-limited behaviour for such a system (B_{bd} limiting case), the reacto-diffusive length of both X and Y must be exceedingly short.

6.2 Ziemann (2005) dataset

A well-supported kinetic parameter set for the oleic acid–ozone reaction system is provided by Pfrang et al. (2010), which used the accommodation coefficient $\alpha_{s,0,X}$ as a fitting parameter to match model output to the experimental results of Ziemann (2005). In that study, the decreasing oleic acid content of 200 nm radius particles reacting with ozone at a molecular number density of $\sim 6.95 \times 10^{13}\,\mathrm{cm}^{-3}$ in an environmental chamber was measured via Thermal Desorption Particle Beam Mass Spectrometry. The parameter set of Pfrang et al. is displayed in column 2 of Table 6 and will be referred to as base case 1 (bc1). The bc1 parameter set does not include a gas-phase diffusivity of ozone in air. Unless otherwise noted, we used $D_{g,X} = 0.14\,\mathrm{cm}^2\,\mathrm{s}^{-1}$ (Massman, 1998). We begin our analysis by replicating the bc1 fit from Pfrang et al. (2010), resulting in very good agreement with the experimental data as shown in Fig. 6a. While this fit does not fall into a limiting case (see Sect. 4.2), it shows low values for both saturation ratios SSR and BSR as well as a gas phase mixing parameter $C_{g,X} \sim 1$, altogether indicative of the SB^{α} regime (see Fig. 3b). The classification parameters are given along with the input parameter values in Table 6 for two different points in reaction course.

Although the bc1 parameter set provides an excellent fit to the experimental results of Ziemann (2005), other studies have provided additional information which suggest that the oleic acid diffusion coefficient $D_{b,Y}$ is significantly higher than the original value of $1 \times 10^{-10}\,\mathrm{cm}^2\,\mathrm{s}^{-1}$ (Shiraiwa et al., 2012a; Hearn et al., 2005) and that the desorption lifetime of ozone ($\tau_{d,X}$) is in the order of nanoseconds for polycyclic aromatic hydrocarbons (PAH, cf. Maranzana et al., 2005; Shiraiwa et al., 2011b) as well as for graphene (Lee et al., 2009). In a modified fit, bc1* (Table 6, column 3), we adopt the value proposed by Shiraiwa et al. (2012a), $1.9 \times 10^{-7}\,\mathrm{cm}^2\,\mathrm{s}^{-1}$ and set $\tau_{d,X} = 1 \times 10^{-8}$ s. The change in $D_{b,Y}$ has only a small impact on the overall reaction speed, as diffusion of oleic acid is not involved in the limiting process (accommodation of ozone to the surface). The reduced surface desorption lifetime decreases the role of surface reactions so that the modified bc1* can be assigned B_{α} behaviour. The fit is also displayed in Fig. 6a.

Table 5. Comparison of limiting cases proposed in this study to cases of the oleic acid–ozone system in previous studies. A "–" symbol indicates no relationship. The numberings refer to the nomenclature in the original publications.

This study	Worsnop et al. (2002)	Smith et al. (2002)	Hearn et al. (2005)
S_{rx}	Case 4	Case 2	Case 3
S_{bd}	Case 5	–	Case 4
S_{α}	–	–	–
S_{gd}	–	–	–
B_{rx}	Case 3	Case 1a	Case 1
B^{rd}_{trad} [a]	Case 2	Case 1b	Case 2
B_{bd}	–	–	–
B_{α}	Case 1[b]	–	–
B_{gd}		–	–

[a] Note that B^{rd}_{trad} is not a limiting case, but a distinct scenario in the reaction-diffusion regime.
[b] Case 1 of Worsnop et al. (2002) includes a range of cases inside the B^{mt} regime.

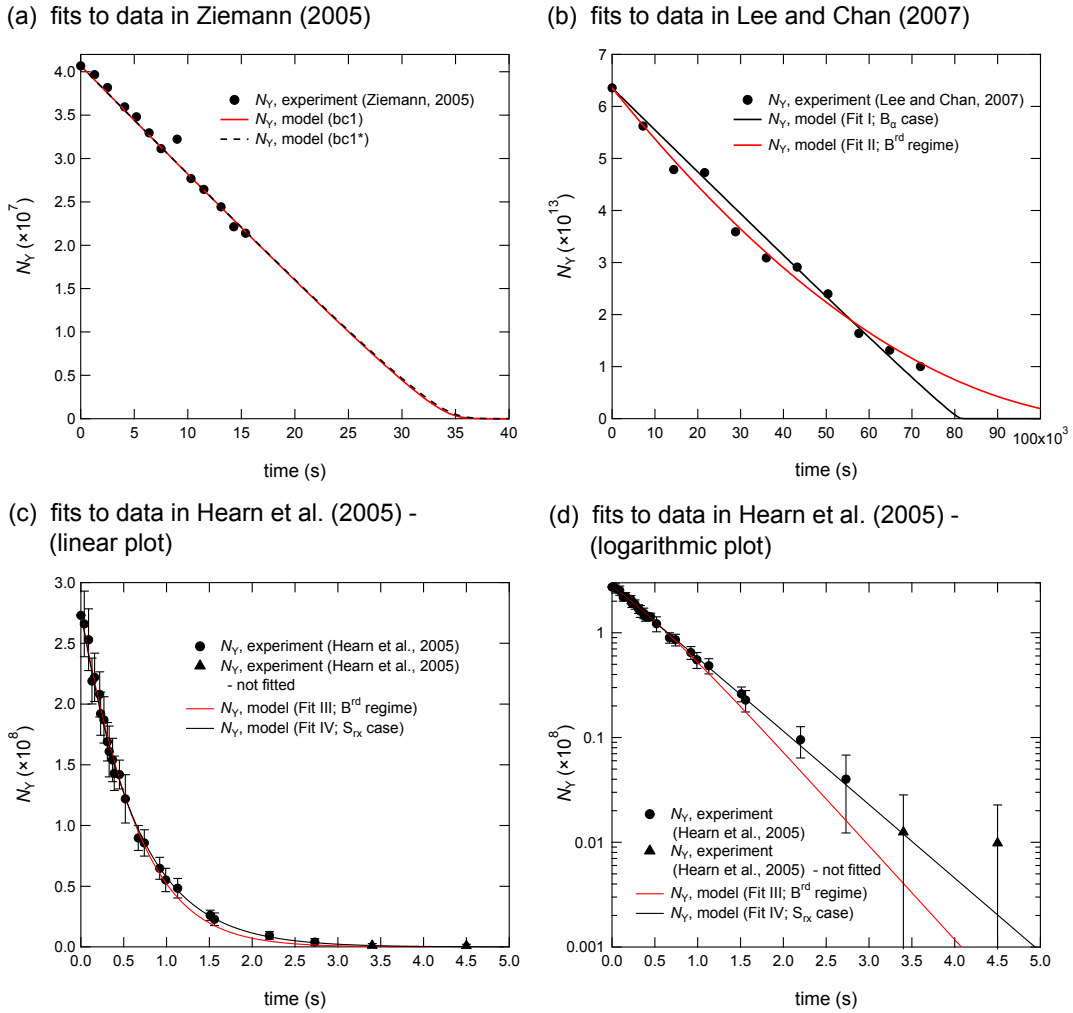

Fig. 6. Comparison of experimental and modelled data of various limiting cases, using time invariant kinetic parameters. In **(a)** the two parameter sets bc1 and bc1* lead to the same correlation with the experimental data and show the appropriate linear decay. In **(b)**, data from Lee and Chan (2007) show another mostly linear decay of bulk material. This can be realised with two KM-SUB parameter sets similar to bc1* showing B_α and B^{rd} behaviour, respectively. In **(c)**, data from Hearn et al. (2005) show a nonlinear decay that thus can not be described by accommodation-limited cases. The B^{rd} and S_{rx} fits shown are in excellent agreement with the experimental data. **(d)** reveals in a logarithmic representation that the quality of Fit III is lower after ~ 2 s and 85 % of the reaction. The last two points of this dataset (black triangles) were excluded from the fit as their value is not significantly different from zero.

6.3 Lee and Chan (2007) dataset

Lee and Chan (2007) used raman spectroscopy to measure the decay of oleic acid in particles exposed to $\sim 6.36 \times 10^{12}$ cm^{-3} ozone in an electrodynamic balance. We apply a multi-parameter fit to this dataset to find fits in reasonable proximity to the bc1* parameter set (Fits I–II, Table 6). Note that some values, including especially $\alpha_{s,0,X}$, are poorly constrained by experiment and were given large tolerances during the fitting process. Figure 2 in Lee and Chan (2007) shows the decay of oleic acid in two particles, the smaller of which was chosen for modelling in this study. The exact particle size was not reported in the original publication and particle size has thus been used as a fit parameter. We have varied the particle diameter between 40–70 µm along with the non-bracketed parameters in Fits I (B_α case) and II (B^{rd} regime) given in Table 6. Both fits are in good agreement the experimental data, as shown in Fig. 6b.

The two fits shown here were calculated assuming a particle diameter of 40 µm for the smaller particle, which is within the size range estimated by Lee and Chan (2007). Due to the large particle size in this dataset, the layer spacing scheme in KM-SUB had to be altered to achieve numerical convergence of the modelling result. From a total of 200 computed layers, 40 were chosen to form a narrowly resolved surface region. Each of these layers was attributed a depth of about 10 ozone monolayers (4 nm). The residual space was then equally distributed in depth among the 160 remaining layers.

Table 6. Kinetic parameter sets for KM-SUB that represent possible fits to experimental data provided by Ziemann (2005), Lee and Chan (2007) and Hearn et al. (2005). bc1, bc1* and Fit I are obtained by adjusting $\alpha_{s,0,X}$ while Fits II to IV are multi-parameter fits, obtained by least-squares fitting of modelled to experimental data. Even though Fits II and III do not exhibit limiting case behaviour, they can still be assigned as a bulk reaction limited by reaction and diffusion (reacto-diffusion limitation). Values that were fixed during the fitting procedures are marked with square brackets.

Parameters	bc1[a] Ziemann	bc1* Ziemann	Fit I Lee and Chan	Fit II Lee and Chan	Fit III Hearn	Fit IV Hearn
k_{BR} $\left(\frac{cm^3}{mol\,s}\right)$	$[1.70\times10^{-15}]$	$[1.70\times10^{-15}]$	$[1.70\times10^{-15}]$	2.52×10^{-16}	3.47×10^{-17}	1.72×10^{-17}
k_{SLR} $\left(\frac{cm^2}{mol\,s}\right)$	$[6.00\times10^{-12}]$	$[6.00\times10^{-12}]$	$[6.00\times10^{-12}]$	$[6.00\times10^{-12}]$	$[6.00\times10^{-12}]$	2.90×10^{-12}
$D_{b,X}$ $\left(\frac{cm^2}{s}\right)$	$[1.00\times10^{-5}]$	$[1.00\times10^{-5}]$	$[1.00\times10^{-5}]$	$[1.00\times10^{-5}]$	$[1.00\times10^{-5}]$	$[1.00\times10^{-5}]$
$D_{b,Y}$ $\left(\frac{cm^2}{s}\right)$	$[1.00\times10^{-10}]$	$[1.90\times10^{-7}]$	$[1.90\times10^{-7}]$	$[1.90\times10^{-7}]$	$[1.90\times10^{-7}]$	$[1.90\times10^{-7}]$
$H_{cp,X}$ $\left(\frac{mol}{cm^3\,atm}\right)$	$[4.80\times10^{-4}]$	$[4.80\times10^{-4}]$	$[4.80\times10^{-4}]$	6.51×10^{-5}	8.81×10^{-4}	4.91×10^{-5}
$\tau_{d,X}$ (s)	$[1.00\times10^{-2}]$	$[1.00\times10^{-8}]$	$[1.00\times10^{-8}]$	$[1.00\times10^{-8}]$	$[1.00\times10^{-8}]$	1.10×10^{-4}[b]
$\alpha_{s,0,X}$ (–)	4.20×10^{-4}	4.61×10^{-4}	3.04×10^{-4}	4.18×10^{-2}	2.81×10^{-2}	3.08×10^{-2}
$D_{g,X}$ $\left(\frac{cm^2}{s}\right)$	$[1.4\times10^{-1}]$	$[1.4\times10^{-1}]$	$[1.4\times10^{-1}]$	$[1.4\times10^{-1}]$	$[1.4\times10^{-1}]$	$[1.4\times10^{-1}]$
10 % reaction course						
STLR	0.310	4.63×10^{-7}	3.52×10^{-7}	1.37×10^{-3}	2.06×10^{-4}	0.966
SR	0.082	0.079	0.031	0.905	0.951	0.996
MP	0.999	0.999	0.965	0.483	0.744	0.999
50 % reaction course						
STLR	0.259	3.61×10^{-7}	2.61×10^{-7}	9.00×10^{-4}	3.14×10^{-4}	0.964
SR	0.056	0.108	0.044	0.928	0.969	0.998
MP	0.999	0.999	0.966	0.482	0.7455	0.999
Regime/Limiting case	SB^{α}	B_{α}[c]	B_{α}	B^{rd}	B^{rd}	S_{rx}

[a] As provided by (Pfrang et al., 2010).
[b] This value implies formation of an intermediate at the particle surface.
[c] SR at 50 % reaction course is slightly outside the numerical criterion for this assignment.

The consequences of using an insufficient number of layers, leading to non-resolved (step) gradients are briefly addressed in Appendix C.

Both Fit I and Fit II are consistent with the observed decay and could only be distinguished from one another in fit quality in the final stages of the reaction, for which no data are available. However, Fit I directly matches the B_{α} assignment that was made for the dataset of Ziemann (2005), while Fit II would only match a nonlinear decay. Indeed, most previous observations of this system, which are summarised in the comprehensive review of Zahardis and Petrucci (2007), were generally nonlinear in time. This is an example of the logical error which arises when limiting case behaviour observed under one condition (small particles, high oxidant concentration) is assumed to apply elsewhere (very large particles, much lower oxidant concentration). We therefore continue with a more in-depth analysis of a dataset measured with smaller particles at high oxidant concentration that shows a pronounced nonlinearity and includes data to the very end of the reaction.

6.4 Hearn et al. (2005) dataset

A second multi-parameter fit was applied to the aerosol Chemical Ionization Mass Spectrometric measurements in Hearn et al. (2005) (650 nm diameter oleic acid particles reacting with 2.76×10^{15} cm^{-3} ozone in an aerosol flow tube). As shown in Fig. 6c, the resulting fits exhibit behaviour indicative of the B^{rd} regime (bulk reaction limited by chemical reaction and/or bulk diffusion) and the S_{rx} limiting case (surface reaction limited by chemical reaction), respectively. Although both Fit III and Fit IV resemble the experimental data reasonably when viewed on a linear scale, the logarithmic representation of Fig. 6d shows that Fit III deviates marginally from the data after 2.0 s. This was already discussed by Hearn et al. for the traditional reacto-diffusive case B^{rd}_{trad}, which is a subset of the B^{rd} regime. The B^{rd}_{trad} case has

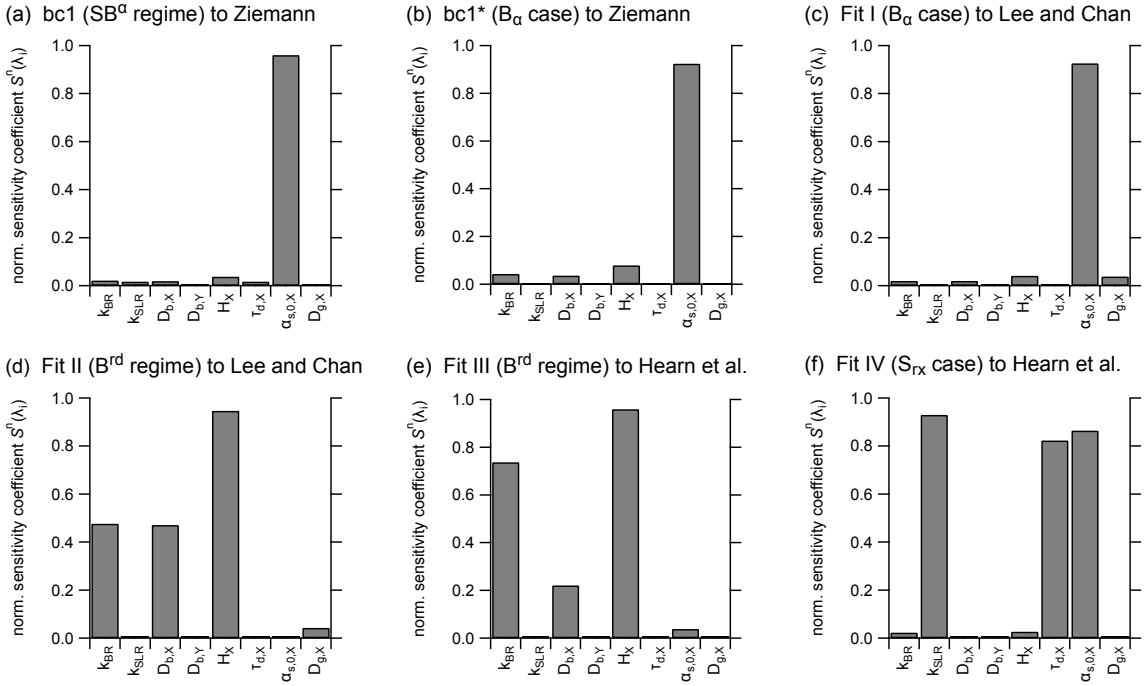

Fig. 7. Sensitivity profiles of parameter sets for a KM-SUB simulation of oleic acid–ozone. The parameter values used to generate these fits are shown in Table 6. Datasets are: **(a)** and **(b)**, Ziemann (2005); **(c)** and **(d)**, Lee and Chan (2007); **(e)** and **(f)**, Hearn et al. (2005). These sensitivity tests corroborate the limiting case and regime assignments made in this study, and indicate that the 9 : 1 criterion is sufficient to separate limiting case behaviours. The sensitivity coefficients were determined via Morris' Elementary Effects method for global sensitivity analysis (Morris, 1991) as recommended by Saltelli et al. (2008).

a quadratic-like functional form in $N_Y(t)$ that is not able to fit the experimentally observed mono-exponential decay. In contrast to the "ideal" B^{rd}_{trad} case, Fit III does not show a true quadratic decay shape and lies significantly closer to the experimental data compared to the fit shown in Fig. 2 of Hearn et al. (2005). This improved fit arises because Fit III does not exactly match the B^{rd}_{trad} scenario and its kinetic behaviour changes towards B_{rx} as the reaction proceeds.

A rather different picture of the internal structure of the aerosol particle is provided with Fit IV, showing an excellent fit to the experimental data in reasonable proximity to the original bc1 parameter set of Pfrang et al. (2010). This fully-saturated surface reaction is consistent with the conclusion of Hearn et al. (2005), who suggested that the reaction occurs exclusively on the particle surface as a result of a quasi-smectic structure of the uppermost oleic acid layer that is impenetrable by ozone due to slow diffusion and fast reaction.

We note that the surface reaction behaviour in Fit IV is only achieved using a $\tau_{d,X}$ which significantly exceeds the values inferred from molecular dynamics simulations as discussed in Sect. 6.2 above. Such a value would be acceptable only if a long-lived intermediate was formed at the particle surface (as discussed in Shiraiwa et al. (2011b) for $PAH + O_3$).

Both Fit III and Fit IV are in reasonable agreement with the single experimental decay in Fig. 6. However, further experimental results of Hearn et al. with differently sized particles indicate that the initial reaction rate scales inversely with the particle radius ($S^n(r_p) = -1$), which is typical for systems that are limited by a surface-related process such as S_{rx}, B_α or B^{rd}_{trad} (see Table 4). A more detailed discussion of the size-dependent data can be found in Appendix E.

6.5 Sensitivity profiles of displayed limiting cases

As discussed in Sect. 4.3, we recommend sensitivity analysis to confirm that the numerical criteria chosen result in distinct and well-behaved limiting cases. Figure 7 shows the sensitivity profiles of the six parameter sets found for the oleic acid–ozone system. In each case, the assignment is supported by the sensitivity analysis. Sensitivity coefficients are given at 10 % reaction course as this not only avoids the initial, highly transient behaviour which is expected as the surface and first bulk layers come into equilibrium with the gas phase, but also minimises the error associated with neglecting reaction products in the depth-resolved model.

The interpretation of the fits to Ziemann (2005) data, panels a and b of Fig. 7 is relatively straightforward. As expected from Table 3, these fits are only sensitive to the accommodation coefficient $\alpha_{s,0,X}$. Indeed, in panel a, only $\alpha_{s,0,X}$ is indicated as a direct control on the result of the calculation, in accordance with the accommodation regime (SB$^{\alpha}$). In panel

b, the sensitivity to $\alpha_{s,0,X}$ remains high while some minor dependence on parameters related to bulk reaction ($H_{cp,X}$, k_{BR}, $D_{b,X}$) is observed, both in agreement with the assignment as B_α limiting case (bulk reactions limited by accommodation).

Panels c and d show sensitivity analyses of fits to the Lee and Chan (2007) data and reveal very typical behaviour for the B_α case and the B^{rd} regime, respectively. While Fit I in panel c is completely governed by the $\alpha_{s,0,X}$ parameter, Fit II in panel d shows the traditional reacto-diffusive behaviour with a balanced sensitivity towards the reaction and diffusion process. In both cases, the large particle radius leads to a slight influence of gas-phase diffusion as indicated by sensitivity to $D_{g,X}$.

The interpretation of the fits to Hearn et al. (2005) data, panels e and f of Fig. 7 also confirms our assignments. In panel e, the parameters indicate a mixture of bulk reaction and bulk diffusion limiting cases (B^{rd} regime). Unlike Fit II in panel d, this case does not coincide with the traditional B^{rd}_{trad} case, as it shows a slight predominance towards reaction limitation and thus B_{rx} behaviour. This example demonstrates the breadth of possible behaviours for cases that do not fall into a distinct limiting case but rather exhibit regime behaviour. In panel f, the surface reaction rate coefficient k_{SLR} as well as the parameters determining the surface coverage ($\tau_{d,X}$ and $\alpha_{s,0}$) are influential. Thus, S_{rx} behaviour was correctly assigned.

In general, sensitivity coefficients were not observed to vary significantly over time once a quasi-stationary state of transport and reaction was reached. In the event that behaviour is not consistent throughout the reaction, a change in regime or limiting case behaviour can be detected by a change in classification parameters and the sensitivity coefficients follow accordingly. For example, classification parameters for Fit III (Table 6) show an increase in mixing parameter BMP_{XY} over time, indicating a smooth transition from B^{rd} regime towards B_{rx} limiting case behaviour. This is accompanied by a decrease in sensitivity towards the bulk diffusion coefficient $D_{b,X}$ from $S^n(D_{b,X}) = 0.22$ at 10 % reaction course to 0.16 at 50 % reaction course and 0.04 at 90 % reaction course.

In interpreting these sensitivity analyses, a low sensitivity does not necessarily mean that a process related to that parameter is unimportant, only that modest changes in that parameter do not have a strong influence on the model result. This could be the case if a parameter is obviated (e.g. the Henry's law constant in a system which reacts exclusively at the surface, in which case it could take on any value) or if a process is saturated (e.g. the reaction rate coefficient in an accommodation-limited case, for which modest changes in k_{BR} would not matter as the reaction would remain "fast" compared to the accommodation process). Overall, the simple 9 : 1 numerical criteria proposed in Sect. 4.2 were sufficient for this system, but should be revisited for each new chemical system to ensure that limiting cases and regimes are well-behaved (that is, influenced by only one or two processes, respectively).

6.6 Conclusions from the case study

In summary, analysis of three literature datasets of the oleic acid–ozone reaction system led to six different sets of kinetic parameters for the applied kinetic model KM-SUB. The proposed classification scheme was applied to these fits, leading to assignments of limiting cases or regimes. However, underlying kinetic parameters could not be determined uniquely and no final limiting case assignment could be made. This is, however not the result of a deficiency in the classification scheme. Rather, it highlights the inherent complexity of experimental kinetics and the fitting process necessary to infer kinetic parameters from experimental data. Parameters which are not among the limiting parameters of the reaction system (cf. Table 3 and Fig. 7) do not directly influence the reaction rate and are thus poorly constrained by experiments. Single measurements in one kinetic regime can usually only determine one (or a few) parameter(s), and put constraints on others.

Consequently, none of the example parameter sets given here was able to fit all three experimental datasets. A parameter set which fully represents the underlying kinetic parameters in the oleic acid–ozone system will thus require further experimental and theoretical studies in which multiple datasets are simultaneously fitted (a global fit). These datasets should ideally be obtained under vastly differing conditions (reaction time, particle size and oxidant concentration), thereby changing the kinetic regime and providing constraints on a wider variety of kinetic parameters.

7 Summary and conclusions

The development of depth-resolved models for aerosol chemistry has prompted the more sophisticated, systematic classification of the kinetic behaviour of aerosol particles proposed here. The set of limiting cases and associated symbols proposed above should allow a more complete and more intuitive discussion of aerosol particle behaviour, especially in systems which exhibit stiff coupling of physical and/or chemical processes. In particular, the more complete treatment of mass transfer limitation presented in this study not only allows for analysis of such systems, but may also assist in interpreting and reconciling previous studies.

Limiting case or kinetic regime assignments facilitate the interpretation of experimental data since, in principle, only the rate limiting process(es) have to be considered when calculating or analysing reactive uptake. During an experimental study, results can be compared to the characteristic behaviours described in Sect. 5 which may provide insight into the kinetic behaviour of aerosol particles. If the experimental results match a profile of a limiting case, the predicted

sensitivity of the assigned case to experimental conditions may be useful in guiding follow-up experiments.

As outlined above, a single chemical reaction system can exhibit different kinetic behaviours depending on reaction conditions such as concentration levels and particle sizes. The classification scheme proposed here provides a means of characterising a specific reaction system under specific conditions, but the underlying parameters which drive the physical and chemical behaviour remain the most valuable information which models can extract from experimental data. This is particularly important for the extrapolation of laboratory results to atmospherically relevant conditions, a task which demands a well-constrained parameter set to provide reliable results. Therefore, we emphasise the need for experiments at different time scales, particle sizes and reactant concentrations, to provide enough constraints for accurate determination of fundamental kinetic parameters. In light of the breakdown of the exposure metric (oxidant concentration $\times$ time) for some aerosol behaviours, we recommend that studies which use the exposure metric should also provide independent concentration and time data for future reanalysis.

Multi-parameter fitting of three different datasets for the benchmark system of oleic acid reacting with ozone has shown that the available data can be represented by different sets of kinetic parameters that do not correspond to a single kinetic behaviour (regime or limiting case). Using only one dataset at a time for the fitting of several kinetic parameters resulted in an under-determined system.

We conclude that for a well-constrained kinetic parameter set, several datasets should be taken into account simultaneously to provide a sufficiently broad set of constraints for the fitting result. These sets must include a wide range of experimental conditions, since non-limiting parameters are only poorly constrained by experimental data. Multi-parameter fitting to multiple datasets for extraction of kinetic parameters would therefore be of general importance for modelling of multiphase chemistry, but requires a significantly higher technical effort. The prospects and challenges of multi-dimensional fitting to elucidate the kinetic parameters of aerosol reaction systems will thus be addressed in detail in a follow-up study, building on the classification framework provided here.

Appendix B

Additional regimes

In addition to the reaction-diffusion and mass transfer regimes used throughout this work, there are many other combinations of limiting cases to form regimes which are possible. Sorting by mixing parameter MP leads to the distinction in Fig. S1a, the diffusion regime and the reaction-accommodation regime. This separation is less common than that shown in Fig. 3a for analysis of chemical reactivity. The typical example of a system in the reaction-accommodation regime arises when a particle is well-mixed and neither saturated nor starved on trace gas X, indicated by SSR and/or BSR ≈ 0.5. Here, reaction and accommodation occur on similar time scales and are thus closely coupled. Another possibility is shown in Fig. S1b, in which the separation is made between chemical rate limitation ("reaction regime") and all other possibilities ("mass transport regime"). We view the mass transport regime (not to be confused with the mass transfer regime SB^{mt}) in Fig. S1b as too broad to be useful, as systems lying in this regime may encompass every limitation on chemical reaction rate except the actual rate coefficient.

Appendix C

Strong bulk concentration gradients not equivalent to diffusion limitation

As already described in Sect. 2.2, the reaction-diffusion regime encompasses all cases limited by chemical reaction and/or bulk diffusion and the traditional reacto-diffusive case within this regime, B^{rd}_{trad}, occurs when STLR ≈ 0, BSR ≈ 1, $BMP_X \approx 0$ and $BMP_Y \approx 1$. In this situation, the surface and first subsurface bulk layer are saturated with X and the short reacto-diffusive length of X limits the reaction volume and thus reactive uptake. Because reaction and diffusion of X are inherently coupled in the B^{rd}_{trad} case, this case does not exhibit B_{bd} behaviour even though it shows a strong gradient in X. This would violate the definition of single-process limitation for limiting cases given in Sect. 2.1.

In addition to the B^{rd}_{trad} case, another behaviour can also be observed when $BMP_X \approx 0$, $BMP_Y \approx 1$, SSR ≈ 1, but BSR ≈ 0. Here, the surface is saturated with X but the transfer from surface to bulk is inefficient compared to reaction in the bulk. Since BSR ≈ 0 in this situation, this case is correctly assigned as a B_α case, and has a behaviour which is consistent with the archetypal B_α case described in Sect. 5.1. We will distinguish this surface to bulk transfer-limited case from the gas to surface transfer-limited case by referring to each as $B_{\alpha,s\rightarrow b}$ and $B_{\alpha,g\rightarrow s}$, respectively.

Typically, the values of SSR and BSR are expected to be similar (for an overview of the relationship between SSR and BSR for different limiting cases and regimes, see Table S3). As suggested by the name "surface to bulk transfer-limited", a discrepancy between SSR and BSR arises in the $B_{\alpha,s\rightarrow b}$ case. This situation depends crucially on the layer spacing in the model. Such a discrepancy between SSR and BSR could arise when the reacto-diffusive length is so short that it falls below layer spacing, which is often constrained to be one molecular length (e.g. a monolayer of Y) or larger. In such a situation, the assumption of internally well-mixed model layers is violated and the quasi-static surface layer acts as a diffusional bottleneck that has to be surpassed before bulk

Table A1. List of symbols and abbreviations.

Symbol	Meaning	SI Unit
$\alpha_{b,X}$	bulk accommodation coefficient of X	
$\alpha_{s,X}$	surface accommodation coefficient of X	
$\alpha_{s,0,X}$	surface accommodation coefficient of X on an adsorbate-free surface	
γ_X	uptake coefficient of X (normalised by gas kinetic flux of surface collisions)	
$\gamma_{eff,X}$	effective uptake coefficient of X (normalised by average gas kinetic flux)	
δ_Y	effective molecular length of Y	m
$\theta_{s,X}$	surface coverage by X (sorption layer)	
$\theta_{s,max,X}$	maximum surface coverage by X (sorption layer)	
$\theta_{s,sat,X}$	saturation surface coverage by X (sorption layer)	
λ_i	kinetic input parameter i	
λ_X	mean free path of X in the gas phase	m
$\tau_{d,X}$	desorption lifetime of X	s
ω_X	mean thermal velocity of X	$m\,s^{-1}$
bc1	base case 1 input parameter set	
bc1*	modified base case 1 input parameter set	
BMP_X	mixing parameter for bulk diffusion of X (bulk reaction)	
BMP_Y	mixing parameter for bulk diffusion of Y (bulk reaction)	
BMP_{XY}	joint mixing parameter for bulk diffusion of X and Y (bulk reaction)	
BSR	bulk saturation ratio	
$C_{g,X}$	gas-phase diffusion correction factor for X and mixing parameter for gas phase X	
$D_{b,X}$	particle bulk diffusion coefficient of X	$m^2\,s^{-1}$
$D_{g,X}$	gas-phase diffusion coefficient of X	$m^2\,s^{-1}$
$H_{cp,X}$	Henry's law coefficient of X	$mol\,m^{-3}\,Pa^{-1}$
k_a	first-order adsorption rate coefficient of X	$m\,s^{-1}$
k_d	first-order desorption rate coefficient of X	s^{-1}
k_{BR}	second-order rate coefficient for bulk reactions	$m^3\,s^{-1}$
k_{SLR}	second-order rate coefficient for surface layer reactions	$m^2\,s^{-1}$
$K_{ads,X}$	adsorption equilibrium constant of X	m^3
$K_{sol,cc,X}$	dimensionless solubility or gas-particle partitioning coefficient of X	
Kn_X	Knudsen number for X	
$l_{rd,X}$	reacto-diffusive length of X in Y	m
L_k	loss rate upon bulk reaction in layer k	s^{-1}
L_s	loss rate upon surface reaction	s^{-1}
L_{tot}	total loss rate (of surface and bulk reaction)	s^{-1}
SR	saturation ratio	
n	number of bulk layers in discretized representation of the particle	
N_Y	number of molecules of Y left in the aerosol particle	
r_p	particle radius	m
$S(\lambda_i)$	model sensitivity towards λ_i	
$S^n(\lambda_i)$	normalised model sensitivity towards λ_i	
SMP_Y	mixing parameter for bulk mixing of Y (surface reaction)	
SR	saturation ratio	
SSR	surface saturation satio	
STLR	surface to total loss rate ratio	
t	time	s
T	temperature	K
V_k	volume of layer k	m^3
X	trace gas species	
$[X]_{eff}$	effective bulk concentration of X experienced by reacting Y	m^{-3}
$[X]_g$	gas-phase number concentration of X	m^{-3}
$[X]_{gs}$	near-surface gas-phase number concentration of X	m^{-3}
$[X]_s$	surface number concentration of X (sorption layer)	m^{-2}
$[X]_{ss}$	subsurface number concentration of X (quasi-static surface layer)	m^{-2}
$[X]_{s,max}$	maximum surface number concentration of X (sorption layer)	m^{-2}
$[X]_{s,sat}$	saturation surface number concentration of X (sorption layer)	m^{-2}
$[X]_b$	particle bulk number concentration of X	m^{-3}
$[X]_{bk}$	number concentration of X in k-th bulk layer	m^{-3}
$[X]_{b,sat}$	saturation particle bulk number concentration of X	m^{-3}
Y	bulk material species	
Y_{model}	model output	

reaction can occur. This effectively decouples the reaction and diffusion process. However, the treatment of competing reaction and diffusion at the molecular level might not be well-represented by the kinetic model applied here and thus lies beyond the scope of this paper.

A more intuitive example for a $B_{\alpha,s\rightarrow b}$ case is a particle that is coated by an inert and only slowly penetrable shell such as a monolayer of saturated fatty acids (Rouvière and Ammann, 2010).

Appendix D

Idealised limiting cases

The complete list of input parameters and experimental conditions for the idealised limiting cases employed in Sect. 5 is given in Tables S2 and S3. As in all other calculations in this work, it was assumed that all kinetic (e.g. k_{BR}, $D_{b,X}$, $D_{b,Y}$) and environmental (e.g. $[X]_g$, r_p, T) parameters remain constant as the reaction proceeds. Single-process limitation was ensured by disabling competing processes ($\lambda_i = 0$) and increasing the speed of non-limiting processes ($\lambda_i = 1$). To achieve similar uptake coefficients, the kinetic parameters were tuned so that an aerosol particle with 100 nm radius was processed in ~ 100 s. The parameter sets themselves are thus not based on physically correct scenarios, but represent systems which exhibit pure, single-process limiting behaviour.

Appendix E

Particle size-dependent data

Hearn et al. (2005) use initial loss rates measured at different particle sizes to further narrow down the kinetic limiting behaviour of the oleic acid–ozone reaction system. A model system's response to changes in particle size can be inferred by means of sensitivity analysis, which was conducted for Fits III and IV of Fig. 6c, d. Fit IV was found to match the experimentally observed inverse response of reaction rate to particle size ($S^n(r_p) = -0.99$), whereas Fit III shows rather an inverse root dependence ($S^n(r_p) = -0.51$). Thus, and in agreement with the original study of Hearn et al. (2005), we conclude that S_{rx} is the only single limiting case that fits the experimental observations of both decay shape and scaling of initial reaction rate with particle size. However, a behaviour which mixes the characteristics of more than one limiting case might also fit the data well, even though the limiting cases which it most closely resembles would fail individually. The Fit III parameter set presented here follows this logic by mixing the behaviours of B^{rd}_{trad} and B_{rx} to adequately represent both the near-exponential decay of N_Y as a function of time (B_{rx}) and the scaling of the initial decay rate with particle radius (B^{rd}_{trad}). Although the agreement of Fit III with the experimental $N_Y(t)$ and $S^n(r_p)$ is not as good as that of Fit IV, both are in reasonable proximity to experimentally measured values. This opens up another possibility for modelling of the oleic acid–ozone system that has yet to be proven by a well-fitting kinetic parameter set.

Supplementary material related to this article is available online at: http://www.atmos-chem-phys.net/13/6663/2013/acp-13-6663-2013-supplement.pdf.

Acknowledgements. T. Berkemeier acknowledges support from the European Union Lifelong Learning Programme. A. J. Huisman was supported by the United States National Science Foundation under award no. IRFP 1006117 and by ETH Zürich. M. Ammann appreciated support by the Swiss National Science Foundation (grant no. 130175). M. Shiraiwa is supported by the Japan Society for the Promotion of Science (JSPS) Postdoctoral Fellowship for Research Abroad and the EU project PEGASOS (grant no. 265148). Any opinions, findings, and conclusions or recommendations expressed in this material are those of the authors and do not necessarily reflect the views of the US National Science Foundation. T. Berkemeier and A. J. Huisman thank U. Krieger and T. Peter for their support and for many useful conversations. T. Berkemeier would like to thank P. Ziemann, G. Smith, C. Chan and A. Lee for providing original datasets.

The service charges for this open access publication have been covered by the Max Planck Society.

Edited by: V. F. McNeill

References

Abbatt, J. P. D., Lee, A. K. Y., and Thornton, J. A.: Quantifying trace gas uptake to tropospheric aerosol: recent advances and remaining challenges, Chem. Soc. Rev., 41, 6555–6581, doi:10.1039/C2CS35052A, 2012.

Ammann, M., Rossler, E., Strekowski, R., and George, C.: Nitrogen dioxide multiphase chemistry: uptake kinetics on aqueous solutions containing phenolic compounds, Phys. Chem. Chem. Phys., 7, 2513–2518, doi:10.1039/B501808K, 2005.

Bates, D. V.: Detection of chronic respiratory bronchiolitis in oxidant-exposed populations: analogy to tobacco smoke exposure, Environ. Health Pers., 101, 217–218, available at: http://www.ncbi.nlm.nih.gov/pmc/articles/PMC1519706/, 1993.

Behr, P., Morris, J. R., Antman, M. D., Ringeisen, B. R., Splan, J. R., and Nathanson, G. M.: Reaction and desorption of HCl and HBr following collisions with supercooled sulfuric acid, Geophys. Res. Lett., 28, 1961–1964, doi:10.1029/2000GL012716, 2001.

Behr, P., Scharfenort, U., Ataya, K., and Zellner, R.: Dynamics and mass accommodation of HCl molecules on sulfuric acid-water surfaces, Phys. Chem. Chem. Phys., 11, 8048–8055, doi:10.1039/B904629A, 2009.

Cariboni, J., Gatelli, D., Liska, R., and Saltelli, A.: The role of sensitivity analysis in ecological modelling, Ecol. Model., 203, 167–182, doi:10.1016/j.ecolmodel.2005.10.045, 2007.

Carslaw, K. S., Boucher, O., Spracklen, D. V., Mann, G. W., Rae, J. G. L., Woodward, S. and Kulmala, M.: A review of natural aerosol interactions and feedbacks within the Earth system, Atmos. Chem. Phys., 10, 1701–1737, doi:10.5194/acp-10-1701-2010, 2010.

Crowley, J. N., Ammann, M., Cox, R. A., Hynes, R. G., Jenkin, M. E., Mellouki, A., Rossi, M. J., Troe, J., and Wallington, T. J.: Evaluated kinetic and photochemical data for atmospheric chemistry: Volume V – heterogeneous reactions on solid substrates, Atmos. Chem. Phys., 10, 9059–9223, doi:10.5194/acp-10-9059-2010, 2010.

Danckwerts, P. V.: Absorption by simultaneous diffusion and chemical reaction into particles of various shapes and into falling drops, Trans. Faraday Soc., 47, 1014–1023, doi:10.1039/TF9514701014, 1951.

Davidovits, P., Hu, J. H., Worsnop, D. R., Zahniser, M. S., and Kolb, C. E.: Entry of gas molecules into liquids, Faraday Discuss., 100, 65–81, doi:10.1039/FD9950000065, 1995.

Davidovits, P., Kolb, C. E., Williams, L. R., Jayne, J. T., and Worsnop, D. R.: Mass accommodation and chemical reactions at gas–liquid interfaces, Chem. Rev., 106, 1323–1354, doi:10.1021/cr040366k, 2006.

Deiber, G., George, Ch., Le Calvé, S., Schweitzer, F., and Mirabel, Ph.: Uptake study of $ClONO_2$ and $BrONO_2$ by Halide containing droplets, Atmos. Chem. Phys., 4, 1291–1299, doi:10.5194/acp-4-1291-2004, 2004.

Donaldson, D. J., Ravishankara, A. R., and Hanson, D. R.: Detailed Study of $HOCl + HCl \rightarrow C_l2 + H_2O$ in Sulfuric Acid, J. Phys. Chem. A, 101, 4717–4725, doi:10.1021/jp9633153, 1997.

Dunker, A. M.: The decoupled direct method for calculating sensitivity coefficients in chemical kinetics, J. Chem. Phys., 81, 2385–2393, doi:10.1063/1.447938, 1984.

George, I. J., Matthews, P. S., Brooks, B., Goddard, A., Whalley, L. K., Baeza-Romero, M. T., and Heard, D. E.: Heterogeneous Uptake of HO_2 Radicals onto Atmospheric Aerosols, abstract A43D-0186, presented at Fall Meeting, AGU, San Francisco, Calif., 5–9 December, 2011.

Hallquist, M., Wenger, J. C., Baltensperger, U., Rudich, Y., Simpson, D., Claeys, M., Dommen, J., Donahue, N. M., George, C., Goldstein, A. H., Hamilton, J. F., Herrmann, H., Hoffmann, T., Iinuma, Y., Jang, M., Jenkin, M. E., Jimenez, J. L., Kiendler-Scharr, A., Maenhaut, W., McFiggans, G., Mentel, Th. F., Monod, A., Prévôt, A. S. H., Seinfeld, J. H., Surratt, J. D., Szmigielski, R., and Wildt, J.: The formation, properties and impact of secondary organic aerosol: current and emerging issues, Atmos. Chem. Phys., 9, 5155–5236, doi:10.5194/acp-9-5155-2009, 2009.

Hanson, D. R. and Lovejoy, E. R.: Heterogeneous reactions in liquid sulfuric acid: $HOCl + HCl$ as a model system, J. Phys. Chem.-US, 100, 6397–6405, doi:10.1021/jp953250o, 1996.

Hanson, D. R., Ravishankara, A. R., and Solomon, S.: Heterogeneous reactions in sulfuric acid aerosols: a framework for model calculations, J. Geophys. Res., 99, 3615–3629, doi:10.1029/93JD02932, 1994.

Heal, M. R., Kumar, P. and Harrison, R. M.: Particles, air quality, policy and health., Chem. Soc. Rev., 41, 6606–6630, doi:10.1039/c2cs35076a, 2012.

Hearn, J. D., Lovett, A. J., and Smith, G. D.: Ozonolysis of oleic acid particles: evidence for a surface reaction and secondary reactions involving Criegee intermediates, Phys. Chem. Chem. Phys., 7, 501–511, doi:10.1039/B414472D, 2005.

Hu, J. H., Shi, Q., Davidovits, P., Worsnop, D. R., Zahniser, M. S., and Kolb, C. E.: Reactive uptake of Cl_2(g) and Br_2(g) by aqueous surfaces as a function of Br^- and I^- ion concentration: the effect of chemical reaction at the interface, J. Phys. Chem., 99, 8768–8776, doi:10.1021/j100021a050, 1995.

IPCC: Climate Change 2007: The Physical Science Basis, Contribution of Working Group I to the Fourth Assessment Report of the Intergovernmental Panel on Climate Change, Cambridge University Press, Cambridge, United Kingdom and New York, NY, USA, 2007.

Jakab, G. J., Spannhake, E. W., Canning, B. J., Kleeberger, S. R., and Gilmour, M. I.: The effects of ozone on immune function, Environ. Health Pers., 103, 77–89, available at: http://www.ncbi.nlm.nih.gov/pmc/articles/PMC1518840/, 1995.

Kanakidou, M., Seinfeld, J. H., Pandis, S. N., Barnes, I., Dentener, F. J., Facchini, M. C., Van Dingenen, R., Ervens, B., Nenes, A., Nielsen, C. J., Swietlicki, E., Putaud, J. P., Balkanski, Y., Fuzzi, S., Horth, J., Moortgat, G. K., Winterhalter, R., Myhre, C. E. L., Tsigaridis, K., Vignati, E., Stephanou, E. G., and Wilson, J.: Organic aerosol and global climate modelling: a review, Atmos. Chem. Phys., 5, 1053–1123, doi:10.5194/acp-5-1053-2005, 2005.

Knipping, E. M. and Dabdub, D.: Modeling Cl_2 formation from aqueous NaCl particles: Evidence for interfacial reactions and importance of Cl_2 decomposition in alkaline solution, J. Geophys. Res., 107, 4360, doi:10.1029/2001JD000867, 2002.

Knipping, E. M., Lakin, M. J., Foster, K. L., Jungwirth, P., Tobias, D. J., Gerber, R. B., Dabdub, D., and Finlayson-Pitts, B. J.: Experiments and simulations of ion-enhanced interfacial chemistry on aqueous NaCl aerosols, Science, 288, 301–306, doi:10.1126/science.288.5464.301, 2000.

Kolb, C., Worsnop, D., Jayne, J., and Davidovits, P.: Comment on mathematical models of the uptake of $ClONO_2$ and other gases by atmospheric aerosols, J. Aerosol Sci., 29, 893–897, doi:10.1016/S0021-8502(97)10022-2, 1998.

Kolb, C. E., Cox, R. A., Abbatt, J. P. D., Ammann, M., Davis, E. J., Donaldson, D. J., Garrett, B. C., George, C., Griffiths, P. T., Hanson, D. R., Kulmala, M., McFiggans, G., Pöschl, U., Riipinen, I., Rossi, M. J., Rudich, Y., Wagner, P. E., Winkler, P. M., Worsnop, D. R., and O' Dowd, C. D.: An overview of current issues in the uptake of atmospheric trace gases by aerosols and clouds, Atmos. Chem. Phys., 10, 10561–10605, doi:10.5194/acp-10-10561-2010, 2010.

Koop, T., Bookhold, J., Shiraiwa, M., and Pöschl, U.: Glass transition and phase state of organic compounds: dependency on molecular properties and implications for secondary organic aerosols in the atmosphere, Phys. Chem. Chem. Phys., 13, 19238–19255, doi:10.1039/C1CP22617G, 2011.

Laskin, A., Gaspar, D. J., Wang, W., Hunt, S. W., Cowin, J. P., Colson, S. D., and Finlayson-Pitts, B. J.: Reactions at interfaces as a source of sulfate formation in sea-salt particles, Science, 301, 340–344, doi:10.1126/science.1085374, 2003.

Lee, A. K. and Chan, C. K.: Single particle Raman spectroscopy for investigating atmospheric heterogeneous reactions of organic aerosols, Atmos. Environ., 41, 4611–4621, doi:10.1016/j.atmosenv.2007.03.040, 2007.

Lee, G., Lee, B., Kim, J., and Cho, K.: Ozone adsorption on graphene: ab initio study and experimental validation, J. Phys. Chem. C., 113, 14225–14229, doi:10.1021/jp904321n, 2009.

Mahowald, N., Ward, D. S., Kloster, S., Flanner, M. G., Heald, C. L., Heavens, N. G., Hess, P. G., Lamarque, J.-F., and Chuang, P. Y.: Aerosol Impacts on Climate and Biogeochemistry, Annu Rev. Environ. Resour., 36, 45–74, doi:10.1146/annurev-environ-042009-094507, 2011.

Maranzana, A., Serra, G., Giordana, A., Tonachini, G., Barco, G., and Causà, M.: Ozone interaction with polycyclic aromatic hydrocarbons and soot in atmospheric processes: theoretical density functional study by molecular and periodic methodologies, J. Phys. Chem. A, 109, 10929–10939, doi:10.1021/jp053672q, 2005.

Martien, P. T. and Harley, R. A.: Adjoint sensitivity analysis for a three-dimensional photochemical model: application to Southern California, Environ. Sci. Technol., 40, 4200–4210, doi:10.1021/es051026z, 2006.

Massman, W.: A review of the molecular diffusivities of H_2O, CO_2, CH_4, CO, O_3, SO_2, NH_3, N_2O, NO, and NO_2 in air, O_2 and N_2 near STP, Atmos. Environ., 32, 1111–1127, doi:10.1016/S1352-2310(97)00391-9, 1998.

McConnell, R., Berhane, K., Gilliland, F., London, S. J., Islam, T., Gauderman, W. J., Avol, E., Margolis, H. G., and Peters, J. M.: Asthma in exercising children exposed to ozone: a cohort study, Lancet, 359, 386–391, doi:10.1016/S0140-6736(02)07597-9, 2002.

Mikhailov, E., Vlasenko, S., Martin, S. T., Koop, T., and Pöschl, U.: Amorphous and crystalline aerosol particles interacting with water vapor: conceptual framework and experimental evidence for restructuring, phase transitions and kinetic limitations, Atmos. Chem. Phys., 9, 9491–9522, doi:10.5194/acp-9-9491-2009, 2009.

Morris, J. R., Behr, P., Antman, M. D., Ringeisen, B. R., Splan, J., and Nathanson, G. M.: Molecular beam scattering from supercooled sulfuric acid: collisions of HCl, HBr, and HNO_3 with 70 wt D_2SO_4, J. Phys. Chem. A, 104, 6738–6751, doi:10.1021/jp000105o, 2000.

Morris, M.: Factorial sampling plans for preliminary computational experiments, Technometrics, 33, 161–174, available at: http://www.jstor.org/stable/10.2307/1269043, 1991.

Nel, A.: Air pollution-related illness: effects of particles, Science, 308, 804–806, doi:10.1126/science.1108752, 2005.

Oldridge, N. W. and Abbatt, J. P. D.: Formation of gas-phase bromine from interaction of ozone with frozen and liquid NaCl/NaBr solutions: quantitative separation of surficial chemistry from bulk-phase reaction, J. Phys. Chem. A, 115, 2590–2598, doi:10.1021/jp200074u, 2011.

Pfrang, C., Shiraiwa, M., and Pöschl, U.: Coupling aerosol surface and bulk chemistry with a kinetic double layer model (K2-SUB): oxidation of oleic acid by ozone, Atmos. Chem. Phys., 10, 4537–4557, doi:10.5194/acp-10-4537-2010, 2010.

Pfrang, C., Shiraiwa, M., and Pöschl, U.: Chemical ageing and transformation of diffusivity in semi-solid multi-component organic aerosol particles, Atmos. Chem. Phys., 11, 7343–7354, doi:10.5194/acp-11-7343-2011, 2011.

Pöschl, U.: Atmospheric Aerosols: Composition, Transformation, Climate and Health Effects, Angew. Chem. Int. Ed., 44, 7520–7540, doi:10.1002/anie.200501122, 2005.

Pöschl, U., Rudich, Y., and Ammann, M.: Kinetic model framework for aerosol and cloud surface chemistry and gas-particle interactions – Part 1: General equations, parameters, and terminology, Atmos. Chem. Phys., 7, 5989–6023, doi:10.5194/acp-7-5989-2007, 2007.

Ravishankara, A. R.: Heterogeneous and multiphase chemistry in the troposphere, Science, 276, 1058–1065, doi:10.1126/science.276.5315.1058, 1997.

Ravishankara, A. R. and Longfellow, C. A.: Reactions on tropospheric condensed matter Plenary Lecture, Phys. Chem. Chem. Phys., 1, 5433–5441, doi:10.1039/A905660B, 1999.

Renbaum, L. H. and Smith, G. D.: Artifacts in measuring aerosol uptake kinetics: the roles of time, concentration and adsorption, Atmos. Chem. Phys., 11, 6881–6893, doi:10.5194/acp-11-6881-2011, 2011.

Rouvière, A. and Ammann, M.: The effect of fatty acid surfactants on the uptake of ozone to aqueous halogenide particles, Atmos. Chem. Phys., 10, 11489–11500, doi:10.5194/acp-10-11489-2010, 2010.

Rouvière, A., Sosedova, Y., and Ammann, M.: Uptake of ozone to deliquesced KI and mixed KI/NaCl aerosol particles, J. Phys. Chem. A, 114, 7085–7093, doi:10.1021/jp103257d, 2010.

Saltelli, A., Ratto, M., Andres, T., Campolongo, F., Cariboni, J., Gatelli, D., Saisana, M., and Tarantola, S.: Global sensitivity analysis: the primer, Wiley Online Library, doi:10.1002/9780470725184.fmatter, last access: 15 November 2011, 2008.

Schwartz, S.: Mass-Transport Considerations Pertinent to Aqueous Phase Reactions of Gases in Liquid-Water Clouds, NATO ASI Series, vol. G6, Springer Verlag, Heidelberg, Germany, chemistry of multiphase atmospheric systems, 1986.

Schwartz, S. and Freiberg, J. E.: Mass-transport limitation to the rate of reaction of gases in liquid droplets: application to oxidation of SO_2 in aqueous solutions, Atmos. Environ., 15, 1129–1144, doi:10.1016/0004-6981(81)90303-6, 1981.

Seinfeld, J. H. and Pandis, S. N.: Atmospheric Chemistry and Physics: From Air Pollution to Climate Change, Wiley, New York, 2006.

Shaka', H., Robertson, W. H., and Finlayson-Pitts, B. J.: A new approach to studying aqueous reactions using diffuse reflectance infrared Fourier transform spectrometry: application to the uptake and oxidation of SO2 on OH-processed model sea salt aerosol, Phys. Chem. Chem. Phys., 9, 1980–1990, doi:10.1039/B612624C, 2007.

Shiraiwa, M., Garland, R. M., and Pöschl, U.: Kinetic double-layer model of aerosol surface chemistry and gas-particle interactions (K2-SURF): Degradation of polycyclic aromatic hydrocarbons exposed to O_3, NO_2, H_2O, OH and NO_3, Atmos. Chem. Phys., 9, 9571–9586, doi:10.5194/acp-9-9571-2009, 2009.

Shiraiwa, M., Pfrang, C., and Pöschl, U.: Kinetic multi-layer model of aerosol surface and bulk chemistry (KM-SUB): the influence of interfacial transport and bulk diffusion on the oxidation of oleic acid by ozone, Atmos. Chem. Phys., 10, 3673–3691, doi:10.5194/acp-10-3673-2010, 2010.

Shiraiwa, M., Ammann, M., Koop, T., and Pöschl, U.: Gas uptake and chemical aging of semisolid organic aerosol particles, P. Natl. Acad. Sci. USA, 108, 11003–11008, doi:10.1073/pnas.1103045108, 2011a.

Shiraiwa, M., Sosedova, Y., Rouvière, A., Yang, H., Zhang, Y., Abbatt, J. P. D., Ammann, M., and Pöschl, U.: The role of long-lived reactive oxygen intermediates in the reaction of ozone with aerosol particles, Nat. Chem., 3, 291–295, doi:10.1038/nchem.988, 2011b.

Shiraiwa, M., Pfrang, C., Koop, T., and Pöschl, U.: Kinetic multi-layer model of gas-particle interactions in aerosols and clouds (KM-GAP): linking condensation, evaporation and chemical reactions of organics, oxidants and water, Atmos. Chem. Phys., 12, 2777–2794, doi:10.5194/acp-12-2777-2012, 2012a.

Shiraiwa, M., Pöschl, U., and Knopf, D. A.: Multiphase chemical kinetics of NO_3 radicals reacting with organic aerosol components from biomass burning, Environ. Sci. Technol., 46, 6630–6636, doi:10.1021/es300677a, 2012b.

Shiraiwa, M., Selzle, K., Yang, H., Sosedova, Y., Ammann, M., and Pöschl, U.: Multiphase chemical kinetics of the nitration of aerosolized protein by ozone and nitrogen dioxide, Environ. Sci. Technol., 46, 6672–6680, doi:10.1021/es300871b, 2012c.

Shiraiwa, M., Selzle, K. and Pöschl, U.: Hazardous components and health effects of atmospheric aerosol particles: reactive oxygen species, soot, polycyclic aromatic compounds and allergenic proteins., Free Radical Res., 46(8), 927–939, doi:10.3109/10715762.2012.663084, 2012d.

Smith, G. D., Woods, E., DeForest, C. L., Baer, T., and Miller, R. E.: Reactive uptake of ozone by oleic acid aerosol particles: application of single-particle mass spectrometry to heterogeneous reaction kinetics, J. Phys. Chem. A, 106, 8085–8095, doi:10.1021/jp020527t, 2002.

Smith, G. D., Woods, E., Baer, T., and Miller, R. E.: Aerosol uptake described by numerical solution of the diffusion–reaction equations in the particle, J. Phys. Chem. A, 107, 9582–9587, doi:10.1021/jp021843a, 2003.

Stevens, B. and Feingold, G.: Untangling aerosol effects on clouds and precipitation in a buffered system., Nature, 461, 607–613, doi:10.1038/nature08281, 2009.

Streets, D. G., Bond, T. C., Lee, T., and Jang, C.: On the future of carbonaceous aerosol emissions, J. Geophys. Res., 109, D24212, doi:10.1029/2004JD004902, 2004.

Tong, H.-J., Reid, J. P., Bones, D. L., Luo, B. P., and Krieger, U. K.: Measurements of the timescales for the mass transfer of water in glassy aerosol at low relative humidity and ambient temperature, Atmos. Chem. Phys., 11, 4739–4754, doi:10.5194/acp-11-4739-2011, 2011.

Virtanen, A., Joutsensaari, J., Koop, T., Kannosto, J., Yli-Pirila, P., Leskinen, J., Makela, J. M., Holopainen, J. K., Pöschl, U., Kulmala, M., Worsnop, D. R., and Laaksonen, A.: An amorphous solid state of biogenic secondary organic aerosol particles, Nature, 467, 824–827, doi:10.1038/nature09455, 2010.

Worsnop, D. R., Morris, J. W., Shi, Q., Davidovits, P., and Kolb, C. E.: A chemical kinetic model for reactive transformations of aerosol particles, Geophys. Res. Lett., 29, 1996, doi:10.1029/2002GL015542, 2002.

Yu, H., Kaufman, Y. J., Chin, M., Feingold, G., Remer, L. A., Anderson, T. L., Balkanski, Y., Bellouin, N., Boucher, O., Christopher, S., DeCola, P., Kahn, R., Koch, D., Loeb, N., Reddy, M. S., Schulz, M., Takemura, T., and Zhou, M.: A review of measurement-based assessments of the aerosol direct radiative effect and forcing, Atmos. Chem. Phys., 6, 613–666, doi:10.5194/acp-6-613-2006, 2006.

Zahardis, J. and Petrucci, G. A.: The oleic acid-ozone heterogeneous reaction system: products, kinetics, secondary chemistry, and atmospheric implications of a model system – a review, Atmos. Chem. Phys., 7, 1237–1274, doi:10.5194/acp-7-1237-2007, 2007.

Ziemann, P. J.: Aerosol products, mechanisms, and kinetics of heterogeneous reactions of ozone with oleic acid in pure and mixed particles, Faraday Discuss., 130, 469–490, doi:10.1039/B417502F, 2005.

Ziemann, P. J. and Atkinson, R.: Kinetics, products, and mechanisms of secondary organic aerosol formation, Chem. Soc. Rev., 41, 6582–6605, doi:10.1039/c2cs35122f, 2012.

Zobrist, B., Marcolli, C., Pedernera, D. A., and Koop, T.: Do atmospheric aerosols form glasses?, Atmos. Chem. Phys., 8, 5221–5244, doi:10.5194/acp-8-5221-2008, 2008.

Zobrist, B., Soonsin, V., Luo, B. P., Krieger, U. K., Marcolli, C., Peter, T., and Koop, T.: Ultra-slow water diffusion in aqueous sucrose glasses, Phys. Chem. Chem. Phys., 13, 3514–3526, doi:10.1039/C0CP01273D, 2011.

B.2. Shiraiwa *et al.*, Atmos. Chem. Phys., 2014

Molecular corridors and kinetic regimes in the multiphase chemical evolution of secondary organic aerosol

Manabu Shiraiwa[1], Thomas Berkemeier[1], Katherine A. Schilling-Fahnestock[2], John H. Seinfeld[2], and Ulrich Pöschl[1]

[1]Max Planck Institute for Chemistry, Multiphase Chemistry Department, 55128 Mainz, Germany
[2]California Institute of Technology, Division of Chemistry and Chemical Engineering, 91125 Pasadena, CA, USA

Atmospheric Chemistry and Physics **14**, 8323-8341, (2014).

Author contributions.

MS, TB, JHS and UP designed research. MS, TB, KAS, JHS and UP discussed results. MS performed kinetic modelling. MS and UP wrote the paper.

Atmos. Chem. Phys., 14, 8323–8341, 2014
www.atmos-chem-phys.net/14/8323/2014/
doi:10.5194/acp-14-8323-2014

Atmospheric Chemistry and Physics Open Access

Molecular corridors and kinetic regimes in the multiphase chemical evolution of secondary organic aerosol

M. Shiraiwa[1], T. Berkemeier[1], K. A. Schilling-Fahnestock[2], J. H. Seinfeld[2], and U. Pöschl[1]

[1]Multiphase Chemistry Department, Max Planck Institute for Chemistry, 55128 Mainz, Germany
[2]Division of Chemistry and Chemical Engineering, California Institute of Technology, Pasadena, CA 91125, USA

Correspondence to: M. Shiraiwa (m.shiraiwa@mpic.de)

Received: 21 February 2014 – Published in Atmos. Chem. Phys. Discuss.: 6 March 2014
Revised: 15 July 2014 – Accepted: 16 July 2014 – Published: 20 August 2014

Abstract. The dominant component of atmospheric, organic aerosol is that derived from the oxidation of volatile organic compounds (VOCs), so-called secondary organic aerosol (SOA). SOA consists of a multitude of organic compounds, only a small fraction of which has historically been identified. Formation and evolution of SOA is a complex process involving coupled chemical reaction and mass transport in the gas and particle phases. Current SOA models do not embody the full spectrum of reaction and transport processes, nor do they identify the dominant rate-limiting steps in SOA formation. Based on molecular identification of SOA oxidation products, we show here that the chemical evolution of SOA from a variety of VOC precursors adheres to characteristic "molecular corridors" with a tight inverse correlation between volatility and molar mass. The slope of these corridors corresponds to the increase in molar mass required to decrease volatility by one order of magnitude ($-\mathrm{d}M$ / $\mathrm{dlog}C_0$). It varies in the range of 10–30 g mol^{-1}, depending on the molecular size of the SOA precursor and the O : C ratio of the reaction products. Sequential and parallel reaction pathways of oxidation and dimerization or oligomerization progressing along these corridors pass through characteristic regimes of reaction-, diffusion-, or accommodation-limited multiphase chemical kinetics that can be classified according to reaction location, degree of saturation, and extent of heterogeneity of gas and particle phases. The molecular corridors and kinetic regimes help to constrain and describe the properties of the products, pathways, and rates of SOA evolution, thereby facilitating the further development of aerosol models for air quality and climate.

1 Introduction

Organic aerosol is ubiquitous in the atmosphere and its major component is secondary organic aerosol (SOA) (Jimenez et al., 2009). Reaction of atmospheric volatile organic compounds (VOCs) with oxidants such as OH, O_3, and NO_3 initiate the formation of semi-volatile organic compounds (SVOCs), which can undergo further gas-phase oxidation to form low-volatility organic compounds (LVOCs) that will preferentially partition into the particle phase (Kroll and Seinfeld, 2008; Hallquist et al., 2009; Donahue et al., 2012; Murphy et al., 2014). A fraction of the SVOCs partitions into the particle phase, wherein they can be transformed into LVOCs such as dimers, oligomers, and other high molecular mass compounds (Jang et al., 2002; Kalberer et al., 2006; Ervens et al., 2011; Ziemann and Atkinson, 2012; Shiraiwa et al., 2013a). Some portion of the LVOCs can be transformed back to (semi-)volatile compounds or CO / CO_2 by fragmentation reactions triggered by OH or other oxidants at the particle surface or in the particle bulk (Bertram et al., 2001; Kroll and Seinfeld, 2008; Jimenez et al., 2009). SOA partitioning is also affected by particle-phase state, non-ideal thermodynamic mixing, and morphology (Chang and Pankow, 2006; Zuend and Seinfeld, 2012; Shiraiwa et al., 2013b).

SOA consists of a myriad of organic compounds, of which only 10–30 % have been identified (Goldstein and Galbally, 2007). Common techniques applied for the analysis of SOA are gas chromatography/electron impact ionization mass spectrometry (GC/EI-MS) and liquid chromatography/electrospray ionization mass spectrometry (LC/ESI-MS) (e.g., Surratt et al., 2006). Hard ionization, such as electron impact ionization, generally causes significant fragmentation

of organic molecules, which makes molecular identification challenging, but can provide molecular structural information. The recent advent of soft ionization methods such as electrospray ionization (ESI), matrix-assisted laser desorption ionization (MALDI), atmospheric pressure chemical ionization (APCI), and direct analysis in real time (DART) ionization has facilitated the identification of the dominant fraction of the compounds constituting SOA by preserving analytes as intact or nearly intact during ionization (Kalberer et al., 2006; Williams et al., 2010; Laskin et al., 2012a, b; Chan et al., 2013; Nguyen et al., 2013; Vogel et al., 2013; Schilling-Fahnestock et al., 2014). Taking advantage of such data, here we present a new, 2-D map for SOA evolution of molar mass vs. volatility, which can be linked to kinetic regimes and reaction pathways of formation and aging of SOA that is currently poorly constrained and a major limitation in the understanding and prediction of atmospheric aerosol effects.

2 Molecular corridors for different SOA precursors

Figure 1 shows 2-D maps of molecular weight or molar mass (M) plotted against volatility or saturation mass concentration (C_0) for organic compounds in SOA from a range of anthropogenic and biogenic precursors: dodecane (Fig. 1a, b) (Yee et al., 2012), cyclododecane (Fig. 1c, d), hexylcyclohexane (Fig. 1e, f) (Schilling-Fahnestock et al., 2014), α-pinene (Fig. 1g) (Docherty et al., 2005; Claeys et al., 2007, 2009; Zuend and Seinfeld, 2012; Kahnt et al., 2014; Kristensen et al., 2014), limonene (Fig. 1h) (Jaoui et al., 2006; Kundu et al., 2012), isoprene (Fig. 1i) (Surratt et al., 2006; Surratt et al., 2010; Lin et al., 2012, 2013), glyoxal and methylglyoxal (Fig. 1j) (Lim et al., 2010; Sareen et al., 2010; Zhao et al., 2012). Experimental conditions including oxidants, NO levels, and seed particles used in earlier studies are summarized in Table A1. The experimental conditions and methods applied in this study to analyze the formation and composition of SOA from C_{12} alkanes under low and high NO conditions are detailed in Appendix A and Schilling-Fahnestock et al. (2014). DART is a soft ionization technique of atmospheric pressure ionization that has recently been used for the analysis of a variety of organic compounds with minimal fragmentation (Chan et al., 2013). SOA compounds identified include alcohols, ketones, aldehydes, hydroxycarbonyls, organic hydroperoxides, and nitrates, which are generated in the gas phase (open markers), as well as dihydrofuran, furan, ether, ester, peroxyhemiacetal, hemiacetal, dimer, and imine, which are likely particle-phase products (Ziemann and Atkinson, 2012) (solid markers). Through the combination of an aerosol mass spectrometer (AMS) and DART-MS, close to 100 % identification and quantification of the particle phase for each of the three alkane systems was achieved (Schilling-Fahnestock et al., 2014). Thus, alkane SOA are plotted for low and high NO conditions in separate panels due to large number of identified products, whereas biogenic SOA data are shown in one panel due to the relatively small number of data points.

Vapor pressures and saturation mass concentrations of organic compounds were estimated using the "estimation of vapor pressure of organics, accounting for temperature, intramolecular, and non-additivity effects" (EVAPORATION) model, (Compernolle et al., 2011). The EVAPORATION model estimates vapor pressure of molecules with the following functionalities: aldehyde, ketone, alcohol, ether, ester, nitrate, acid, peroxide, hydroperoxide, peroxy acyl nitrate, and peracid. Organosulfates and imidazoles are not covered and were thus not included in our analysis, although they have been identified in SOA from biogenic precursors and glyoxal (Iinuma et al., 2007; Surratt et al., 2008; Ervens et al., 2011).

The markers in Fig. 1 are color-coded with atomic O : C ratio. Generally, volatility decreases and molar mass increases with chemical aging of SOA both in the gas and particle phases. Consequently, molar mass of oxidation products tightly correlates with volatility with high coefficient of determination (R^2), as summarized in Table 1. The 95 % prediction intervals (dashed lines in Fig. 1) can be regarded as molecular corridors, within which additional unidentified oxidation products are likely to fall. The negative slope of the fit lines corresponds to the increase in molar mass required to decrease volatility by one order of magnitude, $-\mathrm{d}M\,/\,\mathrm{dlog}C_0$. It increases from $\sim 10\,\mathrm{g\,mol^{-1}}$ for glyoxal, and methylglyoxal to $\sim 25\,\mathrm{g\,mol^{-1}}$ for dodecane and cyclododecane, depending on the molecular size of the SOA precursor and the O : C ratio of the reaction products, as will be discussed below. The mean value of $-dM\,/\,\mathrm{dlog}C_0$ average over all investigated systems is $20 \pm 4\,\mathrm{g\,mol^{-1}}$.

The composition of SOA may vary depending not only on the organic precursor, but also on the oxidant and other reaction conditions of formation and aging (Presto et al., 2005; Surratt et al., 2006; Lin et al., 2012, 2013; Kristensen et al., 2014; Loza et al., 2014; Xu et al., 2014). The atomic O : C ratio tends to be higher at high NO concentrations, partly due to the formation of organonitrates (Nguyen et al., 2011; Schilling-Fahnestock et al., 2014). Even though Fig. 1g, h, and i contain biogenic SOA oxidation products measured under different conditions, as specified in Table A1, the molecular corridors are relatively tight with $R^2 > 0.85$. The molecular corridors of alkane SOA formed under low and high NO conditions are also quite similar (Fig. 1a–f). Thus, the molecular corridors of SOA formation appear to be determined primarily by the organic precursor, and the extent to which they are influenced by reaction conditions warrants further studies.

3 Kinetic regimes and limiting cases

Traditionally, SOA formation has been modeled based on instantaneous gas-particle equilibrium partitioning, implicitly

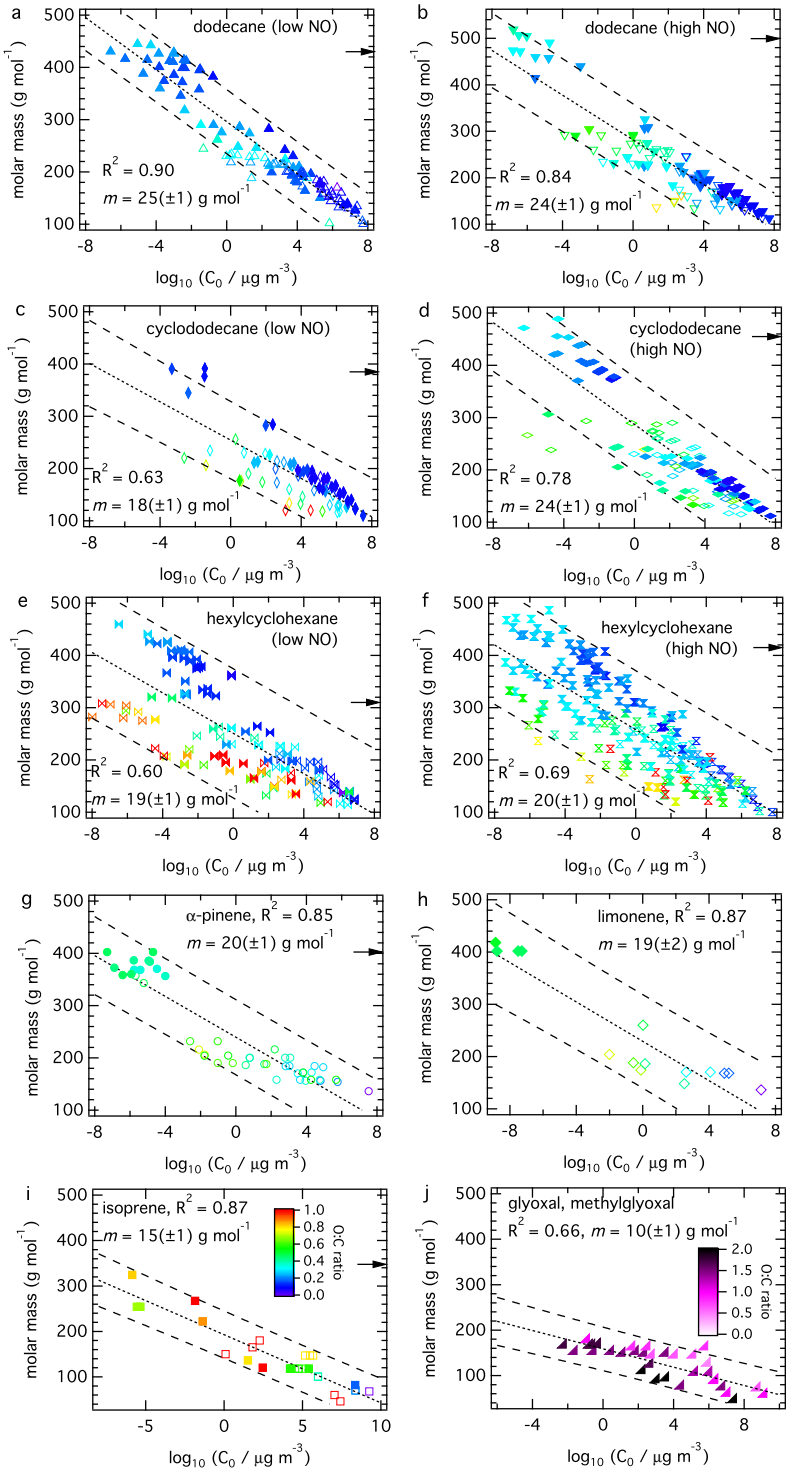

Figure 1. Molecular corridors of SOA evolution for different precursor compounds. Molar mass vs. volatility (saturation mass concentration, C_0) at 298 K for oxidation products of dodecane at **(a)** low and **(b)** high NO condition, cyclododecane at **(c)** low and **(d)** high NO condition, and hexylcyclohexane at **(e)** low and **(f)** high NO condition and **(g)** α-pinene, **(h)** limonene, **(i)** isoprene, and **(j)** glyoxal and methylglyoxal. The open and solid markers correspond to the gas- and particle-phase products, respectively, color-coded by atomic O : C ratio (note different color scale for **j**). With a linear regression analysis, the coefficient of determination (R^2), fitted lines (dotted lines) and their slopes (m), and prediction intervals with 95 % confidence (dashed lines) are shown. The arrows on the right axis indicate average molar mass for isoprene and α-pinene (Kalberer et al., 2006), as well as for alkanes, as measured in this study.

Table 1. Summary of analysis of identified SOA oxidation products. Number of identified oxidation products N, average molar mass M_{ave}, negative slope ($-dM$ / dlogC_0) of fitted lines in Fig. 2 of molar mass vs. logarithm of volatility, coefficients of determination R^2, as well as R^2 for O : C vs. logarithm of volatility.

Precursor	N	M_{ave} (g mol^{-1})	$-dM$ / dlogC_0 (g mol^{-1})	R^2 (molar mass)	R^2 (O : C)
Dodecane, low NO	116	429	25(± 1)	0.90	0.22
Dodecane, high NO	106	495	24(± 1)	0.84	0.29
Cyclododecane, low NO	77	384	18(± 1)	0.63	0.08
Cyclododecane, high NO	122	458	24(± 1)	0.78	0.08
Hexylcyclohexane, low NO	137	310	19(± 1)	0.60	0.05
Hexylcyclohexane, high NO	230	418	20(± 1)	0.69	0.00
α-pinene	47	400*	20(± 1)	0.85	0.13
Limonene	17	–	19(± 2)	0.87	0.38
Isoprene	29	350*	15(± 1)	0.87	0.09
Glyoxal, methylglyoxal	35	-	10(± 1)	0.66	0.16

* Kalberer et al. (2006).

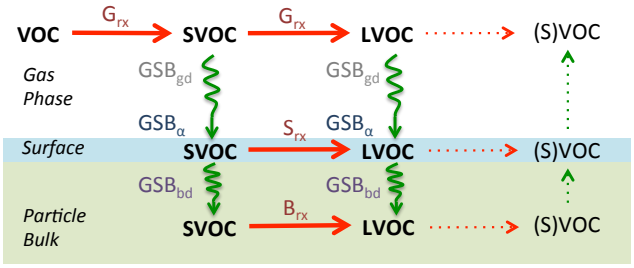

Figure 2. Molecular processes of SOA evolution: schematic outline of formation and aging. Red and green arrows denote chemical reactions and mass transport, respectively. Sequential and parallel reactions in the gas phase, at the particle surface, and in the particle bulk lead to multiple generations of volatile, semi-volatile and low-volatile organic compounds (VOC, SVOC, LVOC). Dotted arrows denote revolatilization resulting from fragmentation reactions. Labels on arrows relate to kinetic regimes outlined in subsequent figure.

assuming that gas-phase reactions are the rate-limiting step of SOA formation and growth (Pankow, 1994; Donahue et al., 2006; Hallquist et al., 2009). Recent studies, however, have shown that mass transport and chemical reaction in the particle phase may also play an important role (Fig. 2) (Ervens et al., 2011; Ziemann and Atkinson, 2012; Shiraiwa et al., 2013a). Recently, Berkemeier et al. (2013) provided a conceptual framework which enables the characterization of heterogeneous reactions and gas uptake in atmospheric aerosols and clouds through a well-defined set of distinct kinetic regimes and limiting cases. We extended this framework to cover the complex interplay of gas- and particle-phase reactions in the evolution of SOA and to enable a systematic classification of rate-limiting processes in the analysis and interpretation of laboratory chamber data and ambient measurements, as well as in the comparison of experimental results with theoretical predictions.

Different types of kinetic behavior can be characterized by three basic criteria as detailed in the Appendix B: (1) the location of the chemical reaction leading to SOA formation or aging (gas phase, particle surface, particle bulk); (2) the saturation ratio of the reactants (ratio of ambient concentration to saturation concentration); and (3) the extent of spatial heterogeneity of the gas and particle phases (concentration gradients). The kinetic regimes and limiting cases defined by these criteria can be visualized on a "kinetic cuboid", in which each axis corresponds to one of the three classification parameters, as shown in Fig. 3a. The symbols "G", "S", and "B" indicate the predominant reaction location: gas phase, particle surface, or particle bulk, respectively. A subscript denotes the rate-limiting process for SOA formation and aging: "rx" indicates chemical reaction; "bd" indicates bulk diffusion; "α" indicates mass accommodation; "gd" indicates gas-phase diffusion. Depending on atmospheric composition and reaction conditions, which vary widely in space and time, the chemical evolution of organic compounds and SOA particles can progress through any of these regimes.

The left part of the cuboid can be regarded as a particle-phase chemistry regime, and the right side as a gas-phase chemistry regime. As shown in Fig. 3b, the particle-phase chemistry regime (SB, including surface (S) or bulk (B) reaction) can be further subdivided into a reaction-diffusion regime (SBrd), where the system is limited by reaction or diffusion in the particle-phase, and a mass-transfer regime (SB^{mt}) limited by mass accommodation at the interface or diffusion through the gas phase (Berkemeier et al., 2013). The gas-phase chemistry regime (G) comprises the traditional scenario of SOA formation determined by a rate-limiting chemical reaction in the gas phase, followed by quasi-instantaneous gas-particle partitioning of the reaction products (G$_{rx}$), corresponding to so-called quasi-equilibrium growth (Shiraiwa and Seinfeld, 2012; Zhang et al., 2012). The rest of the gas-phase chemistry regime is mass transport-limited and corresponds to so-called non-equilibrium growth

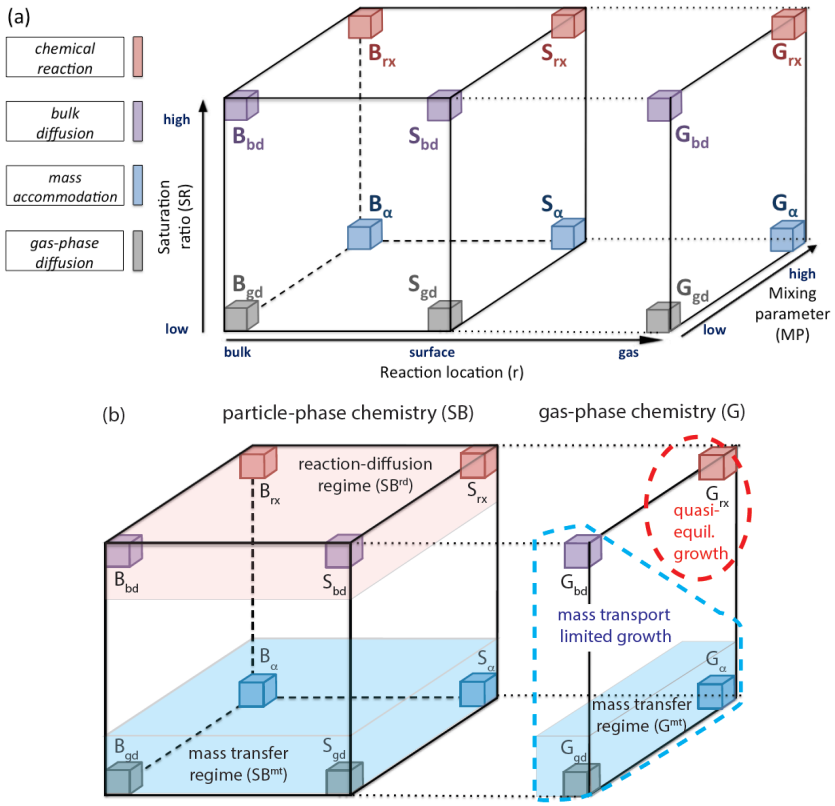

Figure 3. Kinetic regimes and limiting cases of SOA evolution mapped onto the axes of a cuboid representing reaction location, saturation ratio, and mixing parameter. **(a)** Horizontal edges of the cuboid (left to right) correspond to four regimes governed by chemical reaction ("rx", red), bulk diffusion ("bd", purple), mass accommodation ("α", blue), or gas-phase diffusion ("gd", grey). Each of these regimes includes three distinct limiting cases characterized by a single rate-limiting process and a dominant reaction location (particle bulk, B; surface, S; gas phase, G). **(b)** The left side of the cuboid can be regarded as a particle-phase chemistry regime (SB) and subdivided into a reaction-diffusion regime (SB^{rd}) and a mass transfer regime (SB^{mt}). The right side of the cuboid can be regarded as a gas-phase chemistry regime (G) and subdivided into a traditional scenario of "quasi-equilibrium growth", limited only by a gas phase reaction, followed by quasi-instantaneous gas-particle partitioning (G_{rx}) and a mass-transport limited regime of "non-equilibrium growth" that may be kinetically limited by gas-to-particle mass transfer (G^{mt}) or diffusion in the particle (G_{bd}).

(Perraud et al., 2012; Zaveri et al., 2014), which can be kinetically limited by gas-to-particle mass transfer (gas-phase diffusion and accommodation at the interface; G^{mt}) or retarded diffusion in the particle phase (G_{bd}).

4 Characteristic pathways and properties

Figure 4a shows the ensemble of molecular corridors from Fig. 1 with a total of 909 identified oxidation products from seven different SOA precursors. They are constrained by two boundary lines corresponding to the volatility of n-alkanes C_nH_{2n+2} and sugar alcohols $C_nH_{2n+2}O_n$. These lines illustrate the regular dependence of volatility on the molar mass of organic compounds; the different slopes of 30 g mol^{-1} for C_nH_{2n+2} and 12 g mol^{-1} for $C_nH_{2n+2}O_n$ reflect that the decrease of volatility with increasing molar mass is stronger for polar compounds (see Fig. D2 for alternative representation).

Many early generation gas-phase oxidation products of alkanes, as well as dimers or oligomers with low O : C ratio (LOC), fall into a molecular corridor close to the C_nH_{2n+2} line, which we designate as LOC corridor ($-dM$ / dlog$C_0 \geq \sim 25$ g mol^{-1}, blue shaded area). Aqueous-phase reaction and autoxidation products with high O : C ratio (HOC), on the other hand, tend to fall into a corridor near the $C_nH_{2n+2}O_n$ line, which we designate as HOC corridor ($-dM$ / dlogC_0 of $\leq \sim 15$ g mol^{-1}, red shaded area). The area in between is characterized by intermediate O : C ratios and accordingly designated as IOC corridor ($-dM$ / dlog$C_0 \approx \sim 20$ g mol^{-1}). Among the SOA systems investigated in this study, the small precursor VOCs glyoxal, methylglyoxal, and isoprene (C_2–C_5) evolve through the HOC corridor, and the terpenes α-pinene and limonene (C_{10}) through the IOC corridor. The alkanes dodecane and cyclododecane (C_{12}) evolve through the LOC corridor, while hexylcyclohexane exhibits a branching between the LOC and

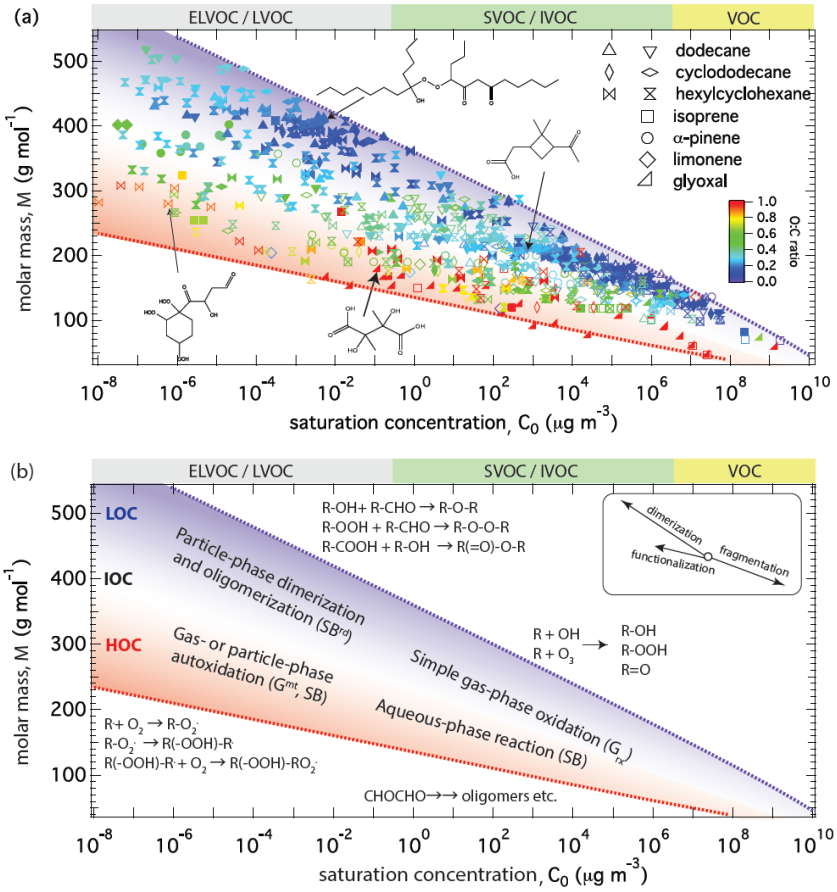

Figure 4. Ensemble of molecular corridors and kinetic regimes of SOA evolution. **(a)** Molar mass vs. volatility (C_0) at 298 K for gas-phase (open) and particle-phase (solid) oxidation products of anthropogenic precursors (dodecane, cyclododecane, hexylcyclohexane) under low/high NO conditions, biogenic precursors (α-pinene, limonene, isoprene) and aqueous-phase reaction products of glyoxal and methylglyoxal. The dotted lines represent linear alkanes C_nH_{2n+2} (purple with O : C = 0) and sugar alcohols $C_nH_{2n+2}O_n$ (red with O : C = 1). Chemical structures of some representative products are shown. **(b)** Characteristic reaction pathways with most probable kinetic regimes. Molecular corridors consists of high, intermediate and low O : C corridors (HOC, red shaded area; IOC, white area; LOC, blue shaded area). SOA products evolve over the molecular corridor driven by three key reaction types of functionalization, oligomerization, and fragmentation, as illustrated in the insert (note different lengths of arrows indicating different intensities of effects on volatility).

HOC corridors, suggesting the involvement of different reaction pathways. For unidentified SOA products, the molecular corridor ensemble in Fig. 4a and alternative representations (Fig. D2a) may also be used as a look-up plot to obtain a rough estimate of volatility by comparison of molar mass and O : C ratio (e.g., from soft-ionization high-resolution mass spectrometry) to the data in the plot.

Characteristic reaction pathways and relevant kinetic regimes are outlined in Fig. 4b. SOA precursor VOCs with high volatility and low molar mass are located in the lower right corner of the molecular corridor ensemble. As illustrated in the insert in Fig. 4b, single-step functionalization usually leads to a small increase in molar mass, corresponding to one order of decrease in volatility (Donahue et al., 2006), while dimerization and oligomerization tend to multiply molar mass, and thus decrease volatility by multiple orders of magnitude (Trump and Donahue, 2014) (e.g., three to four orders of magnitude for alkane and terpene SOA, see Fig. 1). Fragmentation, on the other hand, can lead to a substantial decrease of molar mass and increase in volatility (Bertram et al., 2001; Yee et al., 2012; Schilling-Fahnestock et al., 2014). As a result, simple gas-phase oxidation products are confined to the lower right area in the 2-D space. Such oxidation products ($C_0 > 10\ \mu g\ m^{-3}$) tend to fall into the gas-phase reaction limiting case G_{rx} (quasi-equilibrium growth), as their gas-particle equilibration timescale is on the order of seconds to minutes (Shiraiwa and Seinfeld, 2012) (see Appendices C and D).

Particle-phase dimerization and oligomerization involving two or more molecules usually leads to the formation of compounds with low volatility and high molar mass lying in the upper left area in the 2-D space. The formation of such particle-phase products is likely limited by reaction or diffusion in the particle bulk (SB^{rd}), as rate coefficients for dimer

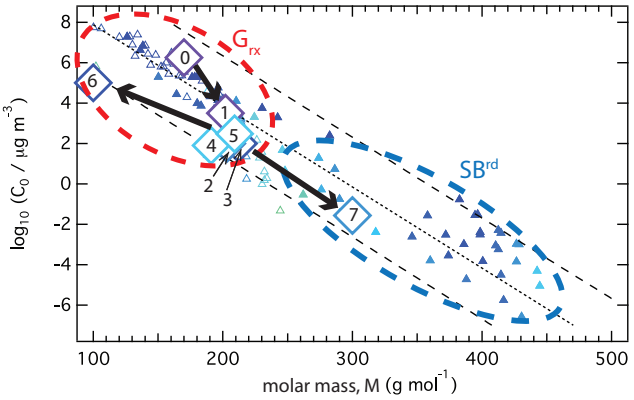

Figure 5. Evolution of reaction pathways over the molecular corridor of dodecane SOA under low NO condition. The large diamonds indicate the surrogate compounds used in the kinetic multi-layer model for gas-particle interactions (KM-GAP) simulations (Appendix D; Shiraiwa et al., 2013a), including the precursor (dodecane, 0), 1st–5th generations of surrogate products of gas-phase oxidation (1–5), gas-phase fragmentation (aldehydes, 6), and particle-phase dimerization products (7). The smaller symbols indicate identified individual products (as shown in Fig. 1a).

formation are relatively low ($< 10\,M^{-1}\,s^{-1}$) (Ziemann and Atkinson, 2012) and large molecules tend to diffuse slowly (Pfrang et al., 2011; Shiraiwa et al., 2011; Abramson et al., 2013; Zhou et al., 2013). An example of reaction pathways leading to dimerization is shown in Fig. 5 for dodecane SOA (Appendix D, Shiraiwa et al., 2013a). Within the molecular corridor of dodecane SOA evolution, Fig. 5 illustrates a specific trajectory from the precursor (dodecane, 0) through multiple generations of surrogate products of gas-phase oxidation and functionalization (multifunctional alcohols, ketones, and peroxides, 1–5), gas-phase fragmentation (aldehydes, 6), and particle-phase dimerization between aldehydes and peroxides to peroxyhemiacetals (7). Numerical model results shown in Figs. 5 and D1 indicate that the trajectory of chemical evolution passes through different kinetic regimes, i.e., from limitation by gas-phase reaction (G_{rx}) to particle-phase reaction and diffusion (SB^{rd}). Note that particle-phase reactions may also be limited by gas-to-particle mass transfer (e.g., accommodation, supply of reactive gases into the particle), when they are sufficiently fast, i.e., catalyzed by acids (Jang et al., 2002; Iinuma et al., 2004; Offenberg et al., 2009; Surratt et al., 2010).

Aqueous-phase processing of glyoxal and methylglyoxal is an efficient pathway for formation of low volatility and semi-volatile HOC compounds (Liggio et al., 2005; Carlton et al., 2007; Lim et al., 2010; Ervens et al., 2011; Zhao et al., 2012). Uptake of glyoxal into the particle phase leads to hydration and acid catalysis to form hemiacetals, aldols, imines, anhydrides, esters, and organosulfates (Lim et al., 2010). Reactive uptake of isoprene epoxydiols (IEPOX) and subsequent formation of oligomers (Surratt et al., 2010; Lin et al., 2012, 2013) also progresses over the HOC corridor. Whether multiphase chemistry of glyoxal and IEPOX is limited by mass transfer or chemical reactions may depend on various factors including reaction rate coefficients, relative humidity, particle pH, and Henry's law constant (Ervens and Volkamer, 2010; McNeill et al., 2012; Kampf et al., 2013).

Recently, highly oxidized, extremely low volatility organic compounds (ELVOC) have been detected in field and chamber experiments (Ehn et al., 2012; Schobesberger et al., 2013; Ehn et al., 2014). Such compounds may populate the upper left corner of the HOC corridor. It has been shown that such compounds can be formed via autoxidation (inter- and intramolecular hydrogen abstraction by peroxy radicals) in the gas and particle phases (Crounse et al., 2013). When they are formed in the gas phase, the equilibration timescale of partitioning is long due to their low volatility, and the SOA growth is limited most likely by mass transfer (gas-phase diffusion and accommodation; G^{mt}) (see Appendix C and Fig. C1) (Pierce et al., 2011; Riipinen et al., 2011; Shiraiwa and Seinfeld, 2012). Note that kinetic limitation by retarded bulk diffusion (G_{bd}) is also possible for semi-volatile and low-volatility products when organic particles adopt amorphous, solid state (Virtanen et al., 2010; Cappa and Wilson, 2011; Shiraiwa et al., 2011; Vaden et al., 2011; Kuwata and Martin, 2012; Perraud et al., 2012; Shiraiwa and Seinfeld, 2012; Renbaum-Wolff et al., 2013; Zaveri et al., 2014). Indeed, recent observation found that some SVOCs do not necessarily adhere to equilibrium partitioning (Vogel et al., 2013).

Formation of high molecular weight SOA compounds from oligomerization or autoxidation results in high average molar mass for the biogenic systems of isoprene and α-pinene (Kalberer et al., 2006), as well as the anthropogenic C_{12} alkanes (Fig. 1 and Table 1; Schilling-Fahnestock et al., 2014). Figure 4a shows that most identified oxidation products with molar masses higher than $300\,g\,mol^{-1}$ are particle-phase products (solid markers). Thus, the relatively high average molar mass observed for laboratory-generated SOA points to the importance of particle-phase chemistry in these systems. Some SOA compounds with higher molar mass are gas-phase oxidation products including ELVOC and ester dimers observed in α-pinene oxidation (Ehn et al., 2014; Kristensen et al., 2014), and there are also some particle-phase products with relatively low molar mass, including furans and dihydrofurans in dodecane and cyclododecane SOA (Yee et al., 2012; Loza et al., 2014), as well as glyoxal and IEPOX products in isoprene SOA (Lim et al., 2010; Surratt et al., 2010). Nevertheless, the clustering of identified reaction products in molecular corridors may facilitate estimation of the relative importance of gas- vs. particle-phase routes to SOA formation (Fig. 1).

Molar mass and O : C ratio also correlate with the glass transition temperature of organic compounds, which tends to rise with increasing molar mass and O : C ratio (Koop et al., 2011). As elevated glass transition temperatures are indicative of semi-solid or amorphous, solid states, SOA evolution

represented in molecular corridors allows one to infer the regime in which particles are likely to become highly viscous. For example, recent experiments have shown an order of magnitude increase in the viscosity of oleic acid particles upon reaction with ozone owing to formation of oligomers (Hosny et al., 2013), and model calculations indicate that this may lead to the formation of surface crusts (Pfrang et al., 2011).

In summary, presenting identified SOA products in a molecular corridor encapsulates fundamental aspects of SOA formation and aging: volatility, molar mass, O : C ratio, and phase state. Such a representation can be used to constrain and/or predict the properties of unidentified SOA oxidation products. The kinetic regimes, within which SOA evolution is occurring along the molecular corridor, facilitate the specification of the rate of progression to higher generation products. Thus, molecular corridors may serve as a basis for compact representation of SOA formation and aging in regional and global models of climate and air quality.

Appendix A: Product analysis of alkane SOA

Photo-oxidation and subsequent SOA formation of *n*-dodecane, cyclododecane, and hexylcyclohexane was conducted in the 28 m^3 Teflon reactors in the Caltech environmental chamber (Yee et al., 2012; Loza et al., 2014; Schilling-Fahnestock et al., 2014). Aqueous H_2O_2 solution was evaporated into the chamber as the OH source, followed by the atomization of an aqueous ammonium sulfate solution generating seed particles, which were subsequently dried. Experiments were conducted under low NO conditions, in which alkyl peroxy radicals (RO_2) react primarily with HO_2, and under high NO conditions, in which RO_2 react primarily with NO (Loza et al., 2014).

SOA particles were collected on Teflon filters (Pall Life Sciences, 47 mm, 1.0 µm pore size). Off-line analysis of collected particles was conducted by solvent extraction and gas chromatography time-of-flight mass spectrometry (GC-TOF-MS, GCT Premier, Waters) and GC / ion trap mass spectrometry (Varian Saturn 2000, Agilent), and by direct analysis in real time (DART) time-of-flight and ion trap mass spectrometry (DART-AccuToF, JEOL USA; Caltech Mini-DART; LTQ, Thermo Fisher). Further details on experimental conditions and analytical methods can be found in Schilling-Fahnestock et al. (2014).

The average molar mass of SOA was estimated by taking the sum of the product of the percent-relative concentration of each compound with respect to the internal standard (dibutyl phthalate present in each filter) by each compound's molar mass. The relative concentration for each compound was obtained through the relationship of ion current intensity and concentration for DART-MS. In DART analysis, ion current intensity (I) is proportional to the concentration (C), vapor pressure (P_{vap}) and proton affinity (A): $I = A P_{vap} C$. This equation is written for both the analyte and the internal standard and then the ratio is calculated, which allows for the cancellation of the proton affinity term. Analyte vapor pressures were estimated by using proposed structures based on HR-MS data-derived formulae and known mechanisms with the EVAPORATION model (Compernolle et al., 2011). When rewritten to solve for the relative concentration of the analyte with respect to the concentration of the internal standard, the equation becomes

$$\frac{C_A}{C_{IS}} = \frac{P_{vap,IS}}{P_{vap,A}} \cdot \frac{I_A}{I_{IS}}.$$

Atomic O : C ratio vs. volatility is used to represent formation and aging of SOA (Jimenez et al., 2009; Donahue et al., 2011). By analogy to Figs. 1 and 4, major oxidation products are shown in Figs. S1 and S2 in the Supplement. The markers are color-coded by molar mass. Upon gas-phase oxidation, volatility decreases and O : C ratio increases, leading to a linear correlation in O : C ratio vs. volatility for gas-phase oxidation products. Particle-phase products, however, exhibit generally lower volatility and O : C ratio as compared to gas-phase oxidation products. Consequently, the overall correlation between O : C ratio and volatility for the full spectrum of SOA products has a low coefficient of determination and wide prediction interval (Table 1, Fig. S1 in the Supplement). Figure S2 in the Supplement shows the summary of O : C ratio vs. volatility, showing that the oxidation products cover almost the full area in this 2-D space. Clear trend has found that volatile compounds have low molar mass, whereas low volatility compounds with low O : C ratio have high molar mass.

Table A1. Experimental conditions in studies identifying oxidation products, as included in Figs. 1 and 4.

	Study	Oxidants	NO	Seed
Dodecane	This study, Schilling-Fahnestock et al. (2014)	OH	Low/high	$(NH_4)_2SO_4$
Cyclododecane		OH	Low/high	$(NH_4)_2SO_4$
Hexylcyclohexane		OH	Low/high	$(NH_4)_2SO_4$
α-pinene	Docherty et al. (2005)	O_3	Low	No seed
	Claeys et al. (2007)	OH	High	No seed
	Claeys et al. (2009)	OH, O_3	High/low	$(NH_4)_2SO_4$, H_2SO_4, $MgSO_4$
	Kahnt et al. (2014)	O_3	High	$(NH_4)_2SO_4$, H_2SO_4
	Kristensen et al. (2014)	OH, O_3	High	$(NH_4)_2SO_4$, H_2SO_4, $MgSO_4$
	Zuend and Seinfeld (2012)	O_3	Low	$(NH_4)_2SO_4$
Limonene	Jaoui et al. (2006)	OH, O_3	High	No seed
	Kundu et al. (2012)	O_3	Low	No seed
Isoprene	Surratt et al. (2006)	OH	High / low	$(NH_4)_2SO_4$, H_2SO_4, no seed
	Surratt et al. (2010)	OH	High / low	$(NH_4)_2SO_4$, H_2SO_4, no seed
	Lin et al (2012)	OH	High	No seed
	Lin et al. (2013)	OH	Low	$(NH_4)_2SO_4$, H_2SO_4, $MgSO_4$

Appendix B: Kinetic regimes for SOA formation

Figure B1 shows a classification scheme for kinetic regimes and limiting cases for SOA formation and aging. Note that the term "limiting case" is reserved for a system that is governed by a single, clearly defined limiting process; the term "kinetic regime" designates a system that is governed by a few (often only one or two) clearly defined rate-limiting processes (Berkemeier et al., 2013). The classification within the particle phase regime (right-hand side of Fig. 3) is explained in detail by Berkemeier et al. (2013). In this study, the gas-phase regime (left-hand side of Fig. 3) extends the classification scheme to SOA formation. The cases of limiting behavior arise from three criteria that are fundamental to formation and partitioning of an oxidation product: (1) the location (gas phase, particle surface, particle bulk) of the reaction leading to SOA formation; (2) the species' saturation ratio (ratio of ambient concentration to saturation concentration) of the oxidation products; and (3) the extent of spatial heterogeneity of the gas and particle phases. Identifying kinetic regimes and limiting cases can be facilitated by an aerosol model, such as the kinetic multi-layer model for gas-particle interactions (KM-GAP) that explicitly resolves mass transport and chemical reactions in the gas and particle phases (Shiraiwa et al., 2012).

B1 Criterion 1: reaction location (gas vs. surface vs. bulk)

Where does formation of oxidation products that contribute to SOA mass predominantly occur, gas phase, particle surface or particle bulk? A two-pronged criterion can be developed. The first sub-criterion evaluates the relative contribution of gas- vs. particle-phase chemistry. The gas- vs. particle-phase contribution ratio (GPCR) can be defined as ratio of the production rate of the oxidation product in the gas phase (P^g) to the total production rate in gas and particle phases ($P^g + P^p$):

$$\mathrm{GPCR} = P^g / (P^g + P^p). \quad \text{(B1)}$$

As GPCR approaches unity, an oxidation product is produced primarily in the gas phase, and as GPCR approaches zero, it is primarily produced in the particle phase.

If particle-phase chemistry dominates ($\mathrm{GPCR} \approx 0$), the surface to total particle-phase contribution ratio (STCR) is used to assess the extent to which production occurs predominantly at the surface or in the bulk. STCR can be calculated using the production rate of the oxidation product at the surface (P^s) and in the particle bulk (P^b):

$$\mathrm{STCR} = P^s/(P^s + P^b). \quad \text{(B2)}$$

If the particle-phase reaction primarily occurs at the surface, STCR approaches unity, and STCR approaches zero if the reaction occurs primarily in the bulk.

B2 Criterion 2: saturation ratio

Is mass transfer of an oxidation product through the gas or into the particle phase limiting SOA growth? After determination of the reaction location, this criterion further classifies the system based on the abundance of oxidation products at the particle surface versus in the near-surface bulk.

In the gas-phase regime, the surface saturation ratio (SSR) can be used to judge the extent to which kinetic limitation of mass transport occurs in the gas phase. With this parameter,

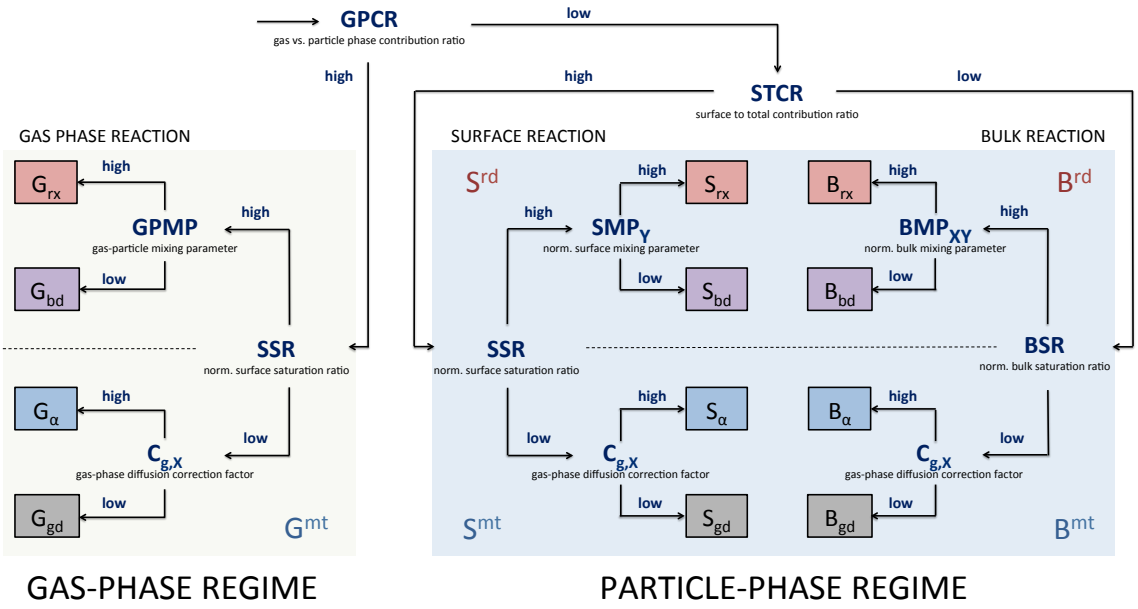

Figure B1. Decision tree for classification and distinction of limiting cases for multiphase chemical evolution of SOA. The classification is based on: (1) the location of the reaction leading to its formation, (2) its saturation ratio, and (3) its mixing parameter to assess the heterogeneity in the gas and particle phases. The resulting limiting cases are shown in the small boxes with reaction location in the gas phase (G), at the surface (S) and in the bulk (B) and limiting processes of chemical reaction (rx), bulk diffusion (bd), mass accommodation (α), and gas-phase diffusion (gd).

the surface concentration of an oxidation product Z, $[Z]_s$, is compared to its surface saturation concentration $[Z]_{s,sat}$. In the absence of reaction or diffusion into the bulk, $[Z]_{s,sat}$ is determined by the gas-phase concentration of Z, $[Z]_g$, and the rates of adsorption and desorption k_a and k_d: $[Z]_{s,sat} = k_a / k_d [Z]_g$ (Pöschl et al., 2007; Berkemeier et al., 2013). The SSR is defined as the ratio of $[Z]_s$ to its saturation concentration at adsorption equilibrium:

$$\mathrm{SSR} = [Z]_s / [Z]_{s,sat}. \quad \text{(B3)}$$

The numerical interpretation of SSR is as follows: as SSR approaches zero, the surface is starved of Z, and the system is limited by mass transfer (G^{mt} regime) either by gas-phase diffusion (G_{gd} limiting case) or surface accommodation (G_{α} limiting case). As SSR approaches unity, the surface is adequately supplied with Z and the system can be limited by production of Z in the gas phase (G_{rx} limiting case) or mass transport into the bulk (G_{bd} limiting case).

In the particle-phase regime, the classification step is based on SSR or the bulk saturation ratio (BSR) to distinguish between systems in the reaction-diffusion regime or the mass-transfer regime (Berkemeier et al., 2013). The BSR is defined analogously to SSR as the ratio of near-surface bulk concentration of an oxidation product to its saturation concentration.

B3 Criterion 3: mixing parameters (MPs)

Is SOA growth limited by diffusion in the gas or particle phase? Depending on the reaction location and saturation ratio, mixing parameters are used to assess the heterogeneity of the gas-particle system. One can define the surface mixing parameter (SMP), the bulk mixing parameter (BMP), the gas-phase diffusion correction factor (C_g), and the gas-particle mixing parameter (GPMP). SMP is defined as the ratio of the actual surface concentration of compound i to the maximum possible surface concentration in the case of perfect particle-phase mixing. BMP is defined using an effective reacto-diffusive length (Berkemeier et al., 2013). As an MP approaches zero, a strong concentration gradient exists and the system is limited by diffusion; as MP approaches unity, the system is well-mixed and limited by reaction.

In mass-transfer limited systems (indicated by a low SR), $C_{g,i}$ distinguishes between gas-phase diffusion limitation and accommodation limitation. $C_{g,i}$ is defined as the ratio of the concentration of compound i in the near-surface gas phase (one mean free path away from the surface) to that in the gas phase far from the particle (Pöschl et al., 2007):

$$C_{g,i} = C_i^{gs} / C_i^{g}. \quad \text{(B4)}$$

As $C_{g,i}$ approaches zero, the compound i exhibits a strong concentration gradient in the gas phase and the system is classified as gas-phase diffusion limited (G_{gd} limiting case); as $C_{g,i}$ approaches unity, the system is designated as accommodation-limited (G_{α} limiting case).

The gas-particle mixing parameter (GPMP) measures the extent to which the gas-particle system is in quasi-equilibrium and is defined as the ratio of equilibrium gas-phase mass concentration of compound i, $C_i^{g,eq}$, to gas-phase mass concentration, C_i^g (far from particle), which is equivalent to the ratio of particle-phase mass concentration, C_i^{PM}, to equilibrium particle-phase mass concentration, $C_i^{PM,eq}$:

$$\mathrm{GPMP}_i = C_i^{g,eq} / C_i^g = C_i^{PM} / C_i^{PM,eq}. \quad \text{(B5)}$$

$C_i^{g,eq}$ and $C_i^{PM,eq}$ can be calculated using an equilibrium partitioning theory (Pankow, 1994; Donahue et al., 2006):

$$C_i^{g,eq} = C_i^* C_i^{PM} / C_{Tot}, \quad \text{(B6)}$$

$$C_i^{PM,eq} = C_i^g C_{Tot} / C_i^*, \quad \text{(B7)}$$

where C_i^* is the effective saturation mass concentration of compound i, and C_{Tot} is the total particle mass concentration. In the case of ideal mixing, C_i^* is equal to the gas-phase saturation mass concentration over the pure subcooled liquid (C_i^0). Note that $C_i^{g,eq}$ can be regarded as a gas-phase mass concentration just above the particle surface, C_i^s, when Raoult's law is strictly obeyed and C_i^s is in equilibrium with the whole particle (i.e., usually the case for liquid particles).

The value of GPMP determines the extent to which SOA growth is controlled by quasi-equilibrium growth or mass transport limited growth. $C_i^g = C_i^{g,eq}$ (or $C_i^{PM} = C_i^{PM,eq}$) at gas-particle equilibrium. The particle still grows, if C_i^g changes slowly and $C_i^{g,eq}$ follows C_i^g instantaneously (quasi-equilibrium growth) (Shiraiwa and Seinfeld, 2012; Zhang et al., 2012). If $C_i^g > C_i^{g,eq}$, compound i will diffuse from the gas to the particulate phase, driven by concentration or partial pressure gradient between the gas and particle phases (non-equilibrium or mass transport limited growth). Thus, the numerical interpretation of GPMP is: (1) as GPMP approaches 0, SOA growth is limited kinetically by mass transport; (2) as GPMP approaches unity, SOA growth is in quasi-equilibrium and the system is subject to the gas-phase reaction limitation case G_{rx} (the system is limited only by the gas-phase formation rate).

Note that GPMP is small for the limiting cases of G_{bd}, G_α, and G_{gd}. In these limiting cases, SOA growth is still sensitive to the gas-phase formation rate (as it determines the gas-phase concentration), but is limited by interfacial transport, which comprises gas-phase diffusion, surface accommodation, and surface-to-bulk transport processes. Gas-phase diffusion and surface accommodation limitation can be differentiated from surface-to-bulk transport limitation either by SSR or by comparing surface (α_s) and bulk (α_b) accommodation coefficients, each of which is resolved by KM-GAP. α_s is defined as the probability of a molecule sticking to the surface upon collision, whereas α_b is defined as the respective probability of a molecule to enter the bulk of the particle (Pöschl et al., 2007; Shiraiwa et al., 2012). If $\alpha_s \approx \alpha_b$, then interfacial transport is not limited by surface-to-bulk exchange, and thus is limited by either gas-phase diffusion or surface accommodation; if $\alpha_s > \alpha_b$, then the interfacial transport is limited by surface-to-bulk transport (dissolution or bulk diffusion). For additional discussion of accommodation vs. surface-bulk exchange, see Appendix C in Berkemeier et al. (2013).

Appendix C: Examples of kinetic regimes and limiting cases

Here we use KM-GAP to model condensation of a semi-volatile compound generated by oxidation of a parent VOC. We assume that the parent VOC with an initial concentration of 10^{10} cm^{-3} is converted to a semi-volatile product with a first-order rate coefficient of 0.1 min^{-1}. Conversion of the first-generation product to higher generation products and particle-phase reactions need not be considered. The initial number and mass concentrations of non-volatile pre-existing particles are taken as 10^3 cm^{-3} and 0.1 µg m^{-3}, respectively. The initial particle size distribution is assumed log-normal with a mean diameter of 50 nm and a standard deviation of 1.5. The required kinetic parameters for the simulation are given in Table C1. The gas-phase diffusion coefficient (D_g) of an oxidation product is varied between 0.01–0.05 cm^2 s^{-1} (Bilde et al., 2003; Bird et al., 2007). The surface accommodation coefficient ($\alpha_{s,0}$) and bulk diffusion coefficient (D_b) are also varied to illustrate the different kinetic regimes and limiting cases for SOA formation in the gas-phase regime.

Figure C1 shows the results of such simulation. The temporal evolution of mass concentration of the parent VOC (black), the oxidation product in the gas phase (C^g, solid blue), in the near-surface gas phase (C^{gs}, dotted blue), in the particle phase (C^{PM}, red), and equilibrium gas-phase concentration ($C^{g,eq}$, dashed blue) are shown. In the simulation presented in Fig. C1a, SOA growth is limited by mass transfer, namely gas-phase diffusion and accommodation (G^{mt} regime, lying between limiting cases G_{gd} and G_α) up to ~10 s, indicated by a low surface saturation ratio (SSR) and a low gas-phase diffusion correction factor ($C_g = C^{gs}/C^g \approx 0.7$). The gas-phase concentration gradient vanishes within ~10 s ($C^{gs} \approx C^g$), and as C^g continues to increase due to the conversion of the parent VOC, $C^{g,eq}$ follows the change in C^g, essentially instantaneously, and C^{PM} increases. In this case, the gas-phase rate of formation of the oxidation product controls particle growth corresponding to the limiting case of G_{rx} (so-called quasi-equilibrium growth) (Shiraiwa and Seinfeld, 2012; Zhang et al., 2012).

In the simulation presented in Fig. C1b with a relatively low surface accommodation coefficient of 10^{-3}, a steep concentration gradient exhibits between the gas phase and the particle surface ($C^g \approx C^{gs} > C^{g,eq}$) during SOA growth. The system is limited by accommodation (G_α), as SSR is low, but C_g is 1. Figure C1c shows the corresponding results for

Table C1. Properties and kinetic parameters of the VOC oxidation product used in the simulations for SOA growth.

Parameter (unit)	Description	(a)	(b)	(c)	(d)
$\alpha_{s,0}$	Surface accommodation coefficient	1	10^{-3}	1	1
τ_d (s)	Desorption lifetime	10^{-6}	10^{-6}	10^{-6}	10^{-6}
C_0 ($\mu g\,m^{-3}$)	Saturation mass concentration	10^3	10^3	10^3	10^{-3}
D_b ($cm^2\,s^{-1}$)	Bulk diffusion coefficient	10^{-5}	10^{-5}	10^{-17}	10^{-5}
D_g ($cm^2\,s^{-1}$)	Gas-phase diffusion coefficient	0.01	0.05	0.05	0.01
k_g (min^{-1})	First-order gas-phase reaction rate coefficient	0.1	0.1	0.1	0.1

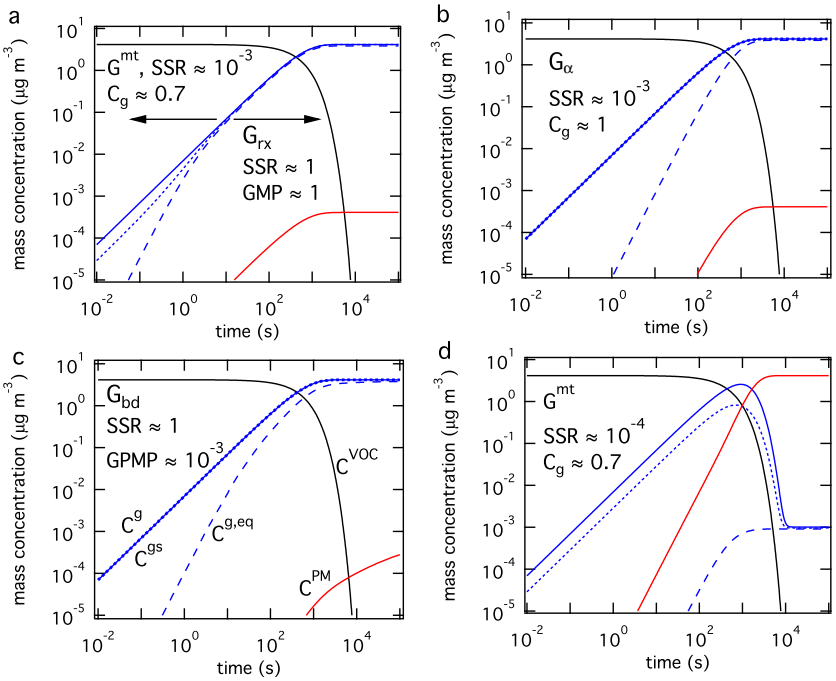

Figure C1. Temporal evolution of mass concentration of the hypothesized VOC oxidation product in the gas phase (solid blue), in the near-surface gas phase (dotted blue), in the particle phase (red), and equilibrium gas-phase concentration (dashed blue). The gas-phase mass concentration of the parent VOC is shown by the black line. For semi-volatile oxidation products with $C^* = 10^3\,\mu g\,m^{-3}$, SOA growth is limited by **(a)** gas-phase reaction (G_{rx}), **(b)** accommodation (G_α), and **(c)** bulk diffusion (G_{bd}). **(d)** shows an exemplary simulation for LVOCs, with $C^* = 10^{-3}\,\mu g\,m^{-3}$ exhibiting kinetic limitation in the gas-particle mass transfer regime (G^{mt}).

particles in an amorphous, semi-solid state with the low bulk diffusion coefficient of $10^{-17}\,cm^2\,s^{-1}$. In this case, particle growth is limited by surface-to-bulk transport (G_{bd}), as SSR is high and GPMP is low. Note that GPMP refers to the gap between C^g and $C^{g,eq}$. The bulk accommodation coefficient α_b is $\sim 10^{-5}$, which is much smaller than the surface accommodation coefficient α_s. Sensitivity studies with varying D_b reveal that, when $D_b < \sim 10^{-15}\,cm^2\,s^{-1}$, the time scales for surface-bulk exchange and bulk diffusion become longer than that of gas-phase diffusion and accommodation (Shiraiwa and Seinfeld, 2012). From the Stokes–Einstein relation, this value corresponds to a viscosity of $\sim 10^7$ Pa s, which is on the same order as the viscosity of α-pinene SOA at 40 % RH (relative humidity) (Renbaum-Wolff et al., 2013). Thus, SOA growth can be limited by bulk diffusion at low RH, whereas surface accommodation becomes more important at high RH.

Figure C1d shows the simulation for gas-phase formation and partitioning of low volatility oxidation products ($C_0 = 10^{-3}\,\mu g\,m^{-3}$) into liquid particles. SSR is low over the course of particle growth, indicating persistence of a strong concentration gradient between the gas phase and the particle surface. The gas-phase diffusion correction factor (C_g) stays at 0.7 up to $\sim 10^3$ s, indicating that near-surface gas phase concentration $[Z]_{gs}$ is depleted by 30 % compared to gas phase concentration $[Z]_g$ due to rapid uptake and slow gas diffusion ($D_g = 0.01\,cm^2\,s^{-1}$). C_g decreases substantially down to ~ 0.2 only when gas-phase formation ceases at $\sim 10^3$–10^4 s. Overall, SOA growth is limited by mass transfer (gas-phase diffusion and accommodation;

G^{mt} regime). When a very low-bulk diffusivity is assumed ($D_b \approx 10^{-19}\,cm^2\,s^{-1}$; figure not shown), SSR is close to 1 and GPMP is very low during particle growth. Thus, the system is limited by bulk diffusion (G_{bd}). Consequently, partitioning of low volatility compounds could be limited by bulk diffusion, when organic particles adopt amorphous solid state (Shiraiwa and Seinfeld, 2012; Zaveri et al., 2014).

Appendix D: Application to chamber data – dodecane photooxidation

Here we apply the classification scheme to experimental data on SOA formation from oxidation of the C_{12} alkane, dodecane ($C_{12}H_{28}$) in the Caltech environmental chamber (Yee et al., 2012). 34 ppb dodecane was oxidized by OH radicals over 20 h in the presence of dry ammonium sulfate seed particles at low concentrations of NO_x, typical of non-urban conditions. KM-GAP was used to simulate the evolution of SOA mass, the organic atomic oxygen-to-carbon (O : C) ratio, and particle-size distribution in the chamber experiments (Shiraiwa et al., 2013a). In the gas phase, SVOCs resulting from up to five generations of OH oxidation are considered. Some of the fourth generation products have been established to be multifunctional carbonyl compounds (aldehydes) that can react in the particle phase with hydroperoxide, hydroxyl, and peroxycarboxylic acid groups, forming peroxyhemiacetal (PHA), hemiacetal, and acylperoxyhemiacetal, respectively (Docherty et al., 2005; Yee et al., 2012; Ziemann and Atkinson, 2012). The observed evolution of the particle size distribution is simulated successfully only if such particle-phase chemistry is included (Shiraiwa et al., 2013a).

Figure 5 shows the span of molar mass and gas-phase saturation concentrations over the pure subcooled liquids (C_i^0) for gas-phase oxidation products and particle-phase products of the dodecane system. The smaller symbols indicate individual products predicted in the dodecane photooxidation chemical mechanism (Yee et al., 2012) and the large solid circles indicate the surrogate compounds used in the KM-GAP simulations (Shiraiwa et al., 2013a). Upon gas-phase multi-generation oxidation, the volatility of SVOCs decreases from $\sim 10^6\,\mu g\,m^{-3}$ (dodecane) to $\sim 1\,\mu g\,m^{-3}$. The particle-phase products have significantly lower volatilities of $\sim 10^{-2}\,\mu g\,m^{-3}$.

Figure D1a and b show the temporal evolution of mass concentration of the first and fifth generation oxidation products in the gas phase (C^g), at the particle surface (C^s), and in the particle phase (C^{PM}). C^g is slightly higher than $C^{g,eq}$ up to ~ 5 h due to continuous generation of oxidation products in the gas phase, and eventually reaching $C^g \approx C^{g,eq}$ for both products (GPMP ≈ 1). Note that mass concentration in the near-surface gas phase (C^{gs}) is identical to C^g, indicating that gas-phase diffusion is not a limiting step. The same trend is seen for other generation products. Thus, the contribution of gas-phase semi-volatile oxidation products to SOA formation is limited by their formation in the gas phase, corresponding to the limiting case of G_{rx}.

Particle-phase products are formed by the reaction of reactive aldehydes with SVOCs in the particle phase. Simulations suggest that this reaction occurs mainly at the surface and in the near-surface bulk (Shiraiwa et al., 2013a). Aldehydes and SVOCs are both saturated in the bulk (BSR is high). A strong concentration gradient of aldehydes in the bulk is predicted, whereas SVOCs are predicted to be essentially homogeneous in the bulk ($BMP_{XY} \approx 0.5$). Bulk reaction is tightly coupled with bulk diffusion, and the system falls into the reaction-diffusion regime (SB^{rd}), particularly the traditional reacto-diffusive case (B^{rd}_{trad}) (Worsnop et al., 2002; Pöschl et al., 2007; Kolb et al., 2010; Berkemeier et al., 2013).

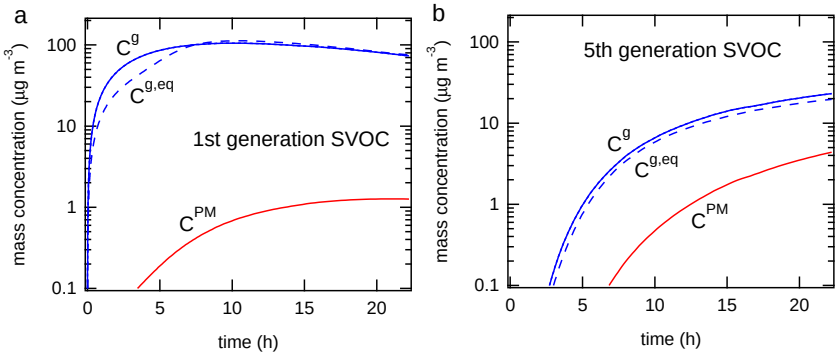

Figure D1. Modeling SOA formation from dodecane photooxidation. Temporal evolution of mass concentration of the **(a)** first and **(b)** five generation products in the gas phases (solid blue), particle phases (red), and equilibrium gas-phase mass concentration (dashed blue).

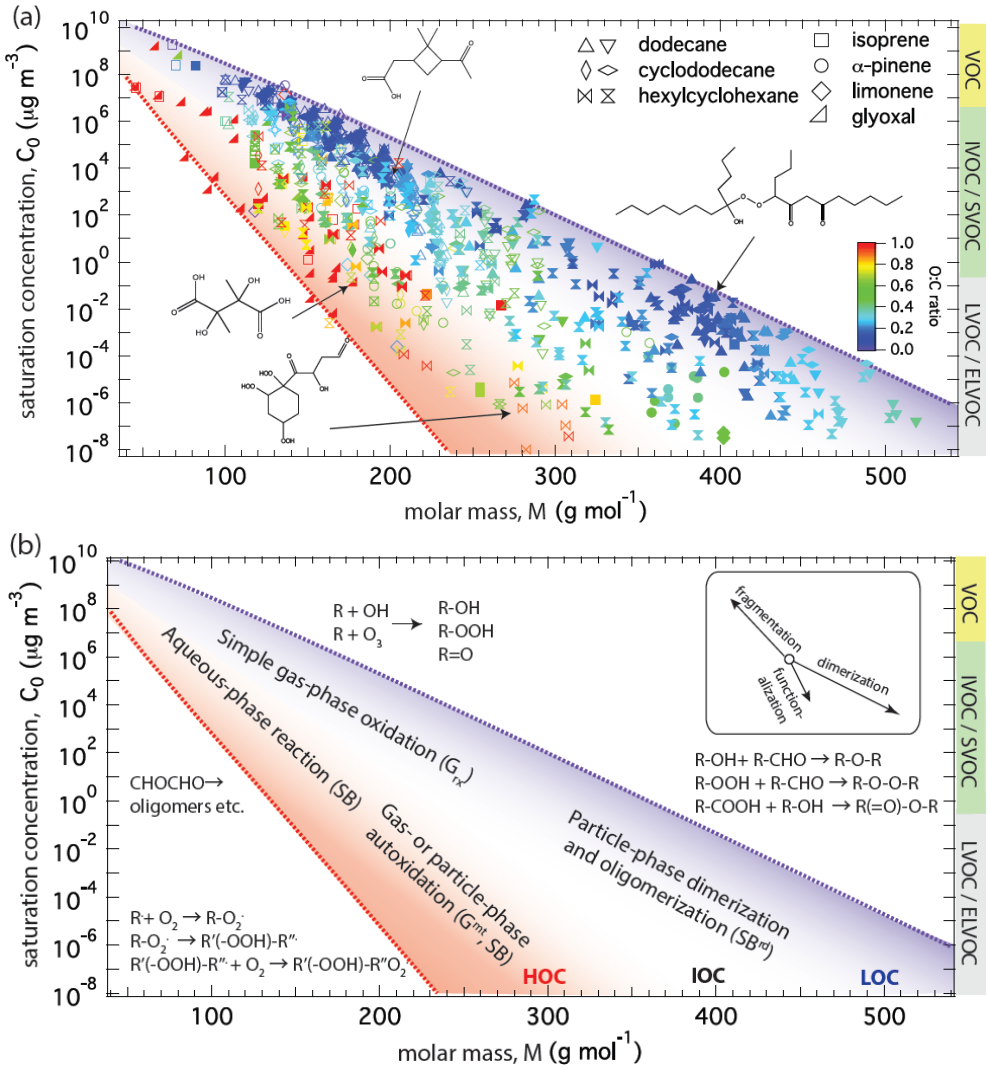

Figure D2. Alternative representation of molecular corridors (Fig. 4) displaying volatility (C_0) as a function of molar mass, which appears more straightforward to use and interpret in mechanistic studies (see Fig. 5) and for direct comparison to mass spectra. Volatility decreases as molar mass increases from left to right, and the slope $\mathrm{d}\log C_0 / \mathrm{d}M$ is steeper for molecules with higher O : C ratio and polarity due to stronger hydrogen bonding and evaporation enthalpy.

The Supplement related to this article is available online at doi:10.5194/acp-14-8323-2014-supplement.

Acknowledgements. This work was funded by the Max Planck Society and US National Science Foundation grant AGS-1057183. M. Shiraiwa, T. Berkemeier and U. Pöschl thank the European Commission project Pan-European gas-aerosols-climate interaction study (No. 265148, PEGASOS). M. Shiraiwa thanks the Japan Society for the Promotion of Science (JSPS) for Postdoctoral Fellowships for Research Abroad.

The service charges for this open access publication have been covered by the Max Planck Society.

Edited by: M. C. Facchini

References

Abramson, E., Imre, D., Beranek, J., Wilson, J. M., and Zelenyuk, A.: Experimental determination of chemical diffusion within secondary organic aerosol particles, Phys. Chem. Chem. Phys., 15, 2983–2991, 2013.

Berkemeier, T., Huisman, A. J., Ammann, M., Shiraiwa, M., Koop, T., and Pöschl, U.: Kinetic regimes and limiting cases of gas uptake and heterogeneous reactions in atmospheric aerosols and clouds: a general classification scheme, Atmos. Chem. Phys., 13, 6663–6686, doi:10.5194/acp-13-6663-2013, 2013.

Bertram, A. K., Ivanov, A. V., Hunter, M., Molina, L. T., and Molina, M. J.: The reaction probability of OH on organic surfaces of tropospheric interest, J. Phys. Chem. A, 105, 9415–9421, 2001.

Bilde, M., Svenningsson, B., Monster, J., and Rosenorn, T.: Even-odd alternation of evaporation rates and vapor pressures of C3-C9 dicarboxylic acid aerosols, Environ. Sci. Technol., 37, 1371–1378, 2003.

Bird, R. B., Stewart, W. E., and Lightfoot, E. N.: Transport Phenomena, 2nd edition, John Wiley & Sons, Inc., New York, 2007.

Cappa, C. D. and Wilson, K. R.: Evolution of organic aerosol mass spectra upon heating: implications for OA phase and partitioning behavior, Atmos. Chem. Phys., 11, 1895–1911, doi:10.5194/acp-11-1895-2011, 2011.

Carlton, A. G., Turpin, B. J., Altieri, K. E., Seitzinger, S., Reff, A., Lim, H. J., and Ervens, B.: Atmospheric oxalic acid and SOA production from glyoxal: Results of aqueous photooxidation experiments, Atmos. Environ., 41, 7588–7602, 2007.

Chan, M. N., Nah, T., and Wilson, K. R.: Real time in situ chemical characterization of sub-micron organic aerosols using Direct Analysis in Real Time mass spectrometry (DART-MS): the effect of aerosol size and volatility, Analyst, 138, 3749–3757, 2013.

Chang, E. I. and Pankow, J. F.: Prediction of activity coefficients in liquid aerosol particles containing organic compounds, dissolved inorganic salts, and water – Part 2: Consideration of phase separation effects by an X-UNIFAC model, Atmos. Environ., 40, 6422–6436, 2006.

Claeys, M., Szmigielski, R., Kourtchev, I., Van der Veken, P., Vermeylen, R., Maenhaut, W., Jaoui, M., Kleindienst, T. E., Lewandowski, M., Offenberg, J. H., and Edney, E. O.: Hydroxydicarboxylic acids: Markers for secondary organic aerosol from the photooxidation of alpha-pinene, Environ. Sci. Technol., 41, 1628–1634, 2007.

Claeys, M., Iinuma, Y., Szmigielski, R., Surratt, J. D., Blockhuys, F., Van Alsenoy, C., Boege, O., Sierau, B., Gomez-Gonzalez, Y., Vermeylen, R., Van der Veken, P., Shahgholi, M., Chan, A. W. H., Herrmann, H., Seinfeld, J. H., and Maenhaut, W.: Terpenylic Acid and Related Compounds from the Oxidation of alpha-Pinene: Implications for New Particle Formation and Growth above Forests, Environ. Sci. Technol., 43, 6976–6982, 2009.

Compernolle, S., Ceulemans, K., and Muller, J. F.: EVAPORATION: a new vapour pressure estimation methodfor organic molecules including non-additivity and intramolecular interactions, Atmos. Chem. Phys., 11, 9431–9450, doi:10.5194/acp-11-9431-2011, 2011.

Crounse, J. D., Nielsen, L. B., Jørgensen, S., Kjaergaard, H. G., and Wennberg, P. O.: Autoxidation of organic compounds in the atmosphere, J. Phys. Chem. Lett., 4, 3513–3520, 2013.

Docherty, K. S., Wu, W., Lim, Y. B., and Ziemann, P. J.: Contributions of organic peroxides to secondary aerosol formed from reactions of monoterpenes with O_3, Environ. Sci. Technol., 39, 4049–4059, 2005.

Donahue, N. M., Robinson, A. L., Stanier, C. O., and Pandis, S. N.: Coupled partitioning, dilution, and chemical aging of semivolatile organics, Environ. Sci. Technol., 40, 2635–2643, 2006.

Donahue, N. M., Epstein, S. A., Pandis, S. N., and Robinson, A. L.: A two-dimensional volatility basis set: 1. organic–aerosol mixing thermodynamics, Atmos. Chem. Phys., 11, 3303–3318, doi:10.5194/acp-11-3303-2011, 2011.

Donahue, N. M., Henry, K. M., Mentel, T. F., Kiendler-Scharr, A., Spindler, C., Bohn, B., Brauers, T., Dorn, H. P., Fuchs, H., Tillmann, R., Wahner, A., Saathoff, H., Naumann, K.-H., Möhler, O., Leisner, T., Müller, L., Reinnig, M.-C., Hoffmann, T., Salo, K., Hallquist, M., Frosch, M., Bilde, M., Tritscher, T., Barmet, P., Praplan, A. P., DeCarlo, P. F., Dommen, J., Prévôt, A. S. H., and Baltensperger, U.: Aging of biogenic secondary organic aerosol via gas-phase OH radical reactions, P. Natl. Acad. Sci. USA, 109, 13503–13508, 2012.

Ehn, M., Kleist, E., Junninen, H., Petaja, T., Lonn, G., Schobesberger, S., Dal Maso, M., Trimborn, A., Kulmala, M., Worsnop, D. R., Wahner, A., Wildt, J., and Mentel, T. F.: Gas phase formation of extremely oxidized pinene reaction products in chamber and ambient air, Atmos. Chem. Phys., 12, 5113–5127, doi:10.5194/acp-12-5113-2012, 2012.

Ehn, M., Thornton, J. A., Kleist, E., Sipila, M., Junninen, H., Pullinen, I., Springer, M., Rubach, F., Tillmann, R., Lee, B., Lopez-Hilfiker, F., Andres, S., Acir, I.-H., Rissanen, M., Jokinen, T., Schobesberger, S., Kangasluoma, J., Kontkanen, J., Nieminen, T., Kurten, T., Nielsen, L. B., Jorgensen, S., Kjaergaard, H. G., Canagaratna, M., Dal Maso, M., Berndt, T., Petaja, T., Wahner, A., Kerminen, V.-M., Kulmala, M., Worsnop, D. R., Wildt, J., and Mentel, T. F.: A large source of low-volatility secondary organic aerosol, Nature, 506, 476–479, 2014.

Ervens, B. and Volkamer, R.: Glyoxal processing by aerosol multiphase chemistry: towards a kinetic modeling framework of secondary organic aerosol formation in aqueous particles, Atmos.

Chem. Phys., 10, 8219–8244, doi:10.5194/acp-10-8219-2010, 2010.

Ervens, B., Turpin, B. J., and Weber, R. J.: Secondary organic aerosol formation in cloud droplets and aqueous particles (aqSOA): a review of laboratory, field and model studies, Atmos. Chem. Phys., 11, 11069–11102, doi:10.5194/acp-11-11069-2011, 2011.

Goldstein, A. H. and Galbally, I. E.: Known and unexplored organic constituents in the earth's atmosphere, Environ. Sci. Technol., 41, 1514–1521, 2007.

Hallquist, M., Wenger, J. C., Baltensperger, U., Rudich, Y., Simpson, D., Claeys, M., Dommen, J., Donahue, N. M., George, C., Goldstein, A. H., Hamilton, J. F., Herrmann, H., Hoffmann, T., Iinuma, Y., Jang, M., Jenkin, M. E., Jimenez, J. L., Kiendler-Scharr, A., Maenhaut, W., McFiggans, G., Mentel, T. F., Monod, A., Prevot, A. S. H., Seinfeld, J. H., Surratt, J. D., Szmigielski, R., and Wildt, J.: The formation, properties and impact of secondary organic aerosol: current and emerging issues, Atmos. Chem. Phys., 9, 5155–5235, doi:10.5194/acp-9-5155-2009, 2009.

Hosny, N. A., Fitzgerald, C., Tong, C., Kalberer, M., Kuimova, M. K., and Pope, F. D.: Fluorescent lifetime imaging of atmospheric aerosols: a direct probe of aerosol viscosity, Faraday Discuss., 165, 343–356, 2013.

Iinuma, Y., Boge, O., Gnauk, T., and Herrmann, H.: Aerosol-chamber study of the alpha-pinene/O_3 reaction: influence of particle acidity on aerosol yields and products, Atmos. Environ., 38, 761–773, 2004.

Iinuma, Y., Muller, C., Berndt, T., Boge, O., Claeys, M., and Herrmann, H.: Evidence for the existence of organosulfates from beta-pinene ozonolysis in ambient secondary organic aerosol, Environ. Sci. Technol., 41, 6678-6683, 2007.

Jang, M. S., Czoschke, N. M., Lee, S., and Kamens, R. M.: Heterogeneous atmospheric aerosol production by acid-catalyzed particle-phase reactions, Science, 298, 814–817, 2002.

Jaoui, M., Corse, E., Kleindienst, T. E., Offenberg, J. H., Lewandowski, M., and Edney, E. O.: Analysis of secondary organic aerosol compounds from the photooxidation of *d*-limonene in the presence of NO_x and their detection in ambient PM2.5, Environ. Sci. Technol., 40, 3819–3828, 2006.

Jimenez, J. L., Canagaratna, M. R., Donahue, N. M., Prevot, A. S. H., Zhang, Q., Kroll, J. H., DeCarlo, P. F., Allan, J. D., Coe, H., Ng, N. L., Aiken, A. C., Docherty, K. S., Ulbrich, I. M., Grieshop, A. P., Robinson, A. L., Duplissy, J., Smith, J. D., Wilson, K. R., Lanz, V. A., Hueglin, C., Sun, Y. L., Tian, J., Laaksonen, A., Raatikainen, T., Rautiainen, J., Vaattovaara, P., Ehn, M., Kulmala, M., Tomlinson, J. M., Collins, D. R., Cubison, M. J., Dunlea, E. J., Huffman, J. A., Onasch, T. B., Alfarra, M. R., Williams, P. I., Bower, K., Kondo, Y., Schneider, J., Drewnick, F., Borrmann, S., Weimer, S., Demerjian, K., Salcedo, D., Cottrell, L., Griffin, R., Takami, A., Miyoshi, T., Hatakeyama, S., Shimono, A., Sun, J. Y., Zhang, Y. M., Dzepina, K., Kimmel, J. R., Sueper, D., Jayne, J. T., Herndon, S. C., Trimborn, A. M., Williams, L. R., Wood, E. C., Middlebrook, A. M., Kolb, C. E., Baltensperger, U., and Worsnop, D. R.: Evolution of organic aerosols in the atmosphere, Science, 326, 1525–1529, 2009.

Kahnt, A., Iinuma, Y., Blockhuys, F., Mutzel, A., Vermeylen, R., Kleindienst, T. E., Jaoui, M., Offenberg, J. H., Lewandowski, M., Böge, O., Herrmann, H., Maenhaut, W., and Claeys, M.: 2-Hydroxyterpenylic acid: An oxygenated marker compound for α-pinene secondary organic aerosol in ambient fine aerosol, Environ. Sci. Technol., 48, 4901–4908, 2014.

Kalberer, M., Sax, M., and Samburova, V.: Molecular size evolution of oligomers in organic aerosols collected in urban atmospheres and generated in a smog chamber, Environ. Sci. Technol., 40, 5917–5922, 2006.

Kampf, C. J., Waxman, E. M., Slowik, J. G., Dommen, J., Pfaffenberger, L., Praplan, A. P., Prevot, A. S. H., Baltensperger, U., Hoffmann, T., and Volkamer, R.: Effective Henry's Law Partitioning and the Salting Constant of Glyoxal in Aerosols Containing Sulfate, Environ. Sci. Technol., 47, 4236–4244, 2013.

Kolb, C. E., Cox, R. A., Abbatt, J. P. D., Ammann, M., Davis, E. J., Donaldson, D. J., Garrett, B. C., George, C., Griffiths, P. T., Hanson, D. R., Kulmala, M., McFiggans, G., Pöschl, U., Riipinen, I., Rossi, M. J., Rudich, Y., Wagner, P. E., Winkler, P. M., Worsnop, D. R., and O' Dowd, C. D.: An overview of current issues in the uptake of atmospheric trace gases by aerosols and clouds, Atmos. Chem. Phys., 10, 10561–10605, doi:10.5194/acp-10-10561-2010, 2010.

Koop, T., Bookhold, J., Shiraiwa, M., and Pöschl, U.: Glass transition and phase state of organic compounds: dependency on molecular properties and implications for secondary organic aerosols in the atmosphere, Phys. Chem. Chem. Phys., 13, 19238–19255, 2011.

Kristensen, K., Cui, T., Zhang, H., Gold, A., Glasius, M., and Surratt, J. D.: Dimer esters in α-pinene secondary organic aerosol: effect of hydroxyl radical, ozone, relative humidity and aerosol acidity, Atmos. Chem. Phys., 14, 4201–4218, doi:10.5194/acp-14-4201-2014, 2014.

Kroll, J. H. and Seinfeld, J. H.: Chemistry of secondary organic aerosol: Formation and evolution of low-volatility organics in the atmosphere, Atmos. Environ., 42, 3593–3624, 2008.

Kundu, S., Fisseha, R., Putman, A. L., Rahn, T. A., and Mazzoleni, L. R.: High molecular weight SOA formation during limonene ozonolysis: insights from ultrahigh-resolution FT-ICR mass spectrometry characterization, Atmos. Chem. Phys., 12, 5523–5536, doi:10.5194/acp-12-5523-2012, 2012.

Kuwata, M. and Martin, S. T.: Phase of atmospheric secondary organic material affects its reactivity, P. Natl. Acad. Sci. USA, 109, 17354–17359, 2012.

Laskin, A., Laskin, J., and Nizkorodov, S. A.: Mass spectrometric approaches for chemical characterisation of atmospheric aerosols: critical review of the most recent advances, Environ. Chem., 9, 163–189, 2012a.

Laskin, J., Eckert, P. A., Roach, P. J., Heath, B. S., Nizkorodov, S. A., and Laskin, A.: Chemical Analysis of Complex Organic Mixtures Using Reactive Nanospray Desorption Electrospray Ionization Mass Spectrometry, Anal. Chem., 84, 7179–7187, 2012b.

Liggio, J., Li, S. M., and McLaren, R.: Heterogeneous reactions of glyoxal on particulate matter: Identification of acetals and sulfate esters, Environ. Sci. Technol., 39, 1532–1541, 2005.

Lim, Y. B., Tan, Y., Perri, M. J., Seitzinger, S. P., and Turpin, B. J.: Aqueous chemistry and its role in secondary organic aerosol (SOA) formation, Atmos. Chem. Phys., 10, 10521–10539, doi:10.5194/acp-10-10521-2010, 2010.

Lin, Y.-H., Zhang, Z., Docherty, K. S., Zhang, H., Budisulistiorini, S. H., Rubitschun, C. L., Shaw, S. L., Knipping, E. M., Edgerton, E. S., Kleindienst, T. E., Gold, A., and Surratt, J. D.: Isoprene Epoxydiols as Precursors to Secondary Organic Aerosol

Formation: Acid-Catalyzed Reactive Uptake Studies with Authentic Compounds, Environ. Sci. Technol., 46, 250-258, 2012.

Lin, Y.-H., Zhang, H., Pye, H. O. T., Zhang, Z., Marth, W. J., Park, S., Arashiro, M., Cui, T., Budisulistiorini, S. H., Sexton, K. G., Vizuete, W., Xie, Y., Luecken, D. J., Piletic, I. R., Edney, E. O., Bartolotti, L. J., Gold, A., and Surratt, J. D.: Epoxide as a precursor to secondary organic aerosol formation from isoprene photooxidation in the presence of nitrogen oxides, P. Natl. Acad. Sci. USA, 110, 6718–6723, 2013.

Loza, C. L., Craven, J. S., Yee, L. D., Coggon, M. M., Schwantes, R. H., Shiraiwa, M., Zhang, X., Schilling, K. A., Ng, N. L., Canagaratna, M. R., Ziemann, P. J., Flagan, R. C., and Seinfeld, J. H.: Secondary organic aerosol yields of 12-carbon alkanes, Atmos. Chem. Phys., 14, 1423–1439, doi:10.5194/acp-14-1423-2014, 2014.

McNeill, V. F., Woo, J. L., Kim, D. D., Schwier, A. N., Wannell, N. J., Sumner, A. J., and Barakat, J. M.: Aqueous-phase secondary organic aerosol and organosulfate formation in atmospheric aerosols: A modeling study, Environ. Sci. Technol., 46, 8075–8081, 2012.

Murphy, B. N., Donahue, N. M., Robinson, A. L., and Pandis, S. N.: A naming convention for atmospheric organic aerosol, Atmos. Chem. Phys., 14, 5825–5839, doi:10.5194/acp-14-5825-2014, 2014.

Nguyen, T. B., Laskin, J., Laskin, A., and Nizkorodov, S. A.: Nitrogen-Containing Organic Compounds and Oligomers in Secondary Organic Aerosol Formed by Photooxidation of Isoprene, Environ. Sci. Technol., 45, 6908–6918, 2011.

Nguyen, T. B., Nizkorodov, S. A., Laskin, A., and Laskin, J.: An approach toward quantification of organic compounds in complex environmental samples using high-resolution electrospray ionization mass spectrometry, Anal. Methods, 5, 72–80, 2013.

Offenberg, J. H., Lewandowski, M., Edney, E. O., Kleindienst, T. E., and Jaoui, M.: Influence of Aerosol Acidity on the Formation of Secondary Organic Aerosol from Biogenic Precursor Hydrocarbons, Environ. Sci. Technol., 43, 7742–7747, 2009.

Pankow, J. F.: An absorption-model of the gas aerosol partitioning involved in the formation of secondary organic aerosol, Atmos. Environ., 28, 189–193, 1994.

Perraud, V., Bruns, E. A., Ezell, M. J., Johnson, S. N., Yu, Y., Alexander, M. L., Zelenyuk, A., Imre, D., Chang, W. L., Dabdub, D., Pankow, J. F., and Finlayson-Pitts, B. J.: Nonequilibrium atmospheric secondary organic aerosol formation and growth, P. Natl. Acad. Sci. USA, 109, 2836–2841, 2012.

Pfrang, C., Shiraiwa, M., and Pöschl, U.: Chemical ageing and transformation of diffusivity in semi-solid multi-component organic aerosol particles, Atmos. Chem. Phys., 11, 7343–7354, doi:10.5194/acp-11-7343-2011, 2011.

Pierce, J. R., Riipinen, I., Kulmala, M., Ehn, M., Petäjä, T., Junninen, H., Worsnop, D. R., and Donahue, N. M.: Quantification of the volatility of secondary organic compounds in ultrafine particles during nucleation events, Atmos. Chem. Phys., 11, 9019–9036, doi:10.5194/acp-11-9019-2011, 2011.

Pöschl, U., Rudich, Y., and Ammann, M.: Kinetic model framework for aerosol and cloud surface chemistry and gas-particle interactions – Part 1: General equations, parameters, and terminology, Atmos. Chem. Phys., 7, 5989–6023, doi:10.5194/acp-7-5989-2007, 2007.

Presto, A. A., Hartz, K. E. H., and Donahue, N. M.: Secondary organic aerosol production from terpene ozonolysis. 2. Effect of NO_x concentration, Environ. Sci. Technol., 39, 7046–7054, 2005.

Renbaum-Wolff, L., Grayson, J. W., Bateman, A. P., Kuwata, K., Sellier, M., Murray, B. J., Schilling, J. E., Martin, S. T., and Bertram, A. K.: Viscosity of α-pinene secondary organic material and implications for particle growth and reactivity, P. Natl. Acad. Sci. USA, 110, 8014–8019, 2013.

Riipinen, I., Pierce, J. R., Yli-Juuti, T., Nieminen, T., Hakkinen, S., Ehn, M., Junninen, H., Lehtipalo, K., Petaja, T., Slowik, J., Chang, R., Shantz, N. C., Abbatt, J., Leaitch, W. R., Kerminen, V. M., Worsnop, D. R., Pandis, S. N., Donahue, N. M., and Kulmala, M.: Organic condensation: a vital link connecting aerosol formation to cloud condensation nuclei (CCN) concentrations, Atmos. Chem. Phys., 11, 3865–3878, doi:10.5194/acp-11-3865-2011, 2011.

Sareen, N., Schwier, A. N., Shapiro, E. L., Mitroo, D., and McNeill, V. F.: Secondary organic material formed by methylglyoxal in aqueous aerosol mimics, Atmos. Chem. Phys., 10, 997–1016, doi:10.5194/acp-10-997-2010, 2010.

Schilling-Fahnestock, K. A., Yee, L. D., Loza, C. L., Coggon, M. M., Schwantes, R., Zhang, X., Dalleska, N. F., and Seinfeld, J. H.: Secondary Organic Aerosol Composition from C_{12} Alkanes, J. Phys. Chem. A, doi:10.1021/jp501779w, 2014.

Schobesberger, S., Junninen, H., Bianchi, F., Lonn, G., Ehn, M., Lehtipalo, K., Dommen, J., Ehrhart, S., Ortega, I. K., Franchin, A., Nieminen, T., Riccobono, F., Hutterli, M., Duplissy, J., Almeida, J., Amorim, A., Breitenlechner, M., Downard, A. J., Dunne, E. M., Flagan, R. C., Kajos, M., Keskinen, H., Kirkby, J., Kupc, A., Kuerten, A., Kurten, T., Laaksonen, A., Mathot, S., Onnela, A., Praplan, A. P., Rondo, L., Santos, F. D., Schallhart, S., Schnitzhofer, R., Sipila, M., Tome, A., Tsagkogeorgas, G., Vehkamaki, H., Wimmer, D., Baltensperger, U., Carslaw, K. S., Curtius, J., Hansel, A., Petaja, T., Kulmala, M., Donahue, N. M., and Worsnop, D. R.: Molecular understanding of atmospheric particle formation from sulfuric acid and large oxidized organic molecules, P. Natl. Acad. Sci. USA, 110, 17223–17228, 2013.

Shiraiwa, M., Ammann, M., Koop, T., and Pöschl, U.: Gas uptake and chemical aging of semisolid organic aerosol particles, P. Natl. Acad. Sci. USA, 108, 11003–11008, 2011.

Shiraiwa, M., Pfrang, C., Koop, T., and Pöschl, U.: Kinetic multilayer model of gas-particle interactions in aerosols and clouds (KM-GAP): linking condensation, evaporation and chemical reactions of organics, oxidants and water, Atmos. Chem. Phys., 12, 2777–2794, doi:10.5194/acp-12-2777-2012, 2012.

Shiraiwa, M. and Seinfeld, J. H.: Equilibration timescale of atmospheric secondary organic aerosol partitioning, Geophys. Res. Lett., 39, L24801, doi:10.1029/2012GL054008, 2012.

Shiraiwa, M., Yee, L. D., Schilling, K. A., Loza, C. L., Craven, J. S., Zuend, A., Ziemann, P. J., and Seinfeld, J. H.: Size distribution dynamics reveal particle-phase chemistry in organic aerosol formation, P. Natl. Acad. Sci. USA, 110, 11746–11750, 2013a.

Shiraiwa, M., Zuend, A., Bertram, A. K., and Seinfeld, J. H.: Gas-particle partitioning of atmospheric aerosols: interplay of physical state, non-ideal mixing and morphology, Phys. Chem. Chem. Phys., 15, 11441–11453, 2013b.

Surratt, J. D., Murphy, S. M., Kroll, J. H., Ng, N. L., Hildebrandt, L., Sorooshian, A., Szmigielski, R., Vermeylen, R., Maenhaut,

W., Claeys, M., Flagan, R. C., and Seinfeld, J. H.: Chemical composition of secondary organic aerosol formed from the photooxidation of isoprene, J. Phys. Chem. A, 110, 9665–9690, 2006.

Surratt, J. D., Gomez-Gonzalez, Y., Chan, A. W. H., Vermeylen, R., Shahgholi, M., Kleindienst, T. E., Edney, E. O., Offenberg, J. H., Lewandowski, M., Jaoui, M., Maenhaut, W., Claeys, M., Flagan, R. C., and Seinfeld, J. H.: Organosulfate formation in biogenic secondary organic aerosol, J. Phys. Chem. A, 112, 8345–8378, 2008.

Surratt, J. D., Chan, A. W. H., Eddingsaas, N. C., Chan, M. N., Loza, C. L., Kwan, A. J., Hersey, S. P., Flagan, R. C., Wennberg, P. O., and Seinfeld, J. H.: Reactive intermediates revealed in secondary organic aerosol formation from isoprene, P. Natl. Acad. Sci. USA, 107, 6640–6645, 2010.

Trump, E. R. and Donahue, N. M.: Oligomer formation within secondary organic aerosols: equilibrium and dynamic considerations, Atmos. Chem. Phys., 14, 3691–3701, doi:10.5194/acp-14-3691-2014, 2014.

Vaden, T. D., Imre, D., Beranek, J., Shrivastava, M., and Zelenyuk, A.: Evaporation kinetics and phase of laboratory and ambient secondary organic aerosol, P. Natl. Acad. Sci. USA, 108, 2190–2195, 2011.

Virtanen, A., Joutsensaari, J., Koop, T., Kannosto, J., YliPirilä, P., Leskinen, J., Mäkelä, J. M., Holopainen, J. K., Pöschl, U., Kulmala, M., Worsnop, D. R., and Laaksonen, A.: An amorphous solid state of biogenic secondary organic aerosol particles, Nature, 467, 824–827, 2010.

Vogel, A. L., Äijälä, M., Corrigan, A. L., Junninen, H., Ehn, M., Petäjä, T., Worsnop, D. R., Kulmala, M., Russell, L. M., Williams, J., and Hoffmann, T.: In situ submicron organic aerosol characterization at a boreal forest research station during HUMPPA-COPEC 2010 using soft and hard ionization mass spectrometry, Atmos. Chem. Phys., 13, 10933–10950, doi:10.5194/acp-13-10933-2013, 2013.

Williams, B. J., Goldstein, A. H., Kreisberg, N. M., and Hering, S. V.: In situ measurements of gas/particle-phase transitions for atmospheric semivolatile organic compounds, P. Natl. Acad. Sci. USA, 107, 6676–6681, 2010.

Worsnop, D. R., Morris, J. W., Shi, Q., Davidovits, P., and Kolb, C. E.: A chemical kinetic model for reactive transformations of aerosol particles, Geophys. Res. Lett., 29, 1–4, 2002.

Xu, L., Kollman, M. S., Song, C., Shilling, J. E., and Ng, N. L.: Effects of NOx on the Volatility of Secondary Organic Aerosol from Isoprene Photooxidation, Environ. Sci. Technol., 48, 2253–2262, 2014.

Yee, L. D., Craven, J. S., Loza, C. L., Schilling, K. A., Ng, N. L., Canagaratna, M. R., Ziemann, P. J., Flagan, R. C., and Seinfeld, J. H.: Secondary organic aerosol formation from low-NO_x photooxidation of dodecane: evolution of multigeneration gas-phase chemistry and aerosol composition, J. Phys. Chem. A, 116, 6211–6230, 2012.

Zaveri, R. A., Easter, R. C., Shilling, J. E., and Seinfeld, J. H.: Modeling kinetic partitioning of secondary organic aerosol and size distribution dynamics: representing effects of volatility, phase state, and particle-phase reaction, Atmos. Chem. Phys., 14, 5153–5181, doi:10.5194/acp-14-5153-2014, 2014.

Zhang, X., Pandis, S. N., and Seinfeld, J. H.: Diffusion-limited versus quasi-equilibrium aerosol growth, Aerosol Sci. Technol., 46, 874–885, 2012.

Zhao, R., Lee, A. K. Y., and Abbatt, J. P. D.: Investigation of Aqueous-Phase Photooxidation of Glyoxal and Methylglyoxal by Aerosol Chemical Ionization Mass Spectrometry: Observation of Hydroxyhydroperoxide Formation, J. Phys. Chem. A, 116, 6253–6263, 2012.

Zhou, S., Shiraiwa, M., McWhinney, R., Pöschl, U., and Abbatt, J. P. D.: Kinetic limitations in gas-particle reactions arising from slow diffusion in secondary organic aerosol, Faraday Discuss., 165, 391–406, 2013.

Ziemann, P. J. and Atkinson, R.: Kinetics, products, and mechanisms of secondary organic aerosol formation, Chem. Soc. Rev., 41, 6582–6605, 2012.

Zuend, A. and Seinfeld, J. H.: Modeling the gas-particle partitioning of secondary organic aerosol: the importance of liquid-liquid phase separation, Atmos. Chem. Phys., 12, 3857–3882, 2012, http://www.atmos-chem-phys.net/12/3857/2012/.

B.3. Berkemeier *et al.*, in preparation, 2016

Technical Note: Monte-Carlo genetic algorithm (MCGA) for model analysis of multiphase chemical kinetics using multiple experimental data sets

Thomas Berkemeier[1], Markus Ammann[2], Ulrich K. Krieger[3], Thomas Peter[3], Peter Spichtinger[4], Ulrich Pöschl[1], Manabu Shiraiwa[1] and Andrew J. Huisman[3,5]

[1]Max Planck Institute for Chemistry, Multiphase Chemistry Department, 55128 Mainz, Germany
[2]Paul Scherrer Institute, Laboratory of Environmental Chemistry, 5232 Villigen PSI, Switzerland
[3]ETH Zurich, Institute for Atmospheric and Climate Science, 8092 Zurich, Switzerland
[4]Johannes Gutenberg University Mainz, Institute for Atmospheric Physics, 55128, Mainz, Germany
[5]Union College, Department of Chemistry, 12308 Schenectady, NY, USA

Author contributions.

TB, MA, UKK, TP, PS, UP, MS and AJH designed research. TB, MA, MS and AJH developed the kinetic model. TB performed kinetic modelling. TB, MA, PS, UP, MS and AJH analysed simulation data. TB, UP, MS and AJH wrote the paper.

Technical Note: Monte-Carlo genetic algorithm (MCGA) for model analysis of multiphase chemical kinetics using multiple experimental data sets

Thomas Berkemeier[1,*], Markus Ammann[2], Ulrich K. Krieger[3], Thomas Peter[3], Peter Spichtinger, Ulrich Pöschl[1], Manabu Shiraiwa[1] and Andrew J. Huisman[5,*]

[1] Max Planck Institute for Chemistry, Multiphase Chemistry Department, 55128, Mainz, Germany

[2] Paul Scherrer Institute, Laboratory of Environmental Chemistry, 5232, Villigen, Switzerland

[3] ETH Zurich, Institute for Atmospheric and Climate Science, 8092, Zurich, Switzerland

[4] Johannes Gutenberg University, Institute for Atmospheric Physics, 55128, Mainz, Gernmany

[5] Union College, Department of Chemistry, 12308, Schenectady, NY USA

Corresponding Authors: T. Berkemeier (t.berkemeier@mpic.de) and A. J. Huisman (huismana@union.edu)

To be submitted to Atmospheric Chemistry and Physics

Introduction

Ideally, fitting a kinetic model to experimental data returns all physical parameters necessary to understand the importance of the processes at work and to predict the outcome of future experiments. Complex kinetic models often require a multitude of kinetic input parameters, some of which are not constrained well experimentally or are merely effective parameters combining a sequence of inherently coupled processes and hence not available from experiment. Finding a set of n input parameters that lead to a match of modeled and experimental data corresponds to optimization of an n-dimensional hyper surface in n+1 dimensional space. The additional dimension is the measure accounting for model-experiment correlation that serves as objective function in the optimization. In general, two main difficulties arise when optimizing complex kinetic models to experimental data:

Firstly, the optimization hyper surface is often non-convex i.e. it will not have only a single minimum due to interactions between non-orthogonal input parameters and scatter in the experimental data. Hence, steepest descent methods fail since they get trapped easily in local minima. Brute-force or exhaustive searches, where an n-dimensional grid is applied to the input parameter space and the fit quality evaluated for every grid point in all n dimensions, are often computationally not feasible.

Global optimization methods however provide means of approximating non-convex optimization problems without premature convergence to solutions coding local optima of the objective function. Examples for these methods are simulated annealing methods and evolutionary algorithms.

Secondly, if only little experimental data is used during the fitting process and input parameters are allowed to move in a large range, the optimization problem might be strongly underdetermined (ill-defined) and multiple solutions may exist. Although models may possess a multitude of kinetic input parameters, they are often driven by only a single or at most a few processes at a certain point in time.(Berkemeier et al., 2013) Thus, while additional datasets under similar conditions are useful, the most effective constraint in fitting parameters will occur when the experimental data sets are collected over a large array of time scales and under a large set of distinct experimental conditions (Berkemeier et al., 2013). In chemical kinetics, the behaviour of the system is characterized by the kinetic regime, which may change during the course of the reaction and with experimental conditions.(Berkemeier et al., 2013) Note that, only a parameter that affects modelling results significantly can be constrained during optimization. Hence, ideally, an exhaustive experimental data set leading to a unique set of kinetic parameters would cover all kinetic regimes possible for a certain reaction system. We therefore recommend using data sets obtained from a range of different experimental techniques to ensure this variability. The objective of every optimization is thus to fit a sufficiently large experimental data set so that only a single fitting parameter set is obtained. These parameters then would be regarded as correct within experimental errors and the approximations of the underlying model. Such a fit is a convenient way to assimilate data from multiple previous studies; data sets can be weighted to reflect confidence in their results, and the final range of accepted parameters then represents a consensus from the fitted data.

The computational feasibility of the optimization depends crucially on the size of the input parameter space, i.e. number and possible range of all parameters. Furthermore, using an unreasonably large range for input parameters increases the possibility of finding non-physical

solutions that fit the experimental data. The input parameter space can be reduced based on *a priori* knowledge. Parameters can be narrowed down in laboratory experiments (e.g. bulk experiments for derivation of trace gas solubility) or can be simply constrained by physics (e.g. diffusion limits of kinetic rate constants). It is thus advised to limit kinetic parameters to their respective upper or lower physical boundaries in optimization runs.

In this study, we present a method combining direct Monte-Carlo sampling of an optimization hyper surface with a genetic algorithm (MCGA method) as heuristic global optimization method that approximates the global optimum for parameter sets of kinetic models. Multiple execution of the search algorithm adds a statistical component and allows evaluating the uniqueness of the best fit obtained. The local environment of optimization results and parameter-parameter correlations are further explored using a simplex expansion method (SIMEX), which utilizes the principle of simplex optimization (Nelder-Mead algorithm, Nelder and Mead (1965)) to perform multi-dimensional variation of optimization results.

Methods

Monte-Carlo Genetic Algorithm (MCGA)

The MCGA algorithm utilizes a two-step approach to find minima on non-convex hyper surfaces. First, a Monte-Carlo (MC) sampling is performed in the large space of possible model input parameters to narrow down the possible solution to smaller areas of interest. Parameter sets are evaluated by the residual between the kinetic model results Y_{mod} and experimental data Y_{exp}. Eq. (1) is used typically as objective function for the optimization and calculates root mean squared deviances for every point in time t and for every experimental parameter set i. Depending on the input data a different objective function may be used, e.g. relative or logarithmic errors.

$$\boldsymbol{R = \sum_{i} \frac{1}{f_i} \sqrt{\frac{1}{j_i} \sum_{i=1}^{n} \left(Y_{\mathbf{mod}}(t_i) - Y_{\mathbf{exp}}(t_i) \right)^2}} \qquad (1)$$

Bias due to data set size is accounted for by weighting by the number of data points c_i in each data set. The weighting factor f_i can be used to assign priority to data sets or account for data quality, since high scatter in an experimental data set translates into higher R and would hence be weighted more strongly, which is often not desirable.

The parameter sets for the MC filtering are generated by random sampling from a distribution of the kinetic parameters. For each parameter, a distribution was obtained by logarithmically spacing in the respective fitting boundaries to account for the large ranges most input parameters can possibly adopt. Note that, depending on the problem, also linear spacing of parameters or different sampling strategies (e.g. Latin hypercube sampling) could be applied.

The genetic algorithm (GA) optimizes parameter sets in a *survival of the fittest* fashion by improving an initial *population* of parameter sets in iteration rounds called generations. Processes known from natural evolution such as survival, recombination, mutation and migration are mimicked to optimize a population consisting of parameter sets. The initial population is formed by the parameter sets with smallest residual R obtained in the Monte-Carlo step. An equal number of random parameter sets are added to ensure diversity within the pool of parameter sets and counteract sampling bias from shallow local minima (Fig. 1).

The few parameter sets with smallest residual R and thus highest correlation are directly transferred into the next generation as so-called *parents* by the *survival* mechanism. The remaining population is recombined to generate new combinations of parameters from the existing sets, forming the *children* of the next generation. To further ensure genetic variability, a mutation scheme alters parameters in a stochastic manner. Both mechanisms enable to overcome local minima, a crucial feature of a global optimization method. Iteration of these steps eventually results in a homogeneous, optimized population and the common parameter set is taken as result. Reseeding of random or pre-sampled data sets from the MC search can be used to maintain genetic variability inside the population. Similarly, *migration* between sub-populations that don't exchange genetic information can optionally be used to sustain genetic variability.

In this study we used the genetic algorithm provided by MathWorks® (Matlab® Global Optimization Toolbox) and created a routine for parallel computation on computer clusters. In a typical setting, the MC step and GA step of the optimization occupied an equal amount of computation time.

Simplex Expansion Method (SIMEX)

Parameter-parameter interactions are desirable evaluation criteria for any kinetic model, but actual covariance matrix or correlation coefficients are unfortunately not feasible in case of heavy global optimization e.g. due to a large number of optimization parameters or long calculation times of a single model evaluation. Hence, often it is therefore not possible to gather the necessary information by re-running the optimization and analyzing an ensemble of individual solutions with statistical techniques (e.g. as used in Arangio et al. (2015)).

An alternative method to investigate parameter-parameter correlations is the newly-developed simplex expansion method (SIMEX, after the simplex optimization method, Nelder and Mead 1965). A simplex is a geometric figure with $n+1$ vertices in n-dimensional space (a triangle on a plane, a tetrahedron in 3D space etc.). In SIMEX, $n+1$ base vectors with coordinates that represent small perturbations of the best fit of a given optimization are expanded in n-dimensional space by the following rules:

1) A random vertex is reflected through the centroid of the simplex.
2) If the objective function at the reflected vertex is below a certain threshold, the reflection is declined. If the objective function at the new vertex is below a certain threshold, an expansion is performed, i.e. the reflected point is moved further away from the centroid of the simplex. If the expansion is below a certain threshold, the step is accepted, otherwise, declined.
3) If the objective function at the reflected vertex is below a certain threshold, a contraction is performed, i.e. the original point is moved further towards the centroid of the simplex.

Following these steps, the simplex will expand until touching the boundaries of the local minimum. At the boundaries, the simplex will contract, allowing the move into confined sub-minima. By allowing some tolerance in the model-experiment-correlation (e.g. a 10 % increase in the objective function), it is possible to locally deflect/perturb the optimal solution on a multi-dimensional level (i.e. multiple parameters). This way, scatter plots of parameter pairs can be obtained and correlation coefficients calculated.

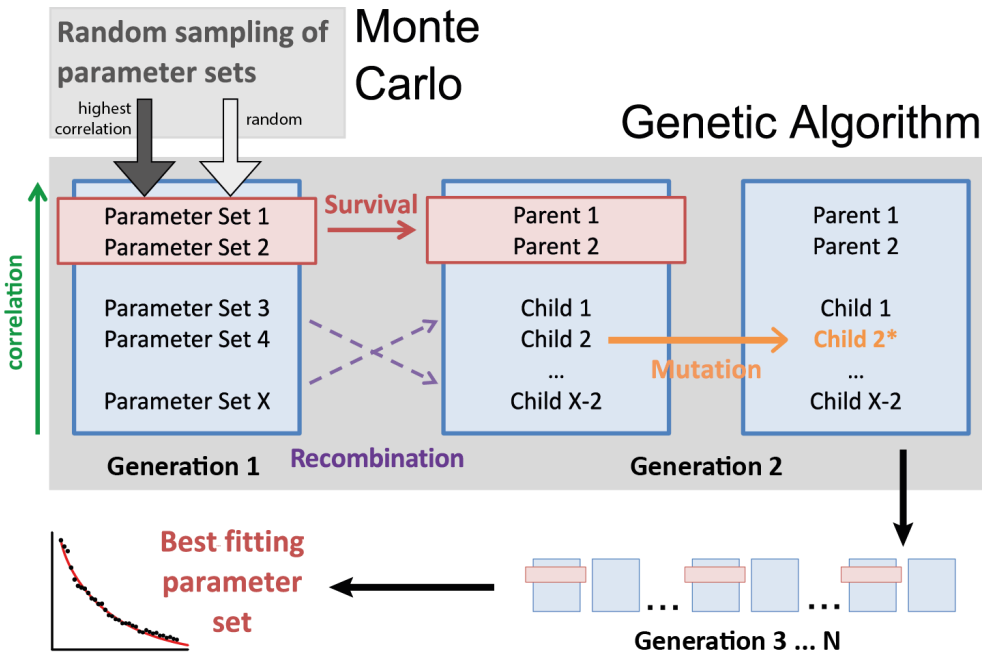

Figure 1. Schematic representation of the MCGA optimzation method consisting of a Monte-Carlo sampling, which feeds into a genetic algorithm. Through survival, recombination and mutation steps, ensembles of kinetic parameter sets (generations) are iteratively improved until a sufficient correlation to the experimental data is obtained.

References

Arangio, A. M., Slade, J. H., Berkemeier, T., Pöschl, U., Knopf, D. A., and Shiraiwa, M.: Multiphase Chemical Kinetics of OH Radical Uptake by Molecular Organic Markers of Biomass Burning Aerosols: Humidity and Temperature Dependence, Surface Reaction, and Bulk Diffusion, J. Phys. Chem. A, 119, 4533–4544, 10.1021/jp510489z, 2015.

Berkemeier, T., Huisman, A. J., Ammann, M., Shiraiwa, M., Koop, T., and Pöschl, U.: Kinetic regimes and limiting cases of gas uptake and heterogeneous reactions in atmospheric aerosols and clouds: a general classification scheme, Atmos. Chem. Phys., 13, 6663-6686, 10.5194/acp-13-6663-2013, 2013.

Nelder, J. A., and Mead, R.: A Simplex Method for Function Minimization, The Computer Journal, 7, 308-313, 10.1093/comjnl/7.4.308, 1965.

B.4. Berkemeier *et al.*, Atmos. Chem. Phys., 2014

Competition between water uptake and ice nucleation by glassy organic aerosol particles

Thomas Berkemeier[1,2], Manabu Shiraiwa[1], Ulrich Pöschl[1] and Thomas Koop[2]

[1]Max Planck Institute for Chemistry, Multiphase Chemistry Department, 55128 Mainz, Germany
[2]Bielefeld University, Faculty of Chemistry, 33615 Bielefeld, Germany

Atmospheric Chemistry and Physics **14**, 12513-12531, (2014).

Author contributions.

TB, MS, UP and TK designed research. TB, MS and TK developed the model. TB performed kinetic modelling. TB and TK analysed simulation data. TB, MS, UP and TK wrote the paper.

Atmos. Chem. Phys., 14, 12513–12531, 2014
www.atmos-chem-phys.net/14/12513/2014/
doi:10.5194/acp-14-12513-2014

Atmospheric Chemistry and Physics
Open Access

Competition between water uptake and ice nucleation by glassy organic aerosol particles

T. Berkemeier[1,2], **M. Shiraiwa**[1], **U. Pöschl**[1], **and T. Koop**[2]

[1]Multiphase Chemistry Department, Max Planck Institute for Chemistry, Mainz, Germany
[2]Faculty of Chemistry, Bielefeld University, Bielefeld, Germany

Correspondence to: T. Berkemeier (t.berkemeier@mpic.de) and T. Koop (thomas.koop@uni-bielefeld.de)

Received: 2 June 2014 – Published in Atmos. Chem. Phys. Discuss.: 20 June 2014
Revised: 9 October 2014 – Accepted: 24 October 2014 – Published: 27 November 2014

Abstract. Organic aerosol particles play a key role in climate by serving as nuclei for clouds and precipitation. Their sources and composition are highly variable, and their phase state ranges from liquid to solid under atmospheric conditions, affecting the pathway of activation to cloud droplets and ice crystals. Due to slow diffusion of water in the particle phase, organic particles may deviate in phase and morphology from their thermodynamic equilibrium state, hampering the prediction of their influence on cloud formation. We overcome this problem by combining a novel semi-empirical method for estimation of water diffusivity with a kinetic flux model that explicitly treats water diffusion. We estimate timescales for particle deliquescence as well as various ice nucleation pathways for a wide variety of organic substances, including secondary organic aerosol (SOA) from the oxidation of isoprene, α-pinene, naphthalene, and dodecane. The simulations show that, in typical atmospheric updrafts, glassy states and solid/liquid core-shell morphologies can persist for long enough that heterogeneous ice nucleation in the deposition and immersion mode can dominate over homogeneous ice nucleation. Such competition depends strongly on ambient temperature and relative humidity as well as humidification rate and particle size. Due to differences in glass transition temperature, hygroscopicity and atomic O / C ratio of the different SOA, naphthalene SOA particles have the highest potential to act as heterogeneous ice nuclei. Our findings demonstrate that kinetic limitations of water diffusion into organic aerosol particles are likely to be encountered under atmospheric conditions and can strongly affect ice nucleation pathways. For the incorporation of ice nucleation by organic aerosol particles into atmospheric models, our results demonstrate a demand for model formalisms that account for the effects of molecular diffusion and not only describe ice nucleation onsets as a function of temperature and relative humidity but also include updraft velocity, particle size and composition.

1 Introduction

Atmospheric aerosol particles influence climate through affecting the earth's radiation budget directly by scattering and absorbing light, and indirectly by acting as nuclei for cloud droplets and ice crystals (Yu et al., 2006; Andreae and Rosenfeld, 2008; IPCC, 2013). Ice nucleation is an important pathway for high-altitude cirrus cloud formation, and it occurs either homogeneously in liquid aerosol particles or heterogeneously in the presence of active ice nuclei (IN), which are solid particles that facilitate nucleation. Homogeneous ice nucleation generally requires high supersaturations in aqueous aerosol droplets, occurring at ice saturation ratios of $S_{\mathrm{ice}} \geq 1.4$ (Koop et al., 2000). Only a small fraction of atmospheric aerosol particles act as IN below this homogeneous ice nucleation threshold (DeMott et al., 2003; Cziczo et al., 2013). Heterogeneous ice nucleation can occur via several pathways such as deposition nucleation, i.e. deposition of gaseous water molecules to form crystalline ice on a solid IN, or immersion freezing, which describes nucleation induced by IN immersed in supercooled aqueous droplets (Pruppacher and Klett, 1997; Hoose and Möhler, 2012).

Organic aerosol particles are ubiquitous and abundant in the atmosphere, but traditionally they are not referred to as effective IN when compared to dust or biological particles (see Hoose and Möhler (2012) and references therein). More

recently, however, several laboratory studies have shown that glassy organic particles can act as IN at low-temperature cirrus conditions in the deposition mode or at slightly elevated temperatures in the immersion mode (Murray et al., 2010; Wagner et al., 2012; Wang et al., 2012; Wilson et al., 2012; Baustian et al., 2013; Schill et al., 2014), in agreement with inferences from field data (Froyd et al., 2010; Knopf et al., 2010, 2014). This IN ability has been observed for a number of different types of particles composed of pure organic substances such as simple sugars and acids (Murray et al., 2010; Wagner et al., 2012; Wilson et al., 2012; Baustian et al., 2013) and biomass burning marker compounds (Wagner et al., 2012; Wilson et al., 2012), for (phase-separated) organic–inorganic mixtures (Wagner et al., 2012; Wilson et al., 2012; Baustian et al., 2013; Schill and Tolbert, 2013), as well as for secondary organic aerosol (SOA) particles derived from aromatic volatile organic compounds (VOCs, Wang et al., 2012) or emerging from aqueous phase reactions (Schill et al., 2014). It has also been proposed recently that formation of highly porous structures upon atmospheric freeze-drying could enhance the IN ability of organic aerosol particles (Adler et al., 2013).

These observations suggest a connection between particle phase state and the resulting predominant ice nucleation pathway (Murray et al., 2010). Organic aerosol particles can adopt liquid, semisolid or solid states, or may even exhibit mixed phases, depending on composition and ambient conditions (Mikhailov et al., 2009; Koop et al., 2011; Vaden et al., 2011; Kuwata and Martin, 2012; Perraud et al., 2012; Song et al., 2012; You et al., 2012; Renbaum-Wolff et al., 2013; Kidd et al., 2014). SOA particles are expected to be liquid at high temperature and high humidity, but they are very likely to exhibit a highly viscous semisolid or even glassy state at low temperature and low humidity (Virtanen et al., 2010; Saukko et al., 2012; Renbaum-Wolff et al., 2013; Shiraiwa et al., 2013a). For example, typical α-pinene-derived secondary organic aerosol particles are expected to be in a glassy state below about 260 K at 30 % relative humidity, whereas at a higher humidity of 80 % such a glass transition is expected at approximately 215 K (Koop et al., 2011). Glassy states are characterized by viscosities greater than 10^{12} Pa s, corresponding to diffusion timescales within these particles that can exceed days or even years (Shiraiwa et al., 2011; Koop et al., 2011; Zhou et al., 2013). Water uptake into glassy aerosols has been shown to occur slowly and to proceed gradually with increasing relative humidity (Mikhailov et al., 2009; Tong et al., 2011; Zobrist et al., 2011; Bones et al., 2012; Price et al., 2014).

Hence, several competing processes can occur in glassy organic aerosol particles during updraft of an air parcel: heterogeneous ice nucleation in the deposition mode onto the glassy solid aerosol surface; diffusion of water into the particle, inducing a gradual phase transition towards the liquid state; and immersion freezing during the transition between both states. In order to determine those atmospheric conditions at which each of these processes dominates, we employ a numerical aerosol diffusion model based on the kinetic multi-layer model for gas–particle interactions in aerosols and clouds (KM-GAP), which explicitly treats mass transport of water molecules in the gas and particle phases (Shiraiwa et al., 2012). Due to experimental constraints associated with very long observation times, parameterizations for water diffusivity in glassy organic material are sparse and hence are only known for a few model compounds. Therefore, water diffusivity in SOA materials from various biogenic and anthropogenic precursors are deduced from water diffusivity parameterizations of model compounds using a semi-empirical physico-chemical model of water diffusion in glass-forming aqueous organics.

2 Modelling approach

2.1 Numerical diffusion model

The numerical diffusion model employed in this study is based on the kinetic multi-layer model for gas–particle interactions in aerosols and clouds, KM-GAP (Shiraiwa et al., 2012). KM-GAP consists of multiple model compartments and layers, respectively: gas phase, near-surface gas phase, sorption layer, surface layer, near-surface bulk, and a number of n bulk layers (cf. Fig. S1). The following processes are considered in KM-GAP: gas-phase diffusion, gas-surface transport, surface-bulk transport, and bulk diffusion. The bulk layers can either grow or shrink in response to mass transport. The initial bulk layer sizes are chosen to be small enough to ensure numerical convergence (usually 100–750 layers), but are not allowed to fall below the molecular length scale (~ 0.3 nm).

The model was complemented by modules predicting homogeneous ice nucleation as a function of water activity according to Koop et al. (2000), heterogeneous ice nucleation at a pre-defined ice supersaturation level, and it considers Kelvin effects. Moreover, a few further conceptual changes have been introduced to the original KM-GAP, including a more explicit treatment of gas diffusion, composition-based bulk diffusion and a mechanism of surface-to-bulk transport facilitated by surface-adsorbed water, as detailed in the following sections. Parameterizations of composition-dependent density, water activity and bulk diffusivity for the sucrose/water system have been adopted from Zobrist et al. (2011). A detailed description of the gas diffusion scheme and a list of all employed parameterizations are provided as supplementary material.

In this study, the model is used to simulate an atmospheric updraft situation by following a preselected trajectory in temperature and relative humidity. It tracks the chemical composition of an amorphous aerosol particle as a function of time and depth below the particle surface in discretized layers, providing concentration profiles of water and organics

at any given time. The equilibrium composition is calculated through a water activity parameterization that translates ambient relative humidity into equilibrium mass fractions of the bulk constituents. Mass fluxes from the far-surface into the near-surface gas phase, onto the particle surface, into as well as between bulk layers are coupled in flux-based differential equations, which are solved with an ordinary differential equation solver using Matlab software (ode23tb).

2.1.1 Ice nucleation modules

Besides water diffusion, the model is able to simulate ice nucleation and growth. However, the initial numerical solution of the differential equations only treats water uptake into the particle. The model registers an ice nucleation event when all necessary conditions in ambient relative humidity and water activity are satisfied. From this point onwards, the model simulates ice crystal growth by deposition of water molecules from the gas phase.

For homogeneous ice nucleation, a stochastic approach based on classical nucleation theory has been chosen. An ice nucleation event is triggered when the probability of the particle being liquid (P_{liq}) falls below 50 %. P_{liq} is the product of the individual probabilities in all n layers, using the homogeneous nucleation rate coefficient for each layer $J_{\mathrm{hom},k}$ as parameterized by Koop et al. (2000). The nucleation rate then translates into P_{liq} by multiplication with layer volume V_k and (numerical) integration with time step dt:

$$P_{\mathrm{liq,tot}}(t) = \int_{t_0}^{t} \prod_{k=1}^{n} \left(1 - J_{\mathrm{hom},k}(t) \cdot V_k(t)\right) \mathrm{d}t. \quad (1)$$

Heterogeneous nucleation is assumed to occur once a certain freezing threshold is exceeded. In this work, we distinguish between heterogeneous ice nucleation thresholds for sucrose and SOA, which have been shown to occur at different ice supersaturations, as summarized by Schill et al. (2014). For sucrose, we apply a linear fit to nucleation data from Baustian et al. (2013), whereas for SOA we fit the nucleation data of naphthalene SOA from Wang et al. (2012) and those of aqueous SOA (aqSOA) from Schill et al. (2014). The fit results are shown in Fig. A1 in Appendix A.

To distinguish between deposition and immersion freezing, additional criteria are employed. For deposition nucleation, the necessary condition is solidness of the outermost layer of the particle, requiring the water activity to be below the quasi-equilibrium glass transition point. In the case of immersion mode nucleation, a 1 nm thick region in the near-surface bulk is required to be entirely liquefied before nucleation can occur in the immersion mode. For this purpose, a 2 nm thick region below the particle surface is finely resolved by multiple bulk layers (cf. Fig. S1).

2.1.2 Bulk diffusion and bulk layer mixing

Bulk diffusion of water is treated as kinetic flux, $J_{\mathrm{b}k,\mathrm{b}k\pm1}$, from one bulk layer (b$k$) to the next (b$k \pm 1$). Because layer thickness is not allowed to fall below the molecular resolution, concentrations in adjacent layers can differ significantly. As in Zobrist et al. (2011), this heterogeneity is accounted for with a virtual mixing scheme for the determination of bulk diffusivities between layers. In this scheme, the composition of a mixture of two subsequent bulk layers is determined and the bulk diffusion coefficient calculated according to the effective composition along the diffusion path. Scenarios with very low diffusivities and hence steep concentration gradients thus lead to situations in which a liquefied layer (high bulk diffusivity of water, $D_{\mathrm{H_2O}}$) "softens" the subsequent glassy layer (low $D_{\mathrm{H_2O}}$), facilitating further diffusion. Such a process can be seen as analogous to a dissolution process, in which the glassy matrix dissolves into nearby water-rich regions.

Diffusion of the organic matrix has been neglected for this study, because the organic molecules investigated here can be expected to diffuse much more slowly than water molecules. Also, in the glassy state, the organic molecules diffuse on a much longer timescale compared to the experimental timescale of minutes to hours (cf. Shiraiwa et al., 2011; Koop et al., 2011).

2.1.3 Surface monolayers and surface softening

The original KM-GAP uses a double monolayer approach to describe the particle surface, comprising a sorption layer and a quasi-static surface layer. In this study the quasi-static surface layer was replaced by a near-surface volume layer similar to that used in Shiraiwa et al. (2013a), which is more suitable for low diffusivity systems.

Surface-adsorbed water can lead to softening of the solid surface (Koop et al., 2011), thereby facilitating exchange between surface and first near-surface bulk layer. In the model, this is accounted for by introducing a surface softening scheme that estimates the surface-to-bulk transport rate by mixing a hypothetical water monolayer with a hypothetical bulk monolayer containing water and bulk material. Using the momentary molar fractions of water ($x_{\mathrm{b1,H_2O}}$) and organics ($x_{\mathrm{b1,org}}$) of the near-surface bulk layer, the effective surface coverages of water ($\theta_{\mathrm{ss,H_2O}}$) and organics ($\theta_{\mathrm{ss,org}}$) at the surface bulk layer can be described as

$$\theta_{\mathrm{ss},i} = \frac{x_{\mathrm{b1},i} \cdot \sigma_i}{x_{\mathrm{b1,org}} \cdot \sigma_{\mathrm{org}} + x_{\mathrm{b1,H_2O}} \cdot \sigma_{\mathrm{H_2O}}}, \quad (2)$$

where σ_i is the molecular cross section of species i (i.e. water (H_2O) or organics (org)). The weight fraction of organics in the "softened" surface is then given by

$$w_{\mathrm{ss,org,mix}} = \frac{\frac{\theta_{\mathrm{ss,org}}}{\sigma_{\mathrm{org}}} \cdot M_{\mathrm{org}}}{\frac{\theta_{\mathrm{ss,org}}}{\sigma_{\mathrm{org}}} \cdot M_{\mathrm{org}} + \left(\frac{\theta_{\mathrm{ss,H_2O}}+1}{\sigma_{\mathrm{H_2O}}}\right) \cdot M_{\mathrm{H_2O}}}, \quad (3)$$

where M_{org} and $M_{\mathrm{H_2O}}$ are the molar mass of organics and water. This process facilitates the initial water uptake into a glassy particle and leads (in most cases) to a sub-surface layer that is in equilibrium with the surrounding gas phase. In the temperature range relevant for immersion freezing, liquefaction of the surface was always obtained at the quasi-equilibrium glass transition point due to the surface softening mechanism. At lower temperatures however (deposition regime), the particle surface was not always in quasi-equilibrium with ambient humidity.

2.2 Estimation of water diffusivity in SOA

For model systems other than sucrose/water, no direct parameterization of water diffusivity in the full atmospherically relevant temperature and composition range is available to date. For compounds chemically similar to sucrose (i.e. organic polyols and acids), we present a scheme that enables estimation of bulk diffusivity data from glass transition and hygroscopicity data. Bulk diffusivity of water is parameterized using a Vogel–Fulcher–Tammann (VFT) approach (Vogel, 1921; Fulcher, 1925; Tammann and Hesse, 1926). The estimation scheme utilizes the structure of the VFT equation, Eq. (S9), and the physical interpretation of its parameters. The method can be described by the following set of assumptions.

1. Two similar organic substances act similarly in the way they approach the glass transition and thus have a similar fragility: $B_{\mathrm{org1}} \approx B_{\mathrm{org2}}$.

2. The same two substances have a similar diffusion coefficient in the high temperature limit: $A_{\mathrm{org1}} \approx A_{\mathrm{org2}}$.

3. A difference in glass transition temperatures ($T_{g,\mathrm{org}}$) between the two substances indicates a difference in Vogel temperatures ($T_{0,\mathrm{org}}$) of the same direction and (relative) magnitude:

$$\frac{T_{0,\mathrm{org1}}}{T_{0,\mathrm{org2}}} \approx \frac{T_{\mathrm{g,org1}}}{T_{\mathrm{g,org2}}}. \quad (4)$$

Thus, diffusivities within an organic substance can be estimated by knowledge of its glass transition curve relative to a known standard with similar chemical functionality. This approach requires knowledge of three parameters for inferring water diffusivity over the full temperature and composition range: the hygroscopicity coefficient, κ_{org}, the glass transition temperature of the pure organic, $T_{\mathrm{g,org}}$, and the Gordon–Taylor coefficient (k_{GT}) of the aqueous organic mixture. For justification, more information on this procedure and a description of how the required input parameters were obtained, see Appendix A. For validation of the estimation scheme, we provide applications to literature ice nucleation experiments in Appendix B.

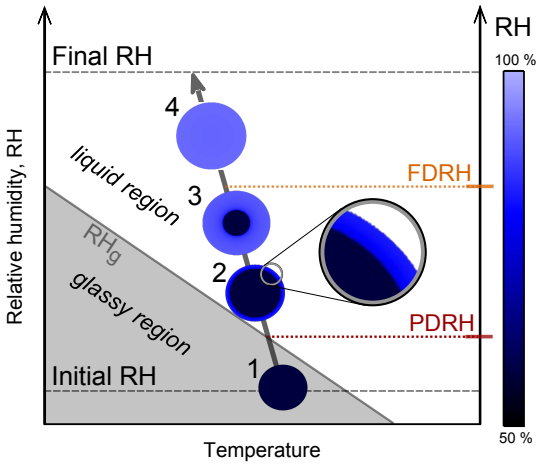

Figure 1. Schematic temporal evolution of particle morphology along a trajectory of an atmospheric updraft (grey arrow). Humidification of ambient air upon adiabatic expansion leads to liquefaction of initially glassy particles (dark blue colour, 1) via core-shell morphologies (2, 3) to liquid particles (light blue colour, 4). Whereas partial deliquescence (PDRH) coincides with RH_g, full deliquescence (FDRH) is delayed to much higher RH, indicating that diffusion processes occur on much longer timescales than humidification. The speed at which particles are humidified along the displayed trajectory corresponds to that typical of cloud chamber or environmental cell experiments (0.1–1.5 K min^{-1}, 1–15 % RH min^{-1}).

3 Results and discussion

3.1 Particle morphology

We investigate ice nucleation in glassy organic aerosols induced by changing ambient conditions during the updraft of an air parcel. In updraft events, adiabatic cooling leads to a decrease in temperature and a corresponding increase of relative humidity (RH). Humidification of air leads to water uptake into the particle phase, causing a humidity-induced phase transition that for glassy aerosol particles has been termed *amorphous deliquescence* (Mikhailov et al., 2009). This process is often kinetically limited by diffusion of water in the particle phase (Zobrist et al., 2011), so that a particle can be out of equilibrium when the timescale of humidification is shorter than that of diffusion.

Amorphous deliquescence is a self-accelerating process since water acts as a plasticizer in the organic matrix (Mikhailov et al., 2009; Zobrist et al., 2011): water molecules taken up by the particle reduce the particle's viscosity and, hence, increase bulk diffusivity locally, thus accelerating the uptake of further molecules. The microphysical consequences of this mechanism are illustrated in Fig. 1, which shows the temporal evolution of particle morphology of a glassy organic aerosol particle exposed to a gradual increase in relative humidity (simulated atmospheric updraft, see also Movie S1). The quasi-equilibrium glass transition of the aqueous organic, RH_g, is shown in grey. With "quasi-equilibrium glass transition", we denote the conditions under which a binary organic–water system would undergo amorphous deliquescence when humidification occurs sufficiently slowly so that equilibrium between ambient RH and water activity is always maintained. Humidification may be fast enough to cause a difference in phase state from equilibrium: water activity, colour-coded from dark blue (low water activity) to light blue (high water activity), trails behind ambient RH due to kinetic limitations in water diffusivity (Koop et al., 2011). Note that when using a constant D_{H_2O}, diffusion gradients appear less pronounced (cf. Fig. S2 and Movie S2). Hence, self-accelerating water diffusion leads to a sharpening of the diffusion gradient that can be close to the molecular length scale (Zobrist et al., 2011).

Several morphological stages can be distinguished during the humidification process in Fig. 1. Starting from a homogeneous, glassy particle (1), an increase in RH first leads to liquefaction of a thin outer layer and emergence of a core-shell morphology (2). This liquid outer layer grows in equilibrium with ambient relative humidity and also extends towards the particle centre by diffusion of water into the glassy organic matrix (3), leading to shrinkage of the residual glassy core until the particle is fully deliquesced (4). Thus, during the continuous amorphous deliquescence process two characteristic instants can be distinguished, each occurring at a different humidity: we define the *partial deliquescence relative humidity* (PDRH) as the point where a thin aqueous outer shell of the particle is homogeneously mixed and the shell's water activity is larger than that of the quasi-equilibrium glass transition. In this study we set the thickness of this surface shell to 1 nm, corresponding to about five monolayers of water. We define the *full deliquescence relative humidity* (FDRH) as the point where the entire particle's water activity corresponds to that of a liquid (i.e. it is larger than that of the quasi-equilibrium glass transition) and the water activity gradient from the surface to the particle core is less than 5 %. Note that, in the case of a sufficiently slow updraft, both PDRH and FDRH would occur at RH_g. In fact, the KM-GAP simulations suggest that, with updraft velocities typical of atmospheric conditions (e.g. 0.01–10 m s^{-1}), PDRH often coincides with RH_g. In contrast, FDRH often extends far into the liquid region of the phase diagram, indicating the importance of kinetic limitations and implying that particles can contain glassy cores even at relative humidities above RH_g due to slow water diffusion.

3.2 Ice nucleation regimes

Next, we investigate by kinetic model simulations the competition between amorphous deliquescence and ice nucleation during an atmospheric updraft. For our initial calculations we use sucrose as a proxy for organic aerosols since detailed physico-chemical parameterizations for water diffusivity, the RH-dependent equilibrium composition as well as glass transition data are available (Zobrist et al., 2011). The heterogeneous ice nucleation onset (RH_{het}) for sucrose was obtained from ice nucleation experiments by Baustian et al. (2013) and is shown as brown dashed lines in Fig. 2. Here we use the ice saturation ratio S_{ice} as an indicator of humidity because it scales with RH according to $S_{ice} = p_{liq,0}(T)/p_{ice}(T) \cdot RH$, but is also a more direct indicator of the supersaturation of ice. $p_{liq,0}$ and p_{ice} indicate here the vapour pressures over pure supercooled water and over ice, respectively.

Figure 2a shows results obtained with KM-GAP simulating the updraft of 100 nm sucrose particles for a wide range of temperatures. Each simulated trajectory started at ice saturation ($S_{ice} = 1$), as is often the case for cloud chamber or environmental cell experiments (Murray et al., 2010; Wang et al., 2012). Temperature was decreased so that the resulting humidification rate was constant at 1 % RH min^{-1}, corresponding to an atmospheric updraft of about 0.2 m s^{-1}, typical of atmospheric gravity waves (Jensen et al., 2005). As expected the FDRH of sucrose particles, indicated by the red solid line, occurs significantly above RH_g at all temperatures. The intersection of RH_{het} with RH_g defines the upper temperature limit for deposition nucleation. Below this temperature, a sucrose particle is a glassy solid when RH_{het} is reached, and hence deposition ice nucleation may occur. Above this temperature, the particle is partially deliquesced when approaching RH_{het} and the glassy core of the particle may act as an IN for immersion freezing. The upper limit of the immersion freezing regime is given by the intersection of RH_{het} with the FDRH line. Above this temperature, particles are already fully deliquesced once RH_{het} is reached. Hence, these particles do not nucleate ice heterogeneously and freeze only at the homogeneous ice nucleation limit (green dashed line; Koop et al., 2000). Finally at $\sim$ 232 K, the homogeneous ice nucleation limit coincides with water saturation (solid black line), and above this temperature the aerosol particles activate into cloud droplets consisting of supercooled water, thus representing the upper limit of the homogeneous ice nucleation regime.

The delay between the nominal quasi-equilibrium glass transition RH_g and the actual full deliquescence at FDRH is governed by the competition between the humidification rate (synonymous to updraft velocity) and timescale for water diffusion within the particle bulk. FDRH will shift towards

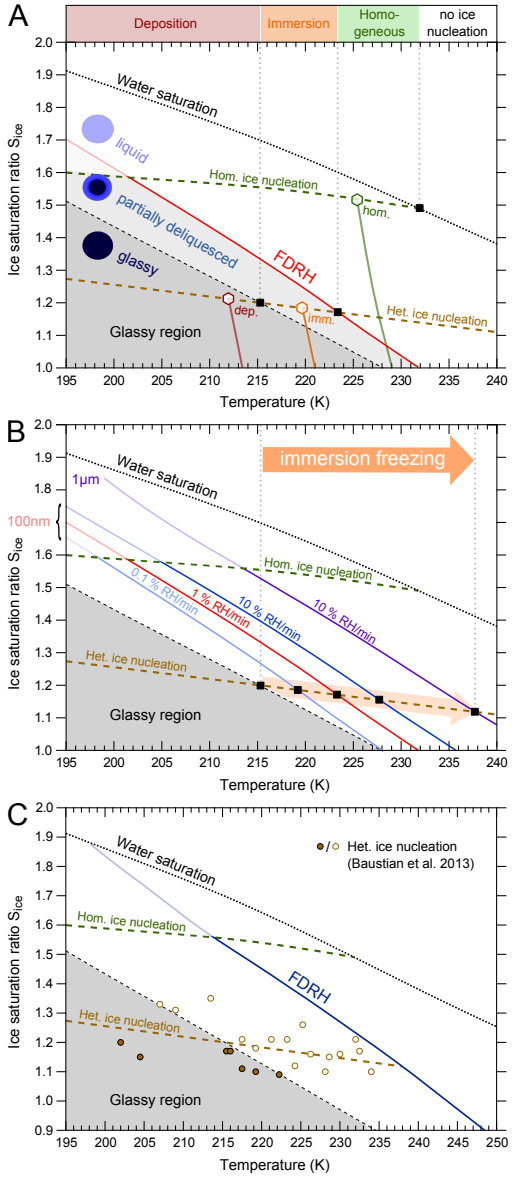

Figure 2. (a) Simulated regimes of heterogeneous and homogeneous ice nucleation in the humidification of sucrose particles. The red solid line indicates full deliquescence relative humidities (FDRH) for 100 nm particles exposed to a humidification rate of 1 % RH min^{-1} ($\approx 0.2\,\mathrm{m\,s}^{-1}$ atmospheric updraft). Example trajectories start at ice saturation, follow a constant dew point line and end at expected ice nucleation (hexagonal markers) with deposition (red), immersion (orange), and homogeneous (green) freezing. **(b)** Effects of different particles sizes and humidification rates on FDRH. The upper boundary for immersion freezing is extended to high temperatures for large particle radii and high humidification rates and is expected to occur up to 238 K for the most extreme scenario (1 µm, 10 % RH min^{-1}, purple solid line). **(c)** Application to the experimental conditions in Baustian et al. (2013), i.e. 4 µm particles humidified at a rate of 1 % RH min^{-1}, leads to FDRH that is able to explain all observed experimental ice onsets (brown circles). The thermodynamic glass transition divides the experimental data in events of deposition ice nucleation (closed circles) and immersion freezing (open circles).

higher relative humidities when higher humidification rates are employed, as shown in Fig. 2b. For example, increasing the rate of humidification to 10 % RH min^{-1}, a value corresponding to an updraft velocity of about $2\,\mathrm{m\,s}^{-1}$ and commonly reached in convective updrafts (Jensen et al., 2005), shifts the FDRH line upwards (solid dark blue line) and thus its intersection with the $\mathrm{RH_{het}}$ line towards higher temperatures. Accordingly, decreasing the updraft velocity to $0.02\,\mathrm{m\,s}^{-1}$, a value found in large-scale, synoptic updrafts (Jensen et al., 2005), leads to an FDRH (solid light blue line) much closer to the quasi-equilibrium glass transition $\mathrm{RH_g}$. Moreover, an increase in particle size delays the deliquescence process (indicated by the solid purple line), since it increases the timescale of diffusion. The range of the immersion freezing regime thus strongly depends on ambient conditions and is extended towards higher temperatures in fast updrafts and for large particles.

Laboratory ice nucleation measurements with sucrose particles (Baustian et al., 2013) are used to validate our model calculations of ice nucleation regimes in Fig. 2c. Baustian et al. (2013) used optical microscopy in conjunction with a cold stage to detect ice nucleation on glassy sucrose particles (4 µm diameter) during humidification (1 % RH min^{-1}), leading to the nucleation onsets shown in Fig. 2c (brown markers). A range of simulations mimicking the experimental conditions at different starting temperatures leads to a continuous FDRH curve (solid blue line) over the entire temperature range. For details on the calculations see Appendix B. The modelled FDRH curve correctly confines the region below which heterogeneous ice nucleation is observed in the experiments. Based on our calculations, the experimental data points below $\mathrm{RH_g}$ (full brown circles) can be assigned to the deposition nucleation regime, whereas points between $\mathrm{RH_g}$ and FDRH (open brown circles) can be assigned to immersion freezing. Additional analyses for validation have been performed for other types of organic particles (Appendix B, Figs. B1 and B2).

3.3 Biogenic and anthropogenic SOA

In order to apply our kinetic model to ice nucleation in SOA, estimates of $D_{\mathrm{H_2O}}$ in SOA material have been inferred. Four major SOA precursors were chosen to represent biogenic and anthropogenic origin, respectively: α-pinene and isoprene, as well as naphthalene and dodecane. Each of these SOA is represented by a choice of marker compounds taken from the literature (cf. Table S1). Water diffusivities are estimated using the scheme described in Sect. 2.2. The heterogeneous ice nucleation onset ($\mathrm{RH_{het}}$, brown dashed line) for SOA was obtained from laboratory measurements by Wang et al. (2012) and Schill et al. (2014) as derived in Fig. A1. Hygroscopicities of the various SOA were taken from Lambe et al. (2011), who suggested that κ_{org} can be parameterized independently of SOA type as function of O / C ratio. In all simulations,

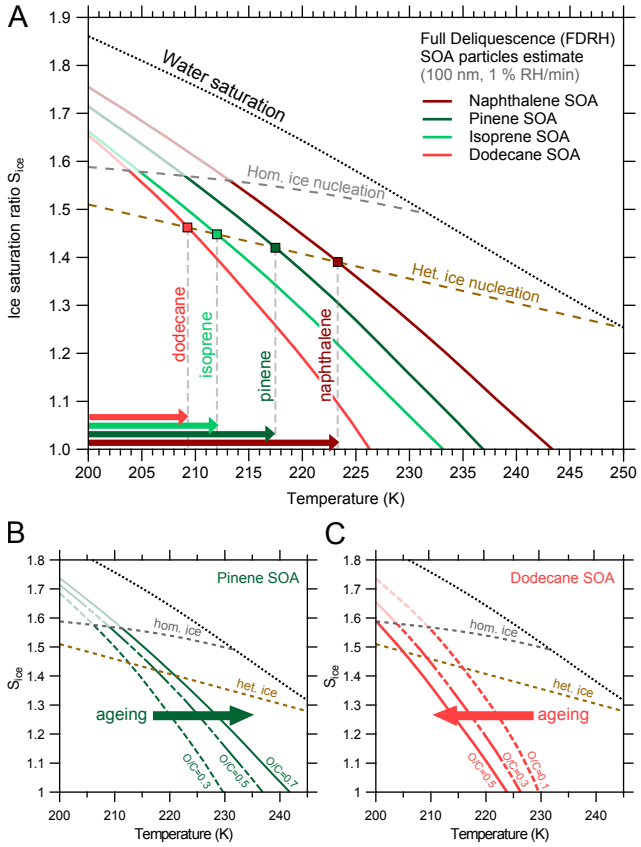

Figure 3. (a) Simulated humidification of SOA particles from the four different precursors α-pinene, isoprene, dodecane and naphthalene. Naphthalene SOA (dark red) shows the latest deliquescence, whereas dodecane SOA (light red) liquefied rather early in the simulations. The two biogenic SOA estimates lie between both extremes with pinene SOA (dark green) showing slightly later deliquescence than isoprene SOA. Intercepts (square markers) with a heterogeneous nucleation onset typical of SOA (brown dashed line) indicate upper temperature limits for immersion freezing (arrows on x axis). The effect of particle ageing also depends on precursor type: pinene SOA **(b)** shows hardening upon increase in O / C (indicated by higher FDRH), whereas dodecane SOA **(c)** exhibits softening (indicated by lower FDRH). Similarly, isoprene and naphthalene SOA show only moderate hardening and softening, respectively (Fig. S5).

particles of 100 nm diameter were humidified at a rate of 1 % RH min^{-1}.

Figure 3a shows the simulation results of FDRH for all four precursor types. Naphthalene SOA is observed to fully deliquesce last due to the high estimated glass transition temperature and low hygroscopicity (cf. Table A1), followed by α-pinene and isoprene. Dodecane SOA showed the earliest deliquescence, reflecting the low glass transition temperature of pure dodecane SOA of $\sim$ 210 K. By comparison of FDRH with measured $\mathrm{RH_{het}}$ on SOA, compound-specific upper temperature limits for heterogeneous ice nucleation on SOA particles can be determined (arrows on x axis, values are given in Table S2). Uncertainty estimates for FDRH and $\mathrm{RH_g}$ of all four precursors classes are given in Fig. S4.

For the calculations in Fig. 3a, we chose an average oxidation state typically observed for SOA from the respective precursor. The atomic oxygen to carbon ratio (O / C) increases upon chemical ageing, thereby affecting hygroscopicity (Lambe et al., 2011) and glass transition temperature (Fig. A2). The resulting effects of chemical ageing on modelled FDRH are shown for α-pinene and dodecane SOA as examples in Fig. 3b and c, respectively. For α-pinene SOA (Fig. 3b), a higher O / C results in hardening of the organic material with ageing, leading to an FDRH increase, whereas for dodecane SOA (Fig. 3c) a higher O / C results in softening, thus leading to earlier deliquescence and an FDRH decrease.

The observed effects can be explained by the competition between a simultaneous increase of hygroscopicity with O / C and an increasing glass transition temperature of the pure organic matrix due to stronger molecular interactions in the highly oxidized organic material. A higher glass transition value enhances the rigidness of the pure organic matrix, whereas a higher hygroscopicity enhances the amount of water taken up by the aqueous organic mixture at a given humidity and thus its plasticizing effect.

Figure 4 illustrates this competition by displaying estimated characteristic timescales of water diffusion in 100 nm diameter SOA particles at 220 K as a function of hygroscopicity (κ_{org}) and glass transition temperature of the pure organic matrix ($T_{\mathrm{g,org}}$). Dotted contour lines show characteristic mass transport times associated with the diffusion coefficient $D_{\mathrm{H_2O}}$ (Shiraiwa et al., 2011). Coloured oval shapes indicate estimated ranges of κ_{org} and $T_{\mathrm{g,org}}$ for the four SOA precursor classes, for three different oxidation states each (cf. Table A1). The arrows pointing from the lowest to the highest oxidation state reveal that both κ_{org} and $T_{\mathrm{g,org}}$ increase with O / C. The slope of these arrows when compared to the slope of the contour lines indicates whether a compound undergoes hardening (steeper slope of arrow) or softening (shallower slope of arrow) during the ageing process. Apparently, both biogenic SOA types undergo hardening upon ageing, whereas the two anthropogenic SOA types undergo softening, with the strongest effects for pinene and dodecane SOA.

The area between 1 s and 1 h represents the timescale of atmospheric updraft processes. For SOA in this range, diffusion processes occur on the same timescales as typical air parcel updrafts, and the predominant cloud formation process depends strongly on atmospheric conditions. All four SOA types fall within or beneath this range, indicating the importance of the actual updraft velocity for ice nucleation on glassy aerosol particles. But it is also obvious that SOA particles from naphthalene are most likely to be subject to kinetic effects and may thus preferably act as IN.

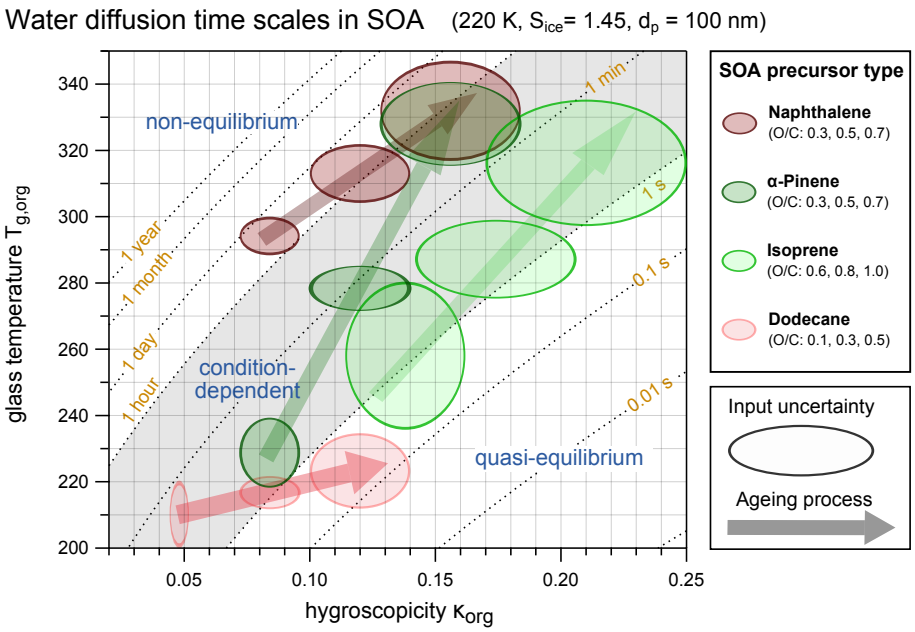

Figure 4. Characteristic timescales of water diffusion in SOA as a function of hygroscopicity, κ_{org}, and glass transition temperatures of the pure organic matrix, $T_{g,org}$. Calculations have been performed at 220 K, $S_{ice} = 1.45$ and for 100 nm particles. Oval shapes confine estimated ranges in κ_{org} and $T_{g,org}$ for the four SOA types in three different oxidation states (Appendix A and Table A1). The grey area indicates the timescale of typical atmospheric updrafts (1 s to 1 h) and thus divides the plot into areas of quasi-equilibrium and non-equilibrium water diffusion. Within the grey area, the relative speed of both processes depends upon the actual atmospheric conditions. The ageing process is indicated by arrows pointing from regions of low O / C to regions of high O / C.

3.4 Model uncertainties

The model results presented in this study are subject to various types of uncertainty. Among these are uncertainties arising from model assumptions such as the validity of first-order Fickian diffusion and the applied schemes for bulk mixing and surface softening (Sects. 2.1.2 and 2.1.3). At present there is a lack of fundamental chemical and physical knowledge for describing these processes in aqueous binary or multicomponent systems. We note, however, that the approach taken here is in agreement with the sparse data on water diffusivities in aqueous organic systems (Zobrist et al., 2011; Shiraiwa et al., 2013b; Lienhard et al., 2014; Price et al., 2014). Model results obtained for aqueous sucrose (Fig. 2) are expected to be reliable because the thermodynamic and kinetic parameters of this benchmark system are well studied and agree within the literature (e.g. Zobrist et al., 2011; Price et al., 2014); on the other hand, model results obtained for SOA (Fig. 3) are subject to larger uncertainties as detailed in the following.

The model neglects liquid–liquid phase separation in the aqueous organic phase (You et al., 2014) by assuming that all SOA components are miscible with water over the entire concentration and temperature range. We note that, for SOA types that typically show only low O / C ratios (e.g. SOA from long-chain aliphatic precursors such as dodecane), insoluble fractions may become important for ice nucleation (see discussion in Sect. B2).

Volatilization of organic material has not been included in the calculations presented above since vapour pressures of typical SOA marker compounds are low under the low temperature conditions employed in this study (Huisman et al., 2013; O'Meara et al., 2014).

Self-diffusion of SOA material has been neglected as diffusion timescales of large organic molecules exceed those of small guest molecules in the SOA matrix by orders of magnitudes (Koop et al., 2011; Shiraiwa et al., 2011).

Minor model uncertainty comes from parameters determining the volume concentration of organic molecules at a given organic mass fraction, i.e. average molar mass M_{org} of the organics and density of the aqueous organic mixture (cf. Table S3). Variation by 100 g mol^{-1} in M_{org} showed no effect on model results; varying ρ_{org} by 0.1 g cm^{-3} showed only a slight influence on aerosol deliquescence humidity on the order of 1 % RH.

The arguably largest source of uncertainty is insufficient knowledge of the thermodynamic input parameters required for the diffusivity estimation scheme (κ_{org}, $T_{g,org}$, k_{GT}, cf. Appendix A). In addition to the general assumptions made in that scheme and the uncertainties in the sucrose parameterization used within the diffusivity estimation scheme, uncertainties in input parameters propagate into an uncertainty in D_{H_2O}, which we assess in Figs. S4 and S6. Figure S4

shows the uncertainty for each specific SOA precursor and a particular O / C ratio by propagating the maximum deviation estimates in κ_{org} and $T_{g,org}$ given in Table A1. Figure S6 shows the full uncertainty towards single model input parameters irrespective of precursor or oxidation state. Among these, κ_{org} seems to be the largest source of uncertainty as the model results are sensitive towards κ_{org} and its numerical value is subject to a rather large variability for atmospherically relevant organic substances (Koop et al., 2011; Lambe et al., 2011; Rickards et al., 2013). Due to a lack of consistent experimental data, a constant κ_{org} is used in this study to parameterize hygroscopicity over the entire concentration and temperature range.

Laboratory experiments that directly probe diffusivity within SOA at room temperature and also at low temperature are highly desirable, as have been done for sucrose and a few other single-compound proxies (Tong et al., 2011; Zobrist et al., 2011; Bones et al., 2012; Lienhard et al., 2014; Price et al., 2014). Moreover, experiment-based water activity parameterizations over a large temperature range are needed, because at least some water-soluble organic oligomers/polymers show a strong temperature dependence of water activity for aqueous mixtures of constant composition (Zobrist et al., 2003). Such improvements would reduce the model uncertainty in future modelling studies substantially.

Another type of uncertainty arises from uncertainty in heterogeneous ice nucleation onsets. To date, little is known about the exact microphysical mechanism by which amorphous organics nucleate ice heterogeneously (Wagner et al., 2012; Marcolli, 2014; Schill et al., 2014). Reported ice nucleation onsets of glassy particles span wide ranges and are most likely substance or substance class-specific (Wilson et al., 2012; Schill et al., 2014). Thus, further laboratory experiments are needed that reveal details on the ice nucleation mechanism and that allow predictions of ice nucleation ability for a wide variety of substances.

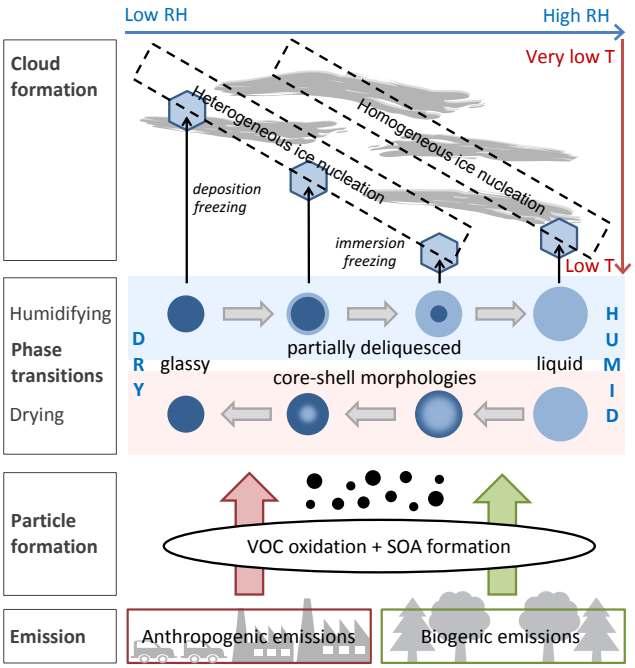

Figure 5. Overview of processes in organic aerosol particles affecting atmospheric cloud formation. Particles form by oxidation of volatile organic compounds (VOCs) originating from anthropogenic and biogenic emissions. The dominating cloud formation process depends on particle phase state, which is a function of temperature and humidity. Humidity-induced phase transitions between phase states may be kinetically limited and occur under formation of partially deliquesced particles with core-shell morphologies. Glassy or partially deliquesced particles are able to undergo heterogeneous ice nucleation, occurring at lower relative humidity or higher temperature than homogeneous ice nucleation of liquid particles.

4 Atmospheric implications of glassy organic IN

Organic aerosols can induce cloud formation via many different pathways depending on ambient conditions and composition. At high temperature and high humidity, liquid organic particles can act as cloud condensation nuclei (CCN). At lower temperatures, they facilitate formation of ice crystals. Figure 5 summarizes how the phase state and morphology of atmospheric organic aerosol particles may vary upon changes in ambient relative humidity (humidity-induced phase transitions). Upon humidifying, the phase state changes from amorphous solid (glassy) over a partially deliquesced state with a solid core residual coated by a liquid shell to a fully deliquesced liquid. Upon drying, the transition may occur via an inverse core-shell morphology, i.e. a liquid coated by a solid shell. Consequently, the particle phase state determines the active ice nucleation pathway: glassy solids can nucleate ice in the deposition mode, partially deliquesced particles with core-shell morphologies may act as IN in the immersion mode and liquid particles nucleate ice homogeneously, at significantly higher ice supersaturation.

From the SOA types investigated in this study, aromatic SOA or highly aged α-pinene SOA may persist in a glassy state to the highest temperatures and humidities and may thus facilitate heterogeneous ice nucleation at temperatures of up to 225 K. Below 210 K, SOA particles from all precursors are expected to be in the glassy state required for heterogeneous ice nucleation. Our microphysical simulations suggest a potential anthropogenic influence of IN from emission of aromatic VOCs and by providing high oxidative capacities in urban areas leading to an increase of ice nucleation in and on glassy organic particles.

Compared to typical atmospheric IN such as dust, soot and biological particles, glassy organic particles require temperatures below $\sim$230 K to nucleate ice heterogeneously (Hoose and Möhler, 2012). This restriction confines their atmospheric activity range to the upper troposphere–lower

stratosphere region. Our simulations confirm that the glassy state is prevalent only up to temperatures of about 200–240 K under typical atmospheric humidities ($S_{ice} \approx 1$), depending on composition.

In this study we show a strong interplay between diffusion timescales in the atmosphere and atmospheric updraft speeds: the stronger the updraft and the larger the particle size, the more kinetic limitations delay the liquefaction of glassy particles. These findings also imply that an ice nucleation onset determined in laboratory studies needs to be interpreted carefully in order to apply it to realistic atmospheric parameters, i.e. humidification rate, particle size and starting humidity. Kinetic limitations are already pronounced at the smallest atmospherically relevant updraft velocities of $0.02\,m\,s^{-1}$. When humidification is fast (e.g. in convective updrafts), the glassy state may persist well above its quasi-equilibrium boundaries. Our simulations on sucrose and SOA particles suggest a shift of the humidity-induced glass transition to higher temperatures by about 5 K when updraft velocities are increased by a factor of 10. Also, the history of an organic particle has effects on its water uptake properties: particles that were equilibrated at lower humidity are expected to deliquesce at higher ice supersaturation. In situations where particles are both equilibrated in dry air ($S_{ice} < 0.9$) and elevated quickly, upper temperature limits for immersion freezing on glassy organics might reach much higher values than the conservative estimates given in this study. Thus, also ice nucleation in mid-altitude clouds may be affected by this heterogeneous ice nucleation pathway.

This study outlines the basic physico-chemical relations and makes a first attempt in quantifying temperature limits for heterogeneous ice nucleation by four generic types of SOA, but further laboratory and modelling studies are needed to provide a comprehensive set of parameterizations to be used in atmospheric models. To assess the global importance of ice nucleation by SOA particles and to quantify the associated aerosol effects on climate, studies with large-scale computational models are needed. As small-scale kinetic processes cannot be treated explicitly in these kinds of models, parameterizations are required that include dependencies on temperature, relative humidity, updraft velocity, particle size and composition.

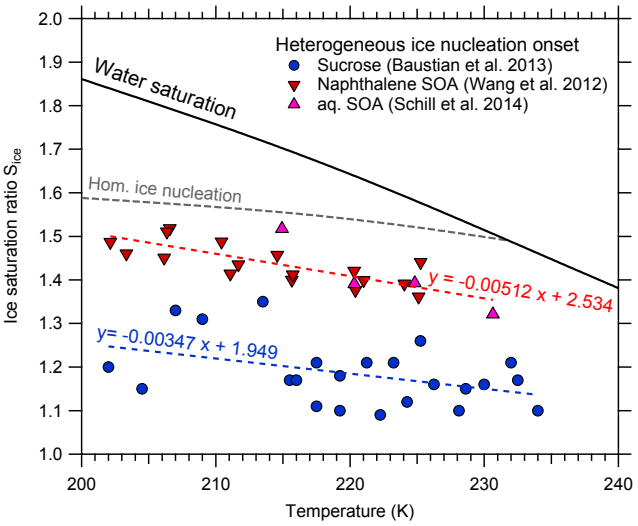

Figure A1. Determination of heterogeneous ice nucleation onsets. For sucrose, data from Baustian et al. (2013) (blue circles) are fitted. For SOA, deposition freezing data on naphthalene SOA from Wang et al. (2012) (red downward triangles) as well as nucleation data on aqSOA from Schill et al. (2014) (pink upward triangles) are used. The resulting linear regression fits (blue and red dashed lines) lie significantly below the homogeneous nucleation limit and are displayed along with their parameterizations.

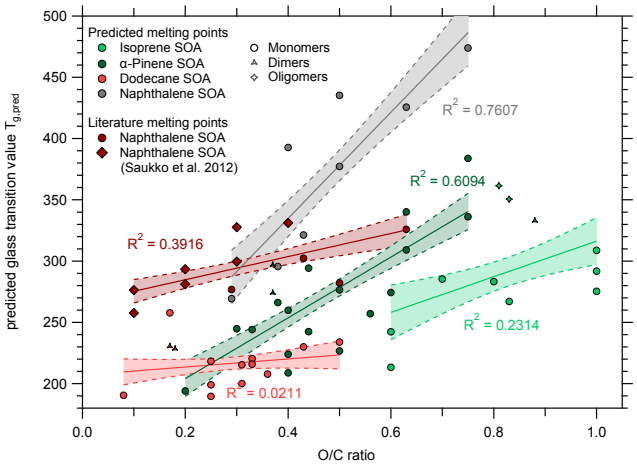

Figure A2. Predicted glass transition values of SOA marker substances as a function of O / C ratio. The predicted $T_{g,org}$ exhibits a linear correlation with O / C for each of the four SOA systems. Solid lines are robust linear regressions using a bisquare weighting function and shaded areas are confidence intervals at the 1σ level. Anthropogenic aliphatic SOA constituents show the lowest values of $T_{g,org}$ and a weak dependence on O / C. In contrast, aromatic SOA shows the highest glass transition values despite a rather low average O / C ratio.

Table A1. Assumed physical properties of SOA classes for use in conjunction with the diffusivity estimation scheme.

SOA Class	O / C	$T_{g,org}$ (K)	k_{GT}	κ_{org}
α-Pinene	0.3	228.9 ± 10.6	2.5	0.084 ± 0.012
	0.5	278.5 ± 7.0	2.5	0.120 ± 0.020
	0.7	328.1 ± 12.8	2.5	0.156 ± 0.028
Isoprene	0.6	258.2 ± 22.2	2.5	0.138 ± 0.024
	0.8	287.2 ± 11.9	2.5	0.174 ± 0.032
	1.0	316.3 ± 19.1	2.5	0.210 ± 0.040
Naphthalene	0.3	294.2 ± 5.7	2.5	0.084 ± 0.012
	0.5	313.1 ± 8.8	2.5	0.120 ± 0.020
	0.7	332.0 ± 15.0	2.5	0.156 ± 0.028
Dodecane	0.1	210.3 ± 9.7	2.5	0.048 ± 0.004
	0.3	216.8 ± 5.1	2.5	0.084 ± 0.012
	0.5	223.4 ± 11.4	2.5	0.120 ± 0.020
Koop SOA	–	270 ± 21	2.5 ± 1	$0.1008^{+0.1008}_{-0.0504}$

Appendix A: Details on the estimation of bulk diffusivities from glass transition and hygroscopicity data

A1 Justification of the method

Even though the estimation scheme described in Sect. 2.2 represents a rather crude estimation of water diffusivities, it builds on basic physical principals: in solutions of chemically similar organic substances (like the mixture of highly functionalized organic species in SOA), the types of molecular interactions are mostly hydrogen bonds and dispersion interactions, irrespective of the actual composition. Differences in diffusive properties are to a substantial degree due to factors such as molar mass and shape, both of which directly affect the glass transition temperature (Koop et al., 2011). The way by which the glass transition is approached is not affected strongly by the SOA type, as all organic compounds relevant for SOA are *fragile* glass formers (Angell, 1985). The proposed method is consistent with the following previous studies.

Rampp et al. (2000) used nuclear magnetic resonance (NMR) spectroscopy to determine water diffusion coefficients in different carbohydrate matrices (sucrose, allosucrose, leucrose, trehalose) and fitted VFT parameters to the temperature and concentration-dependent data sets. Overall, similar VFT parameters A and B were found for these chemically similar substances, even though D_{H_2O} seemed to depend strongly on organic mass fraction, thus supporting assumptions 1 and 2 in Sect. 2.2. The observed concentration dependence was described almost exclusively by a change in T_0, with only small trends in A and minor variation in B, possibly due to experimental error, thus supporting assumption 3 in Sect. 2.2.

Angell (1997) investigated the correlation of Kauzmann temperatures T_k with Vogel temperatures T_0 and found their ratio to be close to unity. The ratio of T_g to T_0 has been shown to be confined to a narrow range between $1.07 < T_g/T_0 < 1.82$ for a wide variety of strongly different substances. This

ratio seems to be correlated in magnitude to the substance's fragility (i.e. VFT parameter B), with high fragilities implying high T_g / T_0 ratios. Conversely, the assumption of similar fragilities (assumption 2) directly points towards similar T_g / T_0 ratios (assumption 3). Accordingly, deducing Vogel temperatures T_0 from glass transition properties seems reasonable.

A2 Estimation of glass transition temperatures $T_{g,org}$

The proposed estimation scheme enables the prediction of bulk diffusion coefficients only from knowledge of glass transition values for the desired RH range. The glass transition curve can be described by three parameters: the glass transition temperature of the pure molecular compound, $T_{g,org}$; the Gordon–Taylor constant, k_{GT}, of the aqueous organic mixture; and the hygroscopicity, κ_{org}, for translating composition into water activity. $T_{g,org}$ exhibits a linear correlation with melting point, T_m, also known as the Boyer–Beaman rule (Koop et al., 2011). T_m can be estimated by group contribution models with knowledge of the chemical structure. We use the melting point prediction model of UPPER (Unified Physical Property Estimating Relationships) as presented by Jain and Yalkowsky (2006) and Jain et al. (2004).

Table S1 shows our choice of marker substances for four different types of SOA along with molar mass, melting points predicted with UPPER and predicted glass transition values based on the Boyer–Beaman rule. The SOA groups were chosen to include SOA from the most commonly studied precursors and are derived from one specified precursor substance each. The groups "α-pinene" and "isoprene" represent SOA from biogenic origin, whereas "naphthalene" and "dodecane" are our choice for precursors of anthropogenic origin.

The group "α-pinene" contains compounds characteristic of photooxidation and ozonolysis of the biogenic SOA precursor α-pinene, which has been chosen as a proxy for the different monoterpene VOCs responsible for biogenic SOA formation. The list contains compounds with the highest yields according to the MCM-based simulations of Shilling et al. (2009) as well as those of Zuend and Seinfeld (2012), who also included two dimer substances. Furthermore, we included 3-MBTCA, a highly oxidized pinene derivative found in ambient samples (Szmigielski et al., 2007) as well as terpenylic acid, a tracer for fresh SOA, along with two of its derivatives (Claeys et al., 2009).

The group "isoprene" contains isoprene-derived compounds found in ambient and laboratory aerosol as suggested by Surratt et al. (2006) and references therein. These authors also proposed a high contribution of esterification products with 2-methylglyceric acid as monomeric unit to SOA mass. Table S1 lists these oligomers up to the tetramer level, where predicted glass transition values start to level off.

The group "naphthalene" represents typical products originating from the oxidation of anthropogenic aromatic precursors. Note that for highly functionalized aromatic compounds, UPPER predicts unusually high values for T_m, which are inconsistent with observations. For example, phthalic acid melts under decomposition (presumably anhydrate formation) at 403 K (Lide, 2005), whereas UPPER suggests a melting point of about 539 K. For this reason, we used only those naphthalene oxidation products for which literature melting points are known, such as the substances given in Saukko et al. (2012) and a number of compounds listed in Kautzman et al. (2010). Note that for the same reason we did not include oligomerization products to the "naphthalene" group. Oligomerization is however also expected for aromatic SOA, shown e.g. by Kalberer et al. (2004), which would lead to higher $T_{g,org}$ (Koop et al., 2011). For these reasons, our estimates for aromatic SOA materials may be regarded as a conservative estimate.

The group "dodecane" in Table S1 lists oxidized organics derived from the C12 straight-chain alkanes to represent the family of similar compounds originating from aliphatic VOCs of anthropogenic origin. The list is a selection from the comprehensive chemical mechanism in Yee et al. (2012) and three compounds from those suggested by Zhang et al. (2014).

The resulting glass transition values are presented in Fig. A2 as a function of atomic O / C ratio, and a clear positive correlation is observed within each group of compounds. Such a correlation between $T_{g,org}$ and O / C has been supported by recent T_g measurements of mixtures of α-pinene-derived oxidation compounds (Dette et al., 2014). In Fig. A2, the solid lines are obtained by linear regressions of the glass transition values using a bisquare weighting function and shaded areas are confidence intervals at the 1σ level. The chosen marker compounds occupy compound-specific ranges of O / C values, which is in part due to a different carbon number in the precursor molecule. To estimate a value characteristic for a mixture of the single compounds, we choose three values of O / C ratios that are typical of the respective group and take at each of those values the corresponding $T_{g,org}$ that arises from the linear fit. The errors are then given by the extension of confidence bands at each point. The results are shown in Table A1.

A3 Estimation of Gordon–Taylor constants k_{GT}

Gordon–Taylor constants are necessary to estimate the glass transition temperatures of compound mixtures. Zobrist et al. (2008) determined Gordon–Taylor constants for a variety of atmospherically relevant substances and SOA proxies. However, data are sparse when compared to the wide structural variety of compounds in SOA, and no clear correlation can be drawn from the molecular structure. For this reason, Koop et al. (2011) recommended the use of a mean Gordon–Taylor constant of $k_{GT} = 2.5 \pm 1$ (cf. Table A1). Figure S6

shows the temperature dependence of FDRH in calculations similar to Figs. 2 and 3, this time using the best guess parameters recommended in Koop et al. (2011). The uncertainty in FDRH that arises from the given input parameter ranges is shown (grey shaded), and also the specific uncertainty from varying k_{GT} between 1.5 and 3.5 is highlighted (orange shaded).

A4 Estimation of hygroscopicities κ_{org}

The hygroscopicity of a compound can be expressed by a single parameter κ_{org}, which is strongly correlated to its degree of oxidation (Petters and Kreidenweis, 2007; Lambe et al., 2011). A typical value for κ_{org} in biogenic SOA particles collected in pristine rainforest environments is 0.1 (Gunthe et al., 2009), which was also used by Koop et al. (2011) for their estimation of glass transition values in biogenic SOA.

For estimation of κ_{org}, we use the parameterization of Lambe et al. (2011) that correlates the O / C ratio of secondary organic material to its hygroscopicity, Eq. (A1).

$$\kappa_{org} = (0.18 \pm 0.04) \cdot \mathrm{O/C} + 0.03. \quad \text{(A1)}$$

Each SOA precursor class is assigned a typical O / C value from previous investigations of marker compounds (cf. Fig A2), and results are shown in Table A1. With the knowledge of $T_{g,org}$, k_{GT} and κ_{org}, the entire glass transition curves for the four SOA types can be calculated, as visualized in Fig. S4. Dashed lines and grey shaded areas indicate ranges of uncertainty.

A5 Evaluation of the method

For evaluation of the performance of the diffusivity estimation scheme, we compare estimated diffusivity values with values obtained in experiments by Price et al. (2014). In these experiments, D_2O–H_2O exchange in an organic matrix at constant temperature and humidity is investigated by Raman spectroscopy. Figure S3 shows the experimentally determined D_{H_2O} values for sucrose and levoglucosan in Price et al., (2014) (blue and red markers) as well as the D_{H_2O} parameterization from Zobrist et al. (2011) (blue solid line). D_{H_2O} in levoglucosan has also been estimated with the diffusivity estimation scheme (red solid line), using input parameters from Zobrist et al. (2008) ($T_{g,org} = 283.6$ K, $k_{GT} = 5.2$). Water activity has been parameterized using the parameters in Table S4. Experimental and estimated values coincide for the highest and lowest water activities but differ under medium conditions due to the different curvature of the base parameterization from Zobrist et al. (2011) that underlies all calculations. However, diffusivities differ only within at most 2 orders of magnitude, which is a considerably small deviation compared to the large set of approximations made here and the difference between experimental techniques.

Figure S3 also shows the ranges of estimated diffusivity coefficients D_{H_2O} for two types of α-pinene SOA: fresh α-pinene SOA (O / C = 0.3, orange dashed line) and aged α-pinene SOA (O / C = 0.7, green dashed line). Dark shadings confined by dotted lines indicate the range of uncertainty at a fixed O / C, corresponding to the input uncertainties used for Fig. S4. Light shadings illustrate how an uncertainty in O / C of ± 0.1 translates into uncertainty in D_{H_2O} and thus accounts for the natural variability within SOA as complex mixture.

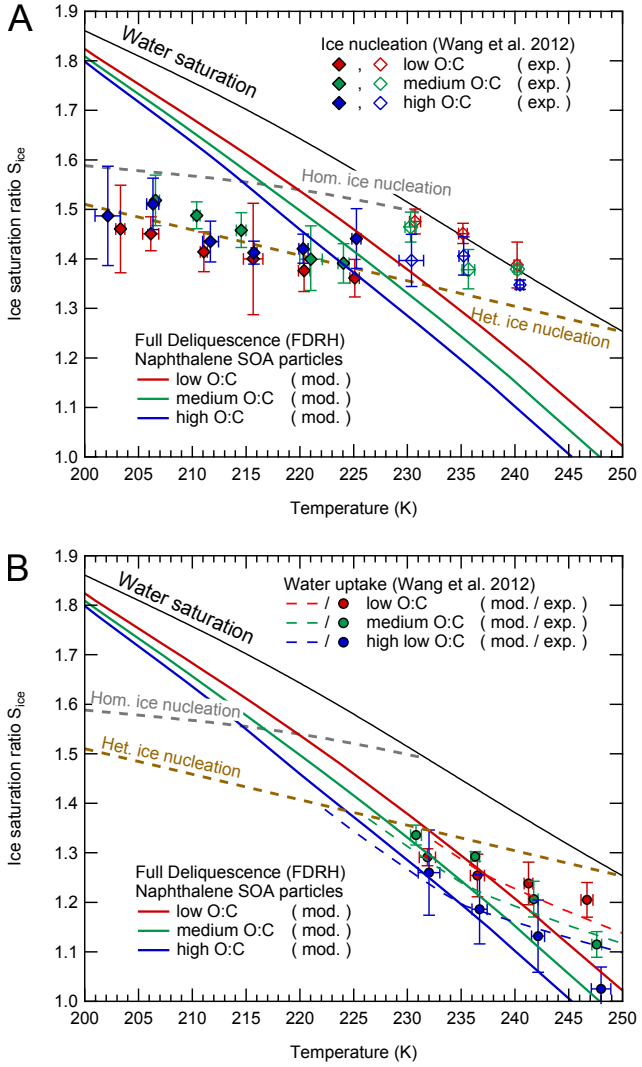

Figure B1. Comparison between calculation results of naphthalene SOA deliquescence and experimental ice nucleation and water uptake data from Wang et al. (2012). For the numerical simulations, aerosol particles are assumed to be 1 µm in diameter and are humidified at a rate of 1 % RH min^{-1}, corresponding to a cooling rate of about 0.1 K min^{-1} as used by Wang et al. (2012).

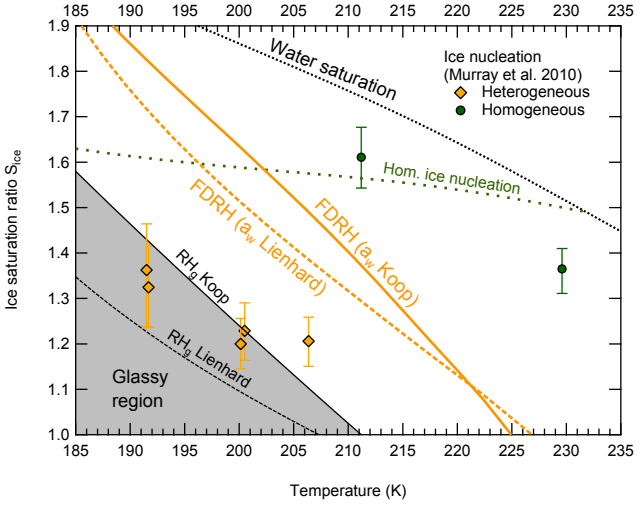

Figure B2. Comparison between calculation results of citric acid aerosol deliquescence (orange lines) and experimental ice nucleation data from Murray et al. (2010) (orange diamonds, green circles). In the numerical simulations, 150 nm diameter aerosol particles are humidified at a rate of 12 % RH min^{-1}, corresponding to a cooling rate of around 1–2 K min^{-1} typical of cloud chamber experiments. Black lines and shaded areas confine the region where a glass is the favoured thermodynamic state. The dashed lines were obtained using the water activity parameterization provided by Lienhard et al. (2012), whereas the solid lines were obtained with the parameterization in Koop et al. (2011).

Appendix B: Application of the model to ice nucleation experiments in the literature

B1 Sucrose experiments

Baustian et al. (2013) investigated sucrose particles deposited on a quartz substrate and humidified inside an experimental flow cell. After cooling and drying below the glass transition, particles with an average diameter of 4 µm were humidified by cooling at a rate of 0.1 K min^{-1}. Humidification was initialized below ice saturation ($S_{\mathrm{ice}} < 0.9$). The resulting heterogeneous ice nucleation onsets (brown circles) are shown in Fig. 2c along with the full deliquescence relative humidity (FDRH, blue solid line) from multiple model runs (spacing: 2 K) mimicking the experimental conditions. Simulations below 215 K (left black square marker) are found to nucleate in the deposition mode, whereas particles in runs between about 215 K and 238 K (right black square marker) are assumed to undergo immersion freezing. This result is compliant with the experimental values, none of which exceeds a nucleation temperature of 235 K. Above 238 K full deliquescence occurs before the ice supersaturation required for heterogeneous ice nucleation (brown dashed line) is reached. Also, homogeneous ice nucleation is not possible anymore below the water saturation limit according to Koop et al. (2000; green dashed line), leaving no remaining ice nucleation pathway.

B2 Naphthalene SOA experiments

Wang et al. (2012) generated SOA by oxidation of naphthalene by OH in a potential aerosol mass (PAM) reactor, deposited the particles on glass slides and investigated the onsets of water uptake and ice nucleation inside an ice nucleation cell that was mounted on a microscope. Experimental results are shown in Fig. B1 for three different SOA oxidation states: low O / C (0.27) given in red, medium O / C (0.54) in green and high O / C (1.0) in blue. For the comparing model simulations, we employ our diffusivity estimation

scheme with the glass transition parameterization for naphthalene given above. A humidification rate of 1 % RH min^{-1} was employed and temperature varied accordingly to maintain a constant dew point. In Fig. B1, the lines of full deliquescence relative humidity (FDRH) divide the measured heterogeneous ice nucleation onsets into two groups, irrespective of the degree of oxidation used in the simulation. Heterogeneous nucleation at or below 225 K is consistent with simulation results (closed diamonds), whereas ice nucleation at or above 230 K cannot be explained with the estimated water diffusion properties (open diamonds). According to the model simulation, naphthalene SOA should be already deliquesced at temperatures and RH where ice nucleation is still experimentally observed. The model simulations thus suggest that solid compounds that remained in the otherwise fully deliquesced particle, possibly insoluble products from naphthalene OH oxidation, nucleated ice heterogeneously with lower efficiency. Such insoluble products are not considered in the model.

The reliability of the method is confirmed by comparing experimental and modelled water uptake onsets that show very good correlation. The modelled water uptake onset was defined as the point where the particle diameter had increased by 100 nm to take into account the fact that experimental onsets were determined by visible inspection under a light microscope.

B3 Citric acid experiments

Murray et al. (2010) observed the process of heterogeneous ice nucleation on glassy aerosol particles by investigating citric acid particles in the AIDA cloud chamber. The experimentally determined onsets of heterogeneous (orange diamonds) and homogeneous ice nucleation (green circles) are shown in Fig. B2 along with results of simulations mimicking the experimental conditions. In the calculations, we assumed a particle diameter of 150 nm and a humidification rate of 12 % RH min^{-1}, corresponding to a cooling rate of 1–2 K min^{-1}. Humidification was initiated at $S_{ice} = 1$ since the cloud chamber walls were covered with ice during the initial cooling process. We performed two series of simulations for two different water activity parameterizations available in the literature. According to the parameterization in Lienhard et al. (2012) (dashed lines), heterogeneous nucleation occurs exclusively above the (equilibrium) glass transition relative humidity RH_g and thus in the immersion freezing regime. With the parameterization from Koop et al. (2011) (solid lines), equilibrium glass transition and full deliquescence occur at later stages in the humidification process. According to this data, only the experimental data point at about 206 K would have occurred in the immersion mode.

At 212 K, ice nucleation occurs only homogeneously in Murray's experiments, indicated by the much later ice nucleation onset. The humidification run started with liquid aerosol particles that showed retarded deliquescence, but were not able to nucleate ice heterogeneously.

The Supplement related to this article is available online at doi:10.5194/acp-14-12513-2014-supplement.

Author contributions. T. Berkemeier, M. Shiraiwa, U. Pöschl and T. Koop designed research; T. Berkemeier, M. Shiraiwa and T. Koop developed the model; T. Berkemeier performed research; T. Berkemeier and T. Koop analysed simulation data; T. Berkemeier, M. Shiraiwa, U. Pöschl and T. Koop wrote the paper.

Acknowledgements. This work was funded by the Max Planck Society (MPG), the Deutsche Forschungsgemeinschaft through the Ice Nuclei Research Unit INUIT (FOR1525, Grant KO 2944/2-1), and the European Commission under the PEGASOS project (grant no. 265148). T. Berkemeier was supported by the Max Planck Graduate Center with the Johannes Gutenberg-Universität Mainz (MPGC). The authors thank P. Spichtinger, U. K. Krieger, D. M. Lienhard, B. P. Luo, T. Peter, A. T. Lambe, S. S. Steimer, D. A. Knopf and H.-P. Dette for stimulating discussions.

The service charges for this open access publication have been covered by the Max Planck Society.

Edited by: D. Topping

References

Adler, G., Koop, T., Haspel, C., Taraniuk, I., Moise, T., Koren, I., Heiblum, R. H., and Rudich, Y.: Formation of highly porous aerosol particles by atmospheric freeze-drying in ice clouds, P. Natl. Acad. Sci. USA, 110, 20414–20419, doi:10.1073/pnas.1317209110, 2013.

Andreae, M. O. and Rosenfeld, D.: Aerosol-cloud-precipitation interactions. Part 1. The nature and sources of cloud-active aerosols, Earth Sci. Rev., 89, 13–41, doi:10.1016/j.earscirev.2008.03.001, 2008.

Angell, C. A.: Strong and fragile liquids, in: Relaxations in Complex Systems, edited by: Ngai, K. and Wright, G. B., National Technical Information Service, I.S. Department of Commerce, Springfield, VA, 1985.

Angell, C. A.: Landscapes with megabasins: polyamorphism in liquids and biopolymers and the role of nucleation in folding and folding diseases, Physica D, 107, 122–142, doi:10.1016/s0167-2789(97)00077-8, 1997.

Baustian, K. J., Wise, M. E., Jensen, E. J., Schill, G. P., Freedman, M. A., and Tolbert, M. A.: State transformations and ice nucleation in amorphous (semi-)solid organic aerosol, Atmos. Chem. Phys., 13, 5615–5628, 10, http://www.atmos-chem-phys.net/13/5615/10/.5194/acp-13-5615-2013, 2013.

Bones, D. L., Reid, J. P., Lienhard, D. M., and Krieger, U. K.: Comparing the mechanism of water condensation and evaporation in glassy aerosol, Proc. Natl. Acad. Sci. USA, 109, 11613–11618, doi:10.1073/pnas.1200691109, 2012.

Claeys, M., Iinuma, Y., Szmigielski, R., Surratt, J. D., Blockhuys, F., Van Alsenoy, C., Boge, O., Sierau, B., Gomez-Gonzalez, Y., Vermeylen, R., Van der Veken, P., Shahgholi, M., Chan, A. W. H., Herrmann, H., Seinfeld, J. H., and Maenhaut, W.: Terpenylic Acid and Related Compounds from the Oxidation of alpha-Pinene: Implications for New Particle Formation and Growth above Forests, Environ. Sci. Technol., 43, 6976–6982, doi:10.1021/es9007596, 2009.

Cziczo, D. J., Froyd, K. D., Hoose, C., Jensen, E. J., Diao, M. H., Zondlo, M. A., Smith, J. B., Twohy, C. H., and Murphy, D. M.: Clarifying the Dominant Sources and Mechanisms of Cirrus Cloud Formation, Science, 340, 1320–1324, doi:10.1126/science.1234145, 2013.

DeMott, P. J., Cziczo, D. J., Prenni, A. J., Murphy, D. M., Kreidenweis, S. M., Thomson, D. S., Borys, R., and Rogers, D. C.: Measurements of the concentration and composition of nuclei for cirrus formation, Proc. Natl. Acad. Sci. USA, 100, 14655–14660, doi:10.1073/pnas.2532677100, 2003.

Dette, H. P., Qi, M. A., Schroder, D. C., Godt, A., and Koop, T.: Glass-Forming Properties of 3-Methylbutane-1,2,3-tricarboxylic Acid and Its Mixtures with Water and Pinonic Acid, J. Phys. Chem. A, 118, 7024–7033, doi:10.1021/jp505910w, 2014.

Froyd, K. D., Murphy, D. M., Lawson, P., Baumgardner, D., and Herman, R. L.: Aerosols that form subvisible cirrus at the tropical tropopause, Atmos. Chem. Phys., 10, 209–218, doi:10.5194/acp-10-209-2010, 2010.

Fulcher, G. S.: Analysis of recent measurements of the viscosity of glasses, J. Am. Ceram. Soc., 8, 339–355, doi:10.1111/j.1151-2916.1925.tb16731.x, 1925.

Gunthe, S. S., King, S. M., Rose, D., Chen, Q., Roldin, P., Farmer, D. K., Jimenez, J. L., Artaxo, P., Andreae, M. O., Martin, S. T., and Pöschl, U.: Cloud condensation nuclei in pristine tropical rainforest air of Amazonia: size-resolved measurements and modeling of atmospheric aerosol composition and CCN activity, Atmos. Chem. Phys., 9, 7551–7575, doi:10.5194/acp-9-7551-2009, 2009.

Hoose, C. and Möhler, O.: Heterogeneous ice nucleation on atmospheric aerosols: a review of results from laboratory experiments, Atmos. Chem. Phys., 12, 9817–9854, doi:10.5194/acp-12-9817-2012, 2012.

Huisman, A. J., Krieger, U. K., Zuend, A., Marcolli, C., and Peter, T.: Vapor pressures of substituted polycarboxylic acids are much lower than previously reported, Atmos. Chem. Phys., 13, 6647–6662, doi:10.5194/acp-13-6647-2013, 2013.

IPCC: Climate Change 2013, The Physical Science Basis, Cambridge University Press, Cambridge, United Kingdom and New York, NY, USA, 2013.

Jain, A., Yang, G., and Yalkowsky, S. H.: Estimation of melting points of organic compounds, Ind. Eng. Chem. Res., 43, 7618–7621, doi:10.1021/ie049378m, 2004.

Jain, A. and Yalkowsky, S. H.: Estimation of melting points of organic compounds-II, J. Pharm. Sci., 95, 2562–2618, doi:10.1002/jps.20634, 2006.

Jensen, E. J., Smith, J. B., Pfister, L., Pittman, J. V., Weinstock, E. M., Sayres, D. S., Herman, R. L., Troy, R. F., Rosenlof, K., Thompson, T. L., Fridlind, A. M., Hudson, P. K., Cziczo, D. J., Heymsfield, A. J., Schmitt, C., and Wilson, J. C.: Ice supersaturations exceeding 100 % at the cold tropical tropopause: implica-

tions for cirrus formation and dehydration, Atmos. Chem. Phys., 5, 851–862, doi:10.5194/acp-5-851-2005, 2005.

Kalberer, M., Paulsen, D., Sax, M., Steinbacher, M., Dommen, J., Prevot, A. S. H., Fisseha, R., Weingartner, E., Frankevich, V., Zenobi, R., and Baltensperger, U.: Identification of polymers as major components of atmospheric organic aerosols, Science, 303, 1659–1662, 2004.

Kautzman, K. E., Surratt, J. D., Chan, M. N., Chan, A. W. H., Hersey, S. P., Chhabra, P. S., Dalleska, N. F., Wennberg, P. O., Flagan, R. C., and Seinfeld, J. H.: Chemical Composition of Gas- and Aerosol-Phase Products from the Photooxidation of Naphthalene, J. Phys. Chem. A, 114, 913–934, doi:10.1021/jp908530s, 2010.

Kidd, C., Perraud, V., Wingen, L. M., and Finlayson-Pitts, B. J.: Integrating phase and composition of secondary organic aerosol from the ozonolysis of α-pinene, Proc. Natl. Acad. Sci. USA, doi:10.1073/pnas.1322558111, 2014.

Knopf, D. A., Wang, B., Laskin, A., Moffet, R. C., and Gilles, M. K.: Heterogeneous nucleation of ice on anthropogenic organic particles collected in Mexico City, Geophys. Res. Lett., 37, L11803, doi:10.1029/2010gl043362, 2010.

Knopf, D. A., Alpert, P. A., Wang, B., O'Brien, R. E., Kelly, S. T., Laskin, A., Gilles, M. K., and Moffet, R. C.: Microspectroscopic imaging and characterization of individually identified ice nucleating particles from a case field study, J. Geophys. Res. Atmos., 119, JD021866, doi:10.1002/2014JD021866 , 2014.

Koop, T., Luo, B. P., Tsias, A., and Peter, T.: Water activity as the determinant for homogeneous ice nucleation in aqueous solutions, Nature, 406, 611–614, doi:10.1038/35020537, 2000.

Koop, T., Bookhold, J., Shiraiwa, M., and Pöschl, U.: Glass transition and phase state of organic compounds: dependency on molecular properties and implications for secondary organic aerosols in the atmosphere, Phys. Chem. Chem. Phys., 13, 19238–19255, 2011.

Kuwata, M. and Martin, S. T.: Phase of atmospheric secondary organic material affects its reactivity, Proc. Natl. Acad. Sci. USA, 109, 17354–17359, doi:10.1073/pnas.1209071109, 2012.

Lambe, A. T., Onasch, T. B., Massoli, P., Croasdale, D. R., Wright, J. P., Ahern, A. T., Williams, L. R., Worsnop, D. R., Brune, W. H., and Davidovits, P.: Laboratory studies of the chemical composition and cloud condensation nuclei (CCN) activity of secondary organic aerosol (SOA) and oxidized primary organic aerosol (OPOA), Atmos. Chem. Phys., 11, 8913–8928, doi:10.5194/acp-11-8913-2011, 2011.

Lide, D. R.: CRC Handbook of Chemistry and Physics, CRC Press, National Institute of Standards and Technology, Boca Raton, FL, 2005.

Lienhard, D. M., Bones, D. L., Zuend, A., Krieger, U. K., Reid, J. P., and Peter, T.: Measurements of Thermodynamic and Optical Properties of Selected Aqueous Organic and Organic-Inorganic Mixtures of Atmospheric Relevance, J. Phys. Chem. A, 116, 9954–9968, doi:10.1021/jp3055872, 2012.

Lienhard, D. M., Huisman, A. J., Bones, D. L., Te, Y. F., Luo, B. P., Krieger, U. K., and Reid, J. P.: Retrieving the translational diffusion coefficient of water from experiments on single levitated aerosol droplets, Phys. Chem. Chem. Phys., 16, 16677–16683, doi:10.1039/c4cp01939c, 2014.

Marcolli, C.: Deposition nucleation viewed as homogeneous or immersion freezing in pores and cavities, Atmos. Chem. Phys., 14, 2071–2104, doi:10.5194/acp-14-2071-2014, 2014.

Mikhailov, E., Vlasenko, S., Martin, S. T., Koop, T., and Pöschl, U.: Amorphous and crystalline aerosol particles interacting with water vapor: conceptual framework and experimental evidence for restructuring, phase transitions and kinetic limitations, Atmos. Chem. Phys., 9, 9491–9522, doi:10.5194/acp-9-9491-2009, 2009.

Murray, B. J., Wilson, T. W., Dobbie, S., Cui, Z. Q., Al-Jumur, S., Mohler, O., Schnaiter, M., Wagner, R., Benz, S., Niemand, M., Saathoff, H., Ebert, V., Wagner, S., and Karcher, B.: Heterogeneous nucleation of ice particles on glassy aerosols under cirrus conditions, Nat. Geosci., 3, 233–237, doi:10.1038/ngeo817, 2010.

O'Meara, S., Booth, A. M., Barley, M. H., Topping, D., and McFiggans, G.: An assessment of vapour pressure estimation methods, Phys. Chem. Chem. Phys., 16, 19453–19469, doi:10.1039/c4cp00857j, 2014.

Perraud, V., Bruns, E. A., Ezell, M. J., Johnson, S. N., Yu, Y., Alexander, M. L., Zelenyuk, A., Imre, D., Chang, W. L., Dabdub, D., Pankow, J. F., and Finlayson-Pitts, B. J.: Nonequilibrium atmospheric secondary organic aerosol formation and growth, Proc. Natl. Acad. Sci. USA, 109, 2836–2841, doi:10.1073/pnas.1119909109, 2012.

Petters, M. D. and Kreidenweis, S. M.: A single parameter representation of hygroscopic growth and cloud condensation nucleus activity, Atmos. Chem. Phys., 7, 1961–1971, doi:10.5194/acp-7-1961-2007, 2007.

Price, H. C., Murray, B. J., Mattsson, J., O'Sullivan, D., Wilson, T. W., Baustian, K. J., and Benning, L. G.: Quantifying water diffusion in high-viscosity and glassy aqueous solutions using a Raman isotope tracer method, Atmos. Chem. Phys., 14, 3817–3830, doi:10.5194/acp-14-3817-2014, 2014.

Pruppacher, H. and Klett, J.: Microphysics of clouds and precipitation, 2 Edn., Kluwer Academic Publishers, Boston, MA, 1997.

Rampp, M., Buttersack, C., and Ludemann, H. D.: c,T-dependence of the viscosity and the self-diffusion coefficients in some aqueous carbohydrate solutions, Carbohyd. Res., 328, 561–572, 2000.

Renbaum-Wolff, L., Grayson, J. W., Bateman, A. P., Kuwata, K., Sellier, M., Murray, B. J., Schilling, J. E., Martin, S. T., and Bertram, A. K.: Viscosity of α-pinene secondary organic material and implications for particle growth and reactivity, Proc. Natl. Acad. Sci. USA, 110, 8014–8019, doi:10.1073/pnas.1219548110 2013.

Rickards, A. M. J., Miles, R. E. H., Davies, J. F., Marshall, F. H., and Reid, J. P.: Measurements of the Sensitivity of Aerosol Hygroscopicity and the kappa Parameter to the O / C Ratio, J. Phys. Chem. A, 117, 14120–14131, doi:10.1021/jp407991n, 2013.

Saukko, E., Lambe, A. T., Massoli, P., Koop, T., Wright, J. P., Croasdale, D. R., Pedernera, D. A., Onasch, T. B., Laaksonen, A., Davidovits, P., Worsnop, D. R., and Virtanen, A.: Humidity-dependent phase state of SOA particles from biogenic and anthropogenic precursors, Atmos. Chem. Phys., 12, 7517–7529, doi:10.5194/acp-12-7517-2012, 2012.

Schill, G. P. and Tolbert, M. A.: Heterogeneous ice nucleation on phase-separated organic-sulfate particles: effect of liquid vs. glassy coatings, Atmos. Chem. Phys., 13, 4681–4695, doi:10.5194/acp-13-4681-2013, 2013.

Schill, G. P., De Haan, D. O., and Tolbert, M. A.: Heterogeneous Ice Nucleation on Simulated Secondary Organic Aerosol, Environ. Sci. Technol., 48, 1675-1682, doi:10.1021/es4046428, 2014.

Shilling, J. E., Chen, Q., King, S. M., Rosenoern, T., Kroll, J. H., Worsnop, D. R., DeCarlo, P. F., Aiken, A. C., Sueper, D., Jimenez, J. L., and Martin, S. T.: Loading-dependent elemental composition of α-pinene SOA particles, Atmos. Chem. Phys., 9, 771–782, doi:10.5194/acp-9-771-2009, 2009.

Shiraiwa, M., Ammann, M., Koop, T., and Pöschl, U.: Gas uptake and chemical aging of semisolid organic aerosol particles, Proc. Natl. Acad. Sci. USA, 108, 11003–11008, doi:10.1073/pnas.1103045108, 2011.

Shiraiwa, M., Pfrang, C., Koop, T., and Pöschl, U.: Kinetic multilayer model of gas-particle interactions in aerosols and clouds (KM-GAP): linking condensation, evaporation and chemical reactions of organics, oxidants and water, Atmos. Chem. Phys., 12, 2777–2794, doi:10.5194/acp-12-2777-2012, 2012.

Shiraiwa, M., Yee, L. D., Schilling, K. A., Loza, C. L., Craven, J. S., Zuend, A., Ziemann, P. J., and Seinfeld, J. H.: Size distribution dynamics reveal particle-phase chemistry in organic aerosol formation, Proc. Natl. Acad. Sci. USA, 110, 11746–11750, doi:10.1073/pnas.1307501110, 2013a.

Shiraiwa, M., Zuend, A., Bertram, A. K., and Seinfeld, J. H.: Gas-particle partitioning of atmospheric aerosols: interplay of physical state, non-ideal mixing and morphology, Phys. Chem. Chem. Phys., 15, 11441–11453, doi:10.1039/C3CP51595H, 2013b.

Song, M., Marcolli, C., Krieger, U. K., Zuend, A., and Peter, T.: Liquid-liquid phase separation and morphology of internally mixed dicarboxylic acids/ammonium sulfate/water particles, Atmos. Chem. Phys., 12, 2691–2712, doi:10.5194/acp-12-2691-2012, 2012.

Surratt, J. D., Murphy, S. M., Kroll, J. H., Ng, N. L., Hildebrandt, L., Sorooshian, A., Szmigielski, R., Vermeylen, R., Maenhaut, W., Claeys, M., Flagan, R. C., and Seinfeld, J. H.: Chemical composition of secondary organic aerosol formed from the photooxidation of isoprene, J. Phys. Chem. A, 110, 9665–9690, doi:10.1021/jp061734m, 2006.

Szmigielski, R., Surratt, J. D., Gomez-Gonzalez, Y., Van der Veken, P., Kourtchev, I., Vermeylen, R., Blockhuys, F., Jaoui, M., Kleindienst, T. E., Lewandowski, M., Offenberg, J. H., Edney, E. O., Seinfeld, J. H., Maenhaut, W., and Claeys, M.: 3-methyl-1,2,3-butanetricarboxylic acid: An atmospheric tracer for terpene secondary organic aerosol, Geophys. Res. Lett., 34, doi:10.1029/2007gl031338, 2007.

Tammann, G. and Hesse, W.: The dependancy of viscosity on temperature in hypothermic liquids, Z. Anorg. Allg. Chem., 156, 14, 1926.

Tong, H.-J., Reid, J. P., Bones, D. L., Luo, B. P., and Krieger, U. K.: Measurements of the timescales for the mass transfer of water in glassy aerosol at low relative humidity and ambient temperature, Atmos. Chem. Phys., 11, 4739–4754, doi:10.5194/acp-11-4739-2011, 2011.

Vaden, T. D., Imre, D., Beranek, J., Shrivastava, M., and Zelenyuk, A.: Evaporation kinetics and phase of laboratory and ambient secondary organic aerosol, Proc. Natl. Acad. Sci. USA, 108, 2190–2195, doi:10.1073/pnas.1013391108, 2011.

Virtanen, A., Joutsensaari, J., Koop, T., Kannosto, J., YliPirilä, P., Leskinen, J., Mäkelä, J. M., Holopainen, J. K., Pöschl, U., Kulmala, M., Worsnop, D. R., and Laaksonen, A.: An amorphous solid state of biogenic secondary organic aerosol particles, Nature, 467, 824–827, doi:10.1038/nature09455, 2010.

Vogel, H.: The temperature dependence law of the viscosity of fluids, Phys. Z., 22, 645–646, 1921.

Wagner, R., Möhler, O., Saathoff, H., Schnaiter, M., Skrotzki, J., Leisner, T., Wilson, T. W., Malkin, T. L., and Murray, B. J.: Ice cloud processing of ultra-viscous/glassy aerosol particles leads to enhanced ice nucleation ability, Atmos. Chem. Phys., 12, 8589–8610, doi:10.5194/acp-12-8589-2012, 2012.

Wang, B. B., Lambe, A. T., Massoli, P., Onasch, T. B., Davidovits, P., Worsnop, D. R., and Knopf, D. A.: The deposition ice nucleation and immersion freezing potential of amorphous secondary organic aerosol: Pathways for ice and mixed-phase cloud formation, J. Geophys. Res. Atmos., 117, D16209, doi:10.1029/2012jd018063, 2012.

Wilson, T. W., Murray, B. J., Wagner, R., Möhler, O., Saathoff, H., Schnaiter, M., Skrotzki, J., Price, H. C., Malkin, T. L., Dobbie, S., and Al-Jumur, S. M. R. K.: Glassy aerosols with a range of compositions nucleate ice heterogeneously at cirrus temperatures, Atmos. Chem. Phys., 12, 8611–8632, doi:10.5194/acp-12-8611-2012, 2012.

Yee, L. D., Craven, J. S., Loza, C. L., Schilling, K. A., Ng, N. L., Canagaratna, M. R., Ziemann, P. J., Flagan, R. C., and Seinfeld, J. H.: Secondary organic aerosol formation from low-NO_x photooxidation of dodecane: evolution of multigeneration gas-phase chemistry and aerosol composition, J. Phys. Chem. A, 116, 6211–6230, doi:10.1021/jp211531h, 2012.

You, Y., Renbaum-Wolff, L., Carreras-Sospedra, M., Hanna, S. J., Hiranuma, N., Kamal, S., Smith, M. L., Zhang, X. L., Weber, R. J., Shilling, J. E., Dabdub, D., Martin, S. T., and Bertram, A. K.: Images reveal that atmospheric particles can undergo liquid-liquid phase separations, Proc. Natl. Acad. Sci. USA, 109, 13188-13193, doi:10.1073/pnas.1206414109, 2012.

You, Y., Smith, M. L., Song, M. J., Martin, S. T., and Bertram, A. K.: Liquid-liquid phase separation in atmospherically relevant particles consisting of organic species and inorganic salts, Int. Rev. Phys. Chem., 33, 43–77, doi:10.1080/0144235x.2014.890786, 2014.

Yu, H., Kaufman, Y. J., Chin, M., Feingold, G., Remer, L. A., Anderson, T. L., Balkanski, Y., Bellouin, N., Boucher, O., Christopher, S., DeCola, P., Kahn, R., Koch, D., Loeb, N., Reddy, M. S., Schulz, M., Takemura, T., and Zhou, M.: A review of measurement-based assessments of the aerosol direct radiative effect and forcing, Atmos. Chem. Phys., 6, 613–666, doi:10.5194/acp-6-613-2006, 2006.

Zhang, X., Schwantes, R. H., Coggon, M. M., Loza, C. L., Schilling, K. A., Flagan, R. C., and Seinfeld, J. H.: Role of ozone in SOA formation from alkane photooxidation, Atmos. Chem. Phys., 14, 1733–1753, doi:10.5194/acp-14-1733-2014, 2014.

Zhou, S., Shiraiwa, M., McWhinney, R., Pöschl, U., and Abbatt, J. P. D.: Kinetic limitations in gas-particle reactions arising from slow diffusion in secondary organic aerosol, Faraday Discuss., 165, 391–406, doi:10.1039/C3FD00030C, 2013.

Zobrist, B., Weers, U., and Koop, T.: Ice nucleation in aqueous solutions of poly ethylene glycol with different molar mass, J. Chem. Phys., 118, 10254–10261, doi:10.1063/1.1571818, 2003.

Zobrist, B., Marcolli, C., Pedernera, D. A., and Koop, T.: Do atmospheric aerosols form glasses?, Atmos. Chem. Phys., 8, 5221–5244, doi:10.5194/acp-8-5221-2008, 2008.

Zobrist, B., Soonsin, V., Luo, B. P., Krieger, U. K., Marcolli, C., Peter, T., and Koop, T.: Ultra-slow water diffusion in aqueous sucrose glasses, Phys. Chem. Chem. Phys., 13, 3514–3526, doi:10.1039/c0cp01273d, 2011.

Zuend, A. and Seinfeld, J. H.: Modeling the gas-particle partitioning of secondary organic aerosol: the importance of liquid-liquid phase separation, Atmos. Chem. Phys., 12, 3857–3882, doi:10.5194/acp-12-3857-2012, 2012.

B.5. Berkemeier *et al.*, Phys. Chem. Chem. Phys., 2016

Ozone uptake on glassy, semi-solid and liquid organic matter and the role of reactive oxygen intermediates in atmospheric aerosol chemistry

Thomas Berkemeier[1], Sarah S. Steimer[2,3], Ulrich K. Krieger[3], Thomas Peter[3], Ulrich Pöschl[1], Markus Ammann[2] and Manabu Shiraiwa[1]

[1]Max Planck Institute for Chemistry, Multiphase Chemistry Department, 55128 Mainz, Germany
[2]Paul Scherrer Institute, Laboratory of Environmental Chemistry, 5232 Villigen PSI, Switzerland
[3]ETH Zurich, Institute for Atmospheric and Climate Science, 8092 Zurich, Switzerland

Physical Chemistry Chemical Physics **18**, 12662-12674, (2016).

Author contributions.

TB, UKK, TP, UP, MA and MS designed research. TB, MA and MS developed the model. TB and MA performed kinetic modelling. TB, SSS, UP, MA and MS analysed simulation data. TB, MA and MS wrote the paper.

PCCP

PAPER

View Article Online
View Journal | View Issue

Cite this: *Phys. Chem. Chem. Phys.*, 2016, **18**, 12662

Ozone uptake on glassy, semi-solid and liquid organic matter and the role of reactive oxygen intermediates in atmospheric aerosol chemistry†

Thomas Berkemeier,*[a] Sarah S. Steimer,[bc] Ulrich K. Krieger,[c] Thomas Peter,[c] Ulrich Pöschl,[a] Markus Ammann[b] and Manabu Shiraiwa*[a]

Received 28th January 2016,
Accepted 7th April 2016

DOI: 10.1039/c6cp00634e

www.rsc.org/pccp

Heterogeneous and multiphase reactions of ozone are important pathways for chemical ageing of atmospheric organic aerosols. To demonstrate and quantify how moisture-induced phase changes can affect the gas uptake and chemical transformation of organic matter, we apply a kinetic multi-layer model to a comprehensive experimental data set of ozone uptake by shikimic acid. The bulk diffusion coefficients were determined to be 10^{-12} cm^2 s^{-1} for ozone and 10^{-20} cm^2 s^{-1} for shikimic acid under dry conditions, increasing by several orders of magnitude with increasing relative humidity (RH) due to phase changes from amorphous solid over semisolid to liquid. Consequently, the reactive uptake of ozone progresses through different kinetic regimes characterised by specific limiting processes and parameters. At high RH, ozone uptake is driven by reaction throughout the particle bulk; at low RH it is restricted to reaction near the particle surface and kinetically limited by slow diffusion and replenishment of unreacted organic molecules. Our results suggest that the chemical reaction mechanism involves long-lived reactive oxygen intermediates, likely primary ozonides or O atoms, which may provide a pathway for self-reaction and catalytic destruction of ozone at the surface. Slow diffusion and ozone destruction can effectively shield reactive organic molecules in the particle bulk from degradation. We discuss the potential non-orthogonality of kinetic parameters, and show how this problem can be solved by using comprehensive experimental data sets to constrain the kinetic model, providing mechanistic insights into the coupling of transport, phase changes, and chemical reactions of multiple species in complex systems.

1 Introduction

Organic compounds are ubiquitous in the earth's atmosphere and constitute a major fraction of atmospheric particulate matter.[1–3] Finely dispersed submicron particles affect climate by scattering sunlight and serving as nuclei for cloud droplets and ice crystals[4] and play a key role in air quality and public health by reducing visibility and posing adverse health effects.[5,6] Most organic aerosols arise from oxidation of volatile organic compounds followed by condensation of oxidation products, so-called secondary organic aerosols (SOA).[2,3,7] After formation, organic aerosols are still subject to chemical processing by reactive trace gases such as ozone,[8,9] ammonia,[10] the hydroxyl[11–13] or nitrate radical,[14,15] influencing chemical composition[16–18] and particle size distribution,[19] and hence, affecting hygroscopicity,[20–22] viscosity,[23] gas-particle partitioning,[24–26] radiative properties,[27] and toxicity.[28] The rate of chemical reactions occurring in aerosol particles depends strongly on their phase state,[8–11,18,29] which varies from liquid to solid depending on composition[30–32] and ambient conditions such as temperature and relative humidity.[33–39] Accordingly, diffusivity of organic molecules[40] and trace gases penetrating the organic matrix[41–44] decreases significantly under cold or dry conditions.

Accurate description of the multiphase reaction kinetics of these systems is vital for understanding the rates at which compounds degrade and oxidants are consumed. Kinetic models commonly evaluate single steps that may limit reaction rate such as mass transfer or chemical reaction. Classical resistor models are computationally inexpensive, but only describe certain aspects of the reaction system in distinct limiting cases.[45,46] These models have difficulty in describing systems which are driven by multiple rate-limiting processes or transition between limiting cases.[47]

[a] *Max Planck Institute for Chemistry, Multiphase Chemistry Department, 55128 Mainz, Germany. E-mail: t.berkemeier@mpic.de, m.shiraiwa@mpic.de*
[b] *Paul Scherrer Institute, Laboratory of Environmental Chemistry, 5232 Villigen PSI, Switzerland*
[c] *ETH Zurich, Institute for Atmospheric and Climate Science, 8092 Zurich, Switzerland*

† Electronic supplementary information (ESI) available. See DOI: 10.1039/c6cp00634e

Hence, the important subset of cases where both the bulk material and the trace gas show diffusion limitation ("counter-diffusion case") cannot be properly described.

Kinetic flux models resolve this problem by tracking reactant concentration as a function of depth,[48–51] which leads to a better description of the processing of organic material in the atmosphere.[8,12,15] However, they are computationally more expensive and rely on a set of kinetic parameters of which not all are directly accessible by experiment. Due to the high number of input parameters, kinetic flux models applied to small data sets are usually not fully constrained, leaving large flexibility in the possible range of input parameters yielding the same or similar model output.[12,47] The two possible solutions to this problem are (i) reduction of the kinetic input parameter set and thus simplification of the kinetic model and loss of information or (ii) extension of the dimensions of the experimental input data set. Added dimensions can be additional experimental observables (*e.g.* reactant concentrations in gas and particle phase, viscosity, system size, refractive indices) or can be varied environmental conditions (reactant concentrations, system size, temperature, relative humidity) or simply an extended observation time scale to encompass more rate-limiting processes.[47,52] A kinetic parameter can only be determined if a related process affects the measured quantity. Care must be taken in case parameters depend on environmental conditions (*e.g.* bulk diffusion coefficients depend on both RH and temperature separately).

These criteria of a wide range of experimental dimensions are fulfilled in a recent study by Steimer *et al.*, who investigated ozonolysis of shikimic acid as model system for chemical processing of organic aerosols.[53] The cyclohexene derivative shikimic acid contains a single double bond that serves as target for ozone. Due to the closed ring structure, ozonolysis does not lead to fragmentation and thus volatilization of the oxidation products. The structural formula of shikimic acid is displayed in Fig. 1A. Pure shikimic acid exhibits a glassy solid phase state with a glass transition temperature of 327 K.[54] Due to the plasticizing effect of water, shikimic acid is expected to cover the full range of (semi-)solid phase states at atmospherically relevant RHs. The experimental study by Steimer *et al.* clearly demonstrated the limitations of classical methods for analysis of heterogeneous kinetics, which motivates the application of the kinetic multi-layer model for aerosol surface and bulk chemistry (KM-SUB)[49] to the kinetic data set in this study. In order to cope with the extended set of kinetic parameters of the kinetic flux model, we apply a global optimization method including a genetic algorithm to find an optimal correlation between model and experiment.

2 Methods

The kinetic experiments have been reported in detail by Steimer *et al.* and will be described only briefly in the following.[53] Experiments were performed in an atmospheric pressure coated wall flow reactor (48 cm length, 1.2 cm inner diameter) with long reaction times and atmospherically relevant oxidant

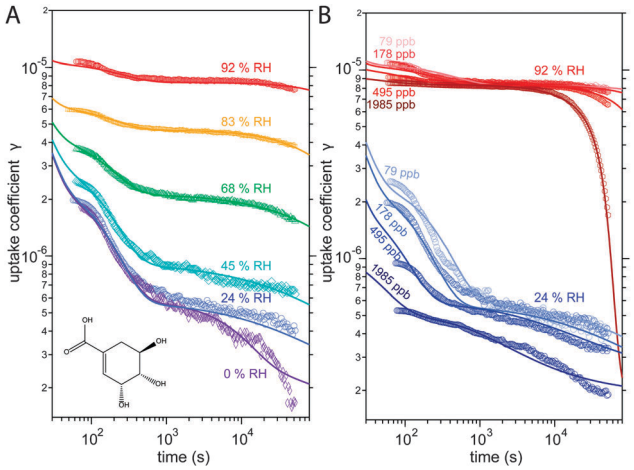

Fig. 1 Observed (markers) and modelled (lines) uptake coefficients of ozone γ onto a thin film of shikimic acid as a function of exposure time. (A) Uptake coefficients at 178 ppb ozone gas phase concentration $[O_3]_g$ at different relative humidities of 0, 24, 45, 68, 83, and 92%. The structural formula of shikimic acid is displayed in the left bottom corner. (B) Uptake coefficients at 24% RH (blue solid lines) and 92% RH (red solid lines) with different $[O_3]_g$ of 79, 178, 495, and 1985 ppb.

concentrations as detailed. The temperature in the reactor was held constant by a thermostat-controlled cooling jacket and RH was adjusted by directing gas flows through tempered water reservoirs.

Measurements were performed at an O_3 concentration of 178 ppb at 6 different relative humidities: 0, 24, 45, 69, 83 and 92% RH. At 24 and 92%, measurements were conducted at three additional O_3 concentrations of 89, 495 and 1985 ppb, giving a total of 12 distinct experimental conditions. The measurement results are ozone uptake coefficients γ, which represent the probability that ozone molecules colliding with a surface are subsequently taken up by the condensed phase.[55] The experimental data is shown Fig. 1.

2.1 Kinetic model

We use the kinetic multi-layer model of aerosol surface and bulk chemistry, KM-SUB, which provides a depth-resolved description of mass transport and chemical reaction in aerosol particles and surface films.[49] KM-SUB resolves the following processes explicitly: gas-phase diffusion, adsorption and desorption, surface–bulk exchange, bulk diffusion of trace gas (X) and bulk material (Y) as well as chemical reactions at the surface and in the bulk. The following three reaction pathways are considered for ozone loss in the KM-SUB representation of the reaction system: a bimolecular surface layer reaction between adsorbed ozone and surface-exposed shikimic acid (SLR1), a bulk reaction between both reactants (BR) and the self-reaction of two ozone molecules adsorbed to the surface (SLR2). Secondary reactions involving oxidation products are neglected for simplicity.

For this study, several modifications have been applied to the original KM-SUB model as outlined below. The kinetic behaviour of a reaction system is described in this modified version of KM-SUB by the thirteen kinetic parameters given in

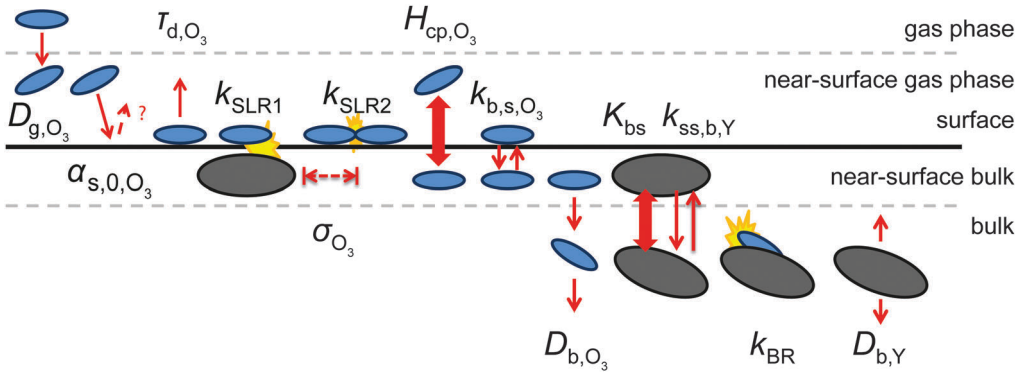

Fig. 2 Schematic representation of the input parameters and processes of KM-SUB in this study. Trace gas and reactive bulk molecules are represented by blue and black ellipses, respectively. Simple red arrows denote transport; broad double-headed arrows indicate partitioning and yellow shapes represent chemical reactions. The parameters include the gas-phase diffusivity (D_{g,O_3}), surface accommodation coefficient ($\alpha_{s,0,O_3}$), desorption lifetime (τ_{d,O_3}), adsorption cross section (σ_{O_3}) and the Henry's law coefficient (H_{cp,O_3}) of ozone; the surface reaction rates (k_{SLR1} and k_{SLR2}), the bulk reaction rate (k_{BR}); the surface–bulk transport rates of ozone (k_{b,s,O_3}) and shikimic acid ($k_{ss,b,Y}$), the surface equilibrium constant of shimic acid (K_{bs}) and the bulk diffusion coefficients of ozone (D_{b,O_3}) and shikimic acid ($D_{b,Y}$).

Table S1 (ESI†). Fig. 2 illustrates the microscopic representations of the processes covered with KM-SUB in this study.

Similar to previous studies[26,47] a near-surface gas-phase layer (extending one mean free path λ_X of the gas molecules from the surface) has been added to explicitly resolve diffusion of gas molecules to the surface. The gas phase diffusion flux J_{diff} from the flow tube centre with far from surface trace gas concentration $[X]_g$ to the near-surface gas phase layer with concentration $[X]_{gs}$ is described following the Knopf–Pöschl–Shiraiwa approach for gas phase diffusion in cylindrical reactors.[56]

$$J_{diff} = \frac{3.66 D_{g,X}\left([X]_g - [X]_{gs}\right)}{(d - 2\lambda_X)}, \quad (1)$$

where $D_{g,X}$ is the gas phase diffusion coefficient and d is the tube radius. Since the gas phase oxidant concentration decreases over the length of the flow tube reactor, we assume an effectively lowered $[X]_g$ that is determined by the dynamic equilibrium between loss to the flow tube walls and resupply by gas flow with volumetric flow rate ϕ.

$$\frac{d[X]_g}{dt} = \frac{\phi}{V_{gs}}\left([X]_{g,0} - [X]_g\right) - J_{diff}\frac{A_{gs}}{V_{gs}} \quad (2)$$

A_{gs} and V_{gs} are the surface area and volume of the near-surface gas phase layer, respectively.

Bulk diffusion is treated as first order process, following Fick's first law of diffusion.[55] While Fickian diffusion is a continuum approach that strictly only applies if molecular motion can be described by random motion of an ensemble of molecules, continuum conditions can always be generated by choosing sufficiently small layer sizes. At low diffusivity and high reactivity, however, the spatial extension of diffusion gradients approaches the molecular length scale, which can induce effects related to coarseness of matter in reaction–diffusion systems. To consider these effects, we chose a lower limit for bulk layer thickness of 0.3 nm, congruent with previous work.[57]

In contrast to the original KM-SUB, the quasi-stationary surface layer (ss) has a certain extent into the particle and hence also constitutes the near-surface bulk. The surface concentration of bulk material (*i.e.*, shikimic acid), $[Y]_{ss}$, can be interpreted as concentration of reactive sites (*i.e.* C–C double bonds) accessible by surface-adsorbed molecules. This entity depends crucially on molecular structure and orientation: molecules may spread out at the surface or form a densely packed monolayer. The reactive site of a molecule in the surface layer might not be facing upwards but be directed away from the surface and may not undergo a surface layer-type reaction.[58] Thus, we define the surface-accessible fraction of reactive sites by defining a surface equilibrium constant K_{bs} that relates an equilibrium near-surface bulk concentration $[Y]_{b1,eq}$ to an equilibrium surface concentration $[Y]_{ss,eq}$. K_{bs} can be interpreted as a depth to which surface-adsorbed ozone molecules can still react with near-surface bulk molecules without undergoing a phase transfer into the bulk phase.

$$K_{bs} = \frac{[Y]_{ss,eq}}{[Y]_{b1,eq}} \quad (3)$$

The RH-dependent initial bulk concentration $[Y]_{b,0}$ is derived from hygroscopicity measurements in an electrodynamic balance.[59] The use of K_{bs} enables to consider ordered surface orientations[58] or increased surface concentrations of surface-active components such as surfactants. This equilibrium is created by relating the rate constants for surface-to-bulk transport, $k_{ss,b,Y}$, and *vice versa*, $k_{b,ss,Y}$, also considering the partial coverage of surface sites θ_{ss}.

$$k_{b,ss,Y} = k_{ss,b,Y}(1 - \theta_{ss})K_{bs} \quad (4)$$

As modification to the original KM-SUB, the surface exchange rates of X and Y have been decoupled from the respective bulk diffusion coefficients. $k_{b,ss,Y}$ and $k_{s,b,X}$ are hence used as separate input parameters. Surface molecules could be either more mobile[60] (as in quasi-liquid surface layers of solids) or more

immobile than molecules in the bulk of a sample (*e.g.* through high surface tension). Analogously, molecules may exchange quickly between surface and near-surface bulk or be locked in either one of both positions, which should be represented by the surface–bulk exchange rates. The total number of surface adsorption sites, N_{max}, is approximated as the inverse of an effective molecular cross section of O_3, σ_{O_3}. In the original KM-SUB approach, σ_{O_3} is assumed to be equivalent to the geometrical size of O_3. However, O_3 molecules might occupy a larger area on the surface than their geometrical size, or the density of stable adsorption sites might be lower than the closest possible packing of O_3. To account for such aspect, σ_{O_3} is used as a fit parameter in this study. The effective molecular cross section of shikimic acid, σ_Y, was assumed to be 3.34×10^{-15} cm^2, limiting its surface concentration to a maximum of $[Y]_{ss,max} = 3 \times 10^{14}$ cm^{-2}. A summary of all input parameters for KM-SUB is given in Table S1 (ESI†).

2.2 Global optimization algorithm

In order to obtain a common kinetic parameter set describing all experimental data sets, we used a global fitting method combining a uniformly-sampled Monte-Carlo (MC) search with a genetic algorithm (GA).[12,47] In the MC search, kinetic input parameters for KM-SUB were varied randomly within individual bounds. All measurements were fitted simultaneously by the model and the correlation between modelled uptake coefficient $\gamma_{mod}(t)$ and experimentally determined uptake $\gamma_{exp}(t)$ evaluated in a least-squares fashion. For each experimental data set i, the residual r_i was calculated in log-space to account for the large range of γ observed during the experiments.

$$r_i = \frac{1}{f_i}\sqrt{\frac{1}{j_i}\sum_{i=1}^{n}\left(\log_{10}(\gamma_{mod}(t_i)) - \log_{10}\left(\gamma_{exp}(t_i)\right)\right)^2} \qquad (5)$$

Each data set was weighted by its number of data points j_i and by a weighting constant f_i that accounts for scatter within each data set. In this study all data sets were weighted equally ($f_i = 1/12$). To ensure correlation between model and experiment over the entire time range, the experimental input data was spaced logarithmically in time. Finally, the tested parameter set is assessed by the sum of the single residuals $R = \sum r_i$. The globally best-fitting parameter sets, *i.e.* the sets with lowest R, are fed into the starting population of a genetic algorithm (GA, Matlab® Global Optimization Toolbox) in which they are optimised by processes mimicking survival, recombination and mutation in evolutionary biology. To ensure diversity within the pool of parameter sets and to counteract the sampling bias from shallow local minima, the same number of random KM-SUB input parameter sets was added to the starting population. In the GA step, the same parameter boundaries were used as in the preceding MC step. The optimization was stopped when the population was homogeneous and thus the increase in correlation with the experimental data ceased. Multiple optimizations were conducted to ensure that using different starting parameter sets would not lead to a better correlation and a global minimum was reached. The bulk diffusion coefficients, D_{b,O_3} and $D_{b,Y}$, are expected to vary with relative humidity,[8] so for each humidity, an individual coefficient was assigned. We also found that varying the rates of surface–bulk transport, $k_{ss,b,Y}$ and k_{b,s,O_3}, the Henry's law solubility coefficient H_{cp,O_3} and the surface equilibrium constant K_{bs} as a function of RH leads to a much better correlation to the experimental data. It was assumed that each parameter is a monotonic function of RH, which reduced the input parameter space dramatically and led to much faster convergence in the MCGA fitting. For all other input parameters, RH dependence was neglected and the same values for the input parameters are used for all experimental conditions. The full list of kinetic parameters obtained by fitting KM-SUB to the 12 experimental data sets is given in Table S2 (ESI†). Some kinetic parameters remained fixed during the fitting process. The gas-phase diffusion coefficient of ozone, D_{g,O_3}, was measured to be 0.14 cm^2 s^{-1}.[61] Kinetic limitation by surface accommodation is not expected in the shikimic acid ozonolysis reaction system with low uptake coefficients ($<10^{-5}$), hence, $\alpha_{s,0}$ was set to 0.5 based on previous studies of kinetic modelling[8,62] and molecular dynamic simulations.[63–65]

In total, we varied 11 parameters, 6 of which were allowed to increase or decrease monotonically over 6 steps in relative humidity. Thus, a total of 41 distinct parameter values were obtained during optimization to the experimental data. Optimization of such a large parameter set is computationally expensive and only feasible on a computer cluster for models like KM-SUB. In a typical optimization 10 million single KM-SUB model runs were performed, requiring about 2 days of computation time on 120 CPUs. After global optimization, a 1D local optimization (golden cut search) was performed to check for local convergence. In this step, the monotonicity restraint of the parameter's RH dependence was not applied. To decrease computation time, the initial global fit was conducted without gas-phase diffusion and gas-phase loss corrections, which accelerated computation by a factor of 10. The obtained result was then optimised locally to re-fit to the experimental data including the additional minor correction terms.

3 Results and discussion

3.1 Uptake data and global optimization results

The experimental uptake coefficients[53] and the corresponding KM-SUB results obtained with the MCGA algorithm are shown in Fig. 1. Panel A shows a clear increase in γ upon increase in RH, consistent with recent experimental data.[8,32] In panel B, the effect of changing gas-phase ozone concentration is displayed for 24% RH (blue lines) and 92% RH (red lines): at high $[O_3]_g$, a lower γ is observed. The correlation between model and experiment is high overall, achieving a low total residual R of 0.020 according to eqn (5).

The plot of uptake data against time reveals a step profile in which several plateaus can be identified. The first prominent plateau in the experimental data occurs at around 100 s and transitions into a second plateau at around 1000 s. In the low RH data we can also find signs for a third plateau at $\sim 5 \times 10^4$ s reaction time. This can be understood by the model results

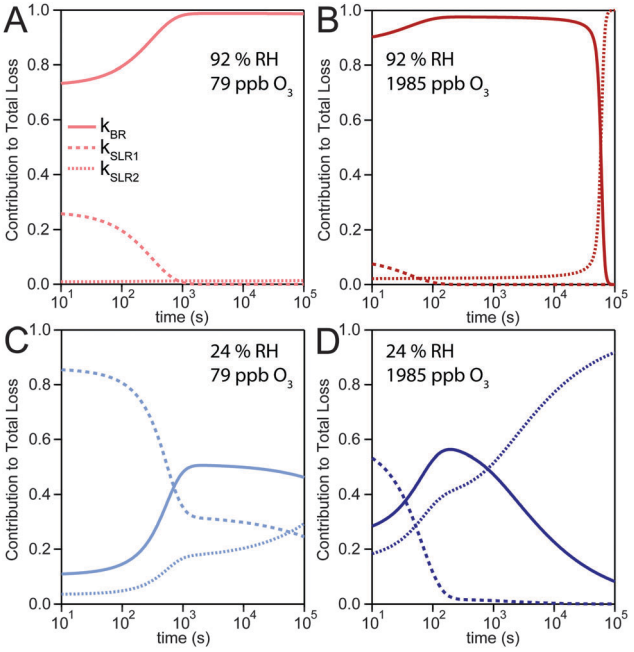

Fig. 3 Contribution of three reaction pathways to the total loss rate of ozone: a bulk reaction between ozone and shikimic acid (BR, solid lines), a bimolecular surface layer reaction between ozone and shikimic acid (SLR1, dashed lines), and the self-reaction of two ozone molecules adsorbed to the surface (SLR2, dotted lines). Modelling results are shown for two relative humidities and two ozone concentrations: (A) 92% RH, 79 ppb O_3, (B) 92% RH, 1985 ppb O_3, (C) 24% RH, 79 ppb O_3, (D) 24% RH, 1985 ppb O_3.

shown in Fig. 3, which details the contribution of the three pathways of ozone loss (SLR1, SLR2, BR) to the total ozone loss at 24 and 92% RH for 79 and 1985 ppb $[O_3]_g$ in the kinetic model.

Until around 1000 s reaction time, surface reaction between ozone and shikimic acid (SLR1, dashed lines) contributes significantly to the overall ozone loss under all conditions. We thus term the initial plateau the surface reaction plateau. This is consistent with previous resistor model descriptions and justified by its inverse O_3 concentration dependence.[53] The integral uptake within this period corresponds roughly to a monolayer of shikimic acid.[53] The relative contribution of SLR1 is highest at low $[O_3]_g$ and dry RH. However, the absolute rate of surface reaction is almost independent of RH and rather a function of $[O_3]_g$.

The contribution of SLR1 becomes very low after 1000 s due to depletion of shikimic acid at the surface except in the case of low $[O_3]_g$ and low RH (panel C), where surface reaction remains substantial as transport of bulk material Y to the surface is sufficiently fast and bulk reaction sufficiently slow to maintain a high quasi-stationary concentration of surface-exposed molecules. After 1000 s, bulk reaction (BR, solid lines) dominates the overall uptake for the majority of the investigated cases. Thus, the second plateau in the experimental uptake data can be termed as the bulk reaction plateau. The model result again confirms the assignment of this kinetic regime based on qualitative arguments with the resistor model.[53] Self-reaction between two ozone molecules at the surface (SLR2, dotted lines) is present at all times and shows a high relative contribution when the overall ozone uptake is low ($\gamma < \sim 10^{-6}$). When the bulk material is used up or strongly shielded by unreactive product, SLR2 will dominate the ozone loss, creating a third plateau on the reaction coordinate, the self-reaction plateau. Note that this case cannot be introduced into a classical resistor model.[53] At lower RH, model and experiment deviate slightly at reaction times $> 2 \times 10^4$ s. This data might however be influenced by a drift of the baseline concentration of ozone (see discussion in ref. 53). This is evident from the curvature of the experimental data after 2×10^4 s: while some of the uptake data at low RH are right-bent (drop in γ accelerates) as is especially pronounced in the 0% RH data set, others are left-bent (drop in γ halts) as can be seen in the 495 ppb and 1985 ppb data set at 24% RH.

The 1985 ppb data set at 92% RH (dark red markers in Fig. 1) shows an important feature that is fully captured by the KM-SUB model: due to fast reaction in the liquid film at high RH and a high ozone concentration, shikimic acid is depleted in the flow reactor which causes a steep drop in γ after about 10^4 s of ozone exposure, providing an important constraint on the magnitude of the bulk reaction rate coefficient, k_{BR}.

3.2 Kinetic regimes of the reaction system

In addition to characterization of the three major pathways of ozone loss, a full determination of the kinetic regime of a reaction system is required for identification of the physical or chemical processes limiting overall gas uptake.[47,66] We characterise the regime by three classification parameters:[20] the contribution of surface reaction to the total chemical loss rate (STLR), the saturation ratio assessing the supply of reactants from the gas phase (SR) and a mixing parameter assessing the extent of spatial heterogeneity in the particle phase (MP). The kinetic regimes and limiting cases defined by these criteria can be visualised in a "kinetic cube", in which each axis corresponds to one of the three classification parameters. At the extremes of the classification parameters (vertices of the kinetic cube), we find the limiting cases usually used in kinetic modelling studies such as a bulk reaction with well-mixed reactants (B_{rx}) or a surface reaction limited by diffusion of bulk material to the surface (S_{bd}).[47] For these cases we assign term-symbol like identification symbols that reveal the predominant reaction location ("G"as phase, "S"urface or "B"ulk) and the limiting process (rx: chemical reaction, bd: bulk diffusion, mt: mass transfer, gd: gas diffusion) of the reaction system. A more detailed description of the concept of kinetic regimes and the kinetic cube can be found in Berkemeier *et al.*[47] and in the ESI† (Section A).

A detailed look into the kinetic regime of the shikimic acid – ozone reaction system is provided in Fig. 4. Fig. 4A shows the temporal evolution of γ at 178 ppb ozone and 24% RH and highlights five distinctive points (yellow circles) on the reaction coordinate. Fig. 4B outlines the corresponding evolution of the kinetic regime in the kinetic cube. Fig. 4C shows a projection of the top plane of the kinetic cube (shaded area in panel B) and compares with the corresponding experiment at 92% RH to outline the differences in the kinetic regimes at higher RH.

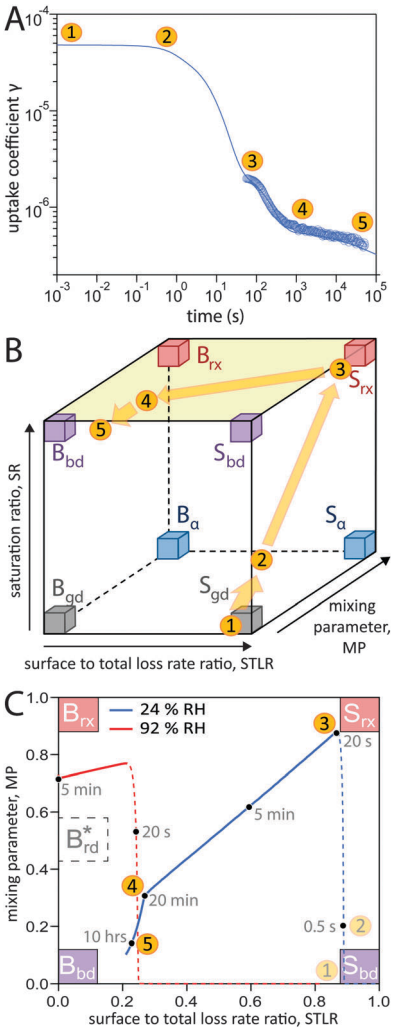

Fig. 4 Temporal evolution of the reaction system's kinetic regime. (A) 5 characteristic points on the reaction coordinate. (B) These points lie on a trajectory through the kinetic cube,[47] representing the change of the limiting process. From an initial gas-diffusion limited surface reaction (S_{gd}), the system transitions into a reaction-rate limited surface reaction (S_{rx}). After an inflection point, the system evolves towards a bulk-diffusion limited bulk reaction (B_{bd}). (C) View at the top plane of the kinetic cube (marked green in panel b) with trajectories at 24% RH (blue solid line) and 92% RH (red solid line). Dashed lines are drawn while not in the top plane (SR < 0.8).

At (1), the near-surface gas phase in the flow reactor is nearly depleted of O_3 due to rapid adsorption of ozone, leading to an effective surface reaction in the absence of competition for adsorption sites. The ozone uptake is thus limited by gas-phase diffusion and falls into the limiting case S_{gd}. At (2), the saturation ratio SR has increased due to accumulation of O_3 molecules, possibly in the form of reactive oxygen intermediates,[62] at the surface. This process continues until (3) when the adsorbed molecules have reached an effective/dynamic Langmuir adsorption equilibrium with the gas phase, reflected by a mixing parameter MP close to 1. At this stage, ozone uptake and loss of bulk material are limited by chemical reaction at the surface and the system falls into the limiting case S_{rx}. After 100 s of reaction time, depletion of surface-exposed bulk material causes a strong concentration gradient of shikimic acid in the bulk (decrease of MP) and bulk reaction becomes more important (decrease of STLR) as shown in Fig. 3. The system now strives towards a dynamic equilibrium at (4), in which bulk reaction and surface reaction are balanced (STLR $\sim$ 0.25) and bulk diffusion of both ozone and shikimic acid severely limits the reaction (MP $<$ 0.4). From that point, changes in the kinetic regime occur very slowly. Over the next hours, the diffusion flux of bulk material to the surface is gradually reduced, as bulk material is increasingly depleted in the near-surface bulk, indicated by a slow decrease in STLR and MP. At (5), the system is mainly limited by bulk diffusion, almost reaching the corresponding limiting case B_{bd}.

Panel C shows that at higher RH (red dashed and solid line), a slightly different route is taken through the kinetic cube compared to the dry state (blue dashed and solid line). The contribution of bulk reaction increases quickly after the start of ozone exposure due to fast bulk diffusion. The system quickly reaches its dynamic equilibrium at a much higher value of MP ($\sim$0.72). Ozone uptake is overall dominated by bulk reaction and diffusion and the system neither occupies a state where both reactants are well-mixed (*i.e.* B_{rx}), nor a state where the reaction is only constrained to the near-surface bulk (traditional reacto-diffusive case, B_{rd}*, ref. 47).

Even though in both cases described in Fig. 4C a dynamic equilibrium is reached after an initial phase of transient behaviour, the steady state behaviour is not compliant with standard limiting cases that can be described by analytical expressions of traditional resistor models.[45–47,67,68] To our knowledge, no analytical expressions are available that describe a system driven by counter-diffusion of two reactive components (B_{bd} limiting case) as observed at low RH. While analytical expressions are well-known for the limiting cases B_{rx} and B_{rd}*, there is no simple model for cases that lie between the two extremes, as observed at high RH.

To illustrate these two types of diffusion behaviour, KM-SUB is used to create time-resolved depth profiles of bulk material as shown in Fig. 5. The analysis shows that under dry conditions shikimic acid is only degraded very close to the surface, in agreement with a study by Steimer *et al.* who showed no visible decay of bulk material using STXM microscopy.[69] Even at 45% RH and after 10^5 seconds reaction time, only the topmost 5% of the 200 nm film show significant loss in bulk material. In this case the reacto-diffusive length of ozone (black dashed lines), *i.e.* the effective depth over which reaction occurs,[70] is merely 0.3% of the total film thickness. Upon increase in RH, elevated bulk diffusion coefficients lead to a larger reaction zone of ozone and shikimic acid as indicated by a larger reacto-diffusive length and hence a broader band of reduced shikimic acid concentrations at the film surface (69% RH and 83% RH). Note that at these intermediate humidities, no chemical gradients were detected using STXM microscopy as particles were already well-mixed at and above 52% RH. This disagreement is most likely due to the uncertainty in determining $D_{b,Y}$ caused by reaction products that might alter the diffusion coefficient inside the organic matrix as discussed in Section 3.3 below. At 92% RH,

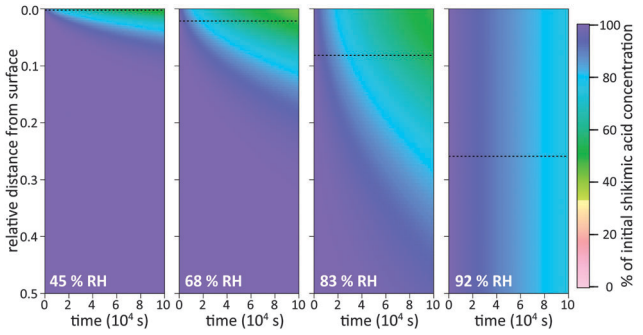

Fig. 5 Depth profiles of shikimic acid concentration in a film during exposure of 178 ppb ozone as a function of time and relative humidity (RH). The *y*-axis depicts the relative distance from the film surface (0 at the surface and 0.5 at half-way through the film). At 83% RH and lower, the concentration of shikimic acid shows radial inhomogeneity. Upon increase in RH the penetration depth of ozone increases, here assessed by the classical reacto-diffusive length of ozone (black dotted line). At 92% RH, shikimic acid is perfectly mixed and decays homogeneously throughout the entire film.

shikimic acid is well-mixed in the model and ozone molecules reach almost the entire film depth, which is again consistent with STXM microscopy. These results on chemical gradients complement recent studies, which proposed the formation of chemical gradients in the oxidation of organic aerosol by OH[12,44] and NO_3.[15] Our study shows chemical gradients even for the much slower reaction of organic aerosols with ozone.

3.3 Kinetic parameters obtained from global optimization

Fig. 6 shows the s-shaped humidity dependence of D_{b,O_3} as determined by global optimization to the experimental data (solid circles). Such functional forms with a constant D_{b,O_3} at low RH and a strong increase at medium RH are consistent with percolation theory,[71] an approach commonly used to describe systems where small molecules percolate through a rigid matrix of larger molecules.[8,19] Measurements of D_{b,H_2O} in shikimic acid by Steimer *et al.*[59] (blue shadings) revealed overall higher diffusion coefficients and no s-shape of the D_{b,H_2O} curve. The D_{b,O_3} curve however closely resembles the estimate of water diffusivity (D_{b,H_2O}) in α-pinene secondary organic aerosol (SOA) of similar oxidation state (molecular O/C ratio of 0.7) obtained with the semi-empirical method described in Berkemeier *et al.*[42] (orange shadings). The values determined for D_{b,O_3} are slightly shifted towards lower diffusivities compared to recent experimental data of less oxidised α-pinene SOA in ref. 54 (green shadings) and ref. 72 (purple shadings), but show the same qualitative shape. The difference is in line with the results of Berkemeier *et al.*,[42] who predicted a decrease in diffusion rates upon chemical ageing, *i.e.* by an increase in molecular O/C ratio. At a molecular O/C ratio of 0.5, the estimated diffusion coefficients of Berkemeier *et al.*[42] coincide with the results of Lienhard *et al.*,[54] who determined the molecular O/C ratio of their SOA samples to 0.53. A part of the difference between D_{b,H_2O} and D_{b,O_3} can be attributed to the molecular size of ozone, which is almost three times larger than water.

Hence, results are closely related, even though the method of determining diffusion coefficients in this paper is conceptually

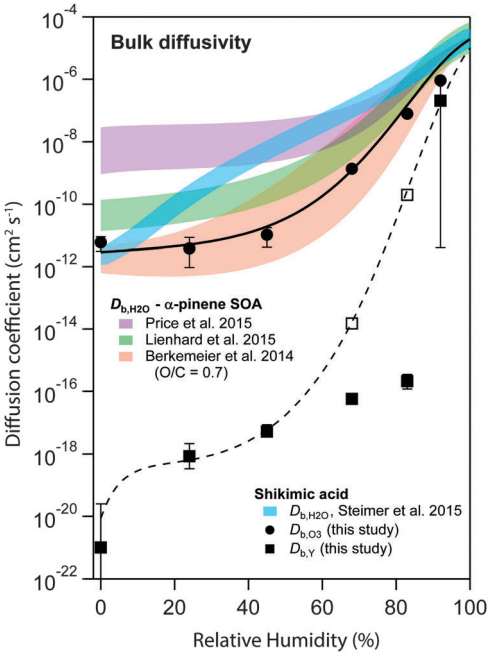

Fig. 6 Humidity dependence of the bulk diffusion coefficients of ozone (D_{b,O_3}, black circles) and shikimic acid ($D_{b,Y}$, black squares) as determined by global optimization to the experimental data set. The black solid and the dashed line represent a fit to a Vignes-type equation for ozone and shikimic acid, respectively. Open square markers indicate model runs including product effects, consistent with the Vignes-type fit. Blue shadings are measurements of water diffusivity in shikimic acid as measured by Steimer *et al.*[59] Red shadings indicate an estimate of water diffusivity in SOA corresponding to the molecular O/C ratio of shikimic acid.[42] Measurements on SOA at slightly lower molecular O/C ratio have been performed by Price *et al.* (purple shadings) and Lienhard *et al.* (green shadings).[54,72]

very different to the established methods for determination of water diffusion coefficients in organic material. In previous work using a steady-state approach, it was not possible to reconcile diffusion coefficients from RH-dependent kinetic data.[53]

The D_{b,O_3} curve can be fitted as a function of molar organic fraction x_{org} by the Vignes-type eqn (6) used in Lienhard *et al.*,[54]

$$D_b = (D_b^w)^{\alpha(1-x_{org})}(D_b^{org})^{\alpha x_{org}} \quad (6)$$

$$\ln \alpha = x_{org}^2(C + 3D - 4Dx_{org}) \quad (7)$$

D_{b,O_3}^w and D_{b,O_3}^{org} are the ozone diffusivity in pure water and pure organics, respectively. The equation uses a correction factor α that has the form of an activity coefficient. The parameters for eqn (6) and (7) used in this study are listed in Table S3 (ESI†).

Fig. 6 also includes the humidity dependence of $D_{b,Y}$, which shows many orders of magnitude lower values than D_{b,O_3}. $D_{b,Y}$ increases from $\sim 10^{-20}$ cm^2 s^{-1} to 10^{-7} cm^2 s^{-1} upon increase of RH, reflecting that the phase state of shikimic acid changes from amorphous solid over semi-solid to liquid (moisture-induced phase transformation[73]), compliant with earlier work.[39] The dashed black line represents a fit using the Vignes-type equation. Note that a good fit was only obtained neglecting the values at 68 and 83% RH. At this intermediate humidity, $D_{b,Y}$ needs to be $\sim 10^{-17}$ cm^2 s^{-1} to explain the slow reduction in γ at

long reaction times seen in the experimental data (*cf.* Fig. 1) as $D_{b,Y}$ controls the slope of this reduction (*cf.* Fig. S1, ESI†). Such low diffusivity would lead to incomplete mixing of bulk material in the model (as discussed in Fig. 5 and Section 3.2), which is not in line with previous results by Steimer *et al.*,[69] who observed well-mixed particles during ozonolysis down to 67% RH using STXM microscopy. This disparity may be caused by product effects not captured by the kinetic model: A slight decrease in D_{b,O_3} or H_{cp,O_3} over time could lead to a similar deceleration of reaction kinetics. A recent study has shown that oxidative processing of organic aerosols can lead to an increase of viscosity, and hence decrease of bulk diffusivity according to the Stokes–Einstein relation.[23] Also, polar products could preferentially adsorb to the surface, blocking surface sites and reducing surface–bulk transport rates. Such product effects reducing diffusivities cannot be distinguished in the model from incomplete transport of shikimic acid to the surface. Test runs with composition-dependent D_{b,O_3} showed that the values of $D_{b,Y}$ indicated by the open square markers in Fig. 6 could be supported by the model if D_{b,O_3} would decrease over the course of the 16 h experiment by factors of 5 and 2.5 at 68% RH and 83% RH, respectively. In this scenario, no diffusion gradients would be present in shikimic acid at 68% and 83% RH (Fig. S2, ESI†), which is in contrast to the results shown in Fig. 6, but consistent with STXM experiments.[53] A thorough discussion of the effect of reaction products on reactive uptake is however beyond the scope of this study as laboratory experiments only measured gas-phase ozone concentrations. The very low values for $D_{b,Y}$ obtained in this study at medium to high RH values should hence be handled with reservation.

Fig. 7 shows the humidity dependence of the Henry's law coefficient of ozone, H_{cp,O_3}, which is used to describe the saturation concentration of ozone in the organic matrix. Henry's law coefficients (green diamonds) were found to decrease with decreasing organic weight fraction, w_{org}, following a logarithmic mixing rule (green solid line), eqn (8). H^{w}_{cp,O_3} and H^{org}_{cp,O_3} are the Henry's law coefficients of ozone in pure water[74] and pure organics, respectively.

$$H_{cp,O_3} = \exp\left((1 - w_{org}) \log\left(H^{w}_{cp,O_3}\right) + w_{org} \log\left(H^{org}_{cp,O_3}\right)\right) \quad (8)$$

The value of 1.8×10^{-4} mol cm^{-3} atm^{-1} determined for H^{org}_{cp,O_3} seems reasonable compared to Henrys law coefficients for decane[75] and oleic acid[67] (dashed black lines in Fig. 7).

The organic acid thus shows an effect similar to the salting-out behaviour known for inorganic solutes, but acts in the opposite direction ("salting-in") comparable to other organic solvents investigated previously such as acetic acid.[76] Error bars in Fig. 6 and 7 represent the interval in which a model parameter can be varied until the total residual R increases by 20%.

Note that these 1-dimensional degrees of freedom are measures of parameter sensitivity and do not consider interactions between model parameters, which will be discussed in Section 3.4. The optimization yielded a bulk reaction rate coefficient k_{BR} of 4.4×10^{-18} cm^3 s^{-1}, which compares well to literature values for similarly functionalised molecules such as maleic acid

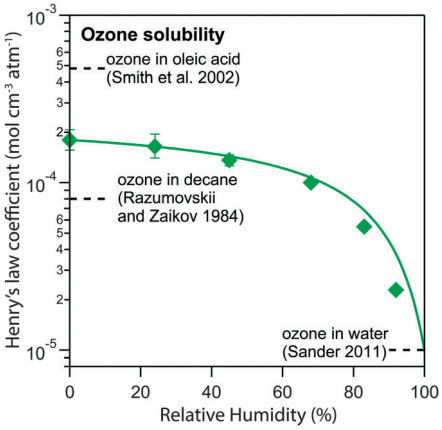

Fig. 7 Henry's law coefficient of ozone H_{cp,O_3} (green diamonds) determined by global optimization to the experimental data set. The data can be explained with a logarithmic mixing rule (green solid line).

(1.7×10^{-18} cm^3 s^{-1}) or fumaric acid (1.0×10^{-17} cm^3 s^{-1}) in aqueous solution.[77] The value is also consistent with the bulk reaction rate coefficient of 6.1×10^{-18} cm^3 s^{-1} obtained by steady-state analysis.[53]

The surface reaction rate coefficient for ozonolysis of shikimic acid k_{SLR1} (8.5×10^{-16} cm^2 s^{-1}) is found to be one order of magnitude higher than the ozone self-reaction rate coefficient k_{SLR2} (4.3×10^{-17} cm^2 s^{-1}). A self-reaction of ozone at the particle surface could not be captured by steady-state analysis using the resistor model approach, leading to overall lower correlation to the experimental data especially at dry RH, or an overestimation of bulk diffusion coefficients at low RH.[53] Including such a self-reaction adds a constant loss term that enables to describe the experimental data at dry RH while staying consistent with data obtained using other experimental techniques.[59,69]

The bulk–surface partitioning parameter K_{bs} also shows humidity-dependence and ranges from 2.0–9.3 $\times 10^{-9}$ cm, indicating that the relative amount of molecules accessible by surface adsorbed reactants increases with humidity. This suggests that shikimic acid molecules are slightly surface active and enrich at the surface of more dilute aqueous solutions. Note that while K_{bs} spans almost one order of magnitude, the surface concentration increases only by 84% over the entire humidity range due to overall dilution of the aqueous solution. The moderate increase could be due to a packing effect: at low RH, molecules might show a random orientation toward the particle surface, while at high RH molecules may form a structured outer layer on top of the aqueous solution. In addition, the mobility of the surface monolayer could play a significant role: at low RH, surface molecules may be immobile and a reactive site that is directed away from the surface would be inaccessible by adsorbed reactants. Such a molecule would not be able to undergo surface layer reaction, which effectively reduces the surface concentration of reaction sites irrespective of the concentration of surface molecules. These findings are supported by Vieceli *et al.*,[58] who demonstrated the importance of molecular orientation and double bond orientation in alkene ozonolysis systems at different phase states using molecular dynamics simulations.

A different interpretation of this enhanced surface reactivity could be influence of water molecules on the chemical reaction as has been observed in the ozonolysis of maleic acid[78] and phosphocholine.[79] This would however require existence of a long-lived reaction intermediate whose decomposition can be induced with water molecules and serves as rate-determining step in the reaction mechanism. We discuss the possibility of such reaction intermediates in Section 3.5.

Analysis of the rate coefficients for surface–bulk exchange k_{b,s,O_3} and $k_{ss,b,Y}$ reveals that the exchange process cannot be described simply by means of diffusion. The surface–bulk exchange rates are accelerated compared to the rates of bulk diffusion layer at low RH and are found to be overall less dependent on RH. Such surface layers of enhanced mobility are well-known in quasi-liquid surface layers of solid surfaces.[60] At low RH, the surface–bulk-exchange rates had thus little influence on calculation results. At higher RH, k_{b,s,O_3} approaches the value expected for a pure diffusive process, whereas $k_{ss,b,Y}$ behaves differently: surface–bulk exchange is slowed down heavily at 92% RH compared to the analogous diffusion process. Hence, replenishment of bulk molecules on the surface is at low RH limited by bulk transport and at high RH limited by bulk–surface exchange. A possible reason is the replacement of shikimic acid molecules at the surface by more polar products, preventing an effective surface reaction after depletion of the initial surface layer. Such a low surface–bulk exchange rate was necessary to describe the experimental data, as otherwise the surface reaction plateau, clearly visible in the experimental data, was not reproduced by the model.

3.4 Uniqueness of the kinetic parameter set

Even though a kinetic parameter set was found to fit an experimental data set sufficiently well, these parameters might not constitute the only set generating the same model output and hence not be a unique solution of the optimization problem. If a subset of parameters is mutually dependent, different combinations of these parameters will give an identical result. It is then not guaranteed that a fitted parameter value equals its physical counterpart. In the following we will refer to such parameter pairs or sets as non-orthogonal parameters. We show that the problem of non-orthogonality can often be overcome by fitting many data sets obtained at various experimental conditions and over long time spans. Two parameters might only differ in their influence on the calculation result at specific points during the reaction course (Fig. S1 and S3, ESI†) or show a different effect on the model output under varying experimental conditions.

The existence of non-orthogonal parameter sets was investigated for many combinations of input parameters by distributing the parameters on two axes and calculating the total residual R as a 2D contour map. Parameters λ_i were varied by a factor $f(\lambda_i)$ yielding $\lambda_i' = f(\lambda_i)\,\lambda_i$ with $f(\lambda_i)$ spanning four orders of magnitude from 0.01 to 100. Parameters on the same axis were varied uniformly. A few selected results computed at 24% RH are shown as contour plots in Fig. 8. By far the most common result of this analysis was a distinct minimum in which also the global fitting result (red cross) fell. An example for this is Fig. 8A, which shows a 2D contour map for the parameters τ_{d,O_3} and σ_{O_3}. While both parameters control the Langmuir adsorption equilibrium concentration of ozone at the surface and are thus potentially non-orthogonal, a distinct minimum was found. The two parameters decouple as experimental data with multiple ozone gas phase concentrations is used and τ_{d,O_3} and σ_{O_3} behave differently upon change in $[O_3]_g$.

Non-orthogonality was observed when k_{BR}, k_{b,s,O_3} and D_{b,O_3} were varied uniformly and plotted against H_{cp,O_3} in Fig. 8B. This finding shows that the values of the parameters H_{cp,O_3}, k_{BR}, k_{b,s,O_3} and D_{b,O_3} cannot be uniquely determined unless any of the parameters is constrained. Note that only the simultaneous increase of the diffusion and reaction parameters can compensate the increase in H_{cp,O_3}, for smaller subsets of the parameters full non-orthogonality was not observed (Fig. 8C). Hence, constraining one of these parameters would determine all others. Since the Henry's law coefficient of ozone can be constrained fairly well in the aqueous solution, the 92% RH data set can be used to constrain all other parameters. By assuming a H_{cp,O_3} between 1–3 $\times$ 10^{-5} mol cm^{-3} atm^{-1}, k_{BR} can be constrained between 3 $\times$ 10^{-18} and 1 $\times$ 10^{-17} cm^2 s^{-1}, D_{b,O_3} between 2–6 $\times$ 10^{-6} cm^2 s^{-1} and k_{b,s,O_3} between 14.5–43.5 cm s^{-1}. The diffusion coefficients D_{b,O_3} and $D_{b,Y}$ were also found to be orthogonal (Fig. 8D). Note that with a larger subset of parameters, the chance of finding

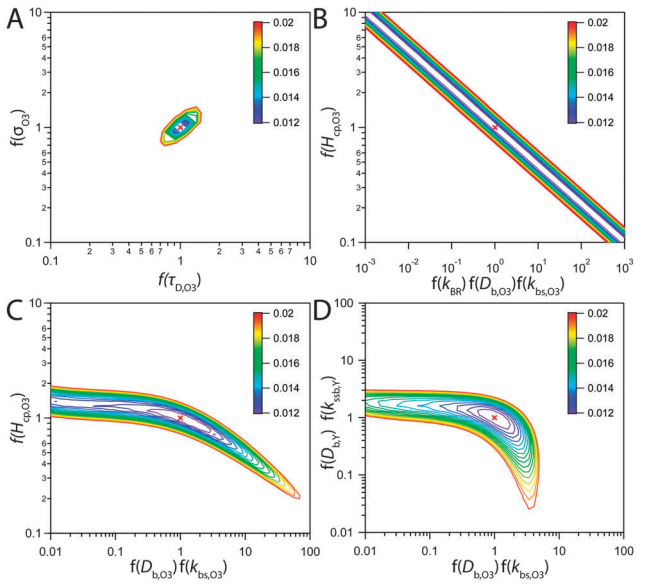

Fig. 8 Total residual R (colour bar) between experimental data and KM-SUB model results in the local environment of the best fitting parameter set (red crosses, *cf.* Table S2, ESI†). The best fit parameters λ_i were multiplied by a factor $f(\lambda_i)$ and the residual calculated after eqn (5) and $R = \sum r_i$, to obtain the depicted contour lines. Panel A shows a distinct minimum in R, indicating that an optimum value for both σ_{O_3} and τ_{d,O_3} was found in the 2D subspace. Panel B shows that when k_{BR}, D_{b,O_3} and k_{b,s,O_3} are varied uniformly against H_{cp,O_3}, a stretched out unconfined minimum is obtained and the parameters are thus non-orthogonal and hence not uniquely defined. Panel C showcases that the same dependence is not observed for subsets of these parameters. Panel D shows that diffusivities of O_3 and shikimic acid are not interchangeable.

non-orthogonal input parameters can be higher. We tested up to four parameters in two dimensions, as this was the maximum computationally feasible. We cannot exclude that more flexibility exists in the choice of kinetic input parameters reproducing the experimental data.

Another way of detecting dependencies between input parameters λ_i is to use sensitivity coefficients $S(\lambda_i)$. Once sensitivity coefficients are obtained this technique is computationally much more efficient as no further model evaluations are needed. A short description of normalised sensitivity coefficients and the method is given in the supplement (Section B). However, no additional co-dependence of parameters was detected using this method.

3.5 ROI reaction mechanism

The desorption lifetime of ozone and the effective molecular cross section of physisorbed ozone are not compliant with a pure physical adsorption process of ozone. In the following we will suggest an alternative reaction mechanism including the formation of reactive oxygen intermediates (ROI) to explain this behaviour.

The desorption lifetime of ozone, τ_{d,O_3}, was determined to be 5.3×10^{-4} s, which is many orders of magnitude larger than the values of order nanoseconds estimated by molecular dynamics simulations[63] and density functional theory.[80] Thus, this value must be an effective value that represents additional processes such as decomposition of ozone and formation of long-lived reactive oxygen intermediates (ROI).[62,81] A physisorption process with unusually long desorption lifetime also leads to artefacts in the simulation data at the sub-minute time scale: a long residence time leads to high initial uptake of ozone onto the organic film, causing the flow tube to deplete on ozone. The experimental data however shows no evidence for full depletion of ozone in the early stages of the experiment,[53] which can only be realised in the kinetic model using desorption lifetimes in the sub-microsecond time range.

The effective molecular cross section of physisorbed ozone, σ_{O_3}, is found to be 2.4×10^{-14} cm^2, which is higher than the geometrical value of 1.5×10^{-15} cm^2, hence effectively reducing the number of sorption sites for ozone. As discussed in Section 2.1 this might be due to electrostatic repulsion of adsorbed molecules or dictated by surface morphology, *i.e.* ozone molecules adsorbing only to certain structural features of the surface. The corresponding maximum surface concentration of adsorbed ozone of 2.4×10^{13} cm^{-2} closely resembles the coverage of surface-accessible double bonds of 1–2 $\times$ 10^{13} cm^{-2} expected from the surface cross section of shikimic acid σ_Y, suggesting that surface-adsorbed molecules may interact with the double bond of shikimic acid and pointing towards formation of ROI on the surface.

Formation of ROI on the surface as a form of ozone chemisorption can also explain the emergence of an additional plateau in the experimental data at very low values of γ: while O_3 molecules are unlikely to react with another directly by simple collision, decomposition into ROI and subsequent recombination of two chemisorbed O_3 molecules could effectively lead to self-reaction of O_3 and explain the non-zero uptake of O_3 onto dry shikimic acid at long reaction times (Fig. 1).

The accepted mechanism of alkene ozonolysis in both, gas and condensed phases, involves formation of a trioxyl diradical (primary ozonide, PO), following the Criegee mechanism.[82–84] The PO further decomposes to a Criegee intermediate and a carbonyl compound.[82] The following chemical mechanism (R1–R3) was used to draw a simplified picture of this rather complicated surface chemistry. Subscripts s and ss denote species adsorbed in the sorption layer or surface-exposed in the quasi-static surface layer, respectively. For ozone from the sorption layer we assume a desorption lifetime of 3.2×10^{-9} s, corresponding to a physisorption energy of 20 kJ mol^{-1}.[62]

$$O_3(s) + Y(ss) \rightarrow \text{ROI-1}(ss) \quad (R1)$$

$$\text{ROI-1}(ss) \rightarrow O_3(s) + Y(ss) \quad (R2)$$

$$\text{ROI-1}(ss) \rightarrow \text{product} \quad (R3)$$

The reaction rate coefficients k_{R1} to k_{R3} were optimised using the MCGA algorithm. k_{R1} was found to be 1×10^{-10} cm^2 s^{-1}, corresponding to an activation energy of 42 kJ mol^{-1}. The back reaction to ozone (R2) was tested, but found to be too slow to influence calculation results, suggesting a relatively stable compound such as PO as intermediate.

Quantum mechanical calculations suggest an activation barrier of $\sim$60 kJ mol^{-1} for the reaction of PO to Criegee intermediates.[86–88] Our model results agree well with these calculations and the corresponding energy profile is shown in Fig. 9.[62]

Note that since no experimental data for decay of the bulk material Y was available, k_{R2} and k_{R3} and the corresponding activation energies could not be uniquely constrained, and hence the identity of the reactive intermediate not unerringly identified. In an alternative formulation of this mechanism, a reversible π-complex between ozone and the double bond could also function as reactive intermediate.[83,84]

While reconciling ozone adsorption properties, the above mechanism cannot fully describe the stable long-term uptake of ozone observed in the experiments under dry conditions since shikimic acid is depleted at the surface under these conditions, hampering the formation of ROI (Fig. S4, ESI†).

Ozone decomposition is known to occur on aromatic surfaces[62] and even on inert surfaces such as mineral dust,[88] demanding an alternative pathway for ozone chemisorption. We thus tested a mechanism involving a second ROI, which can be thought of as oxygen adatom, whose formation is independent of double bond concentration. Formation and consumption of O_2 was neglected in these calculations as its concentration can be assumed constant.

$$O_3(s) \rightarrow \text{ROI-2}(s) + O_2(s) \quad (R4)$$

$$\text{ROI-2}(s) + O_2(s) \rightarrow O_3(s) \quad (R5)$$

$$\text{ROI-2}(s) + Y(ss) \rightarrow \text{product} \quad (R6)$$

$$\text{ROI-2}(s) + \text{ROI-2}(s) \rightarrow O_2(s) \quad (R7)$$

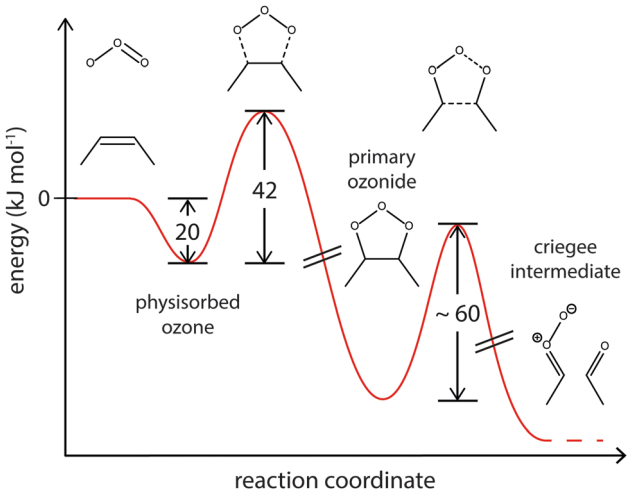

Fig. 9 Suggested energy profile for the surface reaction of shikimic acid with ozone, following a Criegee-type mechanism. The model parameters obtained with global optimization give activation energies of 20 kJ mol^{-1} for desorption of physisorbed oxygen and 42 kJ mol^{-1} for formation of the reactive oxygen intermediate. This intermediate reacts to Criegee intermediates and carbonyl compounds.[85–87]

k_{R4} reveals a fast first-order decomposition of physisorbed ozone at a rate of 7.9×10^4 s^{-1}, corresponding to an activation energy of 40 kJ mol^{-1}. k_{R6} and k_{R7} were determined to 2.5×10^{-14} and 3.1×10^{-14} cm^2 s^{-1}, respectively. The back reaction to ozone (R5) was treated as pseudo-first order reaction and found not to influence ozone loss. Using this mechanism, the self-reaction plateau in the reactive uptake coefficient γ could be reproduced in the kinetic model (Fig. S5, ESI†). Note that the combination of reactions (R4) and (R7) can be regarded as a catalytic cycle of ozone destruction ($2O_3 \rightarrow 3O_2$). The initial reactions of ozone chemisorption and decomposition (R1, R4) exhibit very similar activation energies and also correlate well with previous results on aromatic surfaces,[62] supporting that heterogeneous ozone uptake may exhibit a similar reaction profile on various surfaces.[89] The necessity of two ROIs in the kinetic model to reconcile measurement data indicates that multiple different types of ROI may coexist.

4 Summary and outlook

Multiphase chemistry of ozone plays an important role in degradation and chemical transformation of atmospheric marker substances. The phase state of organic aerosols is expected to vary as a function of environmental conditions such as temperature and relative humidity. Shikimic acid appears to be a good model compound for organic aerosol, as it similarly adopts a (semi)-solid to liquid phase state depending on RH. We demonstrate that phase state strongly affects the rate of reactive uptake and chemical ageing of organic aerosols. The KM-SUB analysis shows that the predominant kinetic regimes change as a function of time and relative humidity and reveals that even the quasi-stationary states along the reaction coordinate cannot be properly described with resistor or simple kinetic models, *i.e.* without the use of depth-resolved computation. Even though depth-resolved computation may be too expensive for large-scale atmospheric models, KM-SUB can be used to develop simple but robust parameterizations for atmospheric models.

The model simulations suggest the formation of reactive oxygen intermediates, likely primary ozonides or O atoms, at the particle surface. Such intermediates can explain the low sorption site density and the long effective desorption lifetime of ozone needed in Langmuir–Hinshelwood type descriptions of this system. The ROIs provide potential pathways for the self-reaction and catalytic destruction of ozone needed to explain the long-term uptake observed under dry conditions.

The ROI-related pathways of ozone degradation at the surface, together with the amorphous solid phase state of organic matter under cold and dry conditions, may help to explain how reactive organic compounds in the bulk of atmospheric aerosol particles are effectively shielded from degradation by ozone. The apparent abundance and longevity of ROIs has implications for human health as they can generate cytotoxic free radicals and cause oxidative stress upon inhalation of particulates.[90]

For future experimental studies, the effect of temperature on reactive gas uptake would be of major interest as temperature affects not only the particle phase state, but also the rates of chemical reactions. Simultaneous detection of both oxidant uptake and decay of bulk material would further constrain the kinetic parameter set. We suggest the use of kinetic flux models alongside future laboratory experiments to detect kinetic regimes and push the reaction system into various cases of well-understood kinetic behaviour through choice of experimental conditions. Large data sets under wide experimental conditions would help to constrain the optimization parameter space and to identify processes necessary for accurate description of the kinetic data. Additional measurements of experimentally accessible physical parameters such as Henry's law and diffusion coefficients as function of humidity and temperature would hereby strongly facilitate the global optimization of models to large experimental data sets. Experiments (or simulations) on the sub-second time scale might help to shine further light on surface adsorption processes. To reveal details about the chemical reaction mechanism, spectroscopic techniques sensitive to short-lived and radical species need to be applied in conjunction with further kinetic experiments and modelling studies to identify the important intermediate species and their interactions.

Acknowledgements

This work was funded by the Max Planck Society (MPG) and the EU project PEGASOS. T. B. was supported by the Max Planck Graduate Center with the Johannes Gutenberg-Universität Mainz (MPGC). M. Ammann acknowledges support by the Swiss National Science Foundation (grant no. 163074). We would like to thank Andrew J. Huisman, Claudia Marcolli, Daniel M. Lienhard, Peter Spichtinger, Andrea Pozzer and Rolf Sander for helpful discussions.

Notes and references

1 M. Kanakidou, *et al.*, *Atmos. Chem. Phys.*, 2005, **5**, 1053–1123.
2 M. Hallquist, *et al.*, *Atmos. Chem. Phys.*, 2009, **9**, 5155–5235.
3 J. L. Jimenez, *et al.*, *Science*, 2009, **326**, 1525–1529.
4 M. O. Andreae and D. Rosenfeld, *Earth-Sci. Rev.*, 2008, **89**, 13–41.
5 U. Pöschl, *Angew. Chem., Int. Ed.*, 2005, **44**, 7520–7540.
6 U. Pöschl and M. Shiraiwa, *Chem. Rev.*, 2015, **115**, 4440–4475.
7 P. J. Ziemann and R. Atkinson, *Chem. Soc. Rev.*, 2012, **41**, 6582–6605.
8 M. Shiraiwa, *et al.*, *Proc. Natl. Acad. Sci. U. S. A.*, 2011, **108**, 11003–11008.
9 S. Zhou, *et al.*, *Faraday Discuss.*, 2013, **165**, 391–406.
10 M. Kuwata and S. T. Martin, *Proc. Natl. Acad. Sci. U. S. A.*, 2012, **109**, 17354–17359.
11 J. H. Slade and D. A. Knopf, *Geophys. Res. Lett.*, 2014, **41**, 5297–5306.
12 A. M. Arangio, *et al.*, *J. Phys. Chem. A*, 2015, **119**, 4533–4544.
13 J. H. Kroll, *et al.*, *J. Phys. Chem. A*, 2015, **119**, 10767–10783.
14 I. J. George and J. P. D. Abbatt, *Nat. Chem.*, 2010, **2**, 713–722.
15 M. Shiraiwa, U. Pöschl and D. A. Knopf, *Environ. Sci. Technol.*, 2012, **46**, 6630–6636.
16 Y. Rudich, N. M. Donahue and T. F. Mentel, *Annu. Rev. Phys. Chem.*, 2007, **58**, 321–352.
17 M. R. Alfarra, *et al.*, *Atmos. Chem. Phys.*, 2012, **12**, 6417–6436.
18 B. Wang, *et al.*, *J. Phys. Chem. A*, 2015, **119**, 4498–4508.
19 M. Shiraiwa, *et al.*, *Proc. Natl. Acad. Sci. U. S. A.*, 2013, **110**, 11746–11750.
20 Y. Rudich, *Chem. Rev.*, 2003, **103**, 5097–5124.
21 F. D. Pope, *et al.*, *Environ. Sci. Technol.*, 2010, **44**, 6656–6660.
22 A. T. Lambe, *et al.*, *Atmos. Chem. Phys.*, 2011, **11**, 8913–8928.
23 N. A. Hosny, *et al.*, *Chem. Sci.*, 2016, **7**, 1357–1367.
24 T. D. Vaden, *et al.*, *Proc. Natl. Acad. Sci. U. S. A.*, 2011, **108**, 2190–2195.
25 J. P. D. Abbatt, A. K. Y. Lee and J. A. Thornton, *Chem. Soc. Rev.*, 2012, **41**, 6555–6581.
26 M. Shiraiwa, *et al.*, *Phys. Chem. Chem. Phys.*, 2013, **15**, 11441–11453.
27 J. Laskin, *et al.*, *Anal. Chem.*, 2010, **82**, 2048–2058.
28 R. D. McWhinney, *et al.*, *Environ. Sci. Technol.*, 2011, **45**, 2131–2136.
29 C. Pfrang, M. Shiraiwa and U. Pöschl, *Atmos. Chem. Phys.*, 2011, **11**, 7343–7354.
30 D. A. Knopf, L. M. Anthony and A. K. Bertram, *J. Phys. Chem. A*, 2005, **109**, 5579–5589.
31 C. Kidd, *et al.*, *Proc. Natl. Acad. Sci. U. S. A.*, 2014, **111**, 7552–7557.
32 F. H. Marshall, *et al.*, *Chem. Sci.*, 2016, **7**, 1298–1308.
33 B. Zobrist, *et al.*, *Atmos. Chem. Phys.*, 2008, **8**, 5221–5244.
34 B. J. Murray, *et al.*, *Nat. Geosci.*, 2010, **3**, 233–237.
35 A. Virtanen, *et al.*, *Nature*, 2010, **467**, 824–827.
36 T. Koop, *et al.*, *Phys. Chem. Chem. Phys.*, 2011, **13**, 19238–19255.
37 E. Saukko, *et al.*, *Atmos. Chem. Phys.*, 2012, **12**, 7517–7529.
38 R. M. Power, *et al.*, *Chem. Sci.*, 2013, **4**, 2597–2604.
39 L. Renbaum-Wolff, *et al.*, *Proc. Natl. Acad. Sci. U. S. A.*, 2013, **110**, 8014–8019.
40 E. Abramson, *et al.*, *Phys. Chem. Chem. Phys.*, 2013, **15**, 2983–2991.
41 H. J. Tong, *et al.*, *Atmos. Chem. Phys.*, 2011, **11**, 4739–4754.
42 T. Berkemeier, *et al.*, *Atmos. Chem. Phys.*, 2014, **14**, 12513–12531.
43 H. C. Price, *et al.*, *Atmos. Chem. Phys.*, 2014, **14**, 3817–3830.
44 J. F. Davies and K. R. Wilson, *Chem. Sci.*, 2015, **6**, 7020–7027.
45 B. J. Finlayson-Pitts and J. N. Pitts, *Chemistry of the upper and lower atmosphere*, Academic Press, San Diego, California, 1999.
46 D. R. Worsnop, *et al.*, *Geophys. Res. Lett.*, 2002, **29**, 57.
47 T. Berkemeier, *et al.*, *Atmos. Chem. Phys.*, 2013, **13**, 6663–6686.
48 G. D. Smith, *et al.*, *J. Phys. Chem. A*, 2003, **107**, 9582–9587.
49 M. Shiraiwa, C. Pfrang and U. Pöschl, *Atmos. Chem. Phys.*, 2010, **10**, 3673–3691.
50 M. Shiraiwa, *et al.*, *Atmos. Chem. Phys.*, 2012, **12**, 2777–2794.
51 P. Roldin, *et al.*, *Atmos. Chem. Phys.*, 2014, **14**, 7953–7993.
52 C. Pfrang, M. Shiraiwa and U. Pöschl, *Atmos. Chem. Phys.*, 2010, **10**, 4537–4557.
53 S. S. Steimer, *et al.*, *Phys. Chem. Chem. Phys.*, 2015, **17**, 31101–31109.
54 D. M. Lienhard, *et al.*, *Atmos. Chem. Phys.*, 2015, **15**, 13599–13613.
55 U. Pöschl, Y. Rudich and M. Ammann, *Atmos. Chem. Phys.*, 2007, **7**, 5989–6023.
56 D. A. Knopf, U. Pöschl and M. Shiraiwa, *Anal. Chem.*, 2015, **87**, 3746–3754.
57 B. Zobrist, *et al.*, *Phys. Chem. Chem. Phys.*, 2011, **13**, 3514–3526.
58 J. Vieceli, O. L. Ma and D. J. Tobias, *J. Phys. Chem. A*, 2004, **108**, 5806–5814.
59 S. S. Steimer, *et al.*, *Atmos. Meas. Tech.*, 2015, **8**, 2397–2408.
60 M. D. Ediger and J. A. Forrest, *Macromolecules*, 2014, **47**, 471–478.
61 W. J. Massman, *Atmos. Environ.*, 1998, **32**, 1111–1127.
62 M. Shiraiwa, *et al.*, *Nat. Chem.*, 2011, **3**, 291–295.
63 J. Vieceli, *et al.*, *J. Phys. Chem. B*, 2005, **109**, 15876–15892.
64 S. Takahama and L. M. Russell, *J. Geophys. Res.: Atmos.*, 2011, **116**, D02203.
65 J. Julin, *et al.*, *J. Phys. Chem. A*, 2013, **117**, 410–420.
66 M. Shiraiwa, *et al.*, *Atmos. Chem. Phys.*, 2014, **14**, 8323–8341.
67 G. D. Smith, *et al.*, *J. Phys. Chem. A*, 2002, **106**, 8085–8095.
68 J. D. Hearn, A. J. Lovett and G. D. Smith, *Phys. Chem. Chem. Phys.*, 2005, **7**, 501–511.
69 S. S. Steimer, *et al.*, *Atmos. Chem. Phys.*, 2014, **14**, 10761–10772.
70 D. R. Hanson, A. R. Ravishankara and S. Solomon, *J. Geophys. Res.: Atmos.*, 1994, **99**, 3615–3629.
71 T. Murata, M. S. Lee and A. Tanioka, *J. Colloid Interface Sci.*, 1999, **220**, 250–254.
72 H. C. Price, *et al.*, *Chem. Sci.*, 2015, **6**, 4876–4883.
73 E. Mikhailov, *et al.*, *Atmos. Chem. Phys.*, 2009, **9**, 9491–9522.
74 R. Sander, *Atmos. Chem. Phys.*, 2015, **15**, 4399–4981.
75 S. D. Razumovskii and G. E. Zaikov, *Ozone and its reactions with organic compounds*, Elsevier, Amsterdam, 1984.
76 A. K. Bin, *Ozone: Sci. Eng.*, 2006, **28**, 67–75.
77 J. Hoigne and H. Bader, *Water Res.*, 1983, **17**, 173–183.

78 P. J. Gallimore, *et al.*, *Atmos. Chem. Phys.*, 2011, **11**, 12181–12195.
79 C. W. Dilbeck and B. J. Finlayson-Pitts, *Phys. Chem. Chem. Phys.*, 2013, **15**, 1990–2002.
80 A. Maranzana, *et al.*, *J. Phys. Chem. A*, 2005, **109**, 10929–10939.
81 U. Pöschl, *et al.*, *J. Phys. Chem. A*, 2001, **105**, 4029–4041.
82 L. Vereecken, D. R. Glowacki and M. J. Pilling, *Chem. Rev.*, 2015, **115**, 4063–4114.
83 E. R. Altwicker and J. Basila, *Tetrahedron*, 1973, **29**, 1969–1974.
84 W. G. Alcock and B. Mile, *J. Chem. Soc., Chem. Commun.*, 1976, 5–6, DOI: 10.1039/c39760000005.
85 M. Olzmann, *et al.*, *J. Phys. Chem. A*, 1997, **101**, 9421–9429.
86 C. A. Taatjes, D. E. Shallcross and C. J. Percival, *Phys. Chem. Chem. Phys.*, 2014, **16**, 1704–1718.
87 K. T. Kuwata, *et al.*, *J. Phys. Chem. A*, 2010, **114**, 9192–9204.
88 C. R. Usher, A. E. Michel and V. H. Grassian, *Chem. Rev.*, 2003, **103**, 4883–4940.
89 J. McCabe and J. P. D. Abbatt, *J. Phys. Chem. C*, 2009, **113**, 2120–2127.
90 S. Enami, M. R. Hoffmann and A. J. Colussi, *Proc. Natl. Acad. Sci. U. S. A.*, 2008, **105**, 7365–7369.

Supplementary Material

Ozone uptake and formation of reactive oxygen intermediates on glassy, semi-solid and liquid organic matter

Thomas Berkemeier[a,*], Sarah S. Steimer[b,c], Ulrich K. Krieger[c], Thomas Peter[c], Ulrich Pöschl[a], Markus Ammann[b] and Manabu Shiraiwa[a,*]

[a]Max Planck Institute for Chemistry, Multiphase Chemistry Department, 55128 Mainz, Germany.

[b]Paul Scherrer Institute, Laboratory of Environmental Chemistry, 5232 Villigen PSI, Switzerland.

[c]ETH Zurich, Institute for Atmospheric and Climate Science, 8092 Zurich, Switzerland.

A. Limiting cases and the kinetic cube

The cases of limiting behaviour are distinguished by three classification parameters:[1] The surface to total loss rate ratio (STLR, decision step 1) assesses the reaction location, the saturation ratio (SR, decision step 2) assesses the supply of reactive gas, and the mixing parameter (MP, decision step 3) assesses the homogeneity of the system.

The classification scheme demands different parameters depending on the outcome of the respective preceding decision step (see Fig. 4 in Berkemeier *et al.*[1]). Most classification parameters require the output of a depth-resolved kinetic model and are given in Eqs. (S1) – (S6), where $[X]_s$, $[Y]_{ss}$, $[X]_{bk}$ and $[Y]_{bk}$ are the concentration of reactants X and Y in the sorption layer (s), quasi-static surface layer (ss) and *k*-th bulk layer (b*k*), respectively.

The STLR is the sole parameter of the first decision step. It compares the rate of ozone loss at the surface to the sum of all losses in the bulk layers, but neglects loss of X by self-reaction.

$$\mathrm{STLR} = \frac{k_{\mathrm{SLR1}}[\mathrm{X}]_\mathrm{s}[\mathrm{Y}]_\mathrm{ss}}{k_{\mathrm{SLR1}}[\mathrm{X}]_\mathrm{s}[\mathrm{Y}]_\mathrm{ss} + \sum_{i=1}^{n} k_{\mathrm{BR}}[\mathrm{X}]_{\mathrm{b}i}[\mathrm{Y}]_{\mathrm{b}i}} \tag{S1}$$

In case of a high contribution of surface reaction (SLR1), the surface saturation ratio (SSR) is used to determine whether the system is close to the (non-reactive) Langmuir adsorption equilibrium or supply of reactive gas by gas diffusion or surface accommodation is limiting the reaction. SSR relates the surface coverage $\theta_{\mathrm{s,X}}$ to its saturation concentration in absence of chemical reaction $\theta_{\mathrm{s,X,sat}}$.

$$\mathrm{SSR} = \frac{\theta_{\mathrm{s,X}}}{\theta_{\mathrm{s,X,sat}}} = \frac{4[\mathrm{X}]_\mathrm{s}}{\omega_{\mathrm{O3}}\alpha_{\mathrm{s},0}\tau_{\mathrm{D,O3}}[\mathrm{X}]_\mathrm{g}} + \sigma_\mathrm{X}[\mathrm{X}]_\mathrm{s} \tag{S2}$$

In case of a high contribution of bulk reaction (BR), the bulk saturation ratio (BSR) determines whether the near-surface bulk (layer b1) is saturated according to Henry's law.

$$\mathrm{BSR} = \frac{[\mathrm{Y}]_{\mathrm{b1}}}{H_{\mathrm{cp,O3}}[\mathrm{X}]_\mathrm{g}} \tag{S3}$$

If saturation of surface or bulk is not achieved, the gas-phase diffusion correction parameter C_g can discriminate between limitation of gas supply by gas diffusion or surface accommodation.

$$C_{\mathrm{g}} = \frac{[\mathrm{X}]_{\mathrm{gs}}}{[\mathrm{X}]_{\mathrm{g}}} \tag{S4}$$

A surface reaction that is not hindered by supply of reactive gas might be limited by diffusion of bulk constituent Y to the surface, which is assessed by the surface mixing parameter, $\mathrm{SMP_Y}$.

$$\mathrm{SMP_Y} = \frac{[\mathrm{Y}]_{\mathrm{b1}}}{\max([\mathrm{Y}]_{\mathrm{b}k})} \tag{S5}$$

A bulk reaction on the other hand can be limited by diffusion of reactive trace gas X, bulk constituent Y, or both. This is assessed by comparing reacto-diffusive lengths l_{rd} to the system size (e.g. particle radius r_{p}). The reacto-diffusive length is calculated analogously to previous works[2], but using effective bulk concentrations $[\mathrm{Y}]_{\mathrm{b,eff}}$ and $[\mathrm{X}]_{\mathrm{b,eff}}$ that account for spatial inhomogeneity of both reaction partners. These effective concentrations can be regarded as average concentrations in the region of overlap of the counter-diffusing species X and Y.

$$\mathrm{BMP_{XY}} = \frac{1}{2}\left(\frac{l_{\mathrm{rd,X}}}{l_{\mathrm{rd,X}} + \frac{r_{\mathrm{p}}}{\exp(1)}} + \frac{l_{\mathrm{rd,Y}}}{l_{\mathrm{rd,Y}} + \frac{r_{\mathrm{p}}}{\exp(1)}}\right) \tag{S6a}$$

with

$$l_{\mathrm{rd,X}} = \sqrt{\frac{D_{\mathrm{b,X}}}{k_{\mathrm{BR}}[\mathrm{Y}]_{\mathrm{b,eff}}}} \tag{S6b}$$

and

$$[\mathrm{Y}]_{\mathrm{b,eff}} = \sum_{j=1}^{n} \frac{k_{\mathrm{BR}}[\mathrm{X}]_{\mathrm{b}j}[\mathrm{Y}]_{\mathrm{b}j}}{\sum_{i=1}^{n} k_{\mathrm{BR}}[\mathrm{X}]_{\mathrm{b}i}[\mathrm{Y}]_{\mathrm{b}i}}[\mathrm{Y}]_{\mathrm{b}j} \tag{S6c}$$

If systems fall between limiting cases, multiple reaction channels contribute, each having their own limiting parameters. The higher level parameters SR and MP (decision steps 2 and 3) are then calculated by weighting with the preceding parameters. Every reaction channel thus contributes to the overall classification parameter.

$$\mathrm{SR} = \mathrm{STLR} \cdot \mathrm{SSR} + (1 - \mathrm{STLR}) \cdot \mathrm{BSR} \tag{S7}$$

$$\begin{aligned}\mathrm{MP} = \mathrm{STLR}\left(\mathrm{SSR} \cdot \mathrm{SMP_Y} + (1 - \mathrm{SSR}) \cdot C_{\mathrm{g}}\right) + (1 - \mathrm{STLR}) \\ \cdot \left(\mathrm{BSR} \cdot \mathrm{BMP_{XY}} + (1 - \mathrm{BSR}) \cdot C_{\mathrm{g}}\right)\end{aligned} \tag{S8}$$

B. Normalized sensitivity coefficients and parameter uniqueness

For every input parameter λ_i, a normalized sensitivity coefficient $S(\lambda_i)$ can be calculated using Morris' elementary effects method[3] and the definition in Eq. S9.

$$S(\lambda_i) = \frac{\lambda_i}{Q_{\mathrm{mod}}} \frac{dQ_{\mathrm{mod}}}{d\lambda_i} = \frac{d \log Q_{\mathrm{mod}}}{d \log \lambda_i} \tag{S9}$$

If, for all times and all conditions, a linear combination of $S(\lambda_i)$'s can be found to express another $S(\lambda_i)$, these parameters are not orthogonal.

$$\sum \nu_i \, S(\lambda_i) = 0 \tag{S10}$$

The orthogonality described above can be seen readily in Figure S3: Summing up the sensitivity coefficients of k_{BR}, $k_{\mathrm{bs,O3}}$ and $D_{\mathrm{b,O3}}$ yields the sensitivity coefficient of $H_{\mathrm{cp,O3}}$.

$$S(k_{\mathrm{BR}}) + S\left(k_{\mathrm{bs,O3}}\right) + S\left(D_{\mathrm{b,O3}}\right) = S(H_{\mathrm{cp,O3}}) \tag{S11}$$

Hence, once normalised sensitivity coefficients $S(\lambda_i)$ are calculated for all input parameters λ_i this method is computationally much more efficient than evaluating the model for all possible combinations of input parameters. We tried all possible combinations of up to 5 parameters λ_i with a discrete set of 16 possible coefficients ν_i: -3, -2, -3/2, -1, -2/3, -1/2, -1/3, -1/4, 1/4, 1/3, 1/2, 2/3, 1, 3/2, 2, 3, and up to 7 parameters λ_i with a smaller set: -2, -1, -1/2, 1/2, 1, 2. Besides the already mentioned, the only other set of linear dependent sensitivities found using this technique was $S(\alpha_{\mathrm{s},0})$ and $S(\tau_{\mathrm{d,O3}})$. This dependence was already known as $\alpha_{\mathrm{s},0}$ was held fixed during the optimization. Note that while this method can detect local dependencies between input parameters, it is not possible to exclude the existence of other, not directly connected minima in the search space such as the alternative high $D_{\mathrm{b,O3}}$ solution described in Sect. 3.3.

Tab S1 Kinetic input parameters for KM-SUB.

Parameter	Unit	Description
k_{BR}	$cm^3\ s^{-1}$	bulk reaction rate coefficient
k_{SLR1}	$cm^2\ s^{-1}$	surface layer reaction rate coefficient
k_{SLR2}	$cm^2\ s^{-1}$	surface layer reaction rate coefficient, self-reaction
$k_{bs,O3}$	$cm\ s^{-1}$	bulk to surface transfer rate coefficient, O_3
$k_{ssb,Y}$	s^{-1}	surface to bulk transfer rate coeff., shikimic acid
$D_{b,O3}$	$cm^2\ s^{-1}$	bulk diffusion coefficient, O_3 in shikimic acid
$D_{b,Y}$	$cm^2\ s^{-1}$	self-diffusion coefficient, shikimic acid
$H_{cp,O3}$	$mol\ cm^{-3}\ atm^{-1}$	Henry's law solubility coeff., O_3 in aq. organics
K_{bs}	cm	surface equilibrium constant, shikimic acid
$\tau_{d,O3}$	s	desorption lifetime, O_3
$\alpha_{s,0}$		surface accommodation coefficient, O_3
$D_{g,O3}$	$cm^2\ s^{-1}$	gas phase diffusivity, O_3
σ_{O3}	cm^2	adsorption cross-section, O_3

Tab S2 Kinetic input parameters for KM-SUB. Parameters marked with an asterisk (*) were not changed during global optimization. In the last row, r_i indicates the residue arising from all data sets at the respective RH using f_i = 1/12. For 24 % and 92 % RH, the residues are given from top to bottom in order of ascending $[O_3]_g$.

Parameter	Unit	0 % RH	24 % RH	45 % RH	69 % RH	83 % RH	92 % RH
Kinetic parameters							
$k_{BR,1}$	$cm^3\ s^{-1}$	4.39×10^{-18}					
$k_{SLR,1}$	$cm^2\ s^{-1}$	8.52×10^{-16}					
$k_{SLR,2}$	$cm^2\ s^{-1}$	4.31×10^{-17}					
$k_{bs,O3}$	$cm\ s^{-1}$	0.60	0.65	0.69	0.83	1.60	23.2
$k_{ssb,Y}$	s^{-1}	9.6×10^{-5}	3.2×10^{-4}	8.3×10^{-4}	8.4×10^{-4}	4.2×10^{-4}	7.0×10^{-8}
$D_{b,O3}$	$cm^2\ s^{-1}$	6.2×10^{-12}	5.3×10^{-12}	6.1×10^{-12}	1.9×10^{-9}	8.0×10^{-8}	9.1×10^{-7}
$D_{b,Y}$	$cm^2\ s^{-1}$	1.0×10^{-21}	8.4×10^{-19}	5.3×10^{-18}	5.1×10^{-17}	2.1×10^{-16}	2.1×10^{-7}
$H_{cp,O3}$	$mol\ cm^{-3}\ atm^{-1}$	1.8×10^{-4}	1.6×10^{-4}	1.4×10^{-4}	1.0×10^{-4}	5.5×10^{-5}	4.0×10^{-5}
K_{bs}	cm	2.0×10^{-9}	2.3×10^{-9}	3.4×10^{-9}	4.1×10^{-9}	3.8×10^{-9}	9.3×10^{-9}
$\tau_{d,O3}$	s	5.32×10^{-4}					
$\alpha_{s,0}$*		0.5					
$D_{g,O3}$*	$cm^2\ s^{-1}$	0.14					
Geometric and thermodynamic parameters							
σ_{O3}	cm^2	2.42×10^{-14}					
σ_Y*	cm^2	3.34×10^{-15}					
$[Y]_{b,0}$*	cm^{-3}	5.27×10^{21}	4.87×10^{21}	4.50×10^{21}	3.84×10^{21}	3.02×10^{21}	2.04×10^{21}
δ_{layer}*	cm	3.0×10^{-8}	3.0×10^{-8}	6.0×10^{-8}	1.0×10^{-7}	2.0×10^{-7}	7.5×10^{-7}
Residuals							
r_i		0.00312	0.00342 0.00323 0.00236 0.00226	0.00159	0.00052	0.00036	0.00093 0.00104 0.00066 0.00086

Tab S3 Fit parameters for diffusivity parameterization in Vignes-type equation (7) and correction factor α, Eq. (8). Diffusion coefficients are given in $cm^2\ s^{-1}$; factors C and D are dimensionless. Values for $D^w_{b,O3}$ were taken from Smith and Kay[4]. $D^w_{b,Y}$ has been estimated based upon work from Delgado[5] on similar organic compounds.

	C	D	D^{org}	D^w
$D_{b,H2O}$ (Steimer *et al.*[6])	0.279	-7.22×10^{-3}	1.71×10^{-12}	1.9×10^{-5}
$D_{b,O3}$ (this study)	-3.336	-1.287	2.90×10^{-12}	1.9×10^{-5}
$D_{b,Y}$ (this study)	-1.218	-2.065	1.17×10^{-20}	1×10^{-5}

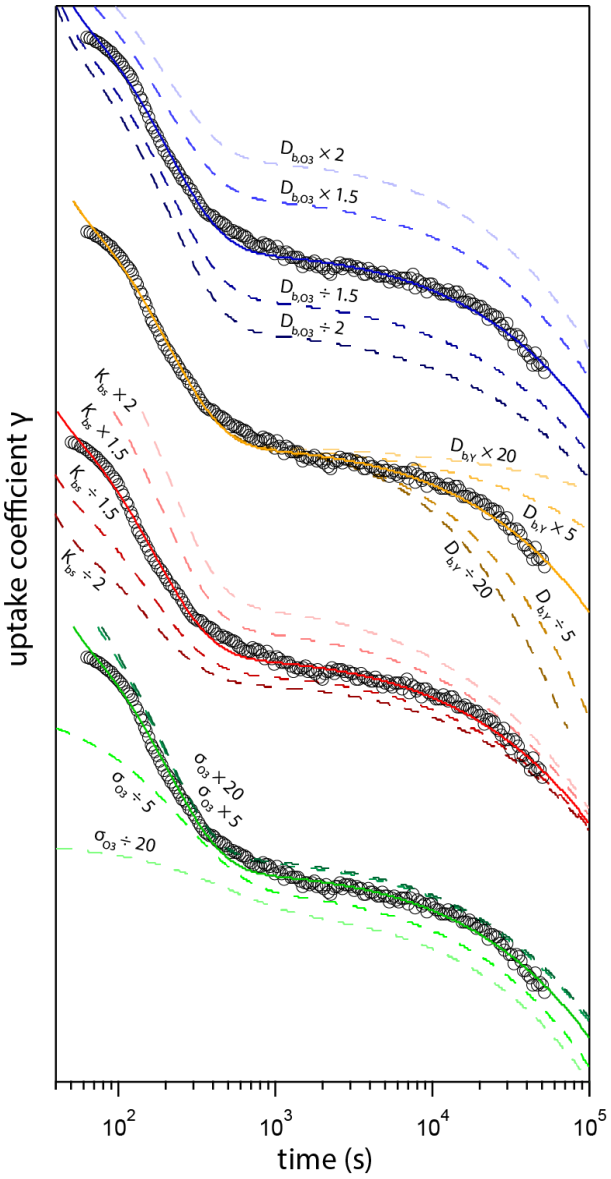

Fig S1 Dependence of uptake coefficient γ on small variations of the parameters $D_{b,O3}$ (blue), $D_{b,Y}$ (orange), K_{bs} (red) and σ_{O3} (green) and comparison to the experimental data at 68 % RH. The best fit (solid lines) is altered considerably if parameters are varied (dashed lines). For very sensitive parameters ($D_{b,O3}$, K_{bs}) already small changes alter the result significantly over the entire time range, whereas other parameters have rather small impact at specific reaction times ($D_{b,Y}$, σ_{O3}). Note that the y-axis is not continuous throughout the figure.

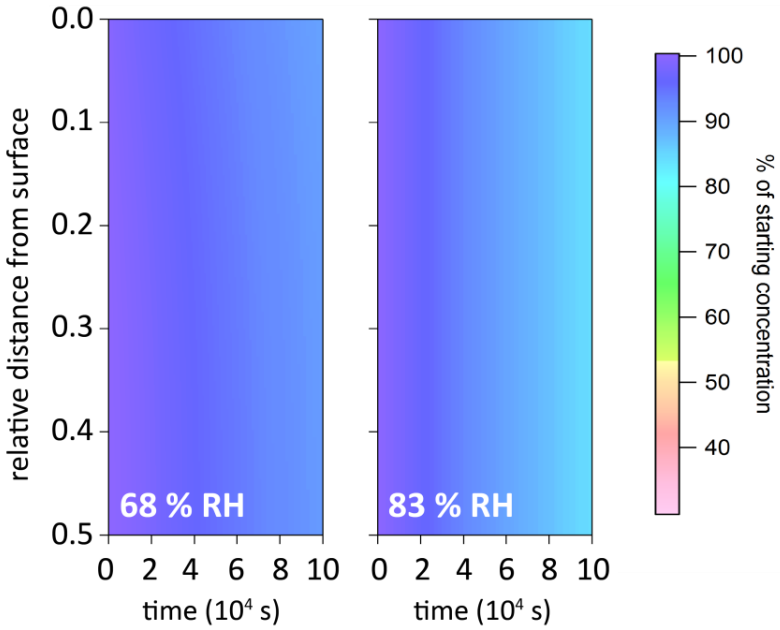

Fig S2 Depth profiles of shikimic acid concentration in a film during exposure of 178 ppb ozone as a function of time and relative humidity (RH), including the effects of reaction products on ozone diffusion. In these model runs, $D_{b,Y}$ is alleviated at 10^{-14} cm^2 s^{-1} and 10^{-10} cm^2 s^{-1} at 67 % and 83 % RH, respectively, and thus a well-mixed bulk matrix obtained.

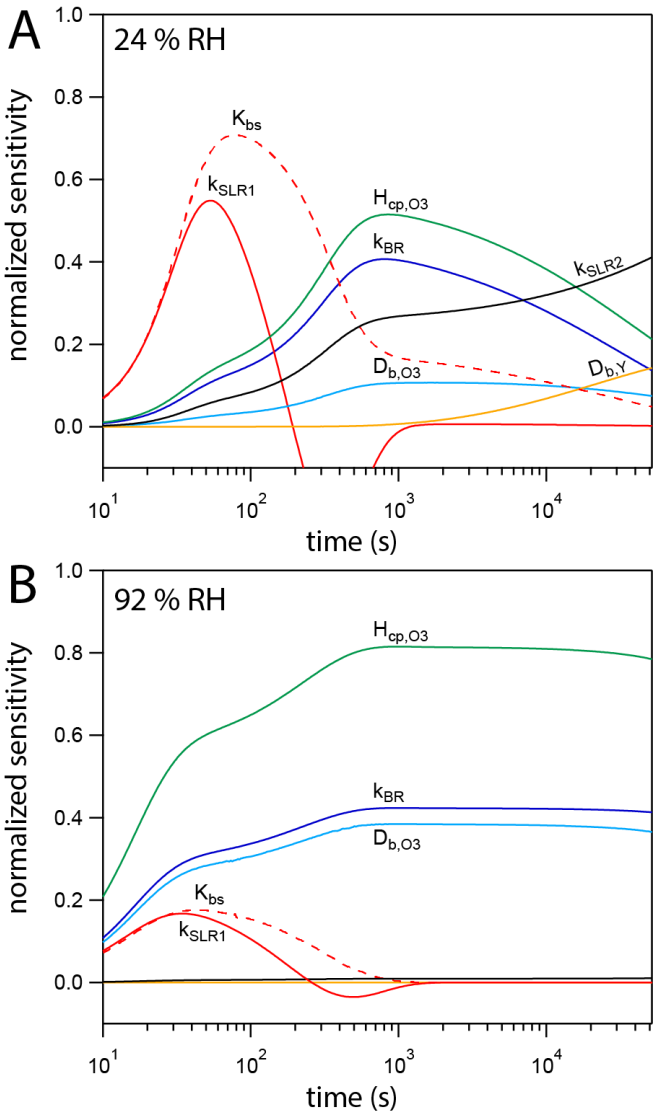

Fig S3 Sensitivity profiles of KM-SUB modelling result for the uptake coefficient γ towards the most influential input parameters for two environmental conditions: (A) 24 % RH and (B) 92 % RH.

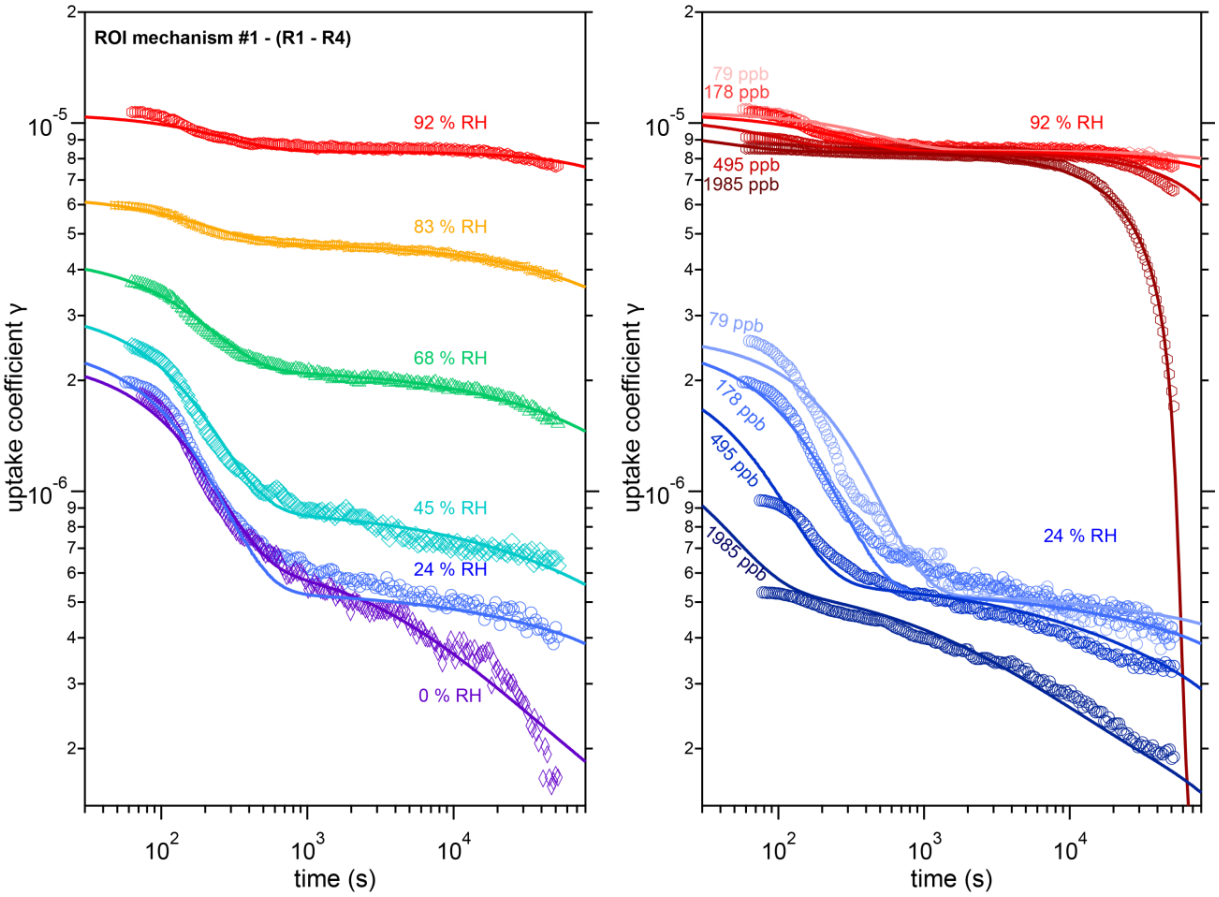

Fig S4 Observed (markers) and modelled (lines) uptake coefficients of ozone γ onto a thin film of shikimic acid as a function of exposure time using ROI mechanism #1 (R1– R4).

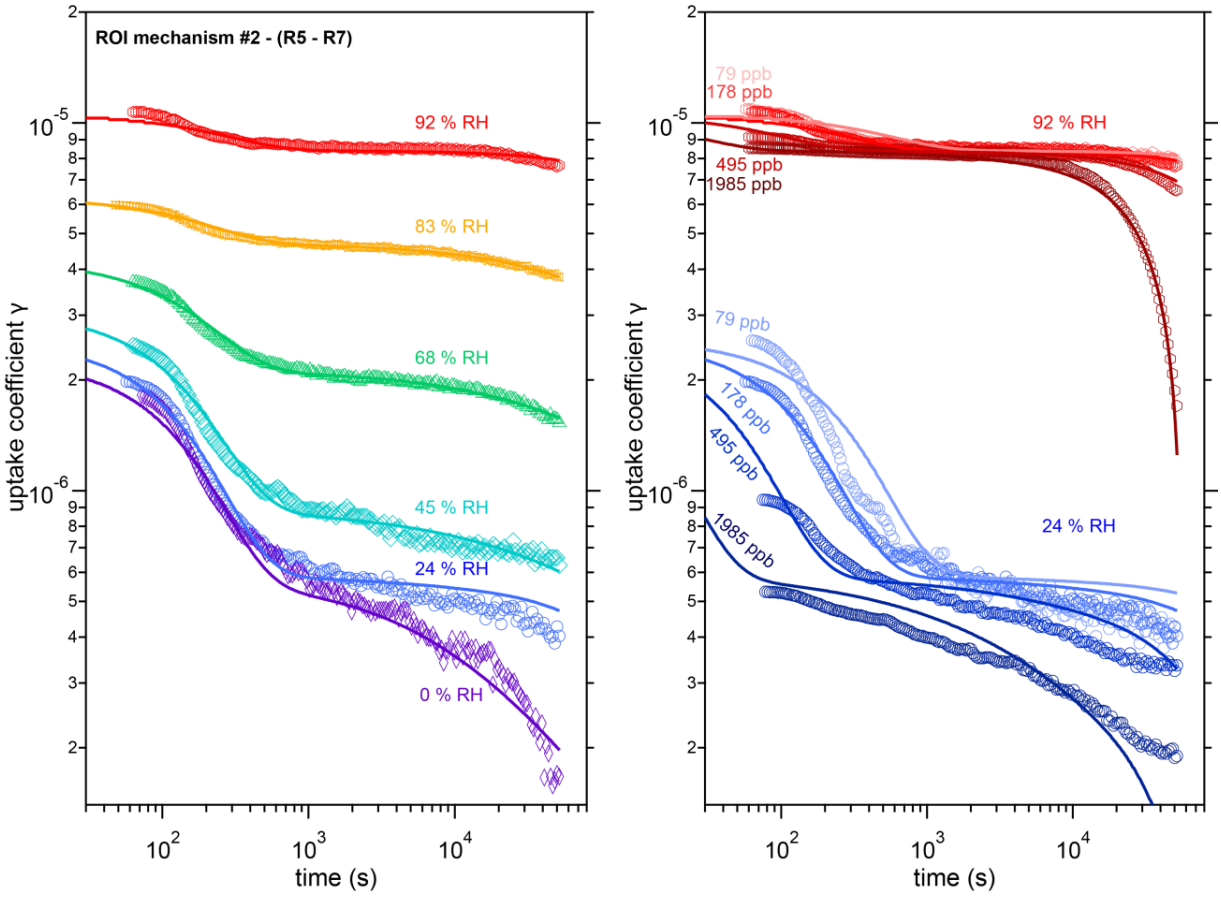

Fig S5 Observed (markers) and modelled (lines) uptake coefficients of ozone γ onto a thin film of shikimic acid as a function of exposure time using ROI mechanism #2 (R5 – R7).

References

1. T. Berkemeier, A. J. Huisman, M. Ammann, M. Shiraiwa, T. Koop and U. Pöschl, *Atmos. Chem. Phys.*, 2013, 13, 6663-6686.
2. D. R. Hanson, A. R. Ravishankara and S. Solomon, *J. Geophys. Res. Atmos.*, 1994, 99, 3615-3629.
3. M. D. Morris, *Technometrics*, 1991, 33, 161-174.
4. R. S. Smith and B. D. Kay, *Nature*, 1999, 398, 788-791.
5. J. Delgado, *J. Phase Equilib. Diffus.*, 2007, 28, 427-432.
6. S. S. Steimer, U. K. Krieger, Y. F. Te, D. M. Lienhard, A. J. Huisman, B. P. Luo, M. Ammann and T. Peter, *Atmos. Meas. Tech.*, 2015, 8, 2397-2408.

B.6. Berkemeier *et al.*, Environ. Sci. Technol., 2016

Organic nitrate contribution to new particle formation and growth in secondary organic aerosols from α-pinene ozonolysis

Thomas Berkemeier[1], Markus Ammann[2], Thomas F. Mentel[3], Ulrich Pöschl[1] and Manabu Shiraiwa[1]

[1]Max Planck Institute for Chemistry, Multiphase Chemistry Department, 55128 Mainz, Germany
[2]Paul Scherrer Institute, Laboratory of Environmental Chemistry, 5232 Villigen PSI, Switzerland
[3]Forschungszentrum Jülich, Institute of Energy and Climate Research, IEK-8, 52428 Jülich, Germany

Environmental Science and Technology, DOI:10.1021/acs.est.6b00961, (2016).

Author contributions.

TB, MA, UP and MS designed research. TB, TFM and MS developed the kinetic model. TB and TFM performed kinetic modelling. TB, MA, TFM, UP and MS analysed simulation data. TB and MS wrote the paper.

Environmental Science & Technology

Article

pubs.acs.org/est

Organic Nitrate Contribution to New Particle Formation and Growth in Secondary Organic Aerosols from α-Pinene Ozonolysis

Thomas Berkemeier,[†] Markus Ammann,[‡] Thomas F. Mentel,[§] Ulrich Pöschl,[†] and Manabu Shiraiwa*[,†]

[†]Multiphase Chemistry Department, Max Planck Institute for Chemistry, Mainz 55128, Germany

[‡]Laboratory of Environmental Chemistry, Paul Scherrer Institute, Villigen 5232, Switzerland

[§]Institute of Energy and Climate Research, IEK-8, Forschungszentrum Jülich, Jülich 52425, Germany

Supporting Information

ABSTRACT: The chemical kinetics of organic nitrate production during new particle formation and growth of secondary organic aerosols (SOA) were investigated using the short-lived radioactive tracer ^{13}N in flow-reactor studies of α-pinene oxidation with ozone. Direct and quantitative measurements of the nitrogen content indicate that organic nitrates accounted for ∼40% of SOA mass during initial particle formation, decreasing to ∼15% upon particle growth to the accumulation-mode size range (>100 nm). Experiments with OH scavengers and kinetic model results suggest that organic peroxy radicals formed by α-pinene reacting with secondary OH from ozonolysis are key intermediates in the organic nitrate formation process. The direct reaction of α-pinene with NO_3 was found to be less important for particle-phase organic nitrate formation. The nitrogen content of SOA particles decreased slightly upon increase of relative humidity up to 80%. The experiments show a tight correlation between organic nitrate content and SOA particle-number concentrations, implying that the condensing organic nitrates are among the extremely low volatility organic compounds (ELVOC) that may play an important role in the nucleation and growth of atmospheric nanoparticles.

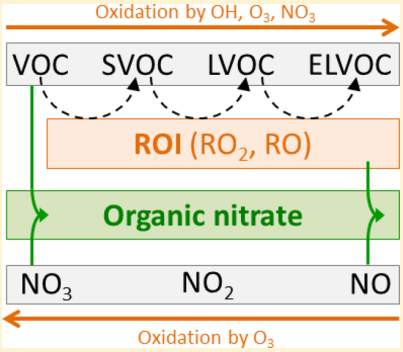

INTRODUCTION

Organic aerosol particles constitute a major fraction of air particulate matter, affecting climate and posing adverse effects on human health.[1−5] These particles are either emitted directly by wood and fossil-fuel combustion, cooking, and natural sources[6] or formed by oxidation of volatile organic compounds (VOCs) by atmospheric oxidants such as ozone (O_3), nitrate (NO_3), and hydroxyl (OH) radicals.[7,8] NO_3 is an important night-time oxidant for VOCs but rapidly undergoes photolysis during day time.[9] OH is the major atmospheric photochemical oxidant during daytime, whereas ozone contributes to VOC oxidation during both day and night-time. Ozonolysis reactions can produce OH in high yields, leading to simultaneous activity of both oxidation processes, even under dark conditions.[10−13]

Nitrogen oxides (NO, $NO_2 \equiv NO_x$) are mainly emitted from fossil-fuel combustion and affect the chemical evolution of VOCs through the formation of organic nitrates.[8,9,14] Organic nitrates are stable and function as a reservoir for the short-lived NO_x species under dry conditions, while in aqueous droplets, they can be rapidly converted to nitric acid (HNO_3).[15−17] Deposition of organic nitrates into lung-lining fluid in the human respiratory tract might lead to the formation of HNO_3 by hydrolysis, a compound known to reduce pulmonary functions upon inhalation.[18]

The formation of organic nitrates hence affects the atmospheric nitrogen budget and alters the total aerosol mass yield from secondary sources.[19−21] The presence of high levels of both NO_x and O_3 generates a competition in VOC oxidation between the two oxidants, NO_3 and O_3. The NO_3 initated oxidation of α-pinene showed low-SOA mass yields in previous laboratory experiments, in contrast to other monoterpenes, including β-pinene and limonene, producing aerosol in high yields.[22−24] To our knowledge, the yield of organic nitrates in the dark ozonolysis of α-pinene has not yet been quantified.

Organic nitrogen compounds can be strong light absorbers, forming so-called brown carbon, which plays an important role in photochemistry and has a net warming effect on earth's climate.[25−28] However, the formation, partitioning, and fate of nitrogen-containing organic compounds in SOA are still poorly understood. Organic nitrates can form in high quantities, as detected in field[29−32] and laboratory[33,34] samples, but quantification with online techniques remains a challenging task. A commonly used online technique is laser-induced fluorescence after the thermal conversion of organic nitrates to NO_2 (TD−LIF).[23,34] Using mass spectrometric techniques, it is often difficult to detect organic nitrates reliably due to the thermal instability of the nitrate group,[35,36] and organic nitrate contents must be inferred indirectly.[37] Fourier transform infrared (FTIR) spectroscopy[35] and high-resolution time-of-

Received: February 24, 2016
Revised: May 18, 2016
Accepted: May 24, 2016
Published: May 24, 2016

DOI: 10.1021/acs.est.6b00961
Environ. Sci. Technol. 2016, 50, 6334−6342

Table 1. Comparison of the Organic Nitrate Fraction Obtained in This Study to Other Aerosol Flow-Tube (AFT) and Environmental Chamber (EC) Experiments as Well as Field Data (field)[a]

ON/OA	precursor	method		references
15−40%	α-pinene	^{13}N tracer	AFT	this study
50−80%	α-pinene[c]	^{13}N tracer	AFT	this study
6−18%	α-pinene[c]	TD−LIF	AFT	Rollins et al.[34]
9−27%	α-pinene[c]	FTIR	EC	Noziere et al.[53]
45−74%	β-pinene[b]	HR-ToF-AMS	EC	Boyd et al.[38]
56%	β-pinene[b]	TD−LIF	EC	Fry et al.[23]
32−41%	β-pinene[b]	HR-ToF-AMS	EC	Fry et al.[33]
36%	limonene[c]	TD−LIF	AFT	Rollins et al.[34]
82%	limonene[b]	TD−LIF	EC	Fry et al.[23]
25%	Δ-carene[c]	TD−LIF	AFT	Rollins et al.[34]
56%	Δ-carene[b]	TD−LIF	EC	Fry et al.[23]
22−23%		HR-ToF-AMS	field	Lee et al.[66]
27−40%		TD−LIF	field	Rollins et al.[32]
23−44%		HR-ToF-AMS	field	Ayres et al.[31]
19−32%		HR-ToF-AMS	field	Xu et al.[65]
5−12%		HR-ToF-AMS	field	Xu et al.[67]

[a]Note that the ON fractions reported in this study are for dark ozonolysis of α-pinene, while most other laboratory studies looked into oxidation by NO_3 or photooxidation by OH, respectively. [b]From NO_3 oxidation. [c]From OH photooxidation.

flight mass spectrometry[38] (HR-ToF-MS) have been used as offline techniques to determine organic nitrogen contents. An overview on previous studies determining the nitrate content in various laboratory aerosol samples is given in Table 1.

In this study, we applied the short-lived radioactive tracer ^{13}N to quantify the amount of organic nitrates produced and retained in SOA particles.[39] This online technique gives an accurate estimate of the total ^{13}N that entered the particle phase and has been used previously to determine gas-particle kinetics and partitioning of nitrogen-containing compounds.[39−44] Experimental conditions such as ozone and NO_x concentrations, relative humidity, light irradiation, and presence of OH scavengers were varied to investigate the kinetic mechanism using an aerosol flow-tube reactor. Box-model simulations based on the Master Chemical Mechanism (MCM)[45,46] were conducted for interpretation of the experimental findings.

MATERIALS AND METHODS

PROTRAC. ^{13}N decays radioactively with a half-life of ∼10 min and is produced online by directing a 11 MeV proton beam through a flow-through gas target, utilizing the ^{16}O(p,α)^{13}N reaction of 10−15% O_2 in He by the PROTRAC (Production of Tracers for Atmospheric Chemistry) facility at Paul Scherrer Institute.[39,43] The initial products are highly oxidized ^{13}N species, which are subsequently reduced to ^{13}NO over a molybdenum converter at 380 °C. ^{13}NO is transported from the production site to the laboratory through a 580 m long polyvinylidene fluoride (PVDF) tube.

Flow-Tube Setup. SOA particles were produced by dark ozonolysis of α-pinene precursor gas (∼1 ppm) in various mixtures of α-pinene, ozone, and NO in an aerosol-flow-tube system (Figure 1). Particles were nucleated homogeneously without seed particles. α-pinene was added to the flow system through a custom built gas diffusion source: in a temperature-controlled 200 mL glass flask, a flow of 50 mL min^{-1} dry N_2 was directed over an α-pinene reservoir with a small orifice of variable size, leading to a stable and adjustable α-pinene concentration (i.e., gas-phase number mixing ratio) of 400−1500 ppb, as confirmed by proton-transfer mass spectrometry (PTR−MS). Ozone was generated by passing synthetic air (50 mL min^{-1}) through a quartz tube exposed to a UV source of adjustable intensity and monitored with a commercial ozone analyzer (Teledyne ML 9810). The ^{13}NO containing gas flow (200 mL min^{-1}) is mixed with nonlabeled ^{14}NO (0−100 mL min^{-1}) from a certified gas cylinder (10 ppm in N_2) to adjust the total NO concentration. The total volume flow through the flow tube system was set to 1.25 L min^{-1}. The length of the aerosol flow tube can be adjusted via movable inlets with a total reactor volume ranging between 0.7−5.5 L, corresponding to a reaction time between 0.5−5 min.

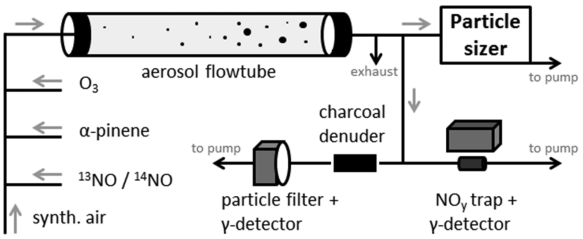

Figure 1. Schematic of the experimental setup. SOA particles were formed by α-pinene ozonolysis in the presence of ^{13}NO and ^{14}NO in an aerosol flow tube. Concentrations of ^{13}N in the gas and particle phases were detected by γ detectors.

Behind the reactor, the gas flow was split 3-fold between a scanning mobility particle sizer (SMPS) system to determine the particle-size distribution and two separate detection systems for ^{13}N species. The total concentration of ^{13}N in the gas and particle phase combined was detected with a packed Co-oxide tube that traps particles and also efficiently binds all gas-phase NO_y species (≡NO_x, NO_3, HNO_x, N_2O_5, and organic nitrates). The Co-oxide (dominated by Co_3O_4) packing was obtained by soaking firebricks in saturated Co-nitrate solution followed by baking at 700 °C.[39] For the quantification of ^{13}N in the particle phase alone, particles were collected on a glass-fiber filter after removing all gas-phase species by a charcoal denuder. CsI scintillation counters (Carroll and Ramsey) were placed behind both a Co-oxide trap and glass fiber filter, and the flux of ^{13}N into both traps was measured at 1 min time resolution. ^{13}N is a well-known positron (β^+) emitter, and the generated positrons annihilate with an electron under the emission of two γ-photons, which were measured by the scintillation counters. The inversion method to derive incoming ^{13}N from integrated γ-ray signals is described in detail elsewhere.[40] All experiments were performed at room temperature (295 K).

Mass Fraction of Organic Nitrates. The mass fraction of organic nitrates $RONO_2$ in the particle phase (w_{ON}) was determined by comparison of the measured particle phase ^{13}N signal intensity (I_p) to the gas-phase ^{13}N signal intensity in the absence of the α-pinene ozonolysis reaction ($I_{g,0}$), measured at the Co-oxide trap. $I_{g,0}$ constitutes the entirety of undecayed ^{13}N at the end of the flow reactor and can easily be correlated to the initial NO gas-phase concentration $c_{NO,0}$. $I_p/I_{g,0} \times c_{NO,0}$ hence provides an absolute number concentration of nitrogen atoms in the particle phase. We assume that particle-phase nitrogen was dominated by organic nitrates and the contribution of inorganic nitrogen (e.g., HNO_3 and N_2O_5) was very small, as confirmed by RH-dependent experiments. Increase in humidity

DOI: 10.1021/acs.est.6b00961
Environ. Sci. Technol. 2016, 50, 6334−6342

should favor inorganic nitrate formation by N_2O_5 hydrolysis to form HNO_3, which was not observed with the ^{13}N signal. Moreover, the box-model simulations have shown that N_2O_5 did not accumulate in significant amounts, as outlined below. In fact, the ^{13}N signals at both detectors were reduced at elevated relative humidity, probably due to the more efficient loss of HNO_3 and N_2O_5 to the flow-reactor walls under humid conditions.[41] There are also potential wall loss effects of O_3, NO_2, and NO_3, which have been considered in the kinetic box model described below. Raw data from a typical experiment is showcased in Figure S1. For each data point, the flow tube system was flushed with synthetic air for 20−30 min until the ^{13}N signal intensity ($I_{g,0}$, black solid line in Figure S1) stabilized. After the simultaneous addition of all reactants, I_p (black solid line in Figure S1) was determined once a steady state in SMPS and scintillation counter signal was reached. With knowledge of the aerosol mass concentration, m_{SOA}, and assuming that each organic nitrate molecule contains only a single $-ONO_2$ function, w_{ON} can be determined by

$$w_{ON} = \frac{I_p M_{ON} c_{NO,0}}{B\lambda I_{g,0} N_A m_{SOA}} \quad (1)$$

where N_A is Avogadro's number. The molar mass M_{ON} was assumed to be 250 ± 50 g mol^{-1}, which was chosen considering the high abundance of nitrated products in the range of 200−250 g mol^{-1} in the MCM[45,46] and observations of highly functionalized nitrated compounds exceeding molar masses of 300 g mol^{-1} in regions dominated by monoterpene SOA.[47] Sum formulas of typical nitrated products from α-pinene ozonolysis are given in Table S1. The scintillation counters register radioactive decay on the basis of the γ quanta generated upon annihilation of the positrons emitted. Because the distance to the scintillation counter and shape of the particle filter versus the Co-oxide trap differ, a proportionality constant B is used to consider the different detector geometries and minor differences in the sensitivity of individual detectors. B was determined to be 0.66 in separate experiments in which a glass fiber filter was loaded with ^{13}N-labeled aerosol and transferred multiple times between both detector setups. A fraction of the aerosol is lost in the charcoal denuder and hence affects the measured particle-phase signal I_p. The fraction was found to be independent of particle size and can thus be accounted for with a simple scaling factor λ = 0.59, as determined by SMPS.

Kinetic Box Model. A simple gas-phase box model is used to quantify important species in the oxidation of α-pinene on the time scale of the flow-tube experiment. We adopt the HO_x and NO_y chemistry from the MCM that consists of 12 reactants in 24 chemical reactions (Table S2).[45,46] We added a simplified mechanism of SOA formation, which is based on MCM but lumps individual compounds into bins of compound classes with similar properties. The added mechanism consists of seven additional reactants in 23 chemical reactions (Table 2 and Figure S2). These reactants include two types of reactive oxygen intermediates (ROI)[5,43] in the form of organic peroxy radicals (RO_2) and alkoxy radicals (RO), which are formed upon initial reaction of α-pinene with O_3 and OH and can be interconverted. All stable, non-nitrated products are lumped into an *organics* bin and assumed inert toward further oxidation. Molecules in an *organic nitrates* bin are formed either via the oxidation of α-pinene with NO_3 or via the reaction of RO_2 with NO. Following the major reaction pathways in MCM, we distinguish three different RO_2 radicals: RO_2^I are produced from α-pinene ozonolysis and are unable to form organic nitrates, and RO_2^{II} are mainly formed from OH oxidation of α-pinene and RO_2^{III} contain a nitrate group. OH is produced secondarily during α-pinene ozonolysis, R1.[10,11,48] Branching between R1 and R2 returns a production efficiency of OH of 85%, which is in line with previous observations.[49] RO radicals are formed by the reaction of RO_2 with NO, NO_3, or RO_2, leading to recycling of HO_2 via reaction R21. We distinguish non-nitrated (RO^I) and nitrated (RO^{II}) forms of RO radicals. When possible, reaction rates were directly adopted from MCM. When reaction rates differed between individual species in a compound class (R8, R9, and R15−R20 in Table 2), an intermediate or representative reaction rate was used in the lumped model.

Table 2. Lumped Reaction Mechanism of α-Pinene Dark Ozonolysis and Reaction Rates at 295 K

no.	reaction	reaction rate
R1	O_3 + α-pinene → RO_2^I + OH	$k_1 = 0.85 \times 9.2 \times 10^{-17}$ cm^3 s^{-1}
R2	O_3 + α-pinene → RO_2^{II}	$k_2 = 0.15 \times 9.2 \times 10^{-17}$ cm^3 s^{-1}
R3	OH + α-pinene → RO_2^{II}	$k_3 = 5.3 \times 10^{-11}$ cm^3 s^{-1}
R4	NO_3 + α-pinene → RO_2^{III}	$k_4 = 6.3 \times 10^{-12}$ cm^3 s^{-1}
R5	NO + RO_2^I → NO_2 + RO^I	$k_5 = 9.1 \times 10^{-12}$ cm^3 s^{-1}
R6	NO_3 + RO_2^I → NO_2 + RO^I	$k_6 = 2.3 \times 10^{-12}$ cm^3 s^{-1}
R7	HO_2 + RO_2^I → *organics*	$k_7 = 2.2 \times 10^{-11}$ cm^3 s^{-1}
R8	NO + RO_2^{II} → *organic nitrates*	$k_8 = 0.17 \times 9.1 \times 10^{-12}$ cm^3 s^{-1}
R9	NO + RO_2^{II} → NO_2 + RO^I	$k_9 = 0.83 \times 9.1 \times 10^{-12}$ cm^3 s^{-1}
R10	NO_3 + RO_2^{II} → NO_2 + RO^I	$k_{10} = 2.3 \times 10^{-12}$ cm^3 s^{-1}
R11	HO_2 + RO_2^{II} → *organics*	$k_{11} = 2.2 \times 10^{-11}$ cm^3 s^{-1}
R12	NO + RO_2^{III} → NO_2 + RO^{II}	$k_{12} = 9.1 \times 10^{-12}$ cm^3 s^{-1}
R13	NO_3 + RO_2^{III} → NO_2 + RO^{II}	$k_{13} = 2.3 \times 10^{-12}$ cm^3 s^{-1}
R14	HO_2 + RO_2^{III} → *organic nitrates*	$k_{14} = 2.2 \times 10^{-11}$ cm^3 s^{-1}
R15	RO_2^I → RO^I	$k_{15} = [RO_2] \times 0.7 \times 1 \times 10^{-13}$ cm^3 s^{-1}
R16	RO_2^I → *organics*	$k_{16} = [RO_2] \times 0.3 \times 1 \times 10^{-13}$ cm^3 s^{-1}
R17	RO_2^{II} → RO^I	$k_{17} = [RO_2] \times 0.7 \times 1 \times 10^{-14}$ cm^3 s^{-1}
R18	RO_2^{II} → *organics*	$k_{18} = [RO_2] \times 0.3 \times 1 \times 10^{-14}$ cm^3 s^{-1}
R19	RO_2^{III} → RO^{II}	$k_{19} = [RO_2] \times 0.8 \times 1 \times 10^{-14}$ cm^3 s^{-1}
R20	RO_2^{III} → *organic nitrates*	$k_{20} = [RO_2] \times 0.2 \times 1 \times 10^{-14}$ cm^3 s^{-1}
R21	RO^I → *organics* + HO_2	$k_{21} = 1 \times 10^6$ s^{-1}
R22	RO^I → RO_2^{II}	$k_{22} = 1 \times 10^6$ s^{-1}
R23	RO^{II} → *organics* + NO_2	$k_{23} = 1 \times 10^6$ s^{-1}
R24	RO^{II} → RO_2^{III}	$k_{24} = 1 \times 10^6$ s^{-1}

The formation of peroxyacyl nitrates (PANs) has been neglected for simplicity because these reactions would have prompted an even more detailed oxidation mechanism, and PANs are not expected to contribute to SOA mass significantly due to their high vapor pressures.[50] The wall loss of a subset of compounds (i.e., O_3, NO_2, NO_3, HNO_3, and N_2O_5) was accounted for using an uptake coefficient γ (Table S3). A substantial fraction of the low-volatility oxidation products (organics and organic nitrates) may also be lost to the reactor walls[51] (as the reactor-wall surface exceeds the aerosol surface considerably), but inclusion of these losses does not affect the merely qualitative result of the calculations and has thus been

DOI: 10.1021/acs.est.6b00961
Environ. Sci. Technol. 2016, 50, 6334−6342

neglected. Limitations due to mixing of gas flows and condensation onto particles was also neglected in the calculation.

To validate the lumped model, we performed calculations including the full MCM mechanism, which returned a good correlation between both approaches (Figure S3). The lumped model with only 23 distinct reactions is thus a valid approximation of the complex explicit mechanism with 894 reactions and suffices for the general mechanistic considerations in this study. Given the comparability of both calculations, such a simplified mechanism may increase the feasibility of more resource intensive calculations such as multiphase chemistry models or regional climate models in future studies.

RESULTS AND DISCUSSION

Quantification of Organic Nitrate. Figure 2a shows the time evolution of particle-number concentration (blue circles) and aerosol mass concentration (orange hexagons) as determined by the SMPS system, assuming an average density of 1.25 g cm^{-3} for SOA compounds.[20,52] The intensity of the ^{13}N particle-phase signal (green squares) was normalized by the ^{13}N gas-phase signal intensity in the absence of the α-pinene ozonolysis, and the numerical value of the normalized signal thus directly represents the fraction of original NO_x that entered the particle phase. In this typical experiment, 1.6 ppm ozone was added in 2-fold excess to 800 ppb NO because both species react quickly on the time scale of a few seconds, in situ forming NO_2.[9] α-Pinene was added in slight excess (1 ppm) to minimize potential nonozonolysis reactions between ozone and organics. Typical experiments reached SOA mass concentrations of up to 500 $\mu g\ m^{-3}$, with a number mean diameter of ~120 nm and a mass mean diameter of ~250 nm. Note that due to experimental constraints on the reaction time and detection sensitivity, the concentrations used in this experiment are larger than typically observed in the atmosphere.

As shown in Figure 2a, the SOA mass increased almost linearly with time throughout the experiment. The ^{13}N particle-phase signal increased strongest in the early stages of the experiment when the SOA concentration was still very low, indicating that the nitrated products must exhibit a low volatility. The ^{13}N signal ceased to increase after ~200 s, correlating well with the particle number concentration. This behavior was reproduced in several experiments (cf. Figure S4), suggesting a relationship between the formation of nitrogen-containing compounds and new particle formation. This observation is in line with previous suggestions that organic nitrates may contribute significantly in atmospheric new-particle-formation events, especially over forested regions.[47]

Figure 2b shows the time evolution of the particle-phase nitrogen content in the particle-phase w_{ON}. w_{ON} was as high as 40% in the beginning and reduced to 15% toward the end of the experiment as the production of organic nitrates ceased and the total SOA mass continued to increase. These are the first measurements of w_{ON} for dark ozonolysis in the literature so far but can be compared to experiments of OH photooxidation and NO_3-induced oxidation, which have been extensively studied, as is summarized in Table 1. Individual reported nitrate contents span wide ranges, representing experimental uncertainty. Compared to other precursors such as limonene and β-pinene, α-pinene produces significantly less organic nitrate. Field studies confirm the high contribution of organic nitrate formation to SOA mass, reaching as high as 44%,[31] which is in line with the organic nitrate content of freshly nucleated SOA in this study.[31]

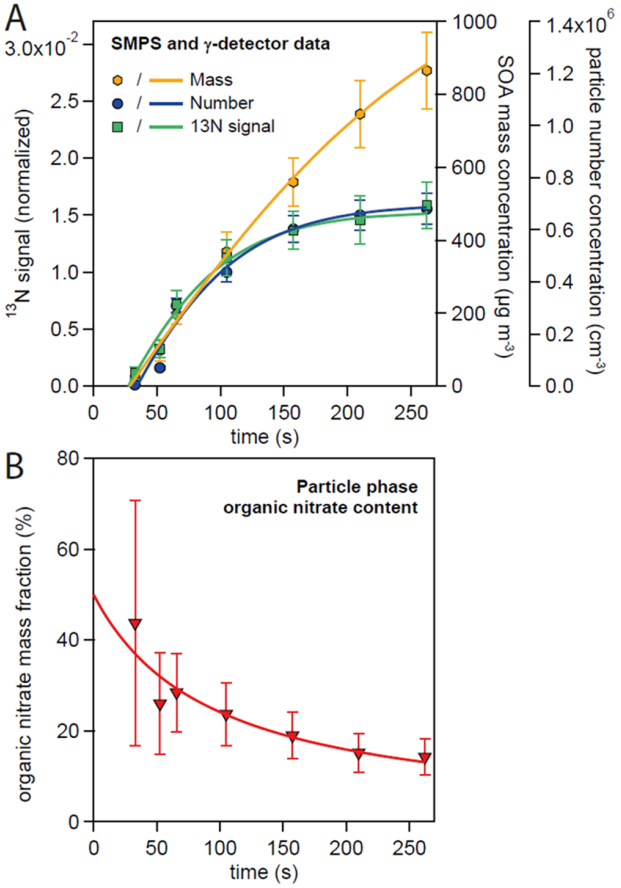

Figure 2. (A) SOA mass concentration (orange hexagons), aerosol particle-number concentration (blue circles), and the normalized ^{13}N signal (green squares) in the particle phase as a function of reaction time in the flow-tube reactor upon mixing of 1600 ppb O_3, 800 ppb NO, and 1000 ppb α-pinene. The solid lines are to guide the eye. (B) Organic nitrate content w_{ON} (red triangles) as a function of reaction time in the flow-tube reactor, assuming one nitrate group per organic molecule with a molar mass of 250 ± 50 g mol^{-1} (eq 1).

As discussed below, the deceleration in organic nitrate production during the course of the experiments is most likely due to depletion of NO in the reactor. In the atmosphere, NO is unlikely to be totally scavenged by ozone during daytime due to the continuous emission of NO_x and photolysis of NO_2. Such a scenario could not be simulated in the flow-tube experiments because the high ozone concentrations, which are necessary to produce a large enough amount of organic aerosol, drives the equilibrium strongly toward NO_2, even under the light conditions possible in our flow-tube setup. Irradiation with UV light (centered around 354 nm) had, in fact, no significant effect within experimental error on both produced SOA mass and strength of the ^{13}N signal (Figure S4).

The addition of an excess of 50 ppm cyclohexane as OH scavenger led to a complete shutdown of new particle formation. Experiments including ammonium sulfate seed particles revealed a strong suppression of SOA mass and the ^{13}N signal once cyclohexane was added. SOA production could be recovered upon increase of ozone concentrations, but the ^{13}N signal stayed low at an elevated background level, as shown

DOI: 10.1021/acs.est.6b00961
Environ. Sci. Technol. 2016, 50, 6334−6342

in Table S4. This suggests that the major pathway of organic nitrate formation occurs via the α-pinene−OH reaction, which is in line with the reaction mechanism proposed in Table 2.

We thus expect organic nitrate formation to be strong under day light conditions, i.e., during OH photooxidation. We performed a separate set of OH photooxidation experiments by in situ photolysis of HONO (see Figure S5 for experimental details). As outlined in Figure S5B, the organic nitrate mass fractions stabilized at ∼50% in the flow-tube reactor. This augmented value is higher than previously determined for the OH photooxidation of α-pinene[34,53] but in line with the proposed reaction mechanism because only RO_2 radicals produced in OH oxidation (RO_2^{II}) contribute to organic nitrate formation.[45,46] A possible reason for the discrepancy between previous studies and this study might be the larger concentration of NO in our experiments, as it is also in situ produced from HONO photolysis, which was expected to limit organic nitrate formation in previous studies.[34] In the atmosphere and under daylight conditions, NO exists in a photostationary state and is only scavenged at high ozone concentrations. Hence, the high organic nitrate contents of up to 44% found in field samples (Table 1) can be understood as a result of both ozonolysis and photooxidation but will also include organic nitrates produced via nighttime NO_3 oxidation. Although oxidation of α-pinene by NO_3 is known to produce anomalously low amounts of SOA and was thus less relevant in the experiments of this study, this reaction pathway can contribute strongly to the production of organic nitrates for other biogenic precursors.[23,38] Note that in the OH photooxidation experiment, as opposed to the ozonolysis experiments, new particle formation could not be directly correlated to the ^{13}N signal (Figure S5a).

Dependence on Environmental Parameters. We investigated the dependence of particle-phase nitrogen on relative humidity, NO_x and O_3 concentrations. Organic nitrates are known to undergo hydrolysis under humid conditions.[15,16] Figure 3a shows the ^{13}N signal measured at three different relative humidities: 0, 30 and 80% RH. The ^{13}N particle-phase signal was further normalized by the produced SOA mass because both signals showed the same scattering pattern between repetitions of the same experiment, indicating uniform nitrogen content. For every humidity displayed in Figure 3a, three full time dependencies have been measured, and the data points represent averages from all runs. Increased relative humidity led to a slight but significant decrease in the ^{13}N signal. It has to be noted that the duration of the experiment is shorter than the expected atmospheric lifetime of tertiary organic nitrates toward hydrolysis of several hours.[16,17,54] Primary and secondary nitrates are not expected to hydrolyze at atmospheric time scales.[55] The small dependence of the ^{13}N signal on relative humidity found in this study is thus expected to be more pronounced at atmospheric time scales.[17]

In a similar fashion, the NO_x concentrations were varied systematically between 1−100 ppb, yielding practically no difference in SOA mass, particle number, and ^{13}N signal, as shown in Figure 3b. Note that in these experiments, the concentrations of NO were much smaller than the O_3 concentration (1350 ppb), so that O_3 remained largely unaffected from immediate titration with NO upon mixing in the flow tube. Varying the O_3 concentration in our experiments strongly affected the mass of non-nitrated organics and, only to a slighter extent, the particle-number concentration and particle-phase nitrogen signal (Figure S6). Note that those

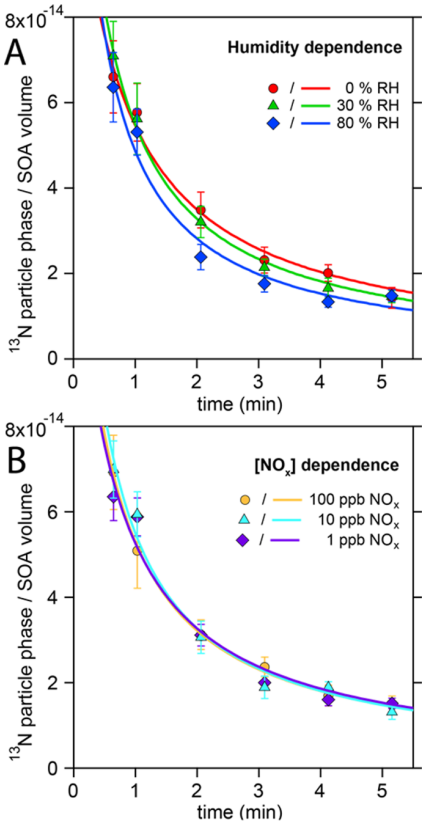

Figure 3. (A) Humidity dependence and (B) ^{14}NO concentration dependence of the ^{13}N signal in the particle phase as a function of reaction time in the flow-tube reactor, normalized by the produced SOA mass. Error bars denote standard deviations between multiple executions of the same experiment. Solid lines are least-squares fits to the data to guide the eye.

experiments were performed under low-NO_X conditions, where only trace amounts of labeled nitrogen were present in the system.

Box-Model Calculations. We applied the kinetic box model to showcase that the data can be qualitatively described with a simple kinetic mechanism. Panels a and b of Figure 4a show the concentration profiles of all major gas-phase species under typical experimental conditions with initial concentrations of 1600 ppb O_3, 1000 ppb α-pinene, and 800 ppb NO. NO (light blue solid line, Figure 4a) is quickly titrated by ozone and RO_2 and drops below 1 ppb after 25 s of the experiment. In this period, a large fraction of the total organic nitrate is formed through the RO_2 + NO channel (light green dashed line, Figure 4b), with most RO_2 originating from the α-pinene + OH reaction. After this point, organic nitrates are mostly produced through the α-pinene + NO_3 channel, leading to a slow but steady increase of the total organic nitrate concentration (dark green solid line). The concentration of in-situ-produced NO_3 stays in the low ppt range. These modeling results are consistent with the experimental observations, where formation of organic nitrates almost ceased after an initial period of fast growth. Predominant formation of organic nitrates via the α-pinene + OH channel at the beginning of the experiment may explain the correlation to new particle formation seen in Figure 2a: organic compounds formed via RO_2 radicals are known to

DOI: 10.1021/acs.est.6b00961
Environ. Sci. Technol. 2016, 50, 6334−6342

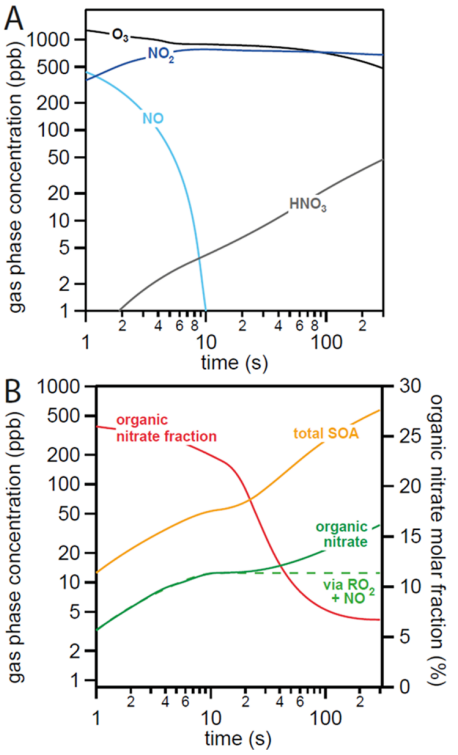

Figure 4. Modeling results showing the gas-phase concentrations of a selection of important (A) inorganic and (B) organic compounds tracked by the lumped chemistry box model. The dark green line represents all organic nitrates produced, whereas the dashed light green line shows only organic nitrates produced via the RO_2 + NO channel, hence excluding the α-pinene + NO_3 channel.

form highly oxidized multifunctional molecules by autoxidation, which may play a major role in new particle formation.[47,56,57]

In the model calculations, organic nitrates constituted up to ~26% of the total number of stable organic molecules in the gas phase (red solid line, Figure 4b), which is on the same order as the particle-phase composition determined in the ^{13}N tracer experiments, and shows the same temporal evolution as it drops to ~7% after 2 min of reaction time. The calculation results deviate from the experiment as organic nitrates were continuously produced via the α-pinene + NO_3 channel in the calculations (dark green solid line, Figure 4b), while in the experiments, no further organic nitrate was detected (Figure 2a), but rather, they followed the behavior of organic nitrates produced via the RO_2 + NO channel (light green dashed line, Figure 4b). Note that the time-dependent particle-phase composition depends not only on the concentrations and vapor pressure of the reaction products but also on their gas and bulk diffusivities in the case of nonequilibrium SOA partitioning: the nitrate-rich organic material condensed onto particles in the early stages of the experiment might not partition back to the gas phase on the time scale of the experiment if organic particles adopt an amorphous solid state.[58,59] In MCM, many stable organic nitrates formed via the α-pinene + NO_3 channel are first-generation products, which may be too volatile to partition into the particle phase in significant amounts and are assumed to play only a minor role in the initial particle nucleation.[59] This observation is consistent with previous results, such as those by Fry et al.[23] and Draper et al.,[24] who observed no aerosol formation from NO_3 oxidation of α-pinene. Further evidence against the significant contribution of the α-pinene + NO_3 channel to SOA mass comes from experiments under UV irradiation, showing a negligible effect of UV light on the ^{13}N signal during experiments (Figure S4). NO_3 photolyses readily at wavelengths in the visible part of the light spectrum.[60] Organic nitrates from the α-pinene + NO_3 channel are thus expected to decrease upon irradiation with UV light.

Future studies would benefit from a more detailed kinetic model, which includes a comprehensive chemical mechanism and also treats the full process of gas-phase oxidation, partitioning into the particle phase, and potential subsequent particle-phase chemistry.[61] Such complex models would, however, need a much larger set of kinetic data than that available in this study to constrain the multitude of model input parameters necessary to describe all important processes.[62,63] The lumped model developed in this study may help to describe the multiphase chemistry of SOA formation in future studies because it strongly reduces the complexity of the chemical mechanism while correctly describing the concentrations of all important gas-phase reactants.

In conclusion, nitrogen containing compounds account for a significant fraction of α-pinene SOA. Using a radioactive tracer method, we found that organic nitrates constitute up to 40% of aerosol mass, with a pronounced influence during the initial formation period of particles. Experiments using OH scavengers showed low particle-phase nitrogen, suggesting that organic nitrate formation is mostly achieved through oxidation with OH to form RO_2 radicals and subsequent reaction with NO, as summarized in Figure 5. Organic nitrates originating from OH oxidation may be extremely low-volatility compounds (ELVOCs), as suggested by the strong abundance of particle-phase nitrates at low aerosol-mass loadings and the tight correlation between organic nitrate content and particle number: strongly reduced particle formation rates in the presence of OH scavengers suggest that organic nitrates and other non-nitrated ELVOCs from OH-initiated oxidation may play an important role in facilitating particle nucleation and initial nanoparticle growth.

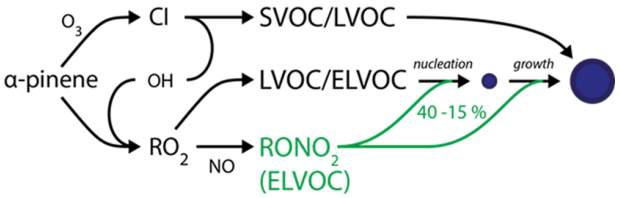

Figure 5. Schematic representation of the key processes explaining the experimental observations. α-Pinene reacts with ozone to Criegee intermediates (CI), which, under elimination of OH, decompose into semivolatile and low-volatile organic compounds (SVOC and LVOC). OH also reacts with α-pinene under the formation of RO_2 radicals that may react with NO to form organic nitrates ($RONO_2$), which are assumed to be of extremely low volatility, or non-nitrated low-volatility and extremely low volatility compounds (LVOC and ELVOC). ELVOCs from the OH oxidation of α-pinene might facilitate particle nucleation and, along with other oxidation products, lead to particle growth through condensation. The organic nitrate content ranges between 40% for freshly nucleated particles and 15% for particles in the accumulation-mode size range.

Strong formation of organic nitrates can significantly affect the atmospheric NO_x budget by reacting as reservoir species or

DOI: 10.1021/acs.est.6b00961
Environ. Sci. Technol. 2016, 50, 6334−6342

by providing a pathway for the deposition of particles and, hence, the removal of NO_y.[17] Because they are present in large amounts in organic aerosol, organic nitrates deposited in the lungs might have implications for human health because they release nitric acid upon hydrolysis. This is especially true in regions with a large contribution of biogenic SOA from monoterpene oxidation to the total aerosol burden, such as the Pacific Northwest, Mountain West, and the southeastern United States.[64,65]

■ ASSOCIATED CONTENT

Supporting Information

The Supporting Information is available free of charge on the ACS Publications website at DOI: 10.1021/acs.est.6b00961.

Experimental details on OH photooxidation experiments and calculations with the extended gas-phase chemistry mechanism. Molar mass of typical nitrated products for α-pinene ozonolysis (Table S1); HO_x and NO_y gas phase chemistry mechanism (Table S2); uptake coefficients for reactor wall losses (Table S3); and experimental data on OH scavenger experiments (Table S4). Experimental raw data from a typical experiment in the flow tube reactor (Figure S1); schematic representation of the reaction mechanism (Figure S2); comparison between lumped and explicit chemistry model (Figure S3); experimental data on UV irradiation experiments (Figure S4); experimental data on OH photooxidation (Figure S5); and experimental data on ozone concentration dependence experiments (Figure S6). (PDF)

■ AUTHOR INFORMATION

Corresponding Author

*Tel: 0049-6131-305-7401; e-mail: m.shiraiwa@mpic.de.

Notes

The authors declare no competing financial interest.

■ ACKNOWLEDGMENTS

This work was funded by the Max Planck Society (MPG) and the EU project PEGASOS. T.B. was supported by the Max Planck Graduate Center with the Johannes Gutenberg-Universität Mainz (MPGC). M.A. appreciates support by the Swiss National Science Foundation (grant no. 149492). We thank Goran Gržinić, Andrea M. Arangio, and Dogushan Kiliç for their help in conducting the experiments and Mario Birrer for technical support as well as Josef Dommen, Thorsten Bartels-Rausch, and Jason D. Surratt for helpful discussions.

■ REFERENCES

(1) Kanakidou, M.; Seinfeld, J. H.; Pandis, S. N.; Barnes, I.; Dentener, F. J.; Facchini, M. C.; Van Dingenen, R.; Ervens, B.; Nenes, A.; Nielsen, C. J.; Swietlicki, E.; Putaud, J. P.; Balkanski, Y.; Fuzzi, S.; Horth, J.; Moortgat, G. K.; Winterhalter, R.; Myhre, C. E. L.; Tsigaridis, K.; Vignati, E.; Stephanou, E. G.; Wilson, J. Organic aerosol and global climate modelling: a review. *Atmos. Chem. Phys.* **2005**, *5*, 1053−1123.

(2) Fuzzi, S.; Andreae, M. O.; Huebert, B. J.; Kulmala, M.; Bond, T. C.; Boy, M.; Doherty, S. J.; Guenther, A.; Kanakidou, M.; Kawamura, K.; Kerminen, V. M.; Lohmann, U.; Russell, L. M.; Pöschl, U. Critical assessment of the current state of scientific knowledge, terminology, and research needs concerning the role of organic aerosols in the atmosphere, climate, and global change. *Atmos. Chem. Phys.* **2006**, *6*, 2017−2038.

(3) IPCC. *Climate Change 2013, The Physical Science Basis*; Cambridge University Press: Cambridge, United Kingdom, 2013.

(4) Jimenez, J. L.; Canagaratna, M. R.; Donahue, N. M.; Prevot, A. S. H.; Zhang, Q.; Kroll, J. H.; DeCarlo, P. F.; Allan, J. D.; Coe, H.; Ng, N. L.; Aiken, A. C.; Docherty, K. S.; Ulbrich, I. M.; Grieshop, A. P.; Robinson, A. L.; Duplissy, J.; Smith, J. D.; Wilson, K. R.; Lanz, V. A.; Hueglin, C.; Sun, Y. L.; Tian, J.; Laaksonen, A.; Raatikainen, T.; Rautiainen, J.; Vaattovaara, P.; Ehn, M.; Kulmala, M.; Tomlinson, J. M.; Collins, D. R.; Cubison, M. J.; Dunlea, E. J.; Huffman, J. A.; Onasch, T. B.; Alfarra, M. R.; Williams, P. I.; Bower, K.; Kondo, Y.; Schneider, J.; Drewnick, F.; Borrmann, S.; Weimer, S.; Demerjian, K.; Salcedo, D.; Cottrell, L.; Griffin, R.; Takami, A.; Miyoshi, T.; Hatakeyama, S.; Shimono, A.; Sun, J. Y.; Zhang, Y. M.; Dzepina, K.; Kimmel, J. R.; Sueper, D.; Jayne, J. T.; Herndon, S. C.; Trimborn, A. M.; Williams, L. R.; Wood, E. C.; Middlebrook, A. M.; Kolb, C. E.; Baltensperger, U.; Worsnop, D. R. Evolution of organic aerosols in the atmosphere. *Science* **2009**, *326* (5959), 1525−1529.

(5) Pöschl, U.; Shiraiwa, M. Multiphase Chemistry at the Atmosphere−Biosphere Interface Influencing Climate and Public Health in the Anthropocene. *Chem. Rev.* **2015**, *115*, 4440−4475.

(6) Robinson, A. L.; Subramanian, R.; Donahue, N. M.; Bernardo-Bricker, A.; Rogge, W. F. Source apportionment of molecular markers and organic aerosol. 3. Food cooking emissions. *Environ. Sci. Technol.* **2006**, *40* (24), 7820−7827.

(7) Hallquist, M.; Wenger, J. C.; Baltensperger, U.; Rudich, Y.; Simpson, D.; Claeys, M.; Dommen, J.; Donahue, N. M.; George, C.; Goldstein, A. H.; Hamilton, J. F.; Herrmann, H.; Hoffmann, T.; Iinuma, Y.; Jang, M.; Jenkin, M. E.; Jimenez, J. L.; Kiendler-Scharr, A.; Maenhaut, W.; McFiggans, G.; Mentel, T. F.; Monod, A.; Prevot, A. S. H.; Seinfeld, J. H.; Surratt, J. D.; Szmigielski, R.; Wildt, J. The formation, properties and impact of secondary organic aerosol: current and emerging issues. *Atmos. Chem. Phys.* **2009**, *9* (14), 5155−5235.

(8) Ziemann, P. J.; Atkinson, R. Kinetics, products, and mechanisms of secondary organic aerosol formation. *Chem. Soc. Rev.* **2012**, *41* (19), 6582−6605.

(9) Seinfeld, J. H.; Pandis, S. N. *Atmospheric chemistry and physics - From air pollution to climate change*; John Wiley & Sons, Inc.: New York, 2006.

(10) Paulson, S. E.; Sen, A. D.; Liu, P.; Fenske, J. D.; Fox, M. J. Evidence for formation of OH radicals from the reaction of O3 with alkenes in the gas phase. *Geophys. Res. Lett.* **1997**, *24* (24), 3193−3196.

(11) Donahue, N. M.; Kroll, J. H.; Anderson, J. G.; Demerjian, K. L. Direct observation of OH production from the ozonolysis of olefins. *Geophys. Res. Lett.* **1998**, *25* (1), 59−62.

(12) Paulot, F.; Crounse, J. D.; Kjaergaard, H. G.; Kurten, A.; St Clair, J. M.; Seinfeld, J. H.; Wennberg, P. O. Unexpected epoxide formation in the gas-phase photooxidation of isoprene. *Science* **2009**, *325* (5941), 730−733.

(13) Taraborrelli, D.; Lawrence, M. G.; Crowley, J. N.; Dillon, T. J.; Gromov, S.; Groß, C. B. M.; Vereecken, L.; Lelieveld, J. Hydroxyl radical buffered by isoprene oxidation over tropical forests. *Nat. Geosci.* **2012**, *5* (3), 190−193.

(14) Renbaum, L. H.; Smith, G. D. Organic nitrate formation in the radical-initiated oxidation of model aerosol particles in the presence of NOx. *Phys. Chem. Chem. Phys.* **2009**, *11* (36), 8040−8047.

(15) Baker, J. W.; Easty, D. M. Hydrolysis of Organic Nitrates. *Nature* **1950**, *166* (4212), 156−156.

(16) Liu, S.; Shilling, J. E.; Song, C.; Hiranuma, N.; Zaveri, R. A.; Russell, L. M. Hydrolysis of Organonitrate Functional Groups in Aerosol Particles. *Aerosol Sci. Technol.* **2012**, *46* (12), 1359−1369.

(17) Pye, H. O. T.; Luecken, D. J.; Xu, L.; Boyd, C. M.; Ng, N. L.; Baker, K. R.; Ayres, B. R.; Bash, J. O.; Baumann, K.; Carter, W. P. L.; Edgerton, E.; Fry, J. L.; Hutzell, W. T.; Schwede, D. B.; Shepson, P. B. Modeling the Current and Future Roles of Particulate Organic Nitrates in the Southeastern United States. *Environ. Sci. Technol.* **2015**, *49* (24), 14195−14203.

(18) Koenig, J. Q.; Covert, D. S.; Pierson, W. E. Effects of inhalation of acidic compounds on pulmonary function in allergic adolescent subjects. *Environ. Health Perspect.* **1989**, *79*, 173−178.

(19) Hatakeyama, S.; Izumi, K.; Fukuyama, T.; Akimoto, H.; Washida, N. Reactions of OH with α-pinene and β-pinene in air: Estimate of global CO production from the atmospheric oxidation of terpenes. *J. Geophys. Res. Atoms.* **1991**, *96* (D1), 947−958.
(20) Kroll, J. H.; Ng, N. L.; Murphy, S. M.; Flagan, R. C.; Seinfeld, J. H. Secondary organic aerosol formation from isoprene photooxidation. *Environ. Sci. Technol.* **2006**, *40* (6), 1869−1877.
(21) Ng, N. L.; Chhabra, P. S.; Chan, A. W. H.; Surratt, J. D.; Kroll, J. H.; Kwan, A. J.; McCabe, D. C.; Wennberg, P. O.; Sorooshian, A.; Murphy, S. M.; Dalleska, N. F.; Flagan, R. C.; Seinfeld, J. H. Effect of NOx level on secondary organic aerosol (SOA) formation from the photooxidation of terpenes. *Atmos. Chem. Phys.* **2007**, *7* (19), 5159−5174.
(22) Spittler, M.; Barnes, I.; Bejan, I.; Brockmann, K. J.; Benter, T.; Wirtz, K. Reactions of NO3 radicals with limonene and α-pinene: Product and SOA formation. *Atmos. Environ.* **2006**, *40*, 116−127.
(23) Fry, J. L.; Draper, D. C.; Barsanti, K. C.; Smith, J. N.; Ortega, J.; Winkler, P. M.; Lawler, M. J.; Brown, S. S.; Edwards, P. M.; Cohen, R. C.; Lee, L. Secondary Organic Aerosol Formation and Organic Nitrate Yield from NO3 Oxidation of Biogenic Hydrocarbons. *Environ. Sci. Technol.* **2014**, *48* (20), 11944−11953.
(24) Draper, D. C.; Farmer, D. K.; Desyaterik, Y.; Fry, J. L. A qualitative comparison of secondary organic aerosol yields and composition from ozonolysis of monoterpenes at varying concentrations of NO2. *Atmos. Chem. Phys.* **2015**, *15* (21), 12267−12281.
(25) Andreae, M. O.; Gelencser, A. Black carbon or brown carbon? The nature of light-absorbing carbonaceous aerosols. *Atmos. Chem. Phys.* **2006**, *6*, 3131−3148.
(26) Laskin, A.; Laskin, J.; Nizkorodov, S. A. Chemistry of Atmospheric Brown Carbon. *Chem. Rev.* **2015**, *115* (10), 4335−4382.
(27) George, C.; Ammann, M.; D'Anna, B.; Donaldson, D. J.; Nizkorodov, S. A. Heterogeneous Photochemistry in the Atmosphere. *Chem. Rev.* **2015**, *115* (10), 4218−4258.
(28) Song, C.; Gyawali, M.; Zaveri, R. A.; Shilling, J. E.; Arnott, W. P. Light absorption by secondary organic aerosol from α-pinene: Effects of oxidants, seed aerosol acidity, and relative humidity. *J. Geophys. Res. Atmos.* **2013**, *118* (20), 11741−11749.
(29) Day, D. A.; Liu, S.; Russell, L. M.; Ziemann, P. J. Organonitrate group concentrations in submicron particles with high nitrate and organic fractions in coastal southern California. *Atmos. Environ.* **2010**, *44* (16), 1970−1979.
(30) Pöhlker, C.; Wiedemann, K. T.; Sinha, B.; Shiraiwa, M.; Gunthe, S. S.; Smith, M.; Su, H.; Artaxo, P.; Chen, Q.; Cheng, Y.; Elbert, W.; Gilles, M. K.; Kilcoyne, A. L. D.; Moffet, R. C.; Weigand, M.; Martin, S. T.; Pöschl, U.; Andreae, M. O. Biogenic potassium salt particles as seeds for secondary organic aerosol in the Amazon. *Science* **2012**, *337* (6098), 1075−1078.
(31) Ayres, B. R.; Allen, H. M.; Draper, D. C.; Brown, S. S.; Wild, R. J.; Jimenez, J. L.; Day, D. A.; Campuzano-Jost, P.; Hu, W.; de Gouw, J.; Koss, A.; Cohen, R. C.; Duffey, K. C.; Romer, P.; Baumann, K.; Edgerton, E.; Takahama, S.; Thornton, J. A.; Lee, B. H.; Lopez-Hilfiker, F. D.; Mohr, C.; Wennberg, P. O.; Nguyen, T. B.; Teng, A.; Goldstein, A. H.; Olson, K.; Fry, J. L. Organic nitrate aerosol formation via NO3 + biogenic volatile organic compounds in the southeastern United States. *Atmos. Chem. Phys.* **2015**, *15* (23), 13377−13392.
(32) Rollins, A. W.; Browne, E. C.; Min, K.-E.; Pusede, S. E.; Wooldridge, P. J.; Gentner, D. R.; Goldstein, A. H.; Liu, S.; Day, D. A.; Russell, L. M.; Cohen, R. C. Evidence for NOx Control over Nighttime SOA Formation. *Science* **2012**, *337* (6099), 1210−1212.
(33) Fry, J. L.; Kiendler-Scharr, A.; Rollins, A. W.; Wooldridge, P. J.; Brown, S. S.; Fuchs, H.; Dubé, W.; Mensah, A.; dal Maso, M.; Tillmann, R.; Dorn, H. P.; Brauers, T.; Cohen, R. C. Organic nitrate and secondary organic aerosol yield from NO3 oxidation of β-pinene evaluated using a gas-phase kinetics/aerosol partitioning model. *Atmos. Chem. Phys.* **2009**, *9* (4), 1431−1449.
(34) Rollins, A. W.; Smith, J. D.; Wilson, K. R.; Cohen, R. C. Real Time In Situ Detection of Organic Nitrates in Atmospheric Aerosols. *Environ. Sci. Technol.* **2010**, *44* (14), 5540−5545.
(35) Bruns, E. A.; Perraud, V.; Zelenyuk, A.; Ezell, M. J.; Johnson, S. N.; Yu, Y.; Imre, D.; Finlayson-Pitts, B. J.; Alexander, M. L. Comparison of FTIR and Particle Mass Spectrometry for the Measurement of Particulate Organic Nitrates. *Environ. Sci. Technol.* **2010**, *44* (3), 1056−1061.
(36) Farmer, D. K.; Matsunaga, A.; Docherty, K. S.; Surratt, J. D.; Seinfeld, J. H.; Ziemann, P. J.; Jimenez, J. L. Response of an aerosol mass spectrometer to organonitrates and organosulfates and implications for atmospheric chemistry. *Proc. Natl. Acad. Sci. U. S. A.* **2010**, *107* (15), 6670−6675.
(37) Zaveri, R. A.; Berkowitz, C. M.; Brechtel, F. J.; Gilles, M. K.; Hubbe, J. M.; Jayne, J. T.; Kleinman, L. I.; Laskin, A.; Madronich, S.; Onasch, T. B.; Pekour, M. S.; Springston, S. R.; Thornton, J. A.; Tivanski, A. V.; Worsnop, D. R. Nighttime chemical evolution of aerosol and trace gases in a power plant plume: Implications for secondary organic nitrate and organosulfate aerosol formation, NO3 radical chemistry, and N2O5 heterogeneous hydrolysis. *J. Geophys. Res.* **2010**, *115*, D12304.
(38) Boyd, C. M.; Sanchez, J.; Xu, L.; Eugene, A. J.; Nah, T.; Tuet, W. Y.; Guzman, M. I.; Ng, N. L. Secondary organic aerosol formation from the beta-pinene+NO3 system: effect of humidity and peroxy radical fate. *Atmos. Chem. Phys.* **2015**, *15* (13), 7497−7522.
(39) Amman, M. Using ^{13}N as tracer in heterogeneous atmospheric chemistry experiments. *Radiochim. Acta* **2001**, *89* (11−12), 831−838.
(40) Kalberer, M.; Tabor, K.; Ammann, M.; Parrat, Y.; Weingartner, E.; Piguet, D.; Rossler, E.; Jost, D. T.; Turler, A.; Gäggeler, H. W.; Baltensperger, U. Heterogeneous chemical processing of $^{13}NO_2$ by monodisperse carbon aerosols at very low concentrations. *J. Phys. Chem.* **1996**, *100* (38), 15487−15493.
(41) Vlasenko, A.; Huthwelker, T.; Gäggeler, H. W.; Ammann, M. Kinetics of the heterogeneous reaction of nitric acid with mineral dust particles: an aerosol flowtube study. *Phys. Chem. Chem. Phys.* **2009**, *11* (36), 7921−7930.
(42) Kerbrat, M.; Huthwelker, T.; Gäggeler, H. W.; Ammann, M. Interaction of Nitrous Acid with Polycrystalline Ice: Adsorption on the Surface and Diffusion into the Bulk. *J. Phys. Chem. C* **2010**, *114* (5), 2208−2219.
(43) Shiraiwa, M.; Sosedova, Y.; Rouviere, A.; Yang, H.; Zhang, Y.; Abbatt, J. P. D.; Ammann, M.; Pöschl, U. The role of long-lived reactive oxygen intermediates in the reaction of ozone with aerosol particles. *Nat. Chem.* **2011**, *3* (4), 291−295.
(44) Gržinić, G.; Bartels-Rausch, T.; Berkemeier, T.; Türler, A.; Ammann, M. Viscosity controls humidity dependence of N2O5 uptake to citric acid aerosol. *Atmos. Chem. Phys.* **2015**, *15* (23), 13615−13625.
(45) Saunders, S. M.; Jenkin, M. E.; Derwent, R. G.; Pilling, M. J. Protocol for the development of the Master Chemical Mechanism, MCM v3 (Part A): tropospheric degradation of non-aromatic volatile organic compounds. *Atmos. Chem. Phys.* **2003**, *3* (1), 161−180.
(46) Jenkin, M. E.; Saunders, S. M.; Pilling, M. J. The tropospheric degradation of volatile organic compounds: a protocol for mechanism development. *Atmos. Environ.* **1997**, *31* (1), 81−104.
(47) Ehn, M.; Thornton, J. A.; Kleist, E.; Sipila, M.; Junninen, H.; Pullinen, I.; Springer, M.; Rubach, F.; Tillmann, R.; Lee, B.; Lopez-Hilfiker, F.; Andres, S.; Acir, I. H.; Rissanen, M.; Jokinen, T.; Schobesberger, S.; Kangasluoma, J.; Kontkanen, J.; Nieminen, T.; Kurten, T.; Nielsen, L. B.; Jorgensen, S.; Kjaergaard, H. G.; Canagaratna, M.; Maso, M. D.; Berndt, T.; Petaja, T.; Wahner, A.; Kerminen, V. M.; Kulmala, M.; Worsnop, D. R.; Wildt, J.; Mentel, T. F. A large source of low-volatility secondary organic aerosol. *Nature* **2014**, *506* (7489), 476−479.
(48) Kroll, J. H.; Hanisco, T. F.; Donahue, N. M.; Demerjian, K. L.; Anderson, J. G. Accurate, direct measurements of oh yields from gas-phase ozone-alkene reactions using an in situ LIF Instrument. *Geophys. Res. Lett.* **2001**, *28* (20), 3863−3866.
(49) Atkinson, R.; Aschmann, S. M.; Arey, J.; Shorees, B. Formation of OH radicals in the gas phase reactions of O3 with a series of terpenes. *J. Geophys. Res. Atoms.* **1992**, *97* (D5), 6065−6073.
(50) Pinho, P. G.; Pio, C. A.; Carter, W. P. L.; Jenkin, M. E. Evaluation of α- and β-pinene degradation in the detailed tropospheric

DOI: 10.1021/acs.est.6b00961
Environ. Sci. Technol. 2016, 50, 6334−6342

chemistry mechanism, MCM v3.1, using environmental chamber data. *J. Atmos. Chem.* **2007**, *57* (2), 171−202.
(51) Matsunaga, A.; Ziemann, P. J. Gas-wall partitioning of organic compounds in a Teflon film chamber and potential effects on reaction product and aerosol yield measurements. *Aerosol Sci. Technol.* **2010**, *44* (10), 881−892.
(52) Kuwata, M.; Zorn, S. R.; Martin, S. T. Using Elemental Ratios to Predict the Density of Organic Material Composed of Carbon, Hydrogen, and Oxygen. *Environ. Sci. Technol.* **2012**, *46* (2), 787−794.
(53) Noziere, B.; Barnes, I.; Becker, K. H. Product study and mechanisms of the reactions of alpha-pinene and of pinonaldehyde with OH radicals. *J. Geophys. Res. Atmos.* **1999**, *104* (D19), 23645−23656.
(54) Bean, J. K.; Hildebrandt Ruiz, L. Gas-particle partitioning and hydrolysis of organic nitrates formed from the oxidation of α-pinene in environmental chamber experiments. *Atmos. Chem. Phys.* **2016**, *16*, 2175−2184.
(55) Darer, A. I.; Cole-Filipiak, N. C.; O'Connor, A. E.; Elrod, M. J. Formation and Stability of Atmospherically Relevant Isoprene-Derived Organosulfates and Organonitrates. *Environ. Sci. Technol.* **2011**, *45* (5), 1895−1902.
(56) Crounse, J. D.; Nielsen, L. B.; Jørgensen, S.; Kjaergaard, H. G.; Wennberg, P. O. Autoxidation of organic compounds in the atmosphere. *J. Phys. Chem. Lett.* **2013**, *4* (20), 3513−3520.
(57) Mentel, T. F.; Springer, M.; Ehn, M.; Kleist, E.; Pullinen, I.; Kurtén, T.; Rissanen, M.; Wahner, A.; Wildt, J. Formation of highly oxidized multifunctional compounds: autoxidation of peroxy radicals formed in the ozonolysis of alkenes − deduced from structure−product relationships. *Atmos. Chem. Phys.* **2015**, *15* (12), 6745−6765.
(58) Vaden, T. D.; Imre, D.; Beranek, J.; Shrivastava, M.; Zelenyuk, A. Evaporation kinetics and phase of laboratory and ambient secondary organic aerosol. *Proc. Natl. Acad. Sci. U. S. A.* **2011**, *108* (6), 2190−2195.
(59) Perraud, V.; Bruns, E. A.; Ezell, M. J.; Johnson, S. N.; Yu, Y.; Alexander, M. L.; Zelenyuk, A.; Imre, D.; Chang, W. L.; Dabdub, D.; Pankow, J. F.; Finlayson-Pitts, B. J. Nonequilibrium atmospheric secondary organic aerosol formation and growth. *Proc. Natl. Acad. Sci. U. S. A.* **2012**, *109* (8), 2836−2841.
(60) Orlando, J. J.; Tyndall, G. S.; Moortgat, G. K.; Calvert, J. G. Quantum yields for nitrate radical photolysis between 570 and 635 nm. *J. Phys. Chem.* **1993**, *97* (42), 10996−11000.
(61) Shiraiwa, M.; Yee, L. D.; Schilling, K. A.; Loza, C. L.; Craven, J. S.; Zuend, A.; Ziemann, P. J.; Seinfeld, J. H. Size distribution dynamics reveal particle-phase chemistry in organic aerosol formation. *Proc. Natl. Acad. Sci. U. S. A.* **2013**, *110* (29), 11746−11750.
(62) Berkemeier, T.; Huisman, A. J.; Ammann, M.; Shiraiwa, M.; Koop, T.; Pöschl, U. Kinetic regimes and limiting cases of gas uptake and heterogeneous reactions in atmospheric aerosols and clouds: a general classification scheme. *Atmos. Chem. Phys.* **2013**, *13* (14), 6663−6686.
(63) Shiraiwa, M.; Berkemeier, T.; Schilling-Fahnestock, K. A.; Seinfeld, J. H.; Poschl, U. Molecular corridors and kinetic regimes in the multiphase chemical evolution of secondary organic aerosol. *Atmos. Chem. Phys.* **2014**, *14* (16), 8323−8341.
(64) Goldstein, A. H.; Koven, C. D.; Heald, C. L.; Fung, I. Y. Biogenic carbon and anthropogenic pollutants combine to form a cooling haze over the southeastern United States. *Proc. Natl. Acad. Sci. U. S. A.* **2009**, *106* (22), 8835−8840.
(65) Xu, L.; Guo, H.; Boyd, C. M.; Klein, M.; Bougiatioti, A.; Cerully, K. M.; Hite, J. R.; Isaacman-VanWertz, G.; Kreisberg, N. M.; Knote, C.; Olson, K.; Koss, A.; Goldstein, A. H.; Hering, S. V.; de Gouw, J.; Baumann, K.; Lee, S.-H.; Nenes, A.; Weber, R. J.; Ng, N. L. Effects of anthropogenic emissions on aerosol formation from isoprene and monoterpenes in the southeastern United States. *Proc. Natl. Acad. Sci. U. S. A.* **2015**, *112* (1), 37−42.
(66) Lee, A. K. Y.; Abbatt, J. P. D.; Leaitch, W. R.; Li, S. M.; Sjostedt, S. J.; Wentzell, J. J. B.; Liggio, J.; Macdonald, A. M. Substantial secondary organic aerosol formation in a coniferous forest: observations of both day and night time chemistry. *Atmos. Chem. Phys. Discuss.* **2015**, *15* (20), 28005−28035.
(67) Xu, L.; Suresh, S.; Guo, H.; Weber, R. J.; Ng, N. L. Aerosol characterization over the southeastern United States using high-resolution aerosol mass spectrometry: spatial and seasonal variation of aerosol composition and sources with a focus on organic nitrates. *Atmos. Chem. Phys.* **2015**, *15* (13), 7307−7336.

DOI: 10.1021/acs.est.6b00961
Environ. Sci. Technol. 2016, 50, 6334−6342

Supporting Information

Organic nitrate contribution to new particle formation and growth in secondary organic aerosols from α-pinene ozonolysis

Thomas Berkemeier[1], Markus Ammann[2], Thomas F. Mentel[3], Ulrich Pöschl[1] and Manabu Shiraiwa[1,*]

[1] Multiphase Chemistry Department, Max Planck Institute for Chemistry, Mainz, Germany

[2] Laboratory of Environmental Chemistry, Paul Scherrer Institute, Villigen, Switzerland

[3] Institute of Energy and Climate Research, IEK-8, Forschungszentrum Jülich, Jülich, Germany

Content

12 pages, 4 tables, 6 figures

OH photooxidation experiments

In the photooxidation experiments, the radioactive tracer is introduced as $HO^{13}NO$. OH radicals form during the photodissociation of HONO under irradiation with UV lamps centered at 350 nm, also releasing the labelled nitrous oxide ^{13}NO. HONO is prepared by reduction of NO_2 gas over a surface of ABTS (diammonium salt of azino-bis(ethylbenzothiazoline-sulfonic acid)). NO_2 is generated by oxidation of NO with an equal amount of ozone in an equilibration volume (~1 min residence time). The photooxidation experiments were carried out at ~10 % RH since the reduction of NO_2 over ATBS required a humidity of 35 % RH.[1]

Calculations with extended gas phase chemistry mechanism

For evaluation of the lumped SOA formation model presented in this study, we directly compare it to a box model running the full Master Chemical Mechanism (MCM).[2, 3] The calculations were performed using FACSIMILE3.05 (AEATechnology) embedded in the EASY modelling environment[4] combining the inorganic section and the full α-pinene mechanism of version MCM 3.3.1 without any changes. Wall losses were the same as in the lumped model; in addition, all radical species were allowed to be lost to the walls with a rate of 5×10^{-7} s^{-1}. Note that while MCM 3.3.1 treats 293 organic species in 942 reactions for the oxidation of α-pinene, still not all possible reaction pathways are considered in MCM as shown by self-generating mechanisms such as GECKO-A, comprising an even larger set on the order of 1×10^5 chemical species.[5-7] These protocols do not discriminate reactions by their potential contribution and hence for many reactions the corresponding rate coefficients are not well-constrained. Furthermore, particle phase composition will depend on other factors, most importantly vapor pressure, but also particle phase chemistry or particle phase state. Due to this inherent complexity, we decided to use the simplest model possible that gives a good first-order approximation of the ongoing chemistry, compared to the MCM mechanism. We will highlight the main differences between modelling results of the lumped model and a box model using the full MCM mechanism in the following. SI Fig. S3 compares two calculations using identical starting concentrations of $[O_3]_0$ = 1000 ppb, $[\alpha\text{-pinene}]_0$ = 1000 ppb and $[NO]_0$ = 500 ppb. For both inorganic (SI Fig. S3a) and organic compounds (SI Fig. S3b), a very close correlation is observed between the full MCM (solid lines) and lumped model (dashed lines). The lumped model shows slightly higher HO_x (≡ OH, HO_2) concentrations and

consequently a higher concentration of HNO_3 and a quicker decay of NO. Concentrations of ozone and NO_2 are almost identical in both models.

Table S1. Molar mass of typical nitrated products found in forested regions and suggested by the Master Chemical Mechanism (MCM) for α-pinene ozonolysis.

Sum formula	Molar mass ($g\ mol^{-1}$)	Reference
$C_{10}H_{15}NO_{11}$	325.2	Ehn, et al. [8]
$C_7H_9NO_6$	203.1	MCM[2, 3]
$C_7H_{11}NO_6$	205.2	MCM[2, 3]
$C_{10}H_{15}NO_4$	213.2	MCM[2, 3]
$C_9H_{15}NO_6$	233.2	MCM[2, 3]
$C_{10}H_{15}NO_6$	245.2	MCM[2, 3]

Table S2. HO_x and NO_y chemistry from the Master Chemical Mechanism (MCM) with reaction rates at 295 K and 0 % RH.

#	Reaction	Reaction rate
RS1	$NO + O_3 \rightarrow NO_2$	$k_1 = 1.7\times10^{-17}$ cm^3 s^{-1}
RS2	$NO_2 + O_3 \rightarrow NO_3$	$k_2 = 3.2\times10^{-17}$ cm^3 s^{-1}
RS3	$2\ NO \rightarrow 2\ NO_2$	$k_3 = 1.1\times10^{-19}$ cm^3 s^{-1}
RS4	$NO + NO_3 \rightarrow 2\ NO_2$	$k_4 = 2.6\times10^{-11}$ cm^3 s^{-1}
RS5	$NO_2 + NO_3 \rightarrow NO + NO_2$	$k_5 = 6.3\times10^{-16}$ cm^3 s^{-1}
RS6	$NO_2 + NO_3 \rightarrow N_2O_5$	$k_6 = 1.3\times10^{-12}$ cm^3 s^{-1}
RS7	$OH + O_3 \rightarrow HO_2$	$k_7 = 7.0\times10^{-14}$ cm^3 s^{-1}
RS8	$OH + H_2O_2 \rightarrow HO_2$	$k_8 = 1.7\times10^{-12}$ cm^3 s^{-1}
RS9	$HO_2 + O_3 \rightarrow OH$	$k_9 = 2.0\times10^{-15}$ cm^3 s^{-1}
RS10	$OH + HO_2 \rightarrow$	$k_{10} = 1.1\times10^{-10}$ cm^3 s^{-1}
RS11	$HO_2 + HO_2 \rightarrow H_2O_2$	$k_{11} = 3.0\times10^{-12}$ cm^3 s^{-1}
RS12	$OH + NO \rightarrow HONO$	$k_{12} = 1.0\times10^{-11}$ cm^3 s^{-1}
RS13	$OH + NO_2 \rightarrow HNO_3$	$k_{13} = 1.2\times10^{-11}$ cm^3 s^{-1}
RS14	$OH + NO_3 \rightarrow HO_2 + NO_2$	$k_{14} = 2.0\times10^{-11}$ cm^3 s^{-1}
RS15	$HO_2 + NO \rightarrow OH + NO_2$	$k_{15} = 8.6\times10^{-12}$ cm^3 s^{-1}
RS16	$HO_2 + NO_2 \rightarrow HO_2NO_2$	$k_{16} = 1.4\times10^{-12}$ cm^3 s^{-1}
RS17	$OH + HO_2NO_2 \rightarrow NO_2$	$k_{17} = 3.3\times10^{-12}$ cm^3 s^{-1}
RS18	$HO_2 + NO_3 \rightarrow OH + NO_2$	$k_{18} = 4.0\times10^{-12}$ cm^3 s^{-1}
RS19	$OH + HONO \rightarrow NO_2$	$k_{19} = 6.0\times10^{-12}$ cm^3 s^{-1}
RS20	$OH + HONO \rightarrow NO_3$	$k_{20} = 8.3\times10^{-13}$ cm^3 s^{-1}
RS21	$HNO_3 \rightarrow$	$k_{21} = 6.0\times10^{-6}$ s^{-1}
RS22	$N_2O_5 \rightarrow$	$k_{22} = 4.0\times10^{-4}$ s^{-1}
RS23	$N_2O_5 \rightarrow NO_2 + NO_3$	$k_{23} = 3.1\times10^{-2}$ s^{-1}
RS24	$HO_2NO_2 \rightarrow HO_2 + NO_2$	$k_{24} = 5.8\times10^{-2}$ s^{-1}

Table S3. Uptake coefficients on the flow reactor walls assumed in the kinetic model.

Species	Γ	References
O_3	5×10^{-8}	Steimer, et al. [9]
NO_2	1×10^{-8}	Crowley, et al. [10]
NO_3	5×10^{-7}	Gržinić, et al. [11]
HNO_3	7×10^{-7}	Vlasenko, et al. [12]
N_2O_5	5×10^{-7}	Gržinić, et al. [11]

Table S4. Experimental results in OH scavenger experiments.

Exp.	$(NH_4)_2SO_4$ seed	cyclohexane [ppm]	α-pinene [ppb]	ozone [ppb]	^{13}N signal []	Particle mass [μg m^{-3}]	Particle number [cm^{-3}]
#1	Off	-	1500	700	not measured	820	4.6×10^5
#2	Off	50	1500	700	not measured	2	1000
#3	On	-	800	-	background	300	6×10^4
#4	on	-	800	700	0.04	570	1.1×10^5
#5	on	50	800	700	0.001	300	8×10^4
#6	on	50	800	1000	0.001	500	1.2×10^5

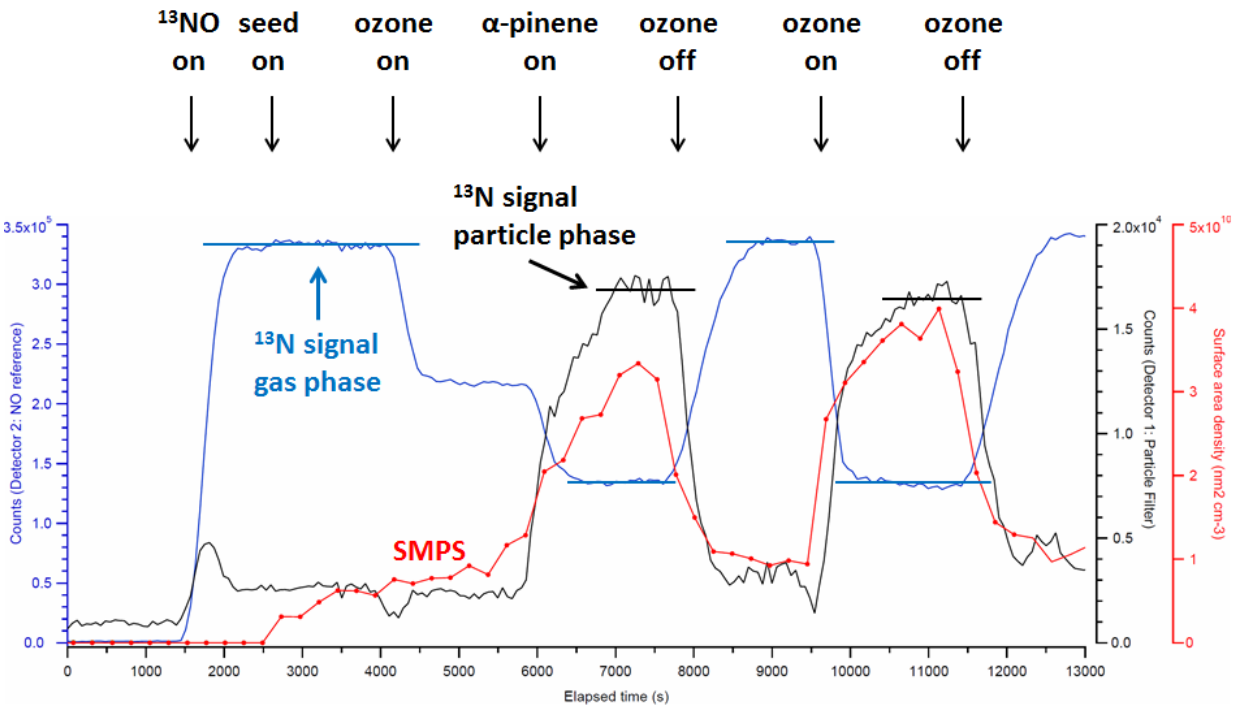

Fig. S1. Experimental raw data from a typical experiment in the flow tube reactor. Under ozone exposure, the ^{13}N signal at the gas-phase detector (blue solid line) drops and the ^{13}N signal at the particle-phase detector (black solid line) increases as nitrated organic compounds are incorporated into aerosol particles. Particle size and number were measured with a scanning mobility particle sizer (SMPS, red solid line). Horizontal lines denote signal averages, once the signal had stabilized. Note that the $NH_4(SO_4)_2$ seed particles used here were not used in the majority of experiments.

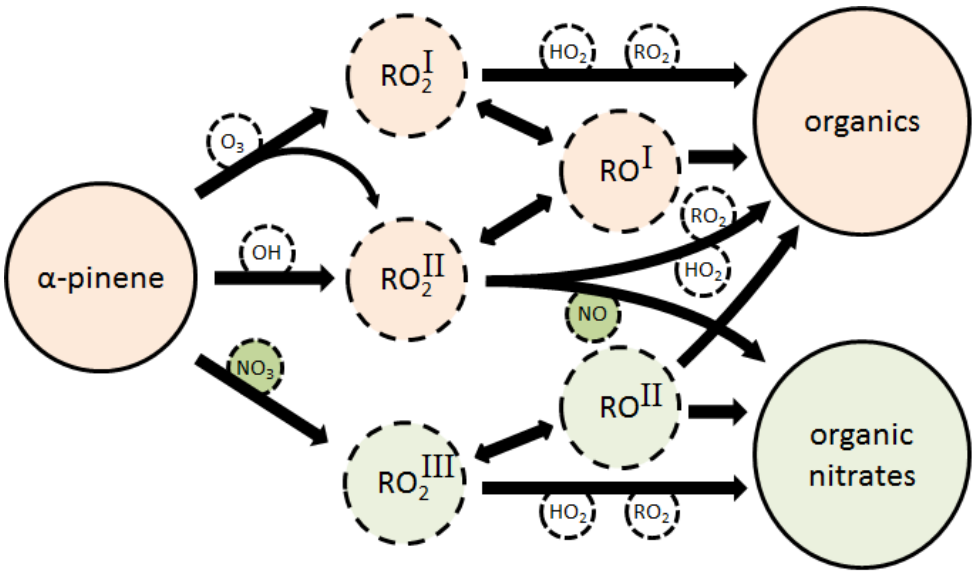

Fig. S2. Schematic representation of the reaction mechanism used in the lumped kinetic box model. Large solid circles denote stable compounds, whereas dashed circles are radical species. Small dashed circles on arrows denote small gas-phase species participating in the reaction; if more than one species is given, the arrow represents two possible reaction pathways. Orange shadings indicate non-nitrated, green shadings indicate nitrated organic compounds. Double arrows between RO and RO_2 species indicate a possible forward and backward reaction. These reactions can be facilitated by reaction with NO or NO_3 (not shown).

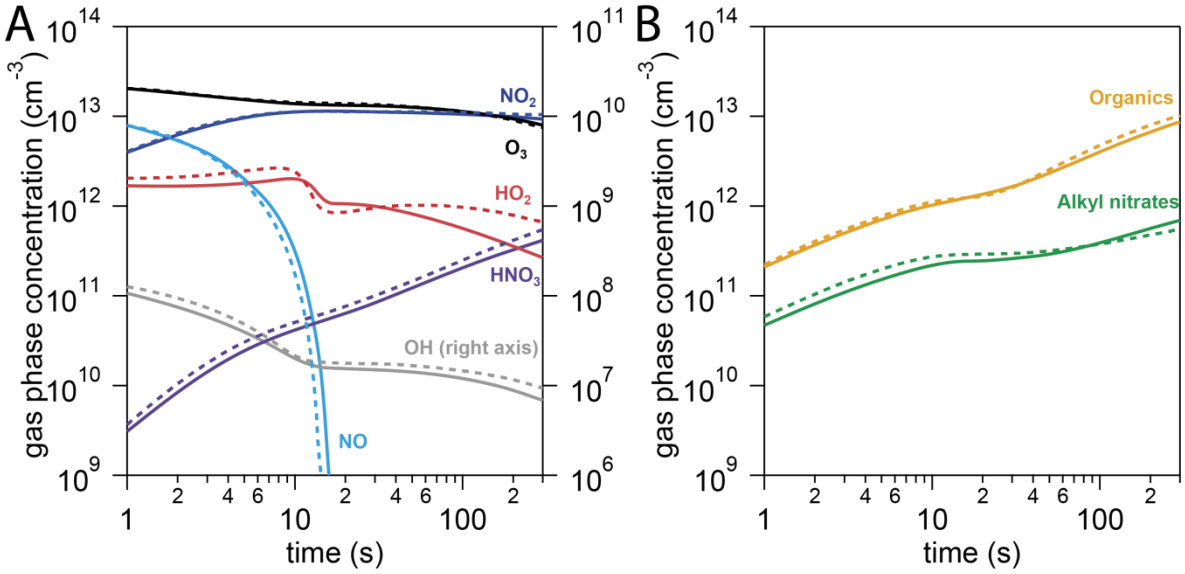

Fig. S3. Comparison of model results from full MCM mechanism (solid lines) and lumped model (dashed lines) showing the gas phase concentrations of a selection of important (a) inorganic and (b) organic compounds. In the MCM representation, the total concentrations were obtained by summing over all organic compounds (excluding CO, CH_4, CO_2) and alkyl nitrates (excluding peroxyacylnitrates (PAN)), respectively.

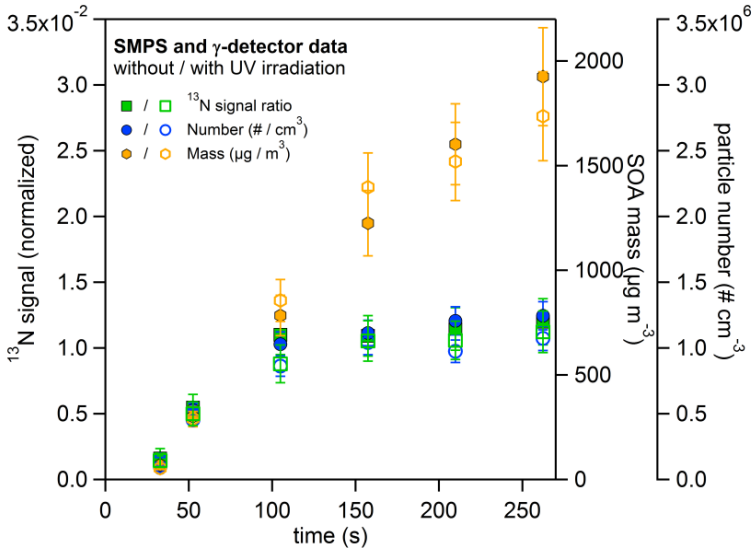

Fig. S4. SOA mass (orange hexagons), aerosol particle number concentration (blue circles) and normalized ^{13}N signal (green squares) in the particle phase as function of reaction time in the flow tube reactor upon mixing of 900 ppb O3, 50 ppb NO and 1000 ppb α-pinene. Open markers represent experimental results upon UV irradiation, whereas closed markers represent separate experiments without irradiation with UV light.

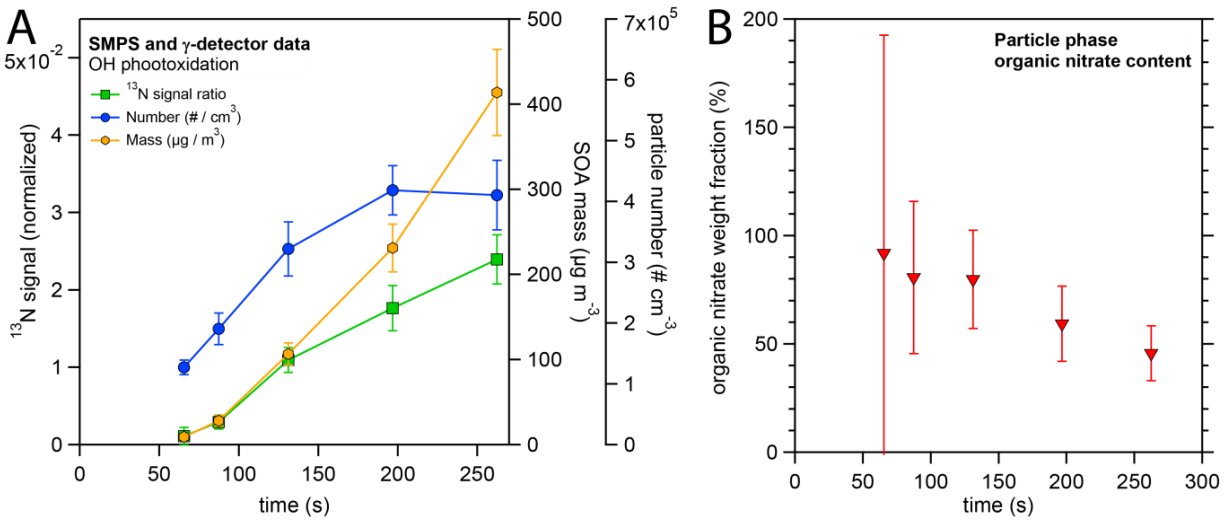

Fig. S5. Panel A: Results for OH photooxidation experiments in the flow tube reactor. SOA mass (orange hexagons), aerosol particle number concentration (blue circles) and normalized ^{13}N signal (green squares) in the particle phase. OH is generated via HONO photolysis. Panel B: Organic nitrate mass fraction as function of reaction time.

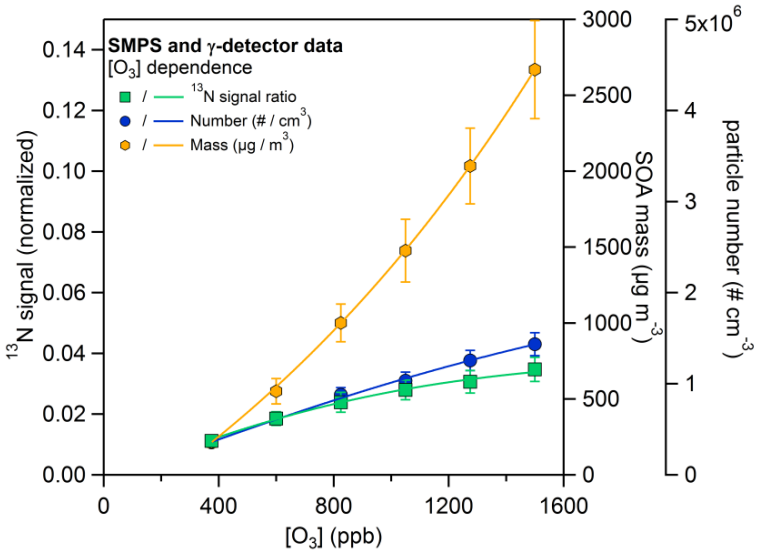

Fig. S6. Ozone concentration dependence of SOA mass (orange hexagons), aerosol particle number concentration (blue circles) and normalized ^{13}N signal (green squares) in the particle phase. Solid lines are to guide the eye.

References

1. Kerbrat, M.; Huthwelker, T.; Gäggeler, H. W.; Ammann, M., Interaction of Nitrous Acid with Polycrystalline Ice: Adsorption on the Surface and Diffusion into the Bulk. *J. Phys. Chem. C* **2010,** *114*, (5), 2208-2219.

2. Jenkin, M. E.; Saunders, S. M.; Pilling, M. J., The tropospheric degradation of volatile organic compounds: a protocol for mechanism development. *Atmos. Environ.* **1997,** *31*, (1), 81-104.

3. Saunders, S. M.; Jenkin, M. E.; Derwent, R. G.; Pilling, M. J., Protocol for the development of the Master Chemical Mechanism, MCM v3 (Part A): tropospheric degradation of non-aromatic volatile organic compounds. *Atmos. Chem. Phys.* **2003,** *3*, (1), 161-180.

4. Brauers, T.; Rohrer, F. Easy AtmoSpheric chemistrY. http://www.fz-juelich.de/iek/iek-8/EN/Expertise/Infrastructure/SAPHIR/Easy/Easy_pdf.pdf?__blob=publicationFile

5. Aumont, B.; Szopa, S.; Madronich, S., Modelling the evolution of organic carbon during its gas-phase tropospheric oxidation: development of an explicit model based on a self generating approach. *Atmos. Chem. Phys.* **2005,** *5*, (9), 2497-2517.

6. Camredon, M.; Aumont, B.; Lee-Taylor, J.; Madronich, S., The SOA/VOC/NOx system: an explicit model of secondary organic aerosol formation. *Atmos. Chem. Phys.* **2007,** *7*, (21), 5599-5610.

7. Valorso, R.; Aumont, B.; Camredon, M.; Raventos-Duran, T.; Mouchel-Vallon, C.; Ng, N. L.; Seinfeld, J. H.; Lee-Taylor, J.; Madronich, S., Explicit modelling of SOA formation from α-pinene photooxidation: sensitivity to vapour pressure estimation. *Atmos. Chem. Phys.* **2011,** *11*, (14), 6895-6910.

8. Ehn, M.; Thornton, J. A.; Kleist, E.; Sipila, M.; Junninen, H.; Pullinen, I.; Springer, M.; Rubach, F.; Tillmann, R.; Lee, B.; Lopez-Hilfiker, F.; Andres, S.; Acir, I. H.; Rissanen, M.; Jokinen, T.; Schobesberger, S.; Kangasluoma, J.; Kontkanen, J.; Nieminen, T.; Kurten, T.; Nielsen, L. B.; Jorgensen, S.; Kjaergaard, H. G.; Canagaratna, M.; Dal Maso, M.; Berndt, T.; Petaja, T.; Wahner, A.; Kerminen, V. M.; Kulmala, M.; Worsnop, D. R.; Wildt, J.; Mentel, T. F., A large source of low-volatility secondary organic aerosol. *Nature* **2014,** *506*, (7489), 476–479.

9. Steimer, S. S.; Berkemeier, T.; Gilgen, A.; Krieger, U. K.; Peter, T.; Shiraiwa, M.; Ammann, M., Shikimic acid ozonolysis kinetics of the transition from liquid aqueous solution to highly viscous glass. *Phys. Chem. Chem. Phys.* **2015,** *17*, 31101-31109.

10. Crowley, J. N.; Ammann, M.; Cox, R. A.; Hynes, R. G.; Jenkin, M. E.; Mellouki, A.; Rossi, M. J.; Troe, J.; Wallington, T. J., Evaluated kinetic and photochemical data for atmospheric chemistry: Volume V - heterogeneous reactions on solid substrates. *Atmos. Chem. Phys.* **2010,** *10*, (18), 9059-9223.

11. Gržinić, G.; Bartels-Rausch, T.; Berkemeier, T.; Türler, A.; Ammann, M., Viscosity controls humidity dependence of N2O5 uptake to citric acid aerosol. *Atmos. Chem. Phys.* **2015,** *15*, (23), 13615-13625.

12. Vlasenko, A.; Huthwelker, T.; Gäggeler, H. W.; Ammann, M., Kinetics of the heterogeneous reaction of nitric acid with mineral dust particles: an aerosol flowtube study. *Phys. Chem. Chem. Phys.* **2009,** *11*, (36), 7921-7930.